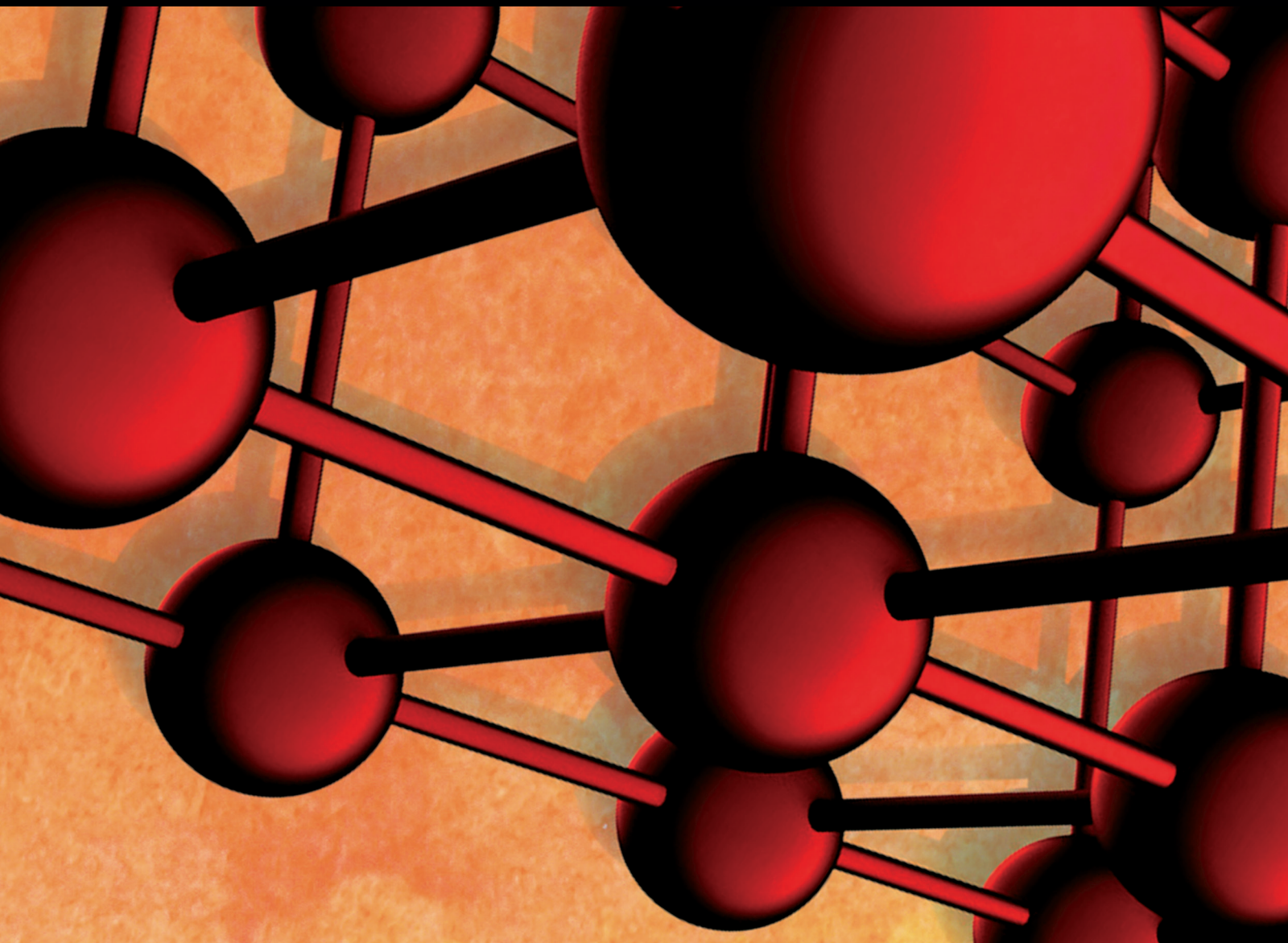


Advances in Materials Science and Engineering

Microscopic Techniques in Material Science: Current Trends in the Area of Blends, Composites, and Hybrid Materials

Lead Guest Editor: Joanna Rydz

Guest Editors: Alena Šišková and Anita Andicsová Eckstein





**Microscopic Techniques in Material Science:
Current Trends in the Area of Blends,
Composites, and Hybrid Materials**

Advances in Materials Science and Engineering

**Microscopic Techniques in Material Science:
Current Trends in the Area of Blends,
Composites, and Hybrid Materials**

Lead Guest Editor: Joanna Rydz

Guest Editors: Alena Šišková and Anita Andicsová Eckstein



Copyright © 2019 Hindawi. All rights reserved.

This is a special issue published in “Advances in Materials Science and Engineering.” All articles are open access articles distributed under the Creative Commons Attribution License, which permits unrestricted use, distribution, and reproduction in any medium, provided the original work is properly cited.

Editorial Board

Antonio Abate, Germany
H.P.S Abdul Khalil, Malaysia
Michael Aizenshtein, Israel
Hamed Akhavan, Portugal
Jarir Aktaa, Germany
Amelia Almeida, Portugal
Rajan Ambat, Denmark
K. G. Anthymidis, Greece
Santiago Aparicio, Spain
Raul Arenal, Spain
Alicia E. Ares, Argentina
Farhad Aslani, Australia
Apostolos Avgeropoulos, Greece
Renal Backov, France
Markus Bambach, Germany
Amit Bandyopadhyay, USA
Massimiliano Barletta, Italy
Stefano Bellucci, Italy
Avi Bendavid, Australia
Brahim Benmokrane, Canada
Jamal Berakdar, Germany
Jean-Michel Bergheau, France
Guillaume Bernard-Granger, France
Giovanni Berselli, Italy
Patrice Berthod, France
Michele Bianchi, Italy
Hugo C. Biscaia, Portugal
Antonio Boccaccio, Italy
Susmita Bose, USA
H. - G. Brokmeier, Germany
Steve Bull, UK
Gianlorenzo Bussetti, Italy
Jose M. Cabrera, Spain
Antonio Caggiano, Germany
Veronica Calado, Brazil
Marco Cannas, Italy
Paolo Andrea Carraro, Italy
Victor M. Castaño, Mexico
Michelina Catauro, Italy
Robert Černý, Czech Republic
Jose Cesar de Sa, Portugal
Daolun Chen, Canada
Wensu Chen, Australia
Francisco Chinesta, France
Er-Yuan Chuang, Taiwan
Gianluca Cicala, Italy
Francesco Colangelo, Italy
Marco Consales, Italy
María Criado, Spain
Gabriel Cuello, France
Lucas da Silva, Portugal
Narendra B. Dahotre, USA
João P. Davim, Portugal
Angela De Bonis, Italy
Abílio De Jesus, Portugal
Luca De Stefano, Italy
Francesco Delogu, Italy
Luigi Di Benedetto, Italy
Aldo Di Carlo, Italy
Maria Laura Di Lorenzo, Italy
Marisa Di Sabatino, Norway
Luigi Di Sarno, Italy
Ana María Díez-Pascual, Spain
Guru P. Dinda, USA
Nadka Tzankova Dintcheva, Italy
Hongbiao Dong, China
Mingdong Dong, Denmark
Frederic Dumur, France
Stanislaw Dymek, Poland
Kaveh Edalati, Japan
Philip Eisenlohr, USA
Claude Estournès, France
Lúis Evangelista, Norway
Michele Fedel, Italy
F. J. Fernández Fernández, Spain
Isabel J. Ferrer, Spain
Paolo Ferro, Italy
Dora Foti, Italy
Massimo Fresta, Italy
Pasquale Gallo, Japan
Germà Garcia-Belmonte, Spain
Santiago Garcia-Granda, Spain
Carlos Garcia-Mateo, Spain
Georgios I. Giannopoulos, Greece
Ivan Giorgio, Italy
Antonio Gloria, Italy
Vincenzo Guarino, Italy
Daniel Guay, Canada
Gianluca Gubbiotti, Italy
Jenö Gubicza, Hungary
Xuchun Gui, China
Benoit Guiffard, France
Ivan Gutierrez-Urrutia, Japan
Hiroki Habazaki, Japan
Simo-Pekka Hannula, Finland
Akbar Heidarzadeh, Iran
David Holec, Austria
Satoshi Horikoshi, Japan
David Houivet, France
Rui Huang, USA
Yi Huang, UK
Michele Iafisco, Italy
Erdir Ibrahim, UK
Saliha Ilican, Turkey
Md Mainul Islam, Australia
Ilia Ivanov, USA
Hom Kandel, USA
kenji Kaneko, Japan
Fuat Kara, Turkey
Katsuyuki Kida, Japan
Akihiko Kimura, Japan
Soshu Kirihara, Japan
Paweł KDoowski, Poland
Jan Koci, Czech Republic
Fantao Kong, China
Ling B. Kong, Singapore
Lingxue Kong, Australia
Pramod Koshy, Australia
Hongchao Kou, China
Alexander Kromka, Czech Republic
Andrea Lamberti, Italy
Luciano Lamberti, Italy
Fulvio Lavecchia, Italy
Marino Lavorgna, Italy
Laurent Lebrun, France
Joon-Hyung Lee, Republic of Korea
Pavel Lejcek, Czech Republic
Cristina Leonelli, Italy
Ying Li, USA
Yuanshi Li, Canada
Yuning Li, Canada
Guang-xing Liang, China

Barbara Liguori, Italy
Jun Liu, China
Meilin Liu, Georgia
Shaomin Liu, Australia
Yunqi Liu, China
Zhiping Luo, USA
Fernando Lusquiños, Spain
Peter Majewski, Australia
Georgios Maliaris, Greece
Muhamamd A. Malik, UK
Dimitrios E. Manolakos, Greece
Necmettin Maraşlı, Turkey
Enzo Martinelli, Italy
Alessandro Martucci, Italy
Yoshitake Masuda, Japan
Bobby Kannan Mathan, Australia
Roshan Mayadunne, Australia
Mamoun Medraj, Canada
Shazim A. Memon, Kazakhstan
Philippe Miele, France
A. E. Miroshnichenko, Australia
Hossein Moayedi, Vietnam
Sakar Mohan, India
Jose M. Monzo, Spain
Michele Muccini, Italy
Alfonso Muñoz, Spain
Roger Narayan, USA
Rufino M. Navarro, Spain
Miguel Navarro-Cia, UK
Ali Nazari, Australia
Behzad Nematollahi, Australia
Luigi Nicolais, Italy
Peter Niemz, Switzerland
Hiroshi Noguchi, Japan
Chérif Nouar, France
Olanrewaju Ojo, Canada
Dariusz Oleszak, Poland
Laurent Orgéas, France
Togay Ozbakkaloglu, UK
Nezih Pala, USA
Marián Palcut, Slovakia
Davide Palumbo, Italy
Gianfranco Palumbo, Italy
A. Maria Paradowska, Australia
Zbyšek Pavlík, Czech Republic
Matthew Peel, UK
Alessandro Pegoretti, Italy
Gianluca Percoco, Italy
Claudio Pettinari, Italy
Giorgio Pia, Italy
Silvia M. Pietralunga, Italy
Daniela Pilone, Italy
Teresa M. Piqué, Argentina
Candido Fabrizio Pirri, Italy
Marinos Pitsikalis, Greece
Alain Portavoce, France
Simon C. Potter, Canada
Ulrich Prah, Germany
Viviana F. Rahhal, Argentina
Carlos R. Rambo, Brazil
Shahed Rasekh, Portugal
Manijeh Razeghi, USA
Paulo Reis, Portugal
Yuri Ribakov, Israel
Aniello Riccio, Italy
Anna Richelli, Italy
Antonio Riveiro, Spain
Marco Rossi, Italy
Sylvie Rossignol, France
Pascal Roussel, France
Fernando Rubio-Marcos, Spain
Francesco Ruffino, Italy
Mark H. Rummeli, China
Pietro Russo, Italy
Antti Salminen, Finland
F.H. Samuel, Canada
MariaGabriella Santonicola, Italy
Hélder A. Santos, Finland
Carlo Santulli, Italy
Fabrizio Sarasini, Italy
Michael J. Schütze, Germany
Raffaele Sepe, Italy
Kenichi Shimizu, USA
Fridon Shubitidze, USA
Mercedes Solla, Spain
Donato Sorgente, Italy
Charles C. Sorrell, Australia
Andres Sotelo, Spain
Costas M. Soukoulis, USA
Damien Soulat, France
Adolfo Speghini, Italy
Antonino Squillace, Italy
Koichi Sugimoto, Japan
Baozhong Sun, China
Sam-Shajing Sun, USA
Youhong Tang, Australia
Kohji Tashiro, Japan
Miguel Angel Torres, Spain
Laszlo Toth, France
Achim Trampert, Germany
Tomasz Trzepieciński, Poland
Matjaz Valant, Slovenia
Luca Valentini, Italy
Ashkan Vaziri, USA
Lijing Wang, Australia
Rui Wang, China
Zhongchang Wang, Portugal
Lu Wei, China
Jörg M. K. Wiezorek, USA
Jiang Wu, China
Guoqiang Xie, China
Dongmin Yang, UK
Zhonghua Yao, China
Hemmige S. Yathirajan, India
Yee-wen Yen, Taiwan
Wenbin Yi, China
Ling Yin, Australia
Tetsu Yonezawa, Japan
Hiroshi Yoshihara, Japan
Belal F. Yousif, Australia
Lenka Zajíčková, Czech Republic
Michele Zappalorto, Italy
Gang Zhang, Singapore
Jinghuai Zhang, China
Li Zhang, China
Meng Zhang, USA
Mikhail Zheludkevich, Germany
Wei Zhou, China
You Zhou, Japan
Hongtao Zhu, Australia
J. A. Fonseca de Oliveira Correia, Portugal

Contents

Microscopic Techniques in Materials Science: Current Trends in the Area of Blends, Composites, and Hybrid Materials

Joanna Rydz , Alena Šišková, and Anita Andicsová Eckstein
Editorial (2 pages), Article ID 9072958, Volume 2019 (2019)

FIB-SEM Three-Dimensional Tomography for Characterization of Carbon-Based Materials

Nan Nan , and Jingxin Wang 
Review Article (8 pages), Article ID 8680715, Volume 2019 (2019)

Scanning Electron Microscopy and Atomic Force Microscopy: Topographic and Dynamical Surface Studies of Blends, Composites, and Hybrid Functional Materials for Sustainable Future

Joanna Rydz , Alena Šišková, and Anita Andicsová Eckstein
Review Article (16 pages), Article ID 6871785, Volume 2019 (2019)

Structures, Morphological Control, and Antibacterial Performance of Ag/TiO₂ Micro-Nanocomposite Materials

Muhammad Akhsin Muflikhun , Alvin Y. Chua , and Gil N. C. Santos
Research Article (12 pages), Article ID 9821535, Volume 2019 (2019)

Mechanical Properties, Failure Mode, and Microstructure of Soil-Cement Modified with Fly Ash and Polypropylene Fiber

Xue-lei Duan , and Jing-shuang Zhang 
Research Article (13 pages), Article ID 9561794, Volume 2019 (2019)

Development, Performance, and Microscopic Analysis of New Anchorage Agent with Heat Resistance, High Strength, and Full Length

Xiaohu Liu , Zhishu Yao , Weipei Xue , and Xiang Li 
Research Article (9 pages), Article ID 4239486, Volume 2019 (2019)

Effects of High-Density Pulse Currents on the Solidification Structures of Cu-SiC_p/AZ91D Composites

Xi Hao, Weixin Hao , Guihong Geng , Teng Ma , Chen Wang, Fuqiang Zhao , Hao Song, and Yugui Li 
Research Article (6 pages), Article ID 1684580, Volume 2019 (2019)

Recent Advances in Characterization Techniques for the Interface in Carbon Nanotube-Reinforced Polymer Nanocomposites

Junjie Chen , Xuhui Gao , and Deguang Xu 
Review Article (24 pages), Article ID 5268267, Volume 2019 (2019)

Microstructure Characteristics of GFRP Reinforcing Bars in Harsh Environment

Hilal El-Hassan , and Tamer El Maaddawy
Review Article (19 pages), Article ID 8053843, Volume 2019 (2019)

Development of Strength for Calcium Aluminate Cement Mortars Blended with GGBS

Hee Jun Yang , Ki Yong Ann , and Min Sun Jung 
Research Article (12 pages), Article ID 9896012, Volume 2019 (2019)

Editorial

Microscopic Techniques in Materials Science: Current Trends in the Area of Blends, Composites, and Hybrid Materials

Joanna Rydz ¹, Alena Šišková,² and Anita Andicsová Eckstein³

¹Centre of Polymer and Carbon Materials, Polish Academy of Sciences, 41-800 Zabrze, Poland

²Institute of Materials and Machine Mechanics, Slovak Academy of Sciences, 845 13 Bratislava, Slovakia

³Polymer Institute, Slovak Academy of Sciences, 845 41 Bratislava, Slovakia

Correspondence should be addressed to Joanna Rydz; jrydz@cmpw-pan.edu.pl

Received 24 July 2019; Accepted 24 July 2019; Published 20 August 2019

Copyright © 2019 Joanna Rydz et al. This is an open access article distributed under the Creative Commons Attribution License, which permits unrestricted use, distribution, and reproduction in any medium, provided the original work is properly cited.

Microscopic techniques such as optical microscopy (conventional light microscopy (LM), fluorescence microscopy (FM), confocal/multiphoton microscopy, and stimulated emission depletion microscopy (STED)), scanning probe microscopy (scanning tunnelling microscopy (STM), atomic force microscopy (AFM), near-field scanning optical microscopy, and others) as well as electron microscopy (scanning electron microscopy (SEM), transmission electron microscopy (TEM), scanning transmission electron microscopy (STEM), and focus ion beam microscopy (FIB)) are often used in materials science. Those techniques make it possible to assess the morphology, composition, physical properties, and dynamic behaviour of materials, thus making a significant contribution to the development of materials science. They are necessary for both the quality control of products and the development of new materials. Design, synthesis, characterisation, and development of useful innovative, technologically advanced, adaptable, and multifunctional materials and devices with lower mass, smaller volume, higher efficiency, and lower cost, in particular novel materials and structures, are rapidly growing fields of materials science. Advanced blends, composites, and hybrid materials are the most-developing classes of new materials based on ceramic, glass, silica, and carbon that lead to numerous technological innovations. Metals and alloys, intermetallic composites, magnetic materials, ionic crystals, covalent crystals, coatings, films, foils, and pigments are used for advanced applications. Above all, functional materials are found applications in automotive and transportation industry, aeronautics and space industry, and energy, engineering, and environmental sectors. New solutions are also

being developed in agriculture and horticulture sectors and packaging and food-service sectors. Knowledge on the relationships between structures, properties, functions, and performance is essential for prospective safe applications of such materials in the areas of human health (in medical, pharmaceutical, and dental industry) and the environment. The study of the physical and technical foundation of the latest developments in the areas described is based on microscopic techniques that are also used in a variety of industrial applications, including topographic and dynamical surface studies of many materials. Fundamental and applied research in emerging application areas in nanotechnology, interfacial science and engineering, advanced manufacturing, catalysis, bioengineering, bio-inspired synthesis, green production routes, sensing, and actuation is often also based on microscopic techniques.

The aim of the Special Issue was not only to present novel achievements and contribution of microscopic techniques to the development of materials science but also to present significant improvements to proven research techniques and recent technical and methodological changes, particularly in applications in the field of human health and the environment. The proposed scope concerned to research on the design, synthesis, characterisation, development, and manufacturing of useful innovative, technologically advanced materials and devices that have general applicability and that form the basis for the evolving knowledge about blends, composites, and hybrid materials. Special emphasis was placed on environmentally friendly blends, composites, and hybrid materials from renewable resources with no adverse effect on the environment, with a short global carbon life cycle, with green

production routes, suitable to recycle materials based on natural, renewable, and synthetic polymers for the sustainable future.

The articles in the special issue focus mainly on the characterisation of new materials using microscopic techniques, especially SEM and AFM. The first paper in this Special Issue presents an overview of the recent advances of the three-dimensional (3D) characterisation of carbon-based materials conducted using focused ion beam-scanning electron microscope (FIB-SEM) tomography. Current studies and further potential applications of the FIB-SEM 3D tomography for carbon-based materials are discussed. The advances of FIB-SEM 3D reconstruction are highlighted to reveal the high and accurate resolution of internal structures of carbon-based materials, as well as suggestions for the adoption and improvement of the FIB-SEM tomography system for broad carbon-based research. The next article provides an overview of topographic and dynamical surface studies of (bio)degradable polymers, in particular aliphatic polyesters, the most promising ones. The (bio)degradation process promotes physical and chemical changes in material properties that can be characterised by microscopic techniques. These changes occurring both under controlled conditions as well as in the processing stage or during use indicate morphological and structural transformations resulting from the deterioration of the material and have a significant impact on the characteristic of materials used in many applications, for example, for use as packaging. The following article examines the structure, morphological control, and antibacterial activity of silver-titanium dioxide (Ag/TiO_2) micro-nanocomposite materials against *Staphylococcus aureus* using SEM, energy dispersive X-ray (EDX) spectroscopy, and AFM. The results revealed that the shape of micro- and nanocomposites materials could be arranged by adjusting the parameters. The proper nanorod structure, ideal for antibacterial applications, is obtained at 1000°C growth temperature during 8 hours of baking. Treating of *S. aureus* stock with Ag/TiO_2 nanocomposites is able to reduce bacterial growth with a significant result. In the next article, a SEM analysis is conducted to investigate the effect of fly ash and polypropylene fibres on the microstructure of soil-cement with different polypropylene fibre contents. Also to solve the problems of failure of pretensioned bolt supports under high ground pressure and temperature, a new kind of anchorage agent with excellent performance has been developed. The reasons for this excellent performance in physical and mechanical tests compared to a conventional full-length anchorage agent were examined, among others, by SEM imaging. Subsequently, Cu-SiCp/AZ91D composites were prepared with high-density pulse currents. The wettability between SiCp and matrix during solidification is improved by coating a $0.095\ \mu\text{m}$ thick copper film on the surface of SiCp. In order to analyse the tissue changes of the samples, SEM analysis of solidification structures at high resolution for elemental scanning was performed. Another review concerns the current state of characterisation techniques for the interface in carbon nanotube-reinforced polymer nanocomposites. The different types of interfaces that exist within the nanocomposites are listed. The emerging

trends in characterisation techniques and methodologies for the interface are presented, and their strengths and limitations are summarised. The intrinsic mechanism of the interactions at the interface between the carbon nanotubes and the polymer matrix is discussed. Special attention is given to the chemical functionalisation of carbon nanotubes. The last review presents critically existing studies on the microstructure of glass fibre reinforced polymers (GFRPs) reinforcing bars exposed to various conditioning regimes. In addition, the review identifies research gaps in the existing knowledge and highlights the directions for future research. Fibre reinforced polymer (FRP) composites are proposed as corrosion-resistant alternatives to traditional steel reinforcement in concrete structures. In this group of composites, GFRPs are the primary selection of FRP for construction applications. Despite the fact that they have many advantages, their widespread use by the industry is hindered due to the deterioration of their performance in severe environmental conditions. The last article examines the development of strength in different calcium aluminate cement (CAC) mixture mortars with granulated ground blast-furnace slag (GGBS). In addition, the pore structure analysis is accompanied to quantify the porosity. The surfaces of the fragment for cement paste of CAC-GGBS mixtures cured at 365 days were investigated using SEM analysis. The presence of stratlingite was detected. To compare atomic ratios (Ca/Al and Si/Al) at the C2ASH phase in the paste of the binary mixtures, EDS analysis was performed simultaneously.

The special issue presents a contemporary overview of latest developments in the field of advanced blends, composites, and hybrid materials, in particular the latest breakthroughs and approaches in the science of those materials leading to the development of the new generation of multifunctional materials with enhanced features and improved properties for the production of high-performance systems and devices using microscopic techniques.

Conflicts of Interest

The editors declare that there are no conflicts of interest.

Joanna Rydz
Alena Šišková
Anita Andicsová Eckstein

Review Article

FIB-SEM Three-Dimensional Tomography for Characterization of Carbon-Based Materials

Nan Nan  and Jingxin Wang 

Division of Forestry and Natural Resources, Davis College of Agriculture, Natural Resources and Design, West Virginia University, Morgantown, WV 26505, USA

Correspondence should be addressed to Jingxin Wang; jxwang@wvu.edu

Received 12 April 2019; Revised 14 June 2019; Accepted 27 June 2019; Published 21 July 2019

Guest Editor: Anita Andicsová Eckstein

Copyright © 2019 Nan Nan and Jingxin Wang. This is an open access article distributed under the Creative Commons Attribution License, which permits unrestricted use, distribution, and reproduction in any medium, provided the original work is properly cited.

A review on the recent advances of the three-dimensional (3D) characterization of carbon-based materials was conducted by focused ion beam-scanning electron microscope (FIB-SEM) tomography. Current studies and further potential applications of the FIB-SEM 3D tomography technique for carbon-based materials were discussed. The goal of this paper is to highlight the advances of FIB-SEM 3D reconstruction to reveal the high and accurate resolution of internal structures of carbon-based materials and provide suggestions for the adoption and improvement of the FIB-SEM tomography system for a broad carbon-based research to achieve the best examination performances and enhance the development of innovative carbon-based materials.

1. Introduction

In the past couple of decades, various carbon-based materials and their applications have been rapidly developed and they have played an important role in modern material sciences. Especially, the utilizations of inexpensive and sustainable carbon materials have been extensively studied for renewable energy storage (e.g., supercapacitors [1–5] and batteries [6–8]), adsorbent (e.g., soil amendment [9–11], water purification [12–14], and gas separation [15–18]), composites with enhanced certain properties (e.g., thermal and mechanical enhancement) [19–22], and catalysts of fuel cells [23] and other chemical reactions [24, 25]. Therefore, along with the electrochemical, chemical, and mechanical properties, it is vital to investigate and further optimize or control the morphologies and internal structural features of the versatile carbon-based materials through design, synthesis, and improvement steps.

To support the advanced product design and processing, three-dimensional (3D) and geometry-sensitive features of the carbon-based materials are desired. However, the most commonly used scanning electron microscope (SEM)

technique is only able to reveal the features on surface of the materials. Transmission electron microscopy (TEM) may be an option and great for characterization at nanoscale, but it is difficult to process the appropriate samples and could be expensive to perform. X-ray tomography allows three-dimensional quantitative measurements with the advantages of nondestruction and relatively high spatial resolution, but due to the restriction on the penetration ability of X-ray, it is not a good option for high-density and large-volume samples [26].

The focused ion beam-scanning electron microscope (FIB-SEM) system is a new approach to investigate the three-dimensional internal structures of various materials because of its good performance and easy process. There are almost no limitations on the specimen materials using this technique [27]. A completed FIB-SEM 3D tomography analysis includes three main sections: FIB-SEM processing, imaging analysis, and quantitative 3D reconstruction. FIB is used for serial sectioning/milling the sample, and SEM can image the exposed cross-sectional region (Figure 1). The FIB and SEM beams have coincident angles of 52/54° (in the current commercial type). Milling rates (ion-beam acceleration voltage and current) in FIB can be varied depending

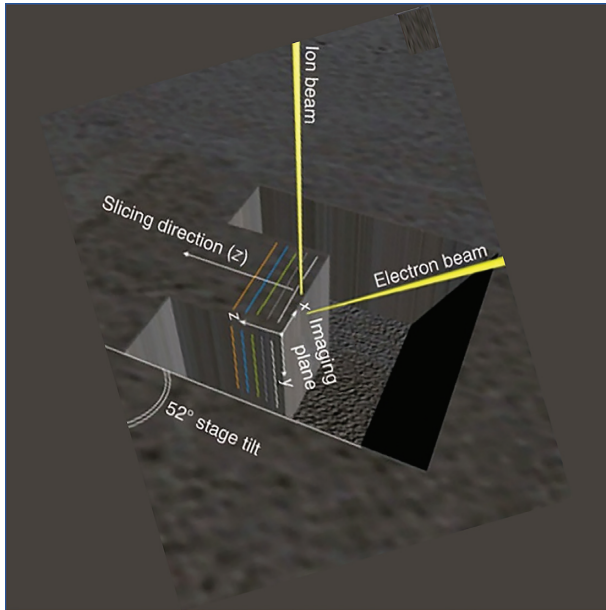


FIGURE 1: The schematic diagram of the FIB-SEM system [26].

on the difference in hardness and geometrical rigid integrity of the sample materials. After the FIB-SEM process, the software (e.g., Avizo) continues to analyze generated data and conduct 3D reconstruction to obtain quantitative 3D tomography results (Figure 2). Additionally, FIB instruments can be equipped with electron dispersive spectroscopy (EDS) and electron back-scatter diffraction (EBSD) collection systems, allowing for chemical, crystallographic, and topological data to be obtained on each slice [28, 29].

The FIB-SEM 3D tomography technology is expected to help advance the research in carbon-based materials. This paper provides an overview of the current status of the FIB-SEM system in carbon-based material science research, discusses the further potential applications of FIB-SEM in carbon and carbon-based materials, including methodology, crucial parameters, and problems and corresponding solutions, and concludes with an assessment of the promising role of the FIB-SEM 3D tomography technique in development of advanced innovative carbon-based materials.

2. FIB-SEM 3D Tomography in Current Carbon-Based Material Studies

In recent years, the FIB-SEM tomography system has been tentatively applied to characterize the microstructures of some carbon-based materials used for the applications of batteries, supercapacitors, and fuel cells. Table 1 lists the majority of carbon-based material studies that used the FIB-SEM tomography system. Generally, in the previous carbon-based material studies, the utilizations of FIB-SEM systems can be classified into two major categories including the 2D observation of the FIB-SEM cross-section images and the visual and quantitative analyses using the 3D reconstruction of the stacking of FIB-SEM cross-section images.

2.1. 2D Observation of FIB-SEM Cross-Sectional Images. FIB-SEM tomography is a very useful approach to investigate the subsurface imaging of various materials. Compared to the conventional SEM that only focuses on the surface morphology, FIB-SEM is able to provide more information of the internal structures through analyzing the 2D cross-sectional images. FIB-SEM is ideally suited for the characterization of micron and submicron scale to a minimum resolution values of about 10–15 nm [26]. The limitations of this technique make it difficult to image the structure that is smaller than 5–10 nm [43]. Figure 3 shows the resolution ranges for several modern tomography methods to meet the needs of different research purposes.

The FIB-SEM has been used to investigate the subsurface images in current studies of carbon-based materials. For instance, Rodriguez et al. [41] used the FIB-SEM to observe the open three-dimensional structure of the modified hierarchical nanoporous carbon (Figure 4(a)). In the study of Yürüm et al. [40], FIB-SEM showed a clear layer of iron oxide particles covering oxidized activated carbon and they found that the uniform layers can rapidly be grown through the microwave hydrothermal synthesis. Zhang et al. [48] showed the core-shell and yolk-shell nanostructures of carbon spheres using FIB-SEM. Ogihara et al. [36] found that the cross-sectional FIB-SEM images of the electrodes indicated that 2,6-Naph(COOLi)₂ particles were covered with conductive nanocarbon and revealed uniform pore structures in the internal. When Liu et al. [31] hybridized graphene in Ni foam using chemical vapor deposition, the FIB-SEM images showed the graphene grown on Ni foam, and the Wrinkle-like graphene with irregular fractures was found to fully cover the Ni foam skeleton. Singh et al. [32] observed the clearly visible interconnected porous layer of nanoporous gold in the pristine nanoporous gold layer with a thickness of ca. 130 nm. The thickness of nanoporous gold-nitrogen-doped carbon nano-onion layer was ca. 750 nm. Shen et al. [33] used FIB-SEM tomography analyses to confirm the fine structure of graphite fluoride-lithium fluoride-lithium (GF-LiF-Li) composite and observed that the GF-LiF-Li composite was composed of three layers, including the top GF-LiF layer, followed by a transitional zone consisting of GF, LiF, and Li metals and a bottom layer consisting solely of Li metal.

2.2. 3D Reconstruction of FIB-SEM Sequential Cross-Sectional Images. Due to limited information extracted from two-dimensional features, the 2D observation cannot be compared to three dimensional and geometry-sensitive features. To reveal the real physical characterization of an element/material and support advanced study, design, and process development, a higher dimensional technology with holistic and accurate information is needed. The FIB-SEM 3D tomography enables the direct observation of the three-dimensional microstructure at nanoscale resolution through the 3D reconstruction of the sequential sets of 2D images. Furthermore, owing to recent advances in imaging and computer technology, numerical simulation based on FIB-SEM 3D tomography technique is one of the most accurate

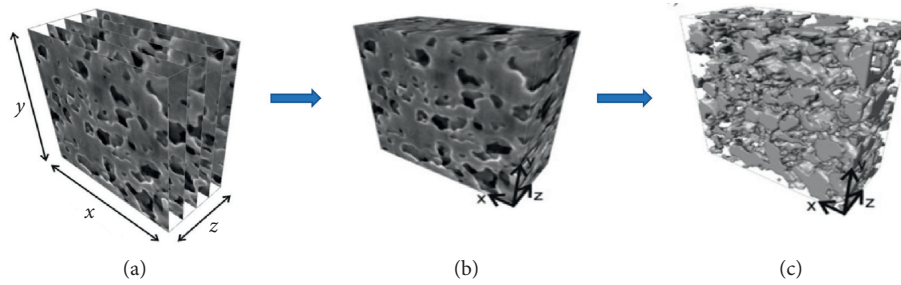


FIGURE 2: The procedures of FIB-SEM 3D reconstruction. (a) Stack of images produced with FIB-SEM, (b) imaging 3D reconstruction, and (c) quantitative 3D reconstruction and modeling [30].

TABLE 1: Short indicative selection of FIB-SEM for carbon-based materials from the literature.

Material	Application	Methodology	Purpose	Year	Reference
Hybrid graphene on Ni foam	Electrode of supercapacitors	Dual Beam Strata 235 (FEI) and Auriga Compact (Zeiss) microscope	To analyze the morphologies and structural features of the composites	2019	[31]
Nanoporous gold-nitrogen-doped carbon nano-onions	Electrode of micro-supercapacitor	FIB-FEG-SEM of Carl Zeiss Auriga Compact-4558	To determine the thickness of the different layers present in the electrode	2019	[32]
Graphite fluoride-lithium	Lithium battery	FIB-SEM, Scios, FEI	To confirm the fine structure of GF-LiF-Li composite	2019	[33]
Carbon nanofiber	Supercapacitor	Auriga Cross Beam, Zeiss Software: Avizo 9.0.0	To examine fiber subsurface microstructure	2018	[34]
Coal	Fuel	FEI Helios Nanolab 650 FIB-SEM system	To quantitative evaluate the 3D characterization of pore-fracture networks of coals	2017	[35]
Conductive carbon black/carbon fiber coating	2,6-Naph(COOLi) ₂ electrodes	FIB: 50 nA current and 7 kV acceleration voltage SEM: operating at 2 kW. Zeiss Auriga 60 dual beam: 20 pA current, 30 kV acceleration voltage, and 9 nm cutting distance	To investigate the nanocarbon coating and the uniformness of pore structures	2016	[36]
Nanoporous carbon-binder	Li-ion batteries	FEI Helios Nanolab 600 FIB-SEM system FIB: 80 pA current and 30 kV acceleration voltage SEM: 5 kV, pixel size of 3 nm	To reconstruct the carbon-binder domain of a LiCoO ₂ battery cathode	2015	[37]
Carbon nanotubes (CNTs) in polymer composites	Nanotechnology	FEI Helios Nanolab 600 FIB-SEM system FIB: 80 pA current and 30 kV acceleration voltage SEM: 3 kV voltage	To investigate the subsurface imaging of CNTs	2015	[38]
Porous carbon-based electrode	Electrode	The voxel size was $10 \times 10 \times 10 \text{ nm}^3$ Software: IMOD, ImageJ, and AVIZO software	To analyze the morphologies and build topographic reconstruction of the porous carbon electrode	2014	[39]
Deposition of porous iron oxide on activated carbon (AC)	Adsorbent	FIB: 10–1 nA current and 30 kV acceleration voltage SEM: 2–5 kV voltage	To understand the nature of iron oxide particles within the pores of AC	2014	[40]
Hierarchical nanoporous carbon synthesized using a hard template method	Electrode	Dual-beam workstation FEI Helios Nanolab 600; a field emission gun SEM	To observe the open 3D porous structure of the carbon	2013	[41]
Nanoporous carbon-supported noble metal catalyst layers	Fuel cells	FIB: 50 pA current and 30 kV acceleration voltage SEM: 2 kV voltage FIB: 27 pA current and 30 kV acceleration voltage SEM: 86 pA current and 5 kV voltage	To characterize porosity, connectivity, and pore-size and grain-size distribution	2013	[42]
Disordered mesoporous carbon with tailored pore size	Fuel cells supercapacitors	The voxel size was $3.57 \times 3.62 \times 10 \text{ nm}^3$ Software: Amira® 5.2 software and MAVI	To visualize and study nonordered pore morphology and quantitatively characterize their physical properties	2013	[30]

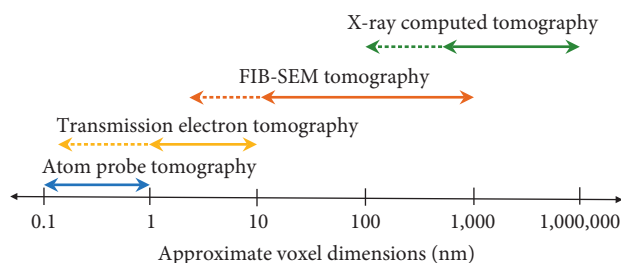


FIGURE 3: The resolution of modern tomographic characterization methods is displayed as an approximate range. Dash lines represent advanced potential range [26, 43–47].

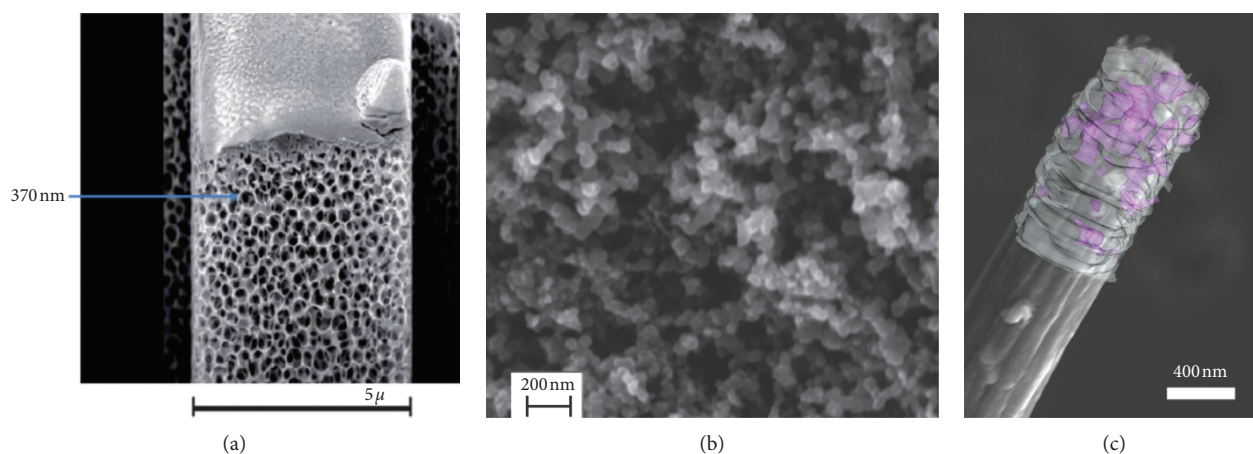


FIGURE 4: FIB-SEM images. (a) Cross-sectional SEM image of a SiO_2 nanoparticle [41], (b) SEM image of microstructure of porous carbon electrode [39], and (c) reconstructed FIB-SEM image applied onto the SEM of a single nanofiber [34].

and effective tools to investigate the nature of material internal structures, such as porous structures [27, 49, 50], phase distribution, crystallographic interfaces, and defect arrangements [26]. However, the quantification errors in the microstructural parameters are inevitable because of the limited sample size and resolutions in the FIB-SEM observation, uncertainty in the image processing (e.g., alignment and segmentation), and the accuracy of the quantification method/model itself applied to the image data [51]. Rapidly advanced FIB, high-resolution SEM, and other observation techniques will assist to mitigate these errors.

Although it is rare, 3D reconstruction using FIB-SEM has been used in several studies of carbon-based materials. For instance, Balach et al. [30] performed a direct and quantitative 3D reconstruction of the internal structure of disordered mesoporous carbon using serial sectioning FIB-SEM with an ion beam current of 27 pA at 30 kV. The samples were reconstructed by the Amira[®] 5.2 software from 25 slices (~10 nm thickness per slice) obtained and further quantitatively analyzed by the software system's Modular Algorithms for Volume Images (MAVI). The total analyzed volume (VT) of material was $0.0625 \mu\text{m}^3$. Their results indicated that FIB-SEM was only able to reveal the 3D shape, distribution, and connectivity of mesopores, since the resolution of SEM was not sufficient for access to pores with a diameter below 2 nm. The structural parameters of the pores including surface area, pore volume, Euler number, total

porosity, and pore size distribution were determined through the 3D reconstruction analysis. Eswara-Moorthy et al. [39] performed a 3D reconstruction of the porous carbon-based electrode using FIB-SEM with an ion beam current of 80 pA at 30 kV (Figure 4(b)). They found that the Pt filling of the pores drastically improved the image contrast between the carbon and the porous phases, and the enhanced image contrast enabled robust semiautomatic demarcation of the interfacial boundaries and subsequent binarization of the images with very high fidelity. Also, through analyzing the 3D reconstruction, the porosity ($72 \pm 2\%$), axial and radial tortuosities (1.45 ± 0.04 and 1.43 ± 0.04), average pore size (90 nm), pore-size-distribution (20–300 nm), surface-to-volume ratio ($46.5 \mu\text{m}^{-1}$), and specific surface area ($13.0 \mu\text{m}^{-1}$) were determined. Their results indicated that porous carbon-based electrode has a very high surface area, which can be more conducive for surface electrochemical reactions. Thiele et al. [42] reported that the FIB-SEM only differentiated the pores and total solid phase from each other, but it was not possible to further differentiate the solid phase into carbon, ionomer, and Pt nanocomponents. FIB-SEM analysis revealed a preferential size in the grain-size-distribution (GSD) of about 65 nm and the pore-size-distribution (PSD) showed highly porous material characteristics with 58% porosity and pores ranging from 7 nm to 350 nm, and 99.9% of the pore area was connected. Liu et al. [34] reconstructed the carbon nanofiber

using FIB-SEM, and the internal MnO particles showed some degree of agglomeration within the fiber (Figure 4(c)). Additionally, the FIB-SEM system was used to characterize microstructural features for three dimensions of carbides in Ni-based high carbon alloy [52] and nanoporous carbon-binder of Li-ion batteries [37].

3. Potential Applications of FIB-SEM 3D Tomography in Carbon-Based Material Studies

To meet the different requirements of various applications for characterization of carbon-based materials, the FIB-SEM 3D tomography will be likely be used to reveal the features or phenomenon in a variety of application fields. It is very valuable to know the potential use of FIB-SEM, what it can do, and possible problems and practical solutions for each specific application.

3.1. Carbons. Tomographic methods using serial-sectioning and imaging processes are suitable for observing the morphology and internal microstructure of carbons, such as graphene, carbon nanotube, carbon black, activated carbon, and biochar, which are extensively used in various applications, for example, quantitative evaluation of the 3D characterization of pore-fracture networks of coals [35], mesoporous carbon [30], and carbon fiber [34]. Moreover, various parameters that are relevant to the microstructures can be numerically evaluated by using the FIB-SEM tomography and implementing 3D reconstruction of serial stacking sectioned SEM images, including surface texture (e.g., roughness), different particle sizes and distribution, and connectivity (pore tortuosity) of the internal material.

In the FIB process, carbons can be classified by volume size. If the initial size of carbon (e.g., a monolithic carbon) is bigger than the best operation range for FIB-SEM, the sample will be adjusted to a proper size for testing. While if the initial size is too small to test by a single sample (e.g., micro/nanocarbon fibers, particles, and nanotubes), a potential method is to cast one or more carbons into a support matrix, such as, epoxy resin [27]. This methodology has been demonstrated by studies of various hierarchical porous materials, such as, zeolite beads [27], silicon [53], monolithic UiO-66-NH₂ material [54], and concrete [46].

The curtain effect may occur in the milling process, which appears as parallel scratches varying in the same direction of ion beam milling and making the image appears to be covered by a semitransparent curtain [27, 55, 56]. The potential reasons are as follows: (1) roughness of the slicing surface varies the angles of the ion beam and causes the differences of the milling rate, and depositing protection layers may mitigate the surface roughness; (2) different characteristics of the elements in the targeting materials can cause curtain effect as well; (3) presence of internal pores in the samples can change the intensity or pathway of ion beam when it passes through the pores. Therefore, currently, the most common and effective curtain-removal solution is adjusting the milling parameters according to the unique

properties of each targeted material or polishing it before milling. Filling the internal pores with additional resin can help recognize the pore region [49, 50].

3.2. Carbon-Based Electrodes. Due to the high energy-to-weight ratio, surface area, conductivity, and micro/nanoporous structure of carbons, porous carbon-based electrodes for the use of various supercapacitors and batteries have gained more attentions recently. Furthermore, porous carbon-based composite electrodes can display both capacitive and faradaic charge storages. Also, carbon electrodes can be involved in much more complex designs to improve the energy density of supercapacitors/batteries [4]. Therefore, it is crucial to accurately examine the porous structures of carbon-based electrodes.

The 3D microstructure of porous electrodes can be investigated by FIB-SEM tomography. The respective morphological characteristics/parameters, volume fraction, spatial distribution, size, connectivity, and tortuosity, can be determined through analyzing the obtained 3D reconstruction using image processing software and modeling. For example, the common used software for image processing includes IMOD, ImageJ [39], Fiji [57], Avizo [34, 35], and Amira 5.5.0 [30, 57]. The algorithm tools for quantification analysis are lab-made MATLAB [58] and Java [59]. The existing reported studies that used the FIB-SEM quantitative 3D reconstruction are porous carbon-based electrode [54], carbon nanofiber based supercapacitor [49], and mesoporous carbon electrode material [56].

3.3. Carbon-Based Catalyst/Coating/Hybrid Layers. The FIB-SEM 3D tomography technique is a useful method for the diagnosis of the catalyst [56, 60], coating [61], or hybrid [31] layer structure as well. It can reconstruct the geometrical properties of the catalyst layer in 3D space. The digital analysis can assist to determine the porosity and the permeability. Also, it is a simple and effective way to understand the degradation mode of the catalyst layer.

The heating/fusion damage may occur in the milling process. It can thermally damage the catalyst layer(s). The liquid nitrogen cooling and thermoelectric cooling via Peltier elements methods have been demonstrated and proved that they can mitigate the heating damage [56]. The thermoelectric cooling is considered to exceed the liquid nitrogen cooling since the thermoelectric cooling enables a short-time sample fabrication at the FIB stage.

3.4. Carbon-Based Polymer Composites. Carbon-based polymer is the most common type of the polymer composites. The addition of carbon fillers likely enhances the certain properties of the polymer to some degrees; for instance, the biochar particle-filled PVA films obtained improved thermal stability, electrical conductivity, and mechanical properties, but the tensile strength of the films was reduced dramatically as the increase of biochar content due to the particle aggregation and porous features of the biochar [20, 62]. Therefore, it is important to investigate the structural

features of the carbon filler and polymer matrix to obtain good designs for fabricating the composites.

The 3D reconstruction using FIB-SEM can be applied to study the dispersion of the carbon filler inside a polymer matrix and the morphology and internal structure of the carbon filler and/or to determine the effect of interphase properties on mechanical properties of nanocomposites [63]. However, several problems can occur during the milling process.

These problems can occur in all types of materials but are more detrimental in polymer composites due to the characteristics of the polymer matrix, such as low thermal conductivity, thermal melt and decomposition temperatures, and mechanical properties. First, the heating damage is always a concern. Cracking caused by the heat produced during processing cannot be dissipated through the low thermal conductive polymer and generates stress to break the polymer with lower mechanical properties. The second one is material redistribution caused by the melt of polymer. The third problem is the curtain effect. The excessive heat can damage the surroundings and leave holes on the sectional surface. Nonetheless, it is possible to mitigate these problems in several ways. As mentioned above, the proper cooling approaches can be applied to prevent the overheating. Also, another option is to directly reduce the energy of heating source, such as ion beam current deduction and acceleration voltage deduction.

4. Summary and Outlook

The FIB-SEM 3D tomography has been applied in the investigation of morphologies and internal structural features of carbon-based materials, especially carbon-based electrodes. However, the utilizations of FIB-SEM 3D tomography in carbon-based materials are still limited, particularly in quantitative 3D reconstruction-related studies. We noticed that it is possible to extend the FIB-SEM 3D tomography to more applications of carbon-based materials, and highly potential areas are the studies in carbons, carbon-based various electrodes, catalyst, coating, or hybrid layers, and polymer composites. However, the digital analyses and modeling mainly relied on the design and coding by researchers, which are difficult to be used as broad as the commercialized software due to the complexity and low versatility of the existing methods. A simple, integrated, and powerful analysis system for both visible and quantitative 3D reconstruction and analysis will further promote the utilization of FIB-SEM tomography. Moreover, to mitigate the quantification errors in the microstructural parameters caused by the limited sample size and resolutions in the FIB-SEM observation, uncertainty in the image processing, and the accuracy of the quantification method itself, the advanced FIB, high-resolution SEM, and powerful data-processing techniques are desired in further studies.

Furthermore, currently, FIB-SEM 3D tomography was only used to reveal the microstructure of the materials, which blocks the development of FIB-SEM as well. For plenty of carbon-based materials, the nanostructures are more important, and TEM can perform better at nanoscale.

One solution is to combine the FIB-SEM and TEM to obtain the 3D micro- and nanostructures, which has been successfully performed in some studies. Another way is to improve the resolution of SEM. A super asymmetric resolution of 3D imaging technique has been reported for nano- and mesoscale morphologies [64].

The FIB-SEM tomography is becoming a routine technique to obtain 3D information on a variety of materials. With the rapid development of FIB-SEM 3D tomography, the enhanced 3D reconstruction technique is most likely to play a significant role in future characterization of carbon-based materials to further improve the products and optimize their performance, reliability, productivity, and production costs.

Conflicts of Interest

The authors declare that they have no conflicts of interest.

Acknowledgments

This work was supported by the Renewable Materials and Bioenergy Research Center in the Division of Forestry and Natural Resources at West Virginia University.

References

- [1] Q. Ke and J. Wang, "Graphene-based materials for supercapacitor electrodes—a review," *Journal of Materiomics*, vol. 2, no. 1, pp. 37–54, 2016.
- [2] Q. Wang, J. Yan, and Z. Fan, "Carbon materials for high volumetric performance supercapacitors: design, progress, challenges and opportunities," *Energy & Environmental Science*, vol. 9, no. 3, pp. 729–762, 2016.
- [3] P. A. Basnayaka and M. K. Ram, "A review of supercapacitor energy storage using nanohybrid conducting polymers and carbon electrode materials," in *Conducting Polymer Hybrids*, V. Kumar, S. Kalia, and H. C. Swart, Eds., pp. 165–192, Springer International Publishing, Cham, Switzerland, 2017.
- [4] A. Borenstein, O. Hanna, R. Attias, S. Luski, T. Brousse, and D. Aurbach, "Carbon-based composite materials for supercapacitor electrodes: a review," *Journal of Materials Chemistry A*, vol. 5, no. 25, pp. 12653–12672, 2017.
- [5] Z. Gao, Y. Zhang, N. Song, and X. Li, "Biomass-derived renewable carbon materials for electrochemical energy storage," *Materials Research Letters*, vol. 5, no. 2, pp. 69–88, 2017.
- [6] M.-S. Balogun, Y. Luo, W. Qiu, P. Liu, and Y. Tong, "A review of carbon materials and their composites with alloy metals for sodium ion battery anodes," *Carbon*, vol. 98, pp. 162–178, 2016.
- [7] M. Keppeler, N. Shen, S. Nageswaran, and M. Srinivasan, "Synthesis of α -Fe₂O₃/carbon nanocomposites as high capacity electrodes for next generation lithium ion batteries: a review," *Journal of Materials Chemistry A*, vol. 4, no. 47, pp. 18223–18239, 2016.
- [8] J. Liang, Z.-H. Sun, F. Li, and H.-M. Cheng, "Carbon materials for Li-S batteries: functional evolution and performance improvement," *Energy Storage Materials*, vol. 2, pp. 76–106, 2016.
- [9] S. Steinbeiss, G. Gleixner, and M. Antonietti, "Effect of biochar amendment on soil carbon balance and soil microbial

- activity,” *Soil Biology and Biochemistry*, vol. 41, no. 6, pp. 1301–1310, 2009.
- [10] J. H. Windeatt, A. B. Ross, P. T. Williams, P. M. Forster, M. A. Nahil, and S. Singh, “Characteristics of biochars from crop residues: potential for carbon sequestration and soil amendment,” *Journal of Environmental Management*, vol. 146, pp. 189–197, 2014.
- [11] T. Xie, B. Y. Sadasivam, K. R. Reddy, C. Wang, and K. Spokas, “Review of the effects of biochar amendment on soil properties and carbon sequestration,” *Journal of Hazardous, Toxic, and Radioactive Waste*, vol. 20, no. 1, article 04015013, 2016.
- [12] S. Wong, N. Ngadi, I. M. Inuwa, and O. Hassan, “Recent advances in applications of activated carbon from biowaste for wastewater treatment: a short review,” *Journal of Cleaner Production*, vol. 175, pp. 361–375, 2018.
- [13] M. I. Inyang, B. Gao, Y. Yao et al., “A review of biochar as a low-cost adsorbent for aqueous heavy metal removal,” *Critical Reviews in Environmental Science and Technology*, vol. 46, no. 4, pp. 406–433, 2016.
- [14] Ihsanullah, A. Abbas, A. M. Al-Amer et al., “Heavy metal removal from aqueous solution by advanced carbon nanotubes: critical review of adsorption applications,” *Separation and Purification Technology*, vol. 157, pp. 141–161, 2016.
- [15] A. F. Ismail and L. I. B. David, “A review on the latest development of carbon membranes for gas separation,” *Journal of Membrane Science*, vol. 193, no. 1, pp. 1–18, 2001.
- [16] W. N. W. Salleh, A. F. Ismail, T. Matsuura, and M. S. Abdullah, “Precursor selection and process conditions in the preparation of carbon membrane for gas separation: a review,” *Separation & Purification Reviews*, vol. 40, no. 4, pp. 261–311, 2011.
- [17] M. Soleimani, G. Gholami, and M. T. Ravanchi, “Application of carbon membranes for gas separation: a review,” *Journal of Industrial Research & Technology*, vol. 3, no. 1, pp. 53–58, 2013.
- [18] M. N. Nejad, M. Asghari, and M. Afsari, “Investigation of carbon nanotubes in mixed matrix membranes for gas separation: a review,” *ChemBioEng Reviews*, vol. 3, no. 6, pp. 276–298, 2016.
- [19] F. Li, Y. Liu, C.-B. Qu et al., “Enhanced mechanical properties of short carbon fiber reinforced polyethersulfone composites by graphene oxide coating,” *Polymer*, vol. 59, pp. 155–165, 2015.
- [20] N. Nan, D. B. DeVallance, X. Xie, and J. Wang, “The effect of bio-carbon addition on the electrical, mechanical, and thermal properties of polyvinyl alcohol/biochar composites,” *Journal of Composite Materials*, vol. 50, no. 9, pp. 1161–1168, 2016.
- [21] Y.-H. Zhao, Y.-F. Zhang, S.-L. Bai, and X.-W. Yuan, “Carbon fibre/graphene foam/polymer composites with enhanced mechanical and thermal properties,” *Composites Part B: Engineering*, vol. 94, pp. 102–108, 2016.
- [22] A. Karaipekli, A. Biçer, A. Sarı, and V. V. Tyagi, “Thermal characteristics of expanded perlite/paraffin composite phase change material with enhanced thermal conductivity using carbon nanotubes,” *Energy Conversion and Management*, vol. 134, pp. 373–381, 2017.
- [23] B. Fang, B. A. Pinaud, and D. P. Wilkinson, “Carbon-supported Pt hollow nanospheres as a highly efficient electrocatalyst for the oxygen reduction reaction,” *Electrocatalysis*, vol. 7, no. 4, pp. 336–344, 2016.
- [24] G. Wu, A. Santandreu, W. Kellogg et al., “Carbon nanocomposite catalysts for oxygen reduction and evolution reactions: from nitrogen doping to transition-metal addition,” *Nano Energy*, vol. 29, pp. 83–110, 2016.
- [25] J. Zhang, L. Qu, G. Shi, J. Liu, J. Chen, and L. Dai, “N,P-codoped carbon networks as efficient metal-free bifunctional catalysts for oxygen reduction and hydrogen evolution reactions,” *Angewandte Chemie International Edition*, vol. 55, no. 6, pp. 2230–2234, 2016.
- [26] S. N. Monteiro and S. Paciornik, “From historical backgrounds to recent advances in 3D characterization of materials: an overview,” *Journal of Minerals, Metals & Materials Society*, vol. 69, no. 1, pp. 84–92, 2017.
- [27] K. Bae, J. W. Kim, J.-W. Son et al., “3D evaluation of porous zeolite adsorbents using FIB-SEM tomography,” *International Journal of Precision Engineering and Manufacturing-Green Technology*, vol. 5, no. 2, pp. 195–199, 2018.
- [28] B. Munch, P. Gasser, L. Holzer, and R. Flatt, “FIB-nanotomography of particulate systems—part II: particle recognition and effect of boundary truncation,” *Journal of the American Ceramic Society*, vol. 89, no. 8, pp. 2586–2595, 2006.
- [29] M. A. Groeber, *Development of an Automated Characterization-Representation Framework for the Modeling of Polycrystalline Materials in 3D*, Ohio State University, Columbus, OH, USA, 2007.
- [30] J. Balach, F. Soldera, D. F. Acevedo, F. Mücklich, and C. A. Barbero, “A direct and quantitative three-dimensional reconstruction of the internal structure of disordered mesoporous carbon with tailored pore size,” *Microscopy and Microanalysis*, vol. 19, no. 3, pp. 745–750, 2013.
- [31] S. Liu, Y. Yin, K. S. Hui, K. N. Hui, S. C. Lee, and S. C. Jun, “Nickel hydroxide/chemical vapor deposition-grown graphene/nickel hydroxide/nickel foam hybrid electrode for high performance supercapacitors,” *Electrochimica Acta*, vol. 297, pp. 479–487, 2019.
- [32] B. K. Singh, A. Shaikh, R. O. Dusane, and S. Parida, “Nanoporous gold-nitrogen-doped carbon nano-onions all-solid-state micro-supercapacitor,” *Nano-Structures & Nano-Objects*, vol. 17, pp. 239–247, 2019.
- [33] X. Shen, Y. Li, T. Qian et al., “Lithium anode stable in air for low-cost fabrication of a dendrite-free lithium battery,” *Nature Communications*, vol. 10, no. 1, p. 900, 2019.
- [34] X. Liu, M. N. Marlow, S. J. Cooper et al., “Flexible all-fiber electrospun supercapacitor,” *Journal of Power Sources*, vol. 384, pp. 264–269, 2018.
- [35] S. Zhou, D. Liu, Y. Cai, Y. Yao, and Z. Li, “3D characterization and quantitative evaluation of pore-fracture networks of two Chinese coals using FIB-SEM tomography,” *International Journal of Coal Geology*, vol. 174, pp. 41–54, 2017.
- [36] N. Ogihara, Y. Ozawa, and O. Hiruta, “A self-assembled intercalated metal-organic framework electrode with outstanding area capacity for high volumetric energy asymmetric capacitors,” *Journal of Materials Chemistry A*, vol. 4, no. 9, pp. 3398–3405, 2016.
- [37] S. Vierrath, L. Zielke, R. Moroni et al., “Morphology of nanoporous carbon-binder domains in Li-ion batteries—a FIB-SEM study,” *Electrochemistry Communications*, vol. 60, pp. 176–179, 2015.
- [38] M. Zhao, B. Ming, J.-W. Kim et al., “New insights into subsurface imaging of carbon nanotubes in polymer composites via scanning electron microscopy,” *Nanotechnology*, vol. 26, no. 16, article 169601, 2015.
- [39] S. K. Eswara-Moorthy, P. Balasubramanian, W. van Mierlo et al., “An in situ SEM-FIB-based method for contrast enhancement and tomographic reconstruction for structural quantification of porous carbon electrodes,” *Microscopy and Microanalysis*, vol. 20, no. 5, pp. 1576–1580, 2014.

- [40] A. Yürüm, Z. Ö. Kocabaş-Ataklı, M. Sezen, R. Semiat, and Y. Yürüm, "Fast deposition of porous iron oxide on activated carbon by microwave heating and arsenic (V) removal from water," *Chemical Engineering Journal*, vol. 242, pp. 321–332, 2014.
- [41] R. C. Rodriguez, A. B. Moncada, D. F. Acevedo, G. A. Planes, M. C. Miras, and C. A. Barbero, "Electroanalysis using modified hierarchical nanoporous carbon materials," *Faraday Discussions*, vol. 164, pp. 147–173, 2013.
- [42] S. Thiele, T. Fürstehaupt, D. Banham et al., "Multiscale tomography of nanoporous carbon-supported noble metal catalyst layers," *Journal of Power Sources*, vol. 228, pp. 185–192, 2013.
- [43] A. P. Cocco, G. J. Nelson, W. M. Harris et al., "Three-dimensional microstructural imaging methods for energy materials," *Physical Chemistry Chemical Physics*, vol. 15, no. 39, pp. 16377–16407, 2013.
- [44] T. L. Burnett, R. Kelley, B. Winiarski et al., "Large volume serial section tomography by Xe plasma FIB dual beam microscopy," *Ultramicroscopy*, vol. 161, pp. 119–129, 2016.
- [45] M. Cantoni and L. Holzer, "Advances in 3D focused ion beam tomography," *MRS Bulletin*, vol. 39, no. 4, pp. 354–360, 2014.
- [46] Y. Song, C. A. Davy, D. Troadec, and X. Bourbon, "Pore network of cement hydrates in a high performance concrete by 3D FIB/SEM—implications for macroscopic fluid transport," *Cement and Concrete Research*, vol. 115, pp. 308–326, 2019.
- [47] D. Wei, S. Jacobs, S. Modla et al., "High-resolution three-dimensional reconstruction of a whole yeast cell using focused-ion beam scanning electron microscopy," *Bio-Techniques*, vol. 53, no. 1, pp. 41–48, 2012.
- [48] Y. Zhang, M. Dong, S. Zhu, C. Liu, and Z. Wen, "MnO₂@colloid carbon spheres nanocomposites with tunable interior architecture for supercapacitors," *Materials Research Bulletin*, vol. 49, pp. 448–453, 2014.
- [49] G. Brus, H. Iwai, M. Mozdziejczak et al., "Combining structural, electrochemical, and numerical studies to investigate the relation between microstructure and the stack performance," *Journal of Applied Electrochemistry*, vol. 47, no. 9, pp. 979–989, 2017.
- [50] R. S. Devarapalli, A. Islam, T. F. Faisal, M. Sassi, and M. Jouiad, "Micro-CT and FIB-SEM imaging and pore structure characterization of dolomite rock at multiple scales," *Arabian Journal of Geosciences*, vol. 10, no. 16, p. 361, 2017.
- [51] M. Kishimoto, *Three-Dimensional Microstructure of Solid Oxide Fuel Cell Anode: Observation, Quantification, and Application to Numerical Analysis*, Kyoto University, Kyoto, Japan, 2013.
- [52] P. Bala, K. Tsyrlin, H. Jaksch, and M. Stepien, "3D reconstruction and characterization of carbides in Ni-based high carbon alloy in a FIB-SEM system," *International Journal of Materials Research*, vol. 106, no. 7, pp. 764–770, 2015.
- [53] D. A. Saab, P. Basset, F. Marty, D. E. Angelescu, and M. Trawick, "Accurate 3D reconstruction of silicon micro/nanostructures, based on high resolution FIB-SEM tomography: application to black silicon," in *Proceedings of the 2014 Symposium on Design, Test, Integration and Packaging of MEMS/MOEMS (DTIP)*, pp. 1–4, Cannes, France, April 2014.
- [54] E. L. Solla, L. Micheron, P. Yot, J. Méndez, and P. Horcajada, "3D reconstruction and porosity study of a hierarchical porous monolithic metal organic framework by FIB-SEM nanotomography," *Microscopy and Microanalysis*, vol. 22, no. S4, pp. 4–5, 2016.
- [55] S. Liu, L. Sun, J. Gao, and K. Li, "A fast curtain-removal method for 3D FIB-SEM images of heterogeneous minerals," *Journal of Microscopy*, vol. 272, no. 1, pp. 3–11, 2018.
- [56] Y. Katayanagi, T. Shimizu, Y. Hashimasa, N. Matsushita, Y. Yamazaki, and T. Yamaguchi, "Cross-sectional observation of nanostructured catalyst layer of polymer electrolyte fuel cell using FIB/SEM," *Journal of Power Sources*, vol. 280, pp. 210–216, 2015.
- [57] A. Etienne, A. Tranchot, T. Douillard, H. Idrissi, E. Maire, and L. Roué, "Evolution of the 3D microstructure of a Si-based electrode for Li-ion batteries investigated by FIB/SEM tomography," *Journal of the Electrochemical Society*, vol. 163, no. 8, pp. A1550–A1559, 2016.
- [58] Z. Liu, Y.-C. K. Chen-Wiegart, J. Wang, S. A. Barnett, and K. T. Faber, "Three-phase 3D reconstruction of a LiCoO₂ cathode via FIB-SEM tomography," *Microscopy and Microanalysis*, vol. 22, no. 1, pp. 140–148, 2016.
- [59] G. Gaiselmann, M. Neumann, L. Holzer, T. Hocker, M. R. Prestat, and V. Schmidt, "Stochastic 3D modeling of La_{0.6}Sr_{0.4}CoO_{3-δ} cathodes based on structural segmentation of FIB-SEM images," *Computational Materials Science*, vol. 67, pp. 48–62, 2013.
- [60] S. Ghosh, H. Ohashi, H. Tabata, Y. Hashimasa, and T. Yamaguchi, "Microstructural pore analysis of the catalyst layer in a polymer electrolyte membrane fuel cell: a combination of resin pore-filling and FIB/SEM," *International Journal of Hydrogen Energy*, vol. 40, no. 45, pp. 15663–15671, 2015.
- [61] H. Aslannejad, S. M. Hassanizadeh, A. Raoof, D. A. M. de Winter, N. Tomozeiu, and M. T. van Genuchten, "Characterizing the hydraulic properties of paper coating layer using FIB-SEM tomography and 3D pore-scale modeling," *Chemical Engineering Science*, vol. 160, pp. 275–280, 2017.
- [62] N. Nan and D. B. DeVallance, "Development of poly(vinyl alcohol)/wood-derived biochar composites for use in pressure sensor applications," *Journal of Materials Science*, vol. 52, no. 13, pp. 8247–8257, 2017.
- [63] A. Sheidaei, M. Baniassadi, M. Banu et al., "3-D microstructure reconstruction of polymer nano-composite using FIB-SEM and statistical correlation function," *Composites Science and Technology*, vol. 80, pp. 47–54, 2013.
- [64] K. Hagita, T. Higuchi, and H. Jinnai, "Super-resolution for asymmetric resolution of FIB-SEM 3D imaging using AI with deep learning," *Scientific Reports*, vol. 8, no. 1, p. 5877, 2018.

Review Article

Scanning Electron Microscopy and Atomic Force Microscopy: Topographic and Dynamical Surface Studies of Blends, Composites, and Hybrid Functional Materials for Sustainable Future

Joanna Rydz ¹, Alena Šišková,² and Anita Andicsová Eckstein³

¹Centre of Polymer and Carbon Materials, Polish Academy of Sciences, 41-800 Zabrze, Poland

²Institute of Materials and Machine Mechanics, Slovak Academy of Sciences, 845 13 Bratislava, Slovakia

³Polymer Institute, Slovak Academy of Sciences, 845 41 Bratislava, Slovakia

Correspondence should be addressed to Joanna Rydz; jrydz@cmpw-pan.edu.pl

Received 2 May 2019; Revised 6 June 2019; Accepted 11 June 2019; Published 10 July 2019

Academic Editor: Candido Fabrizio Pirri

Copyright © 2019 Joanna Rydz et al. This is an open access article distributed under the Creative Commons Attribution License, which permits unrestricted use, distribution, and reproduction in any medium, provided the original work is properly cited.

Microscopic techniques are often used in material science, enabling the assessment of the morphology, composition, physical properties, and dynamic behaviour of materials. The review focuses on the topographic and dynamical surface studies of (bio)degradable polymers, in particular aliphatic polyesters, the most promising ones. The (bio)degradation process promotes physical and chemical changes in material properties that can be characterised by microscopic techniques. These changes occurring both under controlled conditions as well as in the processing stage or during use indicate morphological and structural transformations resulting from the deterioration of the material and have a significant impact on the characteristic of materials used in many applications, for example, for use as packaging.

1. Introduction

Knowledge of the relationships between structure, properties, function, and performance is essential for prospective safe applications of (bio)degradable and/or bio-based polymers in the areas of human health and the environment. The study of the physical and technical basis of the latest developments in the above areas is based quite often on microscopic techniques that are also used in a various industrial applications, including topographic and dynamical surface studies of many materials including polymers. Fundamental research and applied research in emerging areas of applications in nanotechnology, interfacial science and engineering, advanced production, catalysis, bioengineering, bioinspired synthesis, green production routes, sensing, and actuation are often also based on microscopic techniques. Particular emphasis should be placed on environmentally friendly blends, composites, and hybrid materials from renewable resources

without adverse environmental impact, with a short global carbon lifecycle, with green production routes and/or suitable to recycle, materials based on natural, renewable, and synthetic polymers for a sustainable future [1–3].

In recent years, the focus has been taken on the development of novel atomic force microscope (AFM) and scanning electron microscope (SEM) based methods. The SEM and AFM are powerful characterisation tools in polymer science, capable of revealing surface structures. SEM provides a three-dimensional (3D) image with high resolution and is used to characterise the morphology of the sample surface, particle size, microorganism, and fragments. Energy-dispersive (EDS) detector can additionally provide semiquantitative and semiquantitative information on elemental analysis of the surface (topochemical data) and identification of additives and impurities to detect contamination (residues) as well as determine the origin of sample damage [4]. SEM is a powerful visualisation tool used in material science, including in the field of polymer

sciences. Due to the high lateral resolution, large depth of focus, and the facility for X-ray microanalysis, it provides a consistent image of the polymer blends and composites morphology as a nonuniform structure characterised by polymer variable thickness and variable density. For SEM analysis, the surface of nonconductive samples must be coated with a thin layer of gold or platinum. Sometimes, surface pretreatment is carried out by ion sputtering or chemical etching to reveal structural details. In addition, brittle fracture (in liquid nitrogen) can provide information about the internal morphology of polymer matrix. SEM micrographs show that polymer blends and composites can have different surface features and heterogeneous local density of chemical components. SEM images also show surface defects such as cracks, etching residues, differential swelling, depressions, and perforations [5]. However, SEM drawback is that during imaging, the electron beam may permanently damage the observed sample. Degradation, an undesirable effect, can alter or destroy details and consequently change the results and conclusions [6]. By means of AFM technique, in addition to topography imaging at the nanometre scale, the phase imaging mode is actively involved in the mapping of surface heterogeneity of the blends, composites, and hybrid materials because the phase response of the cantilever is sensitive to the surface properties, such as adhesiveness, friction, electrical forces, capacitance, magnetic forces, conductivity, viscoelasticity, surface potential, and resistance without need for sample preparation or vacuum environment [7, 8]. It has been shown that AFM is able to provide both qualitative and semiquantitative information on the deterioration and ageing of materials during degradation [9]. In phase mode imaging, different samples exhibit different interactions with the AFM tip, so the phase shift changes. The properties of the sample affected by interactions with the AFM tip include friction, adhesion, and high elasticity. Using phase mode, images show differences between the local regions on the sample, and this mood is also useful for testing the consistency of coatings and for displaying cracks and other degradation features [10].

Analysis of polymer blends and composites morphology and surface changes (erosion) using AFM and SEM techniques gives a lot of information about various processes and phenomena. The use of a microscope to monitor a number of aspects of the surface degradation of polymer blends and composites in various selected degradation environments allows to track the relationship between surface topography and degradation patterns of materials and provide reliable parameters for predicting of long-term degradation. Likewise, miscibility of blends is one of the most important factors affecting the properties of polymer materials. The surface structure and morphology of (bio)degradable polymer blends have a great impact on the degradation process. Moreover, microscopic observation is a powerful tool to detect 3D printing defects and downstream processing problems, which can also affect the course of degradation of printed items [11]. Farther imaging techniques, such as SEM and AFM, have been developed to observed materials of submicron size, so they can be used to determine

microscopic characteristics of nanomaterials such as shape, size, surface morphology, crystal structure, and dispersion and are an important part of determining phase purity, electronic transition plasmonic character, atomic environment and surface charge, etc. [12, 13]. Also, microscopic examination of electrospun (bio)degradable polymers allows understanding the relationships between processing parameters, morphology of the samples, and their properties. The formed mats have unique characteristics such as high porosity, surface area to volume ratio, permeability, porosity, stability, ease of functionalisation, and excellent mechanical performance [14, 15].

The development of (bio)degradable polymeric materials for many new advanced applications is of great importance not only for usable reasons, but also from the point of environmental protection and sustainable development. The efficient use of these polymers requires basic research necessary to determine the relationship between the structure of such materials, properties, and mechanism of degradation. Therefore, the following overview presents the most important issues in the testing of the behaviour of (bio)degradable polymeric materials in various environments using surface imaging techniques, which have not been presented in one review so far. Microscopic techniques are a tool for studying changes in the surfaces of materials under investigation during various processes and assessing microdamage, such as crack propagation, grain size change, and capability, which allows to provide qualitative and semiquantitative information on degradation and ageing. They are also a sensitive tool to detect the deterioration of the materials tested and characterise mechanisms of the blends and composites reinforcement.

2. Microscopic Investigation of Eco-Friendly Polymer Blends and Composites

2.1. Ageing and Degradation Processes. AFM allows for a microdestructive quantitative distinction between the initial and the final stage of degradation [4]. The polymers before degradation generally have a fairly flat and smooth surface. During degradation, the surface becomes rougher. The dissolution of degradation products and erosion usually create cracks and pores which cause an increase of roughness. Small cracks, formed by water absorption (in case of hydrolytic degradation in aqueous media) or simply erosion of the polymer, increase as contact with water leads to hydrolysis, and locally produced acids catalyse degradation and cause polymer dissolution inside the pores. The depth and/or the number of pores in the surface increased with time, conditions, and degradation media. The surface erosion depends also on the solubility of the low-molar-mass degradation products [16].

Under natural conditions (compost and weather conditions) at the beginning of degradation, cracks on the surface of the polymeric material appear, after which the material begins to disintegrate into pieces in accordance with cracks (disintegration). Degradation under natural conditions of the polylactide (PLA) and PLA/PHB (PHB: poly(3-hydroxybutyrate)) blend, as well as their composite

materials proceeds according to a different mechanism, which reflects the microscopic images. The cracks on the PLA material surface appear, and then the erosion occurred inside deeper part of the material, which indicates a water-catalysed hydrolysis mechanism. For a PLA/PHB blend, the homogeneously licking of the whole surface, layer by layer, is observed, which indicates an enzyme-catalysed hydrolysis mechanism [8, 17, 18]. The degradation of polyesters in a biological environment, including anaerobic and aerobic conditions, activated sludge, public wastefields, and composting facilities, results from enzymatic attack (in the presence of specific enzymes produced by microorganisms such as bacteria and fungi) or simple hydrolysis (water-catalysed cleavage of ester bonds) or both. In contrast to bacterial polyesters, such as polyhydroxyalkanoates (PHAs), which directly undergo biodegradation by many microorganisms present in the environment, the high-molar-mass PLA is colonised by relatively few microorganisms and more frequently takes place the water-catalysed hydrolysis of this material. But in general, for (bio) degradable polymers, the first step of biodegradation under natural and laboratory conditions is a chemical hydrolysis (mainly through random chain scission), which leads to a reduction of molar mass. In the next step, called mineralisation, the oligomers formed are bioassimilated by microorganisms as an energy source [19].

Figure 1 presents SEM micrographs of the surface of the PHA films treated with (i) lipase solution (0.1 g/L) under 30°C and pH = 7.0 for 24 h and (ii) 1 N NaOH at 60°C for 1 h [20].

Many microorganisms, such as extracellular PHB depolymerase, excrete enzymes outside their cell walls. The enzymes first adsorb onto the surface of polymer materials through their substrate-binding domains at the C-terminus and then catalyse the hydrolysis of polymer chains by their catalytic domains at the N-terminus [21]. The enzymes are able to cleave specific bounds in the polymer chain on the surface of the polymer material, which causes the destruction of this material layer by layer (surface erosion, does not occur inside the polymer matrix) (see Figure 1, lipase) [22]. Nonenzymatic hydrolysis of PHAs proceeds from the surface towards the deeper layers. The surface became rougher, and the density of the holes forming on the surface increased (see Figure 1, NaOH) [21].

Investigation of biodegradation of PHA/wood composites using SEM in secondary electron mode showed that despite the low-molar-mass loss, which is characteristic in the first stage of biodegradation, when the surface degrades, layer by layer, the surface of plain PHA had a clearly rough surface with dents after 12 months of burial in soil. The surface of PHA composite with 20% wood was also significantly rougher after soil burial. A network of fungal hyphae filaments has been embedded in the matrix with the presence of spores. The decreases in molar mass of PHA throughout 12 months of soil burial became more severe as the wood content increased [23].

The degradation of PLA and its composites with starch in compost and soil also indicates the process catalysed by enzymes in the case of composites. SEM micrographs (see Figure 2) showed changes in surface morphology (cracks) of

PLA and its composites after degradation in compost and soil for 14 days. (Bio)degradation occurred for all polymer samples tested, but more changes were observed in PLA/starch (50/50) composite than on pure PLA samples. This means that the addition of starch to PLA resulted in their greater biodegradability. Starch was eroded from the surface of the PLA blends, while for pure PLA, degradation occurred in the deeper part of the polymer, suggesting a preferential mechanism of chemical hydrolysis. Degradation occurred faster in compost than in soil [24].

The EDS detector can be used to identify of additives affecting the course of degradation. It was found that differences in the rate of degradation of PLA/PBAT (PBAT: poly(butylene adipate-co-terephthalate)) blends with a similar content of the PLA component may be due to differences in their thickness and/or the presence of commercial additives used during processing. The results indicated that the presence of talc may interfere with the behaviour of materials towards water and consequently alter their degradation profile. EDS analysis of selected regions of PLA/PBAT blends showed the presence of white inclusions (Mg and Si) in the polymeric matrix derived from a commercial additive, hydrated magnesium silicate (talc) (see Figure 3) [25].

2.2. Effects of Miscibility. Observation of the surface morphology by AFM can confirm different miscibilities of the polymer material [8, 26]. The blends with poor miscibility exhibit phase separation of the components, while a homogenous surface morphology is observed for the blend with good miscibility (see Figure 4) [16]. Miscibility and compatibility of polyester blends containing PLA and PHAs, such as PHB or poly(3-hydroxybutyrate-co-3-hydroxyvalerate) (PHBV) depend on the molar mass and crystallinity of the components, on the blending method and the composition of the blend. The blends are immiscible when the molar mass of components is high [27]. A decrease of molar mass of one of the blend components results in a reduction of the phase separation [28].

The diameter and depth of the pit domain of immiscible blends increased as the poly([R,S]-3-hydroxybutyrate) ((R,S)-PHB) component increased in the blends, as observed by AFM. Only in the blend with good miscibility, the surface was completely smooth. The degree of erosion of the polymeric material is strongly dependent on the blend miscibility of the two components. The poor miscibility of the blend with the largest pit domain before degradation promoted greater roughness of the surface during degradation [16].

The cocontinuous phase structure of polymer blend can be confirmed by means of SEM. SEM was used to analyse the effect of a preparation method on the miscibility of PBAT and poly(hydroxy ether) (PH) of bisphenol A blends and the effect of a nondegradable component (PH) in the degradation of PBAT. A continuous morphology of the 50PBAT/50PH blend prepared by casting can be observed. This type of morphology was attributed to phase inversion composition. The morphology of 25PBAT/75PH has a

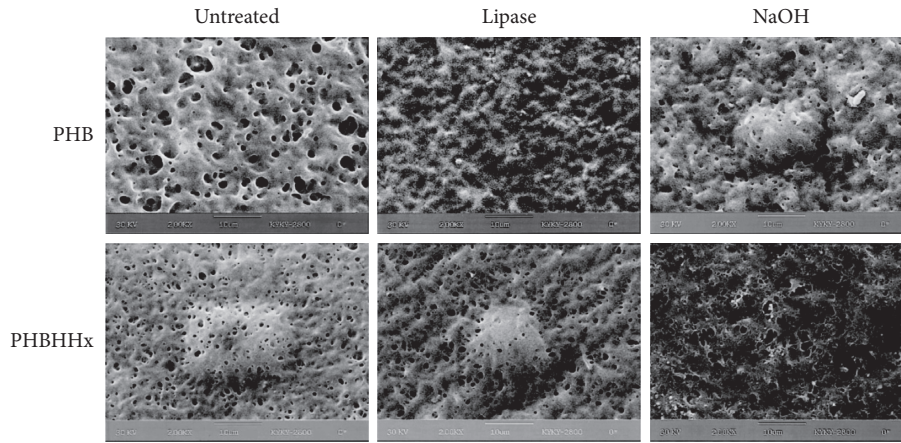


FIGURE 1: SEM micrographs of PHB and poly(3-hydroxybutyrate-co-3-hydroxyhexanoate) (PHBHHx) films before degradation (untreated) and after lipase and 1 N NaOH catalysed hydrolysis (adapted with permission from ref. [20]).

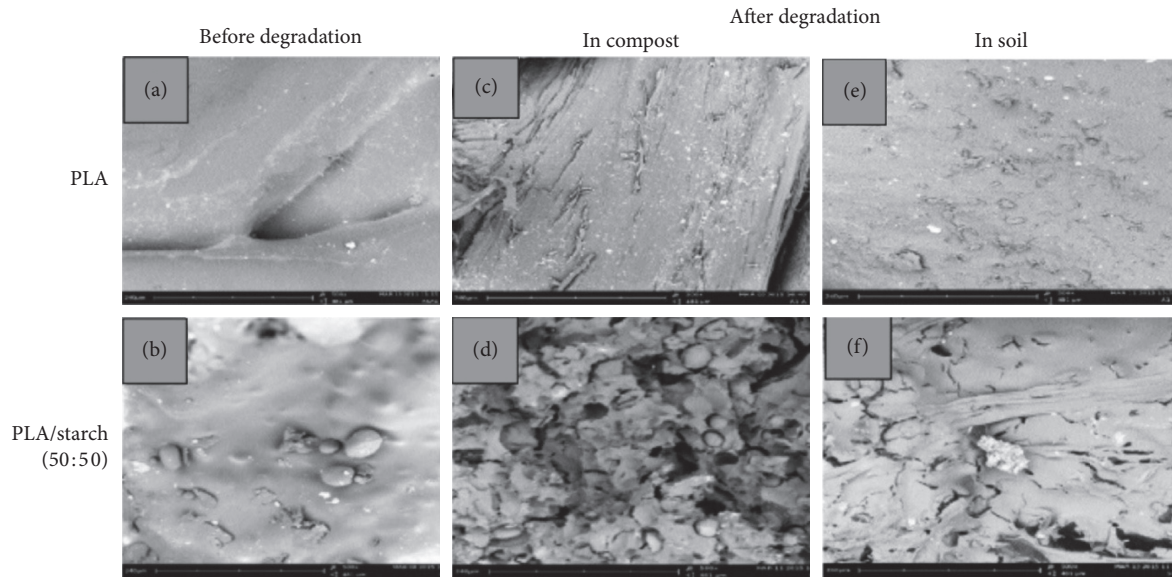


FIGURE 2: SEM images of PLA and PLA/starch (50/50) composite samples surface before degradation (a and b), after degradation in compost (c and d), and after degradation in soil (e and f) for 14 days (adapted with permission from ref. [24]).

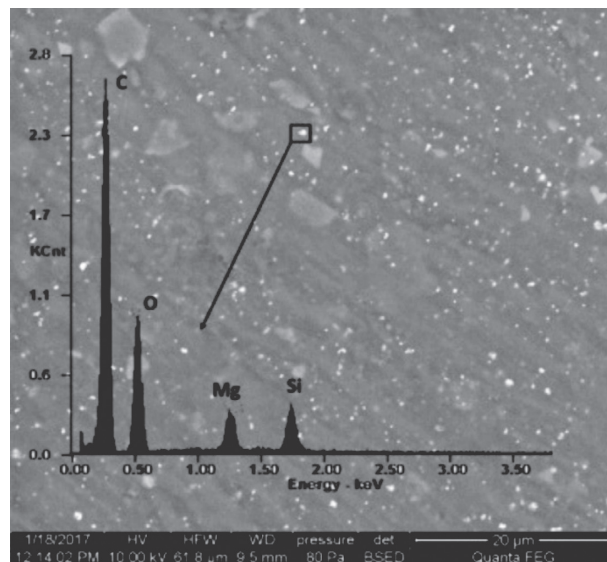


FIGURE 3: SEM-EDS micrograph of PLA/PBAT (40/60) blend surface at a magnification of 2500x (adapted with permission from ref. [25]).

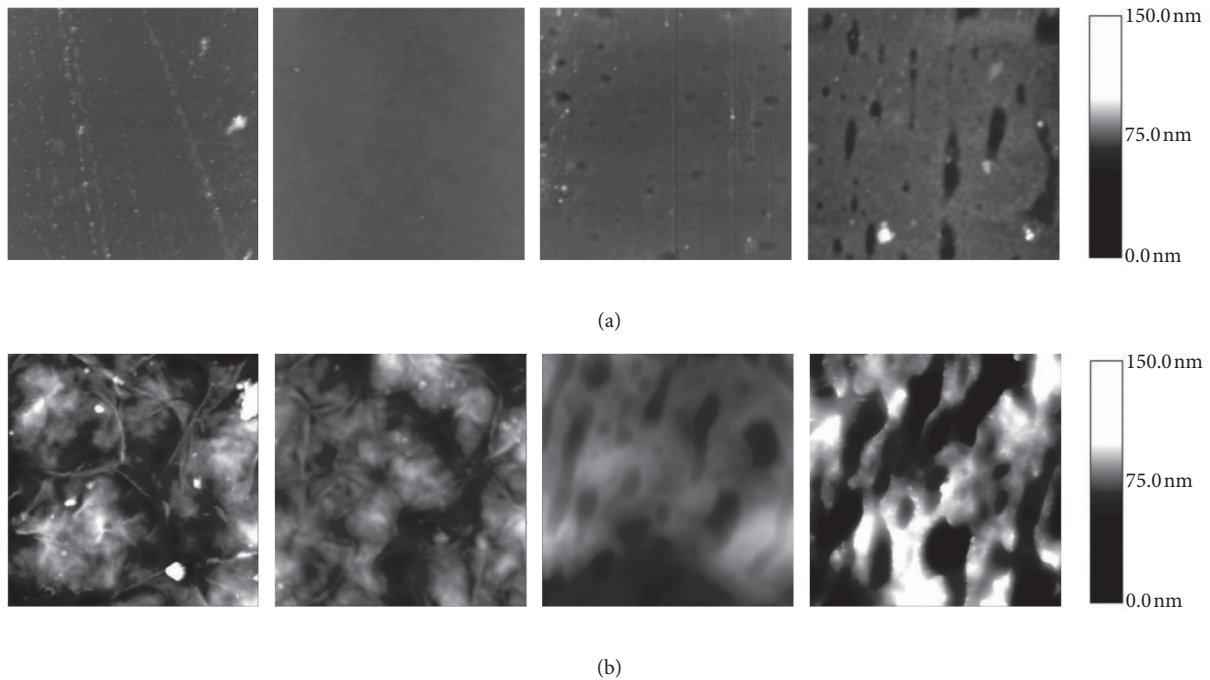


FIGURE 4: Selected $6 \times 6 \mu\text{m}$ AFM images of the surface erosion of PLA, 97PLA/3(R,S)-PHB, 91PLA/9(R,S)-PHB, and 85PLA/15(R,S)-PHB blend samples, respectively, before (a) and after (b) 52 weeks of the degradation process in paraffin (adapted with permission from ref. [16]).

biphasic structure: the adhesion between the two components is very good; however, the blend is immiscible. As expected, the rate of degradation decreased with the addition of PH [29].

The effect of melt viscosity of the two melt blended polymers, PLA and PBAT, on the morphology and mechanical properties of obtained (bio)degradable blends was investigated by means of SEM. Based on the relative melt viscosities of the PLA and PBAT in the processing method, it is possible to calculate the volume fraction in which a cocontinuous phase structure is formed. The SEM image of the fracture surface from the tensile tests for pure PLA exhibited a flat, featureless structure that is typical of brittle fracture. In PBAT/PLA blends with PBAT between 20 and 40 wt%, a cocontinuous phase structure was observed; the fibrils were drawn from the fracture surfaces, which is a common feature of ductile failure. Since PBAT has a much lower yield stress than PLA and undergo plastic deformation at lower stress, these fibrils were caused by a continuous PBAT phase. When PBAT content in the PBAT/PLA blend reached 60 wt%, the continuous PLA phase was no longer visible. Large PLA particles were dispersed in a continuous PBAT phase, and they deboned from the matrix, which caused cracks and flaws at the interface, resulting in relatively poor mechanical properties. When the PBAT content reached 80 wt%, the blend exhibited very ductile behaviour in the tensile test. PLA was still dispersed in the PBAT in the form of particles; however, the particle size was much smaller and the dispersion became much more uniform. The impact of PLA on the mechanical properties was unimportant, and the blend behaved in a similar way to pure PBAT (see Figure 5) [30].

2.3. Three-Dimensional Printing: Defect Detection. 3D printing or additive manufacturing (AM) refers to processes used to create objects in 3D using digital data of the 3D model. To form 3D objects with almost any shape or geometry, subsequent layers of material are applied [31]. 3D printing is a valuable alternative to traditional processing methods in the creation of various products, such as scaffolds for regenerative medicine, artificial tissues and organs, electronics, components for the transportation industry, art objects, etc. This technique has demonstrated exceptional capacities for producing complex structures with precisely tailored physical and mechanical properties, biological functionality, and an easily customisable architecture [32].

Subsequent layers may, however, contain structural interruptions or defects that negatively affect the reliability of the 3D printed object [31]. Also, build direction has a significant effect on the structure and morphology and hence on the properties of elements made using 3D printing (see Figure 6) [33].

When samples are printed horizontally, upper and underside layers have surfaces with a different characteristic. This is due to the fact that one layer is in contact with the 3D printer platform. In the case of fused deposition modelling, rapid prototyping technique, the heated thermoplastic polymer filament is extruded from a tip that moves in the XY plane. The controlled extrusion head deposits the polymer material onto the printer platform, first forming the underside layer. The printer platform is kept at not too high constant temperature (around 65°C for polyesters), whereby the thermoplastic material hardens quickly. However, polymeric material is permanently maintained at a constant temperature during printing which can affect properties of

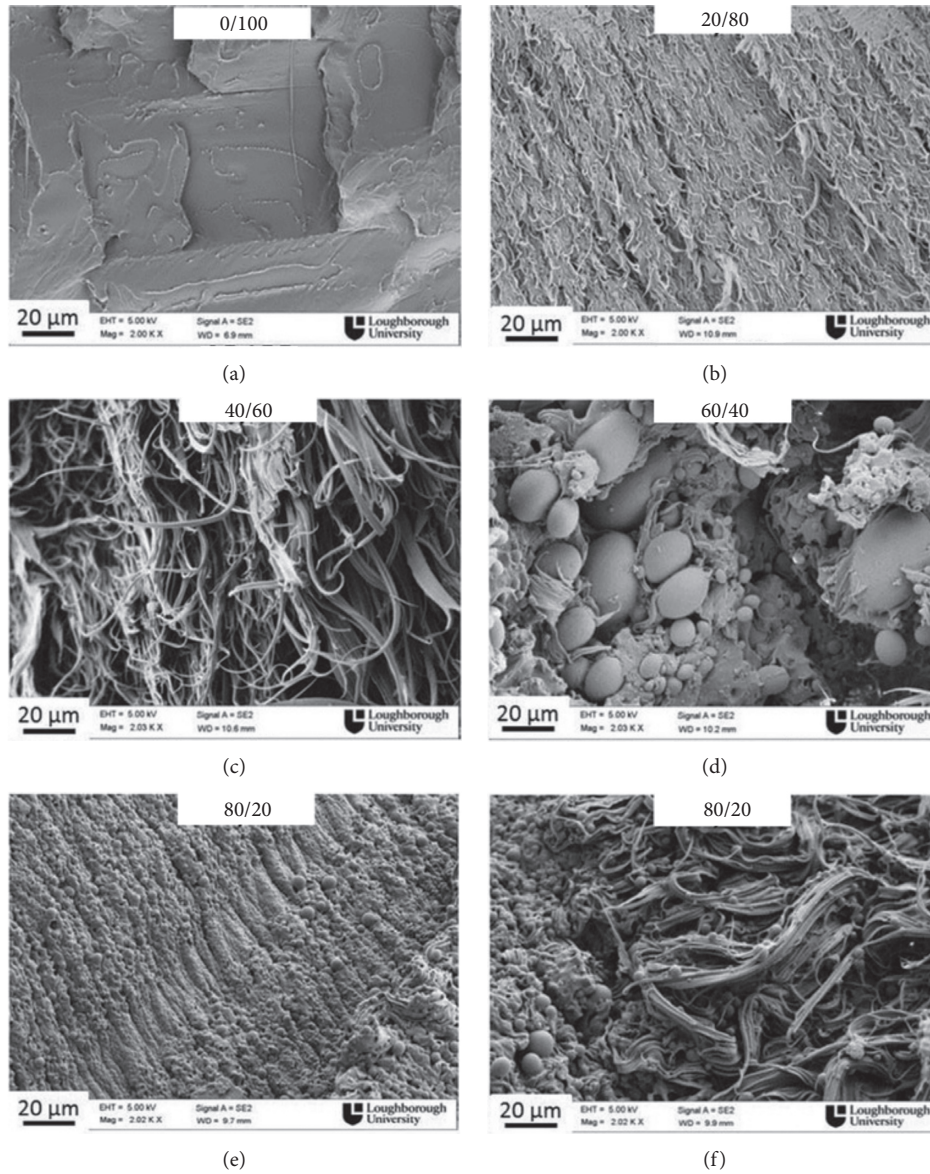


FIGURE 5: SEM micrographs of fracture surfaces from the tensile tests of PBAT/PLA blends (adapted with permission from ref. [30]).

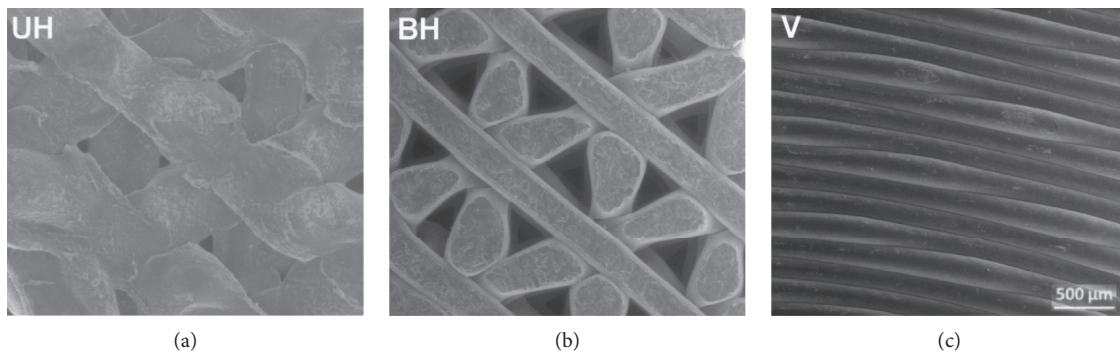


FIGURE 6: SEM micrographs of upper (UH) and underside (BH) layers of samples surface obtained by 3D printing in horizontal (H) and vertical (V) directions (adapted with permission from ref. [33]).

the final element from (bio)degradable polymers, such as PLA or PLA/PHA blend. The extrusion head deposits the material layer by layer in the Z-axis. The process is continued to produce the desired element [34–36]. The upper layer is the furthest from the platform (see Figure 6, UH layer). Vertical direction does not affect the structure of the surfaces of the PLA or PLA/PHA blend because the contact with the printer platform was only at the small area at the base of the sample.

Tissue engineered scaffolds must have an appropriately organised and repeatable microstructure that allows the cells to be assembled in an ordered matrix that ensures the proper perfusion of nutrients. This is what 3D printing technology provides. 3D cylindrical scaffolds made of poly(ϵ -caprolactone) (PCL) were prepared using a bioplotter dispensing machine. In order to obtain a porous but sufficiently stiff 3D structure, the scaffold consisted of filament layers, which were extruded sequentially by the bioplotter with $0^\circ/90^\circ$ pattern. The diameter of the filament ($200\ \mu\text{m}$) depended not only on the internal diameter of the nozzle ($250\ \mu\text{m}$) but also on the deposition speed ($30\text{--}35\ \text{mm/min}$) (see Figure 7) [37].

SEM images allow not only to characterise the morphology of the 3D samples surface but also filament size or microorganism species.

3. Microscopic Methods in Nanomaterial Characterisation

Nanotechnology is one of the fastest growing interdisciplinary areas at present. Nanomaterials are mainly used in electronics, healthcare, cosmetics, construction, and automotive industries. Depending on the application, nanoparticles are divided into two main groups: organic and inorganic. Nanoparticles with inorganic base are fullerene, quantum dot, silica, and gold and with organic base are micelle, dendrimer, liposome, hybrid, nanosphere, and nanocapsule [39].

(Bio)degradable polymers are often used in the preparation of nanomaterials [40]. The applications of (bio)degradable polymeric nanomaterials have a wide range of usability in the field of therapeutics such as diagnostics, imaging, drug delivery, organ implant, tissue engineering, and in area of packaging materials [41]. The type of polymer system, area of applicability, and required particle size determine the type of (bio)degradable polymeric nanomaterials preparation.

The SEM/EDX technique is useful in the research in all works that require the determination of elements, endogenous or exogenous, in tissues, cells, etc., such as drugs delivery. The EDX helps in the detection of nanoparticles used to improve the therapeutic efficacy of certain chemotherapeutic agents. It is also used in the study of environmental pollution and in the characterisation of minerals bioaccumulated in the tissues [42]. Using SEM can be examined, for example, the fine nanoporous aerogels structure, in situ SEM methods investigating the thermal stability of nanoparticles such as graphene/Cu based materials, the effects of electron beam irradiation on the electrical

properties of carbon nanotube yarns, and the nano-indentation work of multiphase thermoelectric material [43]. AFM is used to investigate the size and shape of nanoparticles in 3D mode, to assess the degree of surface coverage with nanoparticles, dispersion of nanoparticles in cells and other matrices/carriers, and precision in lateral dimensions of nanoparticles [44].

The most commonly applicable (bio)degradable polymers are PLA, poly(lactic-co-glicolic acid) (PLGA), and PHBV which themselves form particles or are used as part of copolymers or surface materials for inorganic particles. Biocompatible PLA-based micro- and nanoparticles are prepared by different techniques (Table 1), and the morphology of these nanoparticles is most often investigated by SEM.

PLGA is another widely used (bio)degradable polymer for nanoparticle preparation by the emulsification, solvent evaporation, and nanoprecipitation method [53]. By using various molar masses of PLGA (M_w of 14,500, 45,000, 85,000, 137,000, and 213,000 g/mol), particles were prepared with size $90\text{--}120\ \text{nm}$. The prepared particles were studied as a drug release system [54].

The effect of various preparation conditions on the size and morphology of the PHBV micro- and nanoparticles for potential applications as reinforcement of PHBV/starch matrices was examined using field emission SEM (see Figure 8). The spherical porous micro- and nanoparticles produced by the emulsification/solvent evaporation were with a size of $300\ \text{to}\ 20\ \mu\text{m}$. It has been found that the size, porosity, and the particle size distribution can be controlled by the choice of surfactant and polymer concentration during the emulsification process, while choosing the appropriate antisolvent and adjusting its polarity were crucial for obtaining spherical particles through nanoprecipitation [55].

Studying the cell material interactions is crucial for collecting relevant information on the impact of structure and composition at the atomic and macromolecular level of bioinspired scaffolds. Thus, the assessment of the surface properties can be suitable technique in this regard. AFM has a significant impact on the *in vitro* studies of (bio)degradable materials produced in various forms, i.e., films, fibres, or nanoparticles for tissue engineering and drug delivery, capable of gradual resorption by *ex novo* formation of extracellular matrix with predefined structural/mechanical properties, similar to native tissues [56].

4. Electrospun Eco-Friendly Polymer-Based Blends, Composites, and Hybrid Materials: Microscopic Examinations

Electrospinning is considered as attractive procedure of forming ultra-fine fibres in a nano- and microscale into nonwoven mats due to its simplicity, cost effectiveness, and high rate of production. The schematic representation of the most common electrospinning setup is displayed in Figure 9. The advantage of electrospun nanofibres is mimicking of

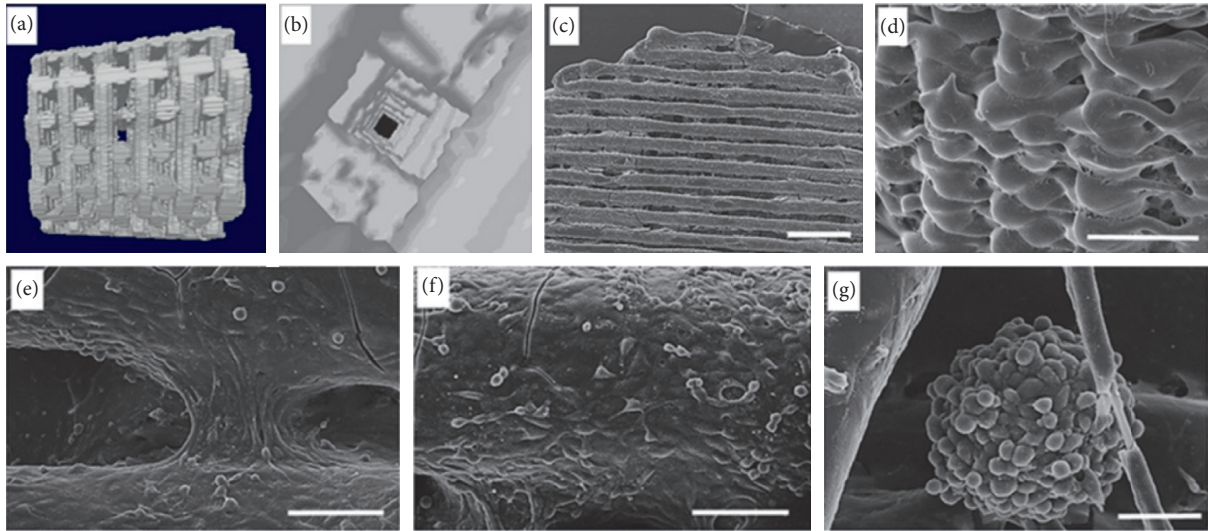


FIGURE 7: SEM micrographs: (a) lateral view of 3D filament-deposited scaffold reconstruction; (b) inner structure of the same scaffold; (c) colonisation of the 3D PCL scaffold in dynamic condition (scale bar 1 mm); (d) high magnification showing the external cell monolayer (scale bar 1 mm); (e) cells bridging the grooves (scale bar 100 μm); (f) cell arrangement suggestive of a new vascular structure (scale bar 100 μm); (g) spheroid of MC63 and human umbilical vein cells generated in dynamic condition (scale bar 50 μm) (adapted with permission from ref. [38]).

TABLE 1: Preparation of PLA base (bio)degradable polymeric nanomaterials.

Preparation techniques	Polymers	Size (nm)	References
Emulsion	PLA	200	[45]
Nanoprecipitation	Polydopamine-modified tocopheryl poly(ethylene glycol succinate)-PLA (TPGS-PLA)	126	[46]
Dialysis	PLA-poly(ethylene glycol)-PLA (PLA-PEG-PLA)	90–330	[47]
Spray drying	PLA	960–3000	[48]
Melting technique	PLA/PLGA	Micro	[49]
Supercritical fluids technique	PLA	Micro	[50]
Microfluid technique	PLA/ $\gamma\text{-Fe}_2\text{O}_3$	Micro	[51]
Template/mould based technique	PLA	Micro	[52]

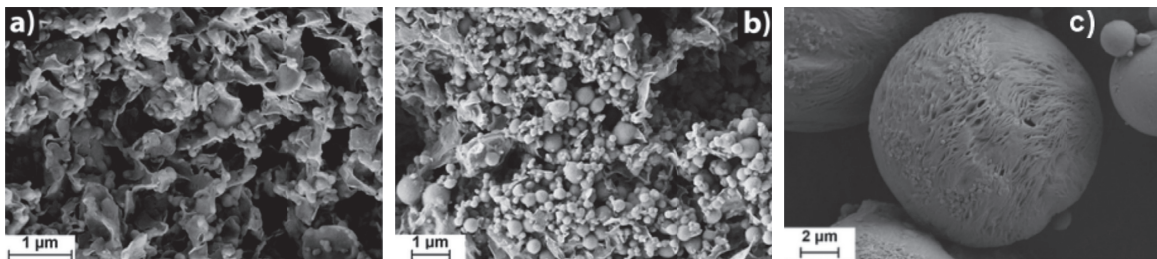


FIGURE 8: Micrographs of micro- and nanoparticles of PHBV prepared by nanoprecipitation method using 0.5% PHBV in dimethylformamide (DMF) as solvent and water as antisolvent (a) and 0.1% PHBV in DMF as solvent and 10% NaCl solution in water as antisolvent (b); microparticles of PHBV prepared by emulsification/solvent evaporation method using 1% PHBV in dichloromethane (DCM) and sodium dodecyl sulphate (SDS) as surfactant in a concentration of 1% (c) (adapted with permission from ref. [55]).

three-dimensional structure of natural extracellular matrix, which predetermine them for biomedical and biotechnological application as tissue engineering, wound dressing, and drug release [57, 58]. Besides this, it can be synthesised and tailored to suit a wide range of others applications including electronics [59, 60], environmental engineering [61, 62], agriculture [63, 64], and food packaging [65, 66].

The high customisation and easy functionalisation of the nanofibres offer numerous opportunities to control and to evaluate the morphology and/or chemical changes on the surface of blends, composites, and hybrids. SEM, transmission electron microscopy (TEM), and AFM may be valid tools for characterising surface topography and understanding the specific mechanical, chemical, and physical

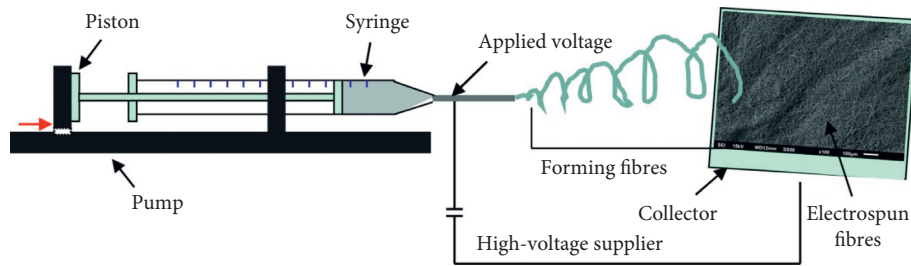


FIGURE 9: Schematic representation of conventional electrospinning setup to prepare electrospun nanofibres (archive of authors).

properties with regards to application of investigated materials [56, 67, 68].

4.1. Electrospinning Process Parameters of (Bio)degradable Polymers. To date, many materials including natural polymers, synthetic polymers, and their mixture have been electrospun. Particularly, (bio)degradable polymers are used extensively in the biomaterial fields including polyesters, such as PLA, poly(glycolic acid) (PGA), PCL, PHB, or polyester copolymers, such as PLGA, PHBV, and PBAT [63, 69, 70].

The parameters influencing the morphology and properties of electrospun fibres can be divided into solution parameters, process parameters, and ambient conditions. The most relevant parameters related to the solution properties are nature of used solvent, its dielectric properties, volatility, boiling point, the solution concentration, and molar masses of polymers that control the viscosity. Into the group of processing parameters belong flow rate through the needle, inner diameter of the needle, needle-to-collector distance, applied voltage, and geometry of collection (static collector or rotating drum). These parameters control the jet formation. The ambient conditions as ambient temperature, humidity, and air flow are influencing the morphology of the products as well [57, 71, 72]. After electrospinning, SEM is performed for morphological analysis generating SEM images, for measuring the fiber diameter, etc. SEM enables the optimisation of electrospinning process for preparation of continuous nanofibres with specific morphology and well-defined physical and mechanical properties, depending on the type of application of the mats.

Most of the studies concern the electrospinning parameters for (bio)degradable polymers trying to understand the electrospinning mechanism. PLA, PCL, and PHB and their blends in the form of nanofibres can be used in a wide variety of biomedical and biotechnological applications. PLA as well as PCL and PHB electrospinning process strongly depends from the type of polymer/solvent system. These (bio)degradable polymers are electrospun from the different single solvent system such as acetone, 2,2,2-trifluoroethanol (TFE), chloroform (TCM), and many others, and continuous fibres are obtained only using solvents with high electrical conductivity. Smooth defect-free nanofibres with a narrow and more homogenous diameter distribution are collected using binary solvent systems such as acetone/DMF or acetone/dimethylacetamide (DMAc) (in the case of PLA) [72], tetrahydrofuran (THF)/methanol, DCM/DMF

(in the case of PCL) [73, 74] (see Figure 10), and TCM/DMF (for electrospinning of PHB) [71].

In case of PCL electrospinning, the variable parameters such as single solvent system, DCM, binary solvent system DCM/DMF 1/1, and concentrations 5 wt.%, 10 wt.%, and 15 wt.% of polymer solution were investigated, respectively.

(Bio)degradable copolymer PLGA was successfully electrospun from DCM and TCM but from hexafluoroisopropanol (HFIP) was generated the narrower fibre diameter distribution [75]. PHBV nanofibrous mats were generated from TCM [76]. Blend of two (bio)degradable polymers PLA and PBAT was electrospun, and the best solution for achieving the smooth fibres was the binary solvent DCM/DMF, but the proportion played an important role, and 3 : 2 was found as the most suitable [77]. Solution concentration which is closely related to viscosity also plays an important role in electrospinning. The increasing concentration leads to the increase of fibre diameters. Too small concentration prevents the nanofibres formation, and instead of fibres, only beads appear [78]. With regards to process parameters of electrospinning of (bio)degradable polymers, in general, at the higher voltage, the jet is unstable; therefore, more homogenous nanofibres at lower applied voltage are formed. In the case of PCL solution in HFIP, the smooth fibres are generated at 15 kV compared to 25 kV when the fibres with high average diameter are formed [79]. Tip to collector distance has a direct effect on the jet flight time and electric field strength. Fibres with small diameters can be formed when the working distance is greater. Reducing the distance shortens the time of jet flight, time of solvent evaporation, and electric field strength; all these conditions result in an increase of bead formation. On the contrary, a very large increase in the needle tip distance to the collector leads to an unstable jet and to beaded structured nanofibres [76].

The ambient conditions affect the morphology of the nanofibres observed by SEM. The collection procedure was studied by SEM. The average diameter of nanofibres collected on static collector was compared to the average diameter collected by rotating drum. The difference lies in directing of the fibres in the mats. From static collector was obtained mats with random placement of the fibre, whilst by rotating drum the aligned fibres in mats were collected. The average diameter of random (559.04 nm) and aligned PHB nanofibres (675 nm) was investigated, and it was shown that there were no significant differences in the diameters. On the other hand, the PLA is very sensitive on humidity. In the spinning process, solvent evaporates from charged jet, but

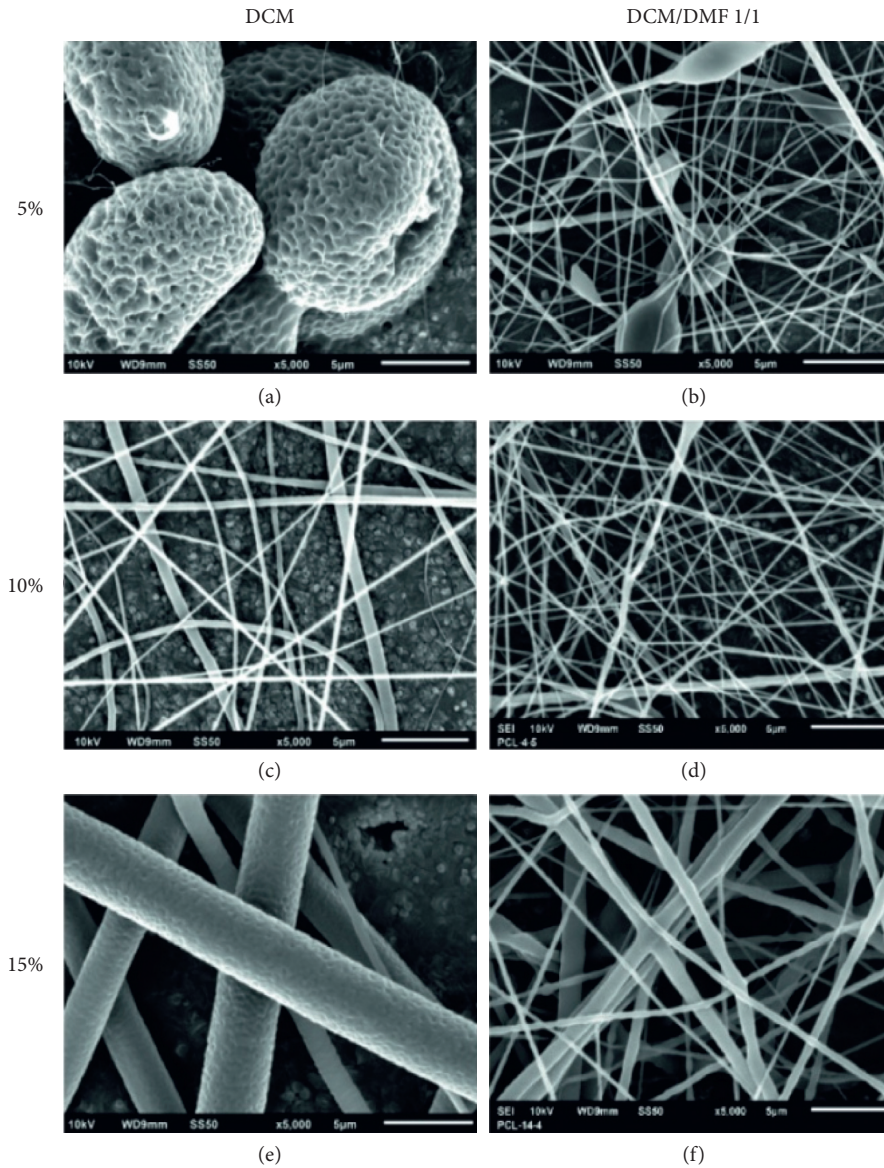


FIGURE 10: SEM micrographs of electrospun PCL at constant conditions: applied voltage = 10 kV, flow rate = 1 ml/h, needle to collector distance = 15 cm, and scale bar = 5 μ m (archive of authors).

water vapour occupies the position of the evaporated solvent. As a result, pores are formed on fibre surface after solidification of the polymeric phase (see Figure 11). The bigger pores formed at higher humidity due to more water vapour replacing the position of the evaporated solvent [80]. The electrospinning mechanism is difficult to understand due to lot of parameters. Microscopic examination enables to adjust the conditions to achieve the required morphology with regards to the application.

Highly porous PLA was electrospun into the liquid collector, hot water bath, at 70°C. The 12 wt.% solutions were prepared by dissolving PLA pellets in TCM. The solution was stirred on a magnetic plate with intensity 615 rpm for 2.5 h. DMF was added to reach required concentrations and for enhanced properties of the solutions. The TCM/DMF ratio was set at 90/10 v/v. The parameters for electrospinning PLA were selected. The solution was electrospun from a

5 mL syringe at the flow rate of 1.2 mL/h. Voltage of 12 kV was applied; needle to collector distance was 15 cm. The average diameter measured from SEM micrographs calculated by ImageJ software was 893 ± 151 nm.

4.2. Microscopic Investigation of Blends, Composites, and Hybrids Based on (Bio)degradable Polymers. Electrospun nanofibres are mimicking of structure of natural extracellular matrix, which predetermine them for application in biomedical field as wound dressing, tissue engineering, and drug release.

The fundamental requirements on the biomaterials used in biomedical field are biocompatibility, mechanical stability, and specific biological properties. Conventional single polymer materials cannot meet these requirements; therefore, multicomponent systems are designed and prepared.

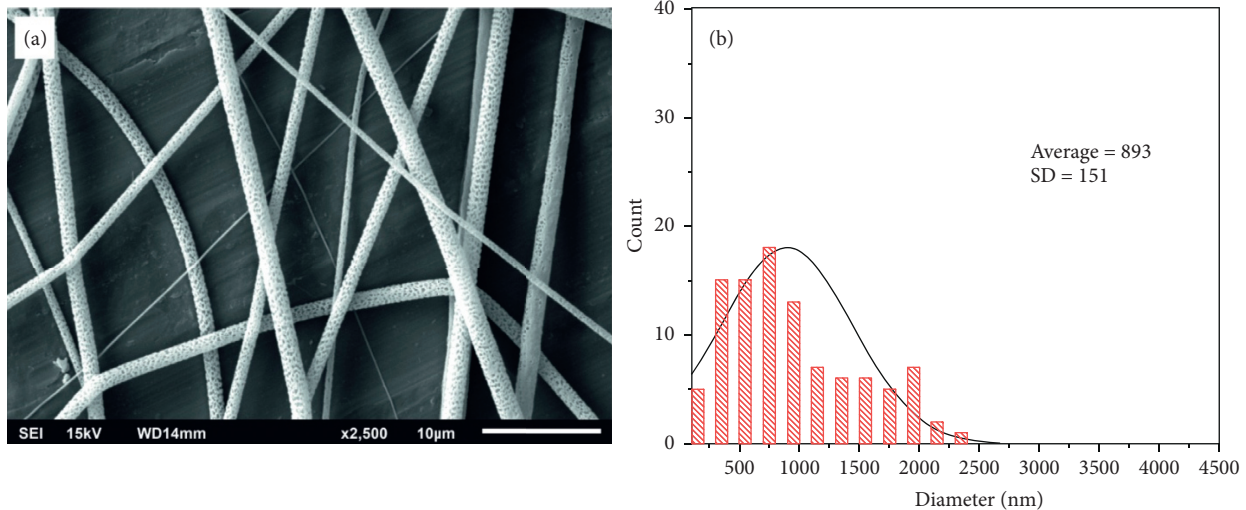


FIGURE 11: SEM micrographs of electrospun highly porous PLA (a) and histogram (b) (archive of authors).

Introduction of biomolecules or inorganic molecules into (bio)degradable polymer matrix is effective to obtain blends, composites, and hybrids with required properties [81].

4.2.1. Wound Healing Dressing. Porous electrospun nanofibrous matrices offer greater surface area and allow high oxygen permeation, easy protrusion of exudates, and protection of wounds from infection, bacterial colonisation, and dehydration. All these properties are important for wound healing dressing. For such application was tested composite containing starch and PCL, nanofibres, which was fabricated by coaxial needle electrospinning technique. Processing parameters such as polymer solution concentration, flow rate, the nozzle-ground distance, or applied voltage had a marked influence on the composite fibre diameter, and morphological study had an importance for the visualisation and understanding of the fibre structure. The SEM visualisation revealed that the PCL component in the electrospun nanocomposite structure was more prone to create fibres, while the starch formed beads. This was because of structural features of starch. Furthermore, a relationship between diameter of the fibres and concentration of starch was observed. The fibre diameter increased with the starch concentration because the bigger beads caused the formation of thicker fibres connecting these beads, also providing better strength. A lower diameter range of fibres was caused by both low viscosity and electrical conductivity, resulting in a low viscoelastic force. In general, a higher concentration of starch denoted the higher viscosity, fibre diameter, and bead formation [82]. In other study, the electrospun mats on the base of blends containing PHBV copolymer and collagen as well as gelatine, respectively, were examined as a biological wound dressing. SEM images showed cell morphology and attachment after *in vitro* culture of human dermal sheath (DS) cells in matrices. DS cells adhered significantly faster to the hydrophilic PHBV/collagen matrix than to hydrophobic PHBV matrix. Whilst DS cells achieved complete confluence into the hydrophilic matrix within 6 hours, at the same time,

these cells were just beginning to attach to the hydrophobic matrix. Nevertheless, wound healing test results showed that the contribution of PHBV/collagen into the healing process was small, although it showed increase in hydrophilicity and faster hydration, better cell attachment, and proliferation compared to PHBV, which was much more mechanically stable. These results indicated that mechanical stability of matrix is more important factor in wound healing than its cell culture activity [83].

4.2.2. Drug Delivery Systems. Electrospinning offers the opportunity to design new systems which act as a vehicle of local drug administration that can release the therapeutic agent at the site of the pathogenic area. Drug delivery on the base of polymer nanofibres is based on the principle that the drug dissolution rate increases with increased surface area. The nanofibrous membrane containing drug can be post-processed into the kind of drug formulation [84].

Biomimetic fibrous scaffolds of PLA and PLA loaded with dipyridamole (DPM) were developed to act as drug delivery system coated on the cardiovascular stents [74]. The evaluation of the surface morphology and topography of PLA scaffold after fabrication, DPM loaded PLA system, coated stent, and delivery system during degradation process was conducted through AFM and SEM. Drug-loaded scaffolds were fabricated with good morphology without beads. The average diameter of blank PLA nanofibres (522 nm) and loaded PLA (556 nm) was calculated by ImageJ software on the basis of SEM images. The degradation study took 90 days, and how scaffolds degrade with hydrolysis was observed. Microscopic evaluation revealed the differences in average diameter of nanofibres. After 30 days, the diameters in both cases (blank and loaded PLA scaffolds) increased due to the swelling of the scaffolds, along the hydrophobicity of the polymer; then in 90 days, the degradation started due to hydrolysis and therefore the diameter decreased. Finally, the total amount of DPM loaded was released through scaffold after 218 days [74]. Electrospun mats for controlled release of

paracetamol were also developed. The SEM study showed that the morphology of electrospun fibres was of a common nature, and they are round-shaped, bead free, randomly arrayed, fibrous, and highly porous mats. The paracetamol crystals were not detected on the surface of fibres. This indicated that the drug was incorporated into the structure of electrospun fibres homogeneously. From SEM images, average diameters were calculated. Then, degradation profiles of fibrous mats were assessed by SEM. Compared to the fine fibres before incubation, the morphology during incubation changed significantly. The fibres after 24 h of incubation at pH 5.6 were swollen and curly, and the samples contained coexisting fibres and films. At pH 4 after 24 h of incubation, only films were detected without any fibres evidence [77]. Drug delivery vehicles can be used also in food packaging with loaded various bactericide agents and compounds with antimicrobial and/or antifungal activity [65, 66].

4.2.3. Tissue Engineering. Tissue engineering or regenerative medicine uses the scaffolds to support the cells to regenerate new extracellular matrix which have been destroyed by diseases, injury, or congenital defects. Electrospinning provides 3D porous mats with high porosity and large surface area, mimicking extracellular matrix structure; therefore, they are considered an excellent candidate for use in regenerative medicine. The requirements for tissue engineering application are biocompatibility and (bio)degradability. Also, scaffold architecture affects cell binding significantly [58]. (Bio)degradable polymers are commonly used as biomaterials for bone repair. To date, PLA, PLGA, PCL, PGA, their blends, composites, and hybrids were investigated for tissue engineering because they meet the most criteria for this application [85]. The bone is a rigid and complex form containing fibrous organic matrix impregnated with inorganic minerals, such as calcium or phosphate. Inorganic minerals provide the hardness and toughness to tissue. For example, alternatively, interest has been paid to a hybrid from PCL fibrous scaffold in combination with silicate-containing hydroxyapatite (SiHA) microparticles to improve cell penetration [86]. The morphology and structure of fibres is important in controlling the adhesion and proliferation of cells; therefore, the surface was investigated by SEM and was characterised by presence of the fibres in micron scale for PCL-SiHA scaffolds. The cell viability, as a crucial issue for the clinical use of 3D scaffolds, was tested by human mesenchymal stem cells (hMSCs) for a site-specific repair [87].

4.2.4. Electronics and Bioelectronics Applications. Electrospinning is a popular method also in the field of sensing or electronics, in general. The (bio)degradable materials are preferred in this direction as well because many studies are focused on creating and investigating environmentally friendly conductive sensors for gases and volatile organic compounds based on (bio)degradable electrospun nanofibres. To design and fabricate of environmentally friendly conductive sensors in moistened environments, the (bio)degradable electrospun nanofibrous polymer blends containing polyaniline (PANi) and PHB [88], PANi and

PLA [89], PLGA, PCL and PANi [90] or composites containing silver ink, PCL and poly(glycerol sebacate) (PGS) for stretchable electronics [91], and electrospun PCL nanofibres modified by polypyrrole [60] have been used. Morphology of (bio)degradable nanofibrous layers mainly by SEM or TEM has been investigated. The quality of nanofibres in the sense of homogeneity/heterogeneity, the beads presence, directing of the nanofibres, average diameter of nanofibres, distribution of active compounds in the nanofibres structures or continuity of coatings, presence of agglomerates, and their size has been evaluated. SEM investigations showed that the conductivity of final products was influenced by the continuity of the coating [60, 91] and/or the distribution of the conductive substance [89, 90]. The individual components could be distinguished within the fibres by TEM for their different electron density [88]. According the SEM images, the outgrowth and viability of cells in the samples after electrical stimulation were also assessed and thus the suitability of final product as a good candidate for electrical conductive scaffolds was determined [90].

5. Conclusions

The (bio)degradable plastics market is relatively new, but involves more and more products that have so far been obtained from nonbiodegradable conventional polymers and is divided mainly between PLA, starch blends, PCL, cellulose, poly(butylene succinate) (PBS), PHAs, and their blends. Advanced (bio)degradable polymer materials are considered for many new applications, e.g., as superconductors or engineering materials. Such materials are also regarded necessary in medical applications. The development of polymeric materials for new applications is therefore of great importance. However, efficient use requires basic research necessary to determine the relationship between the structure of such materials, properties, and mechanism of degradation. Although environmentally friendly polymers have gained much attention as possible substitutes for conventional plastics, factors that affect their durability are often difficult to investigate. Obtaining basic knowledge about these interactions will allow better targeting of innovative applications of advanced (bio)degradable polymeric materials and avoiding problems when using final products. Various techniques are used to analyse polymeric materials. The SEM and AFM techniques are an indispensable tool in studies of polymer blends, composites, and hybrid functional materials such as nanomaterials and characterisation of electrospun nanofibres.

For (bio)degradable polymers, microscopic techniques can provide an accurate scan of surface morphology and give detailed information on sample surfaces heterogeneity at nanometre resolution, providing information about morphological changes during, for example, processing or detecting the elasticity and viscosities of a sample in the case of different substrates or distinguishing polymer phase transition. In addition, microscopic techniques such as AFM or SEM can be used to characterise blend, composite, and hybrid materials in terms of mechanical, physical, thermal, and chemical properties [56].

Conflicts of Interest

The authors declare that there are no conflicts of interest regarding the publication of this article.

Acknowledgments

This work was supported by a Polish-Hungarian Joint Research Project “Controlled release and degradation studies of biodegradable aliphatic polyester derivatives based nanoparticles loaded with organic drug” (2017–2019) and a Polish-Slovak Joint Research Project “Predictive study under composting conditions of bioactive materials obtained by electrospinning” (2019–2021). The authors would like to thank VEGA 2-0135-19 and APVV 15-0545 projects for the support.

References

- [1] R. P. Babu, K. O'Connor, and R. Seeram, “Current progress on bio-based polymers and their future trends,” *Progress in Biomaterials*, vol. 2, no. 1, p. 8, 2013.
- [2] S. Jurczyk, M. Musioł, M. Sobota et al., “(Bio)degradable polymeric materials for sustainable future—part 2: degradation studies of P(3HB-co-4HB)/cork composites in different environments,” *Polymers*, vol. 11, no. 3, p. 547, 2019.
- [3] M. Musioł, H. Janeczek, S. Jurczyk et al., “(Bio)degradation studies of degradable polymer composites with jute in different environments,” *Fibers and Polymers*, vol. 16, no. 6, pp. 1362–1369, 2015.
- [4] M. C. Area and H. Cheradame, “Paper aging and degradation: recent findings and research methods,” *BioResources*, vol. 6, no. 4, pp. 5307–5337, 2011.
- [5] B. Nowak, J. Pająk, and J. Karcz, “Biodegradation of pre-aged modified polyethylene films,” in *Scanning Electron Microscopy*, V. Kazmiruk, Ed., IntechOpen, London, UK, 2012, <https://www.intechopen.com/books/scanning-electron-microscopy/biodegradation-of-pre-aged-modified-polyethylene-films>.
- [6] K. Kersten, *Sample Degradation During SEM Analysis: What Causes It and How to Slow Down the Process*, ThermoFisher Scientific, Waltham, MA, USA, 2018, <https://blog.phenom-world.com/sample-degradation-scanning-electron-microscope-sem>.
- [7] NanoScience Instruments, *Atomic Force Microscopy*, 2019, <https://www.nanoscience.com/techniques/atomic-force-microscopy>.
- [8] Y. Kikkawa, T. Suzuki, T. Tsuge, M. Kanesato, Y. Doi, and H. Abe, “Phase structure and enzymatic degradation of poly(L-lactide)/atactic poly(3-hydroxybutyrate) blends: an atomic force microscopy study,” *Biomacromolecules*, vol. 7, no. 6, pp. 1921–1928, 2006.
- [9] C. Coluzza, M. Bicchieri, M. Monti, G. Piantanida, and A. Sodo, “Atomic force microscopy application for degradation diagnostics in library heritage,” *Surface and Interface Analysis*, vol. 40, no. 9, pp. 1248–1253, 2008.
- [10] U. Maver, T. Velnar, M. Gaberšček, O. Planinšek, and M. Finšgar, “Recent progressive use of atomic force microscopy in biomedical applications,” *TrAC Trends in Analytical Chemistry*, vol. 80, pp. 96–111, 2016.
- [11] H. Mason, *Measuring Equipment Detects 3D Printing Defects*, 2018, <https://www.additivemanufacturing.media/products/measuring-equipment-detects-3d-printing-defects>.
- [12] S. Thomas, R. Thomas, A. Zachariah, and R. Mishra, *Microscopy Methods in Nanomaterials Characterization*, Elsevier, Amsterdam, Netherlands, 2017.
- [13] N. Chouhan, “Silver nanoparticles: synthesis, characterization and applications,” in *Silver Nanoparticles-Fabrication, Characterization and Applications*, K. Maaz, Ed., IntechOpen, London, UK, 2018, <https://www.intechopen.com/books/silver-nanoparticles-fabrication-characterization-and-applications/silver-nanoparticles-synthesis-characterization-and-applications>.
- [14] A. M. Al-Enizi, M. M. Zagho, and A. A. Elzatahry, “Polymer-based electrospun nanofibers for biomedical applications,” *Nanomaterials*, vol. 8, no. 4, 2018.
- [15] J. Zeng, X. Chen, X. Xu et al., “Ultrafine fibers electrospun from biodegradable polymers,” *Journal of Applied Polymer Science*, vol. 89, no. 4, pp. 1085–1092, 2003.
- [16] J. Rydz, K. Wolna-Stypka, G. Adamus et al., “Forensic engineering of advanced polymeric materials. Part 1-degradation studies of polylactide blends with atactic poly[(R,S)-3-hydroxybutyrate] in paraffin,” *Chemical and Biochemical Engineering Quarterly*, vol. 29, no. 2, pp. 247–259, 2015.
- [17] J. Rydz, W. Sikorska, M. Musioł et al., “Degradation of PLA-based (nan)ocomposites in different environments,” in *Nanostructured Materials Application and Innovation Transfer, Nanoscience & Nanotechnology, Issue 14*, E. Balabanova and E. Mileva, Eds., pp. 109–111, BPS Ltd., Sofia, Bulgaria, 2014.
- [18] C. Ha and W.-J. Cho, “Miscibility, properties, and biodegradability of microbial polyester containing blends,” *Progress in Polymer Science*, vol. 27, no. 4, pp. 759–809, 2002.
- [19] J. Rydz, W. Sikorska, M. Musioł, B. Zawidlak-Węgrzyńska, and K. Duale, “Sustainable future alternative: (bio)degradable polymers for the environment,” Chapter 11520, in *Encyclopaedia of Renewable and Sustainable Materials*, S. Hashmi and I. Choudhury, Eds., Elsevier, Amsterdam, Netherlands, 2020, In press.
- [20] K. Zhao, X. Yang, G.-Q. Chen, and J.-C. Chen, “Effect of lipase treatment on the biocompatibility of microbial polyhydroxyalkanoates,” *Journal of Materials Science: Materials in Medicine*, vol. 13, no. 9, pp. 849–854, 2002.
- [21] G. G. Choi, H. W. Kim, and Y. H. Rhee, “Enzymatic and non-enzymatic degradation of poly(3-hydroxybutyrate-co-3-hydroxyvalerate) copolyesters produced by *Alcaligenes* sp. MT-16,” *Journal of Microbiology*, vol. 42, no. 4, pp. 346–352, 2004.
- [22] E. Marten, R.-J. Müller, and W.-D. Deckwer, “Studies on the enzymatic hydrolysis of polyesters I. Low molecular mass model esters and aliphatic polyesters,” *Polymer Degradation and Stability*, vol. 80, no. 3, pp. 485–501, 2003.
- [23] C. M. Chan, L.-J. Vandi, S. Pratt et al., “Insights into the biodegradation of PHA/wood composites: micro- and macroscopic changes,” *Sustainable Materials and Technologies*, vol. 21, Article ID e00099, 12 pages, 2019.
- [24] O. Wilfred, H. Tai, R. Marriott et al., “Biodegradation of polylactic acid and starch composites in compost and soil,” *International Journal of Nano Research*, vol. 1, no. 2, pp. 1–11, 2018.
- [25] M. Musioł, W. Sikorska, H. Janeczek et al., “(Bio)degradable polymeric materials for a sustainable future—part 1. Organic recycling of PLA/PBAT blends in the form of prototype packages with long shelf-life,” *Waste Management*, vol. 77, pp. 447–454, 2018.
- [26] Y. Kikkawa, T. Suzuki, M. Kanesato, Y. Doi, and H. Abe, “Effect of phase structure on enzymatic degradation in poly(L-lactide)/

- atactic poly(3-hydroxybutyrate) blends with different miscibility," *Biomacromolecules*, vol. 10, no. 4, pp. 1013–1018, 2009.
- [27] A. Amor, N. Okhay, A. Guinault, G. Miquelard-Garnier, C. Sollogoub, and M. Gervais, "Combined compatibilization and plasticization effect of low molecular weight poly(lactic acid) in poly(lactic acid)/poly(3-hydroxybutyrate-co-3-hydroxyvalerate) blends," *eXPRESS Polymer Letters*, vol. 12, no. 2, pp. 114–125, 2018.
- [28] C. C. Sarath, R. A. Shanks, and S. Thomas, "Polymer blends," in *Nanostructured Polymer Blends*, S. Thomas, R. Shanks, and S. Chandran, Eds., pp. 1–13, Elsevier, Amsterdam, Netherlands, 2013.
- [29] A. Sangroniz, A. Gonzalez, L. Martin, L. Irueta, M. Iriarte, and A. Etxeberria, "Miscibility and degradation of polymer blends based on biodegradable poly(butylene adipate-co-terephthalate)," *Polymer Degradation and Stability*, vol. 151, pp. 25–35, 2018.
- [30] Y. Deng, C. Yu, P. Wongwiwattana, and N. L. Thomas, "Optimising ductility of poly(lactic acid)/poly(butylene adipate-co-terephthalate) blends through co-continuous phase morphology," *Journal of Polymers and the Environment*, vol. 26, no. 9, pp. 3802–3816, 2018.
- [31] K. Kersten, *How SEM Helps to Detect Additive Manufacturing Defects in a 3D-Printed Object*, ThermoFisher Scientific, Waltham, MA, USA, 2018, <https://blog.phenom-world.com/sem-additive-manufacturing-3d-printing-defects>.
- [32] I. Chiulan, A. N. Frone, C. Brandabur, and D. M. Panaitescu, "Recent advances in 3D printing of aliphatic polyesters," *Bioengineering*, vol. 5, no. 1, p. 2, 2017.
- [33] J. Gonzalez Ausejo, J. Rydz, M. Musioł et al., "A comparative study of three-dimensional printing directions: the degradation and toxicological profile of a PLA/PHA blend," *Polymer Degradation and Stability*, vol. 152, pp. 191–207, 2018.
- [34] S. Daneshmand and C. Aghanajafi, "Description and modeling of the additive manufacturing technology for aerodynamic coefficients measurement," *Strojniški vestnik-Journal of Mechanical Engineering*, vol. 58, no. 2, pp. 125–133, 2012.
- [35] K. G. J. Christiyen, U. Chandrasekhar, and K. Venkateswarlu, "A study on the influence of process parameters on the mechanical properties of 3D printed ABS composite," *IOP Conference Series: Materials Science and Engineering*, vol. 114, article 012109, 2016.
- [36] J. Gonzalez Ausejo, J. Rydz, M. Musioł et al., "Three-dimensional printing of PLA and PLA/PHA dumbbell-shaped specimens of crisscross and transverse patterns as promising materials in emerging application areas: prediction study," *Polymer Degradation and Stability*, vol. 156, pp. 100–110, 2018.
- [37] K. Kyriakidou, G. Lucarini, A. Zizzi et al., "Dynamic co-seeding of osteoblast and endothelial cells on 3D polycaprolactone scaffolds for enhanced bone tissue engineering," *Journal of Bioactive and Compatible Polymers*, vol. 23, no. 3, pp. 227–243, 2008.
- [38] M. Orciani, M. Fini, R. Di Primio, and M. Mattioli-Belmonte, "Biofabrication and bone tissue regeneration: cell source, approaches, and challenges," *Frontiers in Bioengineering and Biotechnology*, vol. 5, no. 17, 15 pages, 2017.
- [39] P. Dobson, H. Jarvie, and S. King, "Nanoparticle," in *Encyclopedia Britannica*, 2019, <https://www.britannica.com/science/nanoparticle>.
- [40] S. K. Mallapragada and B. Narasimhan, *Handbook of Biodegradable Polymeric Materials and Their Applications*, American Scientific Publishers, USA, 2005.
- [41] A. Mahapatro and D. Singh, "Biodegradable nanoparticles are excellent vehicle for site directed *in-vivo* delivery of drugs and vaccines," *Journal of Nanobiotechnology*, vol. 9, no. 55, pp. 1–11, 2011.
- [42] M. Scimeca, S. Bischetti, H. K. Lamsira, R. Bonfiglio, and E. Bonanno, "Energy Dispersive X-ray (EDX) microanalysis: a powerful tool in biomedical research and diagnosis," *European Journal of Histochemistry*, vol. 62, no. 1, article 2841, 2018.
- [43] F. Solá, "Advanced electron microscopy techniques in nanomaterials characterization at NASA Glenn Research Center," in *The Transmission Electron Microscope-Theory and Applications*, K. Maaz, Ed., IntechOpen, London, UK, 2015, <https://www.intechopen.com/books/the-transmission-electron-microscope-theory-and-applications/advanced-electron-microscopy-techniques-in-nanomaterials-characterization-at-nasa-glenn-research-center>.
- [44] S. Mourdikoudis, R. M. Pallares, and N. T. K. Thanh, "Characterization techniques for nanoparticles: comparison and complementarity upon studying nanoparticle properties," *Nanoscale*, vol. 10, no. 27, pp. 12871–12934, 2018.
- [45] M. Zambaux, F. Bonneaux, R. Gref, P. Maincent, E. Dellacherie, and M. J. Alonso, "Influence of experimental parameters on the characteristics of poly(lactic acid) nanoparticles prepared by a double emulsion method," *Journal of Controlled Release*, vol. 50, no. 1–3, pp. 31–40, 1998.
- [46] D. Zhu, W. Tao, H. Zhang et al., "Docetaxel (DTX)-loaded polydopamine-modified TPGS-PLA nanoparticles as a targeted drug delivery system for the treatment of liver cancer," *Acta Biomaterialia*, vol. 30, pp. 144–154, 2016.
- [47] K. Na, K. H. Lee, D. H. Lee, and Y. H. Bae, "Biodegradable thermo-sensitive nanoparticles from poly(L-lactic acid)/poly(ethylene glycol) alternating multi-block copolymer for potential anti-cancer drug carrier," *European Journal of Pharmaceutical Sciences*, vol. 27, no. 2-3, pp. 115–122, 2006.
- [48] F. X. Lacasse, P. Hildgen, and J. N. McMullen, "Surface and morphology of spray-dried pegylated PLA microspheres," *International Journal of Pharmaceutics*, vol. 174, no. 1-2, pp. 101–109, 1998.
- [49] C. Wischke and S. P. Schwendeman, "Principles of encapsulating hydrophobic drugs in PLA/PLGA microparticles," *International Journal of Pharmaceutics*, vol. 364, no. 2, pp. 298–327, 2008.
- [50] P. S. C. Sacchetin, A. R. Morales, A. M. Moraes, and P. D. T. V. E. Rosa, "Formation of PLA particles incorporating 17 α -methyltestosterone by supercritical fluid technology," *Journal of Supercritical Fluids*, vol. 77, pp. 52–62, 2013.
- [51] C.-Y. Liao and Y.-C. Su, "Formation of biodegradable microcapsules utilizing 3D, selectively surface-modified PDMS microfluidic devices," *Biomedical Microdevices*, vol. 12, no. 1, pp. 125–133, 2010.
- [52] Y. Lu, M. Sturek, and K. Park, "Microparticles produced by the hydrogel template method for sustained drug delivery," *International Journal of Pharmaceutics*, vol. 461, no. 1-2, pp. 258–269, 2014.
- [53] A. Kumari, S. K. Yadav, and S. C. Yadav, "Biodegradable polymeric nanoparticles based drug delivery systems," *Colloids and Surfaces B: Biointerfaces*, vol. 75, no. 1, pp. 1–18, 2010.
- [54] G. Mittal, D. K. Sahana, V. Bhardwaj, and M. N. V. Ravi Kumar, "Estradiol loaded PLGA nanoparticles for oral administration: effect of polymer molecular weight and copolymer composition on release behavior *in vitro* and *in vivo*," *Journal of Controlled Release*, vol. 119, no. 1, pp. 77–85, 2007.

- [55] Y. Farrag, B. Montero, M. Rico, L. Barral, and R. Bouza, "Preparation and characterization of nano and micro particles of poly(3-hydroxybutyrate-co-3-hydroxyvalerate) (PHBV) via emulsification/solvent evaporation and nanoprecipitation techniques," *Journal of Nanoparticle Research*, vol. 20, no. 71, p. 17, 2018.
- [56] M. Marrese, V. Guarino, and L. Ambrosio, "Atomic force microscopy: a powerful tool to address scaffold design in tissue engineering," *Journal of Functional Biomaterials*, vol. 8, no. 7, p. 20, 2017.
- [57] A. Rogina, "Electrospinning process: versatile preparation method for biodegradable and natural polymers and bio-composite systems applied in tissue engineering and drug delivery," *Applied Surface Science*, vol. 296, pp. 221–230, 2014.
- [58] S. Agarwal, J. H. Wendorff, and A. Greiner, "Use of electrospinning technique for biomedical applications," *Polymer*, vol. 49, no. 26, pp. 5603–5621, 2008.
- [59] S. Reich, M. Burgard, M. Langner et al., "Polymer nanofiber composite nonwovens with metal-like electrical conductivity," *Flexible Electronics*, vol. 2, no. 1, 2018.
- [60] E. Číková, M. Mičušík, A. Šišková, M. Procházka, P. Fedorko, and M. Omastová, "Conducting electrospun polycaprolactone/polypyrrole fibers," *Synthetic Metals*, vol. 235, pp. 80–88, 2018.
- [61] V. Thavasi, G. Singh, and S. Ramakrishna, "Electrospun nanofibers in energy and environmental applications," *Energy & Environmental Science*, vol. 1, no. 2, pp. 205–221, 2008.
- [62] A. Camire, J. Espinasse, B. Chabot, and A. Lajeunesse, "Development of electrospun lignin nanofibers for the adsorption of pharmaceutical contaminants in wastewater," *Environmental Science and Pollution Research International*, pp. 1–14, 2018.
- [63] V. Buchholz, M. Molnar, H. Wang et al., "Protection of vine plants against esca disease by breathable electrospun antifungal nonwovens," *Macromolecular Bioscience*, vol. 16, no. 9, pp. 1391–1397, 2016.
- [64] M. Noruzi, "Electrospun nanofibres in agriculture and the food industry: a review," *Journal of the Science of Food and Agriculture*, vol. 96, no. 14, pp. 4663–4678, 2016.
- [65] Y. Liu, X. Liang, S. Wang, W. Qin, and Q. Zhang, "Electrospun antimicrobial polylactic acid/tea polyphenol nanofibers for food-packaging applications," *Polymers*, vol. 10, no. 5, pp. 561–575, 2018.
- [66] T. Huang, Y. Qian, J. Wei, and C. Zhou, "Polymeric antimicrobial food packaging and its applications," *Polymers*, vol. 11, no. 3, 2019.
- [67] M. Marrese, V. Cirillo, V. Guarino, and L. Ambrosio, "Short-term degradation of bi-component electrospun fibers: qualitative and quantitative evaluations via AFM analysis," *Journal of Functional Biomaterials*, vol. 9, no. 2, p. 27, 2018.
- [68] B. R. Neugirg, M. Burgard, A. Greiner, and A. Fery, "Tensile versus AFM testing of electrospun PVA nanofibers: bridging the gap from microscale to nanoscale," *Journal of Polymer Science Part B: Polymer Physics*, vol. 54, no. 23, pp. 2418–2424, 2016.
- [69] W. Meng, Z.-C. Xing, K.-H. Jung et al., "Synthesis of gelatin-containing PHBV nanofiber mats for biomedical application," *Journal of Materials Science: Materials in Medicine*, vol. 19, no. 8, pp. 2799–2807, 2008.
- [70] M. Mader, V. Jérôme, R. Freitag, S. Agarwal, and A. Greiner, "Ultraporous, compressible, wetttable polylactide/polycaprolactone sponges for tissue engineering," *Biomacromolecules*, vol. 19, no. 5, pp. 1663–1673, 2018.
- [71] D. M. Correia, C. Ribeiro, J. C. C. Ferreira et al., "Influence of electrospinning parameters on poly(hydroxybutyrate) electrospun membranes fiber size and distribution," *Polymer Engineering & Science*, vol. 54, no. 7, pp. 1608–1617, 2014.
- [72] R. Casasola, N. L. Thomas, A. Trybala, and S. Georgiadou, "Electrospun poly lactic acid (PLA) fibres: effect of different solvent systems on fibre morphology and diameter," *Polymer*, vol. 55, no. 18, pp. 4728–4737, 2014.
- [73] S. Sarabi-Mianaji, J. Scott, and D. J. Y. S. Pagé, "Impact of electrospinning process parameters on the measured current and fiber diameter," *Polymer Engineering & Science*, vol. 55, no. 11, pp. 2576–2582, 2015.
- [74] V. Bakola, V. Karagkiozaki, A. R. Tsiapla et al., "Dipyridamole-loaded biodegradable PLA nanoplateforms as coatings for cardiovascular stents," *Nanotechnology*, vol. 29, no. 27, article 275101, 2018.
- [75] Y. P. Chen, H. Y. Liu, Y. W. Liu, T. Y. Lee, and S. J. Liu, "Determination of electrospinning parameters' strength in poly(D,L)-lactide-co-glycolide micro/nanofiber diameter tailoring," *Journal of Nanomaterials*, vol. 2019, Article ID 2626085, 8 pages, 2019.
- [76] H.-W. Tong and M. Wang, "Electrospinning of poly(hydroxybutyrate-co-hydroxyvalerate) fibrous scaffolds for tissue engineering applications: effects of electrospinning parameters and solution properties," *Journal of Macromolecular Science, Part B*, vol. 50, no. 8, pp. 1535–1558, 2011.
- [77] S. Khatsee, D. Daranarong, W. Punyodom, and P. Worajittiphon, "Electrospinning polymer blend of PLA and PBAT: electrospinnability-solubility map and effect of polymer solution parameters toward application as antibiotic-carrier mats," *Journal of Applied Polymer Science*, vol. 135, no. 28, article 46486, 2018.
- [78] R. Augustine, N. Kalarikkal, and S. Thomas, "Clogging-free electrospinning of polycaprolactone using acetic acid/acetone mixture," *Polymer-Plastics Technology and Engineering*, vol. 55, no. 5, pp. 518–529, 2015.
- [79] M. I. Hassan, T. Sun, and N. Sultana, "Fabrication of nanohydroxyapatite/poly(caprolactone) composite microfibers using electrospinning technique for tissue engineering applications," *Journal of Nanomaterials*, vol. 2014, Article ID 209049, 7 pages, 2014.
- [80] Z. Liu, J. Zhao, W. Li, J. Xing, L. Xu, and J. He, "Humidity-induced porous poly(lactic acid) membrane with enhanced flux for oil-water separation," *Adsorption Science & Technology*, pp. 1–12, 2018.
- [81] Z. C. Xing, S. J. Han, Y. S. Shin, and I. K. Kang, "Fabrication of biodegradable polyester nanocomposites by electrospinning for tissue engineering," *Journal of Nanomaterials*, vol. 2011, Article ID 929378, 18 pages, 2011.
- [82] B. Komur, F. Bayrak, N. Ekren et al., "Starch/PCL composite nanofibers by co-axial electrospinning technique for biomedical applications," *Biomedical Engineering Online*, vol. 16, no. 1, p. 40, 2017.
- [83] I. Han, K. J. Shim, J. Y. Kim et al., "Effect of poly(3-hydroxybutyrate-co-3-hydroxyvalerate) nanofiber matrices cocultured with hair follicular epithelial and dermal cells for biological wound dressing," *Artificial Organs*, vol. 31, no. 11, pp. 801–808, 2007.
- [84] M. Qi, X. Li, Y. Yang, and S. Zhou, "Electrospun fibers of acid-labile biodegradable polymers containing ortho ester groups for controlled release of paracetamol," *European Journal of Pharmaceutics and Biopharmaceutics*, vol. 70, no. 2, pp. 445–452, 2008.
- [85] R. Kroeze, M. Helder, L. Govaert, and T. Smit, "Biodegradable polymers in bone tissue engineering," *Materials*, vol. 2, no. 3, pp. 833–856, 2009.

- [86] S. Shkarina, R. Shkarin, V. Weinhardt et al., "3D biodegradable scaffolds of polycaprolactone with silicate-containing hydroxyapatite microparticles for bone tissue engineering: high-resolution tomography and in vitro study," *Scientific Reports*, vol. 8, no. 8907, p. 13, 2018.
- [87] Z. Sheikh, S. Najeeb, Z. Khurshid, V. Verma, H. Rashid, and M. Glogauer, "Biodegradable materials for bone repair and tissue engineering applications," *Materials*, vol. 8, no. 9, pp. 5744–5794, 2015.
- [88] A. Macagnano, V. Perri, E. Zampetti, A. Bearzotti, and F. De Cesare, "Humidity effects on a novel eco-friendly chemosensor based on electrospun PANi/PHB nanofibres," *Sensors and Actuators B: Chemical*, vol. 232, pp. 16–27, 2016.
- [89] P. S. Picciani, E. Medeiros, E. Venancio, B. Soares, and L. C. Mattoso, "Development of electrospun polyaniline/poly(lactic acid) nanofiber-based sensors," *Sensor Letters*, vol. 14, no. 9, pp. 864–871, 2016.
- [90] H. Farkhondehnia, M. Amani Tehran, and F. Zamani, "Fabrication of biocompatible PLGA/PCL/PANI nanofibrous scaffolds with electrical excitability," *Fibers and Polymers*, vol. 19, no. 9, pp. 1813–1819, 2018.
- [91] A. H. Najafabadi, A. Tamayol, N. Annabi et al., "Biodegradable nanofibrous polymeric substrates for generating elastic and flexible electronics," *Advanced Materials*, vol. 26, no. 33, pp. 5823–5830, 2014.

Research Article

Structures, Morphological Control, and Antibacterial Performance of Ag/TiO₂ Micro-Nanocomposite Materials

Muhammad Akhsin Muflikhun ¹, Alvin Y. Chua ² and Gil N. C. Santos³

¹Department of Mechanical and Industrial Engineering, Faculty of Engineering, Gadjah Mada University, Jl. Grafika No. 2, Yogyakarta 55281, Indonesia

²Department of Mechanical Engineering, De La Salle University, 2401 Taft Avenue, Manila, Philippines

³Department of Physics, De La Salle University, 2401 Taft Avenue, Manila, Philippines

Correspondence should be addressed to Muhammad Akhsin Muflikhun; akhsin.muflikhun@ugm.ac.id

Received 14 February 2019; Revised 1 April 2019; Accepted 9 April 2019; Published 7 May 2019

Guest Editor: Joanna Rydz

Copyright © 2019 Muhammad Akhsin Muflikhun et al. This is an open access article distributed under the Creative Commons Attribution License, which permits unrestricted use, distribution, and reproduction in any medium, provided the original work is properly cited.

Structures, morphological control, and antibacterial activity of silver-titanium dioxide (Ag/TiO₂) micro-nanocomposite materials against *Staphylococcus aureus* are investigated in this study. Horizontal vapor phase growth (HVPG) technique was used to synthesize the Ag/TiO₂ micro-nanomaterials, with parameters of growth temperature and baking time. The materials were characterized by using scanning electron microscopy (SEM), energy dispersive X-ray (EDX) spectroscopy, and atomic force microscope (AFM). The result indicated that the HVPG technique is able to synthesize Ag/TiO₂ with many shapes in micro- and nanoscale such as nanoparticles, nanorods, triangular nanomaterials, and nanotubes. The results showed that the shape of micro- and nanocomposites material could be arranged by adjusting the parameters. The results revealed that the nanorods structure were obtained at 1000°C growth temperature and that 8 hours of baking time was ideal for antibacterial application. Treating the *S. aureus* stock with Ag/TiO₂ nanocomposites is able to reduce bacterial growth with a significant result.

1. Introduction

Recent forays into novel developments of medical research have involved nanomaterials as useful tools to combat cancer or bacteria, viruses, and other microbial pathogens [1–4]. Nanomaterials based on silver, titanium dioxide, carbon, and graphene have been studied for food packaging process, especially for medical applications such as anti-pathogenic activity or tissue regeneration [5–8]. There are eight main applications for nanotechnology in medicine: pathogen detection, protein detection, DNA structure penetration, tissue engineering, tumor eradication, pathogenic cell or molecule eradication, magnetic resonance imaging, and phagokinetic studies [9–11].

Synthetic silver or Ag/TiO₂ nanomaterials have been developed and successfully manufactured by several methods due to the wide applications that are found tremendously in different fields. The synthetic methods include

chemical reduction [12], chemical vapor deposition [13], electrochemical [14], green synthesis [15], HVPG [16–18], microwave [19], photochemical [20], radiation [21], and sonochemical [22].

In the case of synthesized silver-titanium nanocomposite, the research of this material applied in medical and health applications had attracted many researchers. Table 1 shows the use of silver-titanium dioxide nanocomposite material for antibacterial applications that has been performed in the previous study.

The previous study shows nanocomposite materials successfully synthesized by using HVPG technique. This technique offers certain advantages as follows: a large amount of nanocomposites material can be fabricated from the limited amount of powder-form source material, the synthesis occurred at the vacuum condition that minimizes contaminants, and by adjusting baking time and growth temperature, variations of the nanostructures can be

TABLE 1: Previous study of Ag/Ti nanomaterials.

Source	Purpose of the study	Results
Martinez-Gutierrez et al. [23]	To compare the antibacterial properties of Ag, Ti, and Ag/Ti	Silver with size 20 nm to 25 nm was the most effective against bacteria.
Liga et al. [24]	To determine the relationship between silver concentration and its effectiveness to eradicate bacteria	The higher the proportion of silver in the silver-titanium nanoparticles, the more effective the nanomaterials against bacteria.
Motlagh et al. [25]	To determine the relationship between the size of nanomaterials and its effectiveness to eradicate bacteria	Ag/Ti nanomaterials with the size between 10 nm and 30 nm show excellent results against bacteria.
Song et al. [26]	To investigate the advanced applications of Ag/Ti nanomaterials	Ag/Ti nanomaterials have excellent mechanical properties as coating materials that can be implemented in implant technology.
Yang et al. [1]	To investigate the Ag/Ti nanomaterials against bacteria	List of bacteria that can be treated by using Ag/Ti nanomaterials: <i>Staphylococcus aureus</i> , <i>Bacillus subtilis</i> , <i>Candida albicans</i> , <i>Pseudomonas aeruginosa</i> , <i>Escherichia coli</i> , and <i>Klebsiella pneumoniae</i> .
Mei et al. [27]	To investigate the Ag/Ti nanomaterials related to the dental field	Encompassing anodization method was used to synthesize titanium, and plasma immersion ion implantation method was used to synthesize silver that can produce nanotubes and can be effective against bacteria on dental implant cases.
Cao et al. [4]	To explain the application of Ag/Ti nanomaterials that is compatible with osteoblasts	The Ag/Ti nanomaterials were capable and compatible with osteoblasts synthesized using the plasma immersion ion implantation method to produce nanomaterials with size 25 nm.
Wang et al. [28]	To investigate the applications of Ag/Ti nanomaterials synthesized by using hydrothermal and irradiation methods	Ag/Ti nanobelts can be coated into paper sheet applied in food and medical technology.
Besinis et al. [8]	To investigate the best nanomaterials that are used against dental bacterial	Comparison between silver, titanium, and silver-titanium nanomaterials against <i>Streptococcus mutans</i> . The results show that silver is the best material against bacteria.

produced. Moreover, statistics analysis of synthesis nanomaterials by using the HVPG technique reported that it was capable of creating nanomaterials with various shapes such as nanoparticles, nanorods, triangular nanomaterials, and nanotubes. [17, 18, 29, 30]. Table 2 shows the previous work that has been done by researchers regarding synthesized various nanomaterials by using the HVPG technique.

The goal of this study is to investigate the structures and morphological behavior of Ag/TiO₂ micro-nanocomposites materials synthesized by using the HVPG technique. The study also evaluated the antibacterial effect of Ag/TiO₂ nanocomposite materials against the gram-positive bacterium *S. aureus*, one of the species that is commonly infectious to humans [35–37] with bacterial colonies quantified through the pour plate technique. The micro-nanostructures synthesized from the HVPG technique were evaluated by using SEM and EDX to determine the shape of the Ag/TiO₂ micro-nanocomposite. The AFM is used to determine the 3D surface roughness of the nanocomposite to explain the geometrical effect of nanocomposite that can eradicate bacteria. The antibacterial testing was conducted by comparing 2 different types of tubes with and without Ag/TiO₂. By synthesizing the above material with HVPG technique and investigating with SEM, EDX, AFM, and pour plate technique, it is a step forward in the development of manufacturing of silver-

titanium dioxide nanomaterials for antibacterial purposes with a simple, noncontaminant technique, which shapes a variety of nanomaterials.

2. Materials and Methods

The starting material was a mixture of 17.5 mg silver (Ag) powder from Aldrich Corporation and 17.5 mg titanium dioxide (TiO₂) powder from Degussa P25. JEOL JSM-5310 scanning electron microscopy (SEM) was used to image and measure the synthesized nanomaterials found at all three zones of the tube. Energy dispersive X-ray spectroscopy (EDX) was used to determine the composition of the material in terms of silver or titanium dioxide. The 3D surface roughness of nanocomposite material was characterized by using Park System XE-100 atomic force microscopy (AFM).

The silica quartz tubes with an outer diameter of 11 mm and an inner diameter of 8.5 mm are used as the vessels for synthesis. The quartz tubes containing silver and titanium dioxide powder then were evacuated using the thermionic high vacuum system to create vacuum conditions with a pressure of approximately 10⁻⁶ Torr and then sealed. This effectively sterilizes the tubes and removes possible contaminating substances.

Figure 1 shows the nanocomposite materials after sealing and then placed half inside the furnaces and divided into 3

TABLE 2: Previous study of nanomaterials synthesized via HVPG technique.

Source	Materials name	Result
Briones et al. [18]	Tin dioxide (SnO_2)	Nanostructures formed into nanowires and used for gas sensing applications
Shimizu et al. [29]	Skewered phthalocyanine $[\text{Fe}^{\text{III}}(\text{Pc})(\text{SCN})]_n$	Source material can be converted into crystalline nanostructures (nanorods) with $2\ \mu\text{m}$ width and $10\ \mu\text{m}$ length
Quitaneq and Santos [31]	Cadmium Selenide (CdSe)	Nanocrystallites with size 100 nm to 400 nm
Reyes and Santos [32]	Tin dioxide (SnO_2)	Nanostructures formed into nanowires, nanorods, nanoparticles, and nanobelts
Buot and Santos [33]	Carbon-silver (C/Ag)	Micro-nanocomposites with size from 100 nm to $1.5\ \mu\text{m}$ for battery electrode applications
Muffikhun et al. [34]	Silver-graphene (Ag/Ge)	Micro-nanocomposite materials with size from 100 nm to $2\ \mu\text{m}$

zones. The tubes were placed horizontally, with variable baking times of 4, 6, and 8 hours and variable temperatures growth of 800°C , 1000°C , and 1200°C . The tubes were only halfway inserted into the furnace, creating a temperature gradient between the hotter region inside the furnace and the cooler region outside the furnace. Figure 2 schematically depicts the vaporization of the source material located in the furnace and subsequent deposition outside the furnace.

To quantify bacterial colonies, McFarland standard 0.5 was used, with serial dilutions to dilution factors 10^{-3} to 10^{-6} . About 1.5×10^{-8} CFU/mL of inoculum of test organism, which is *S. aureus*, is spread onto the agar plate. The plate was placed on the inoculated plates and then incubated at 37°C for 16–24 hours. The pour plate technique was used to grow the colonies under three different setups: negative control of only the bacterial suspension and two setups with the nanocomposites of 17.5 gram Ag and 17.5 gram TiO_2 [38–40].

A vortex mixer was used to homogenize the *S. aureus* suspension with the Ag/TiO_2 nanocomposites. This was inoculated into Petri dishes and incubated at room temperature for 18 hours before colony counting. Figure 3 shows a flowchart of the experiment conducted in the study.

3. Results and Discussion

3.1. Material Characterization via SEM and EDX. SEM revealed the external morphology of the nanocomposites, while EDX determines its relative composition. Figure 4 shows the SEM image of Ag/TiO_2 material before it was mixed. The results show that most of the materials are macro in size and in bulk form. In this study, the nanomaterials deposited at different zones of the quartz tube were separately investigated by using SEM.

Figure 5 shows the SEM images of the as-prepared hybrid nanocomposite materials Ag/TiO_2 with a baking time of 4 hours. As shown, the materials are not fully transformed to its nanosized form and visible in zone 3 and partially shown in zone 2 both at 800°C of growth temperature. The results indicate that the baking time is not enough to evaporate silver and titanium dioxide macro-materials to nanoscale especially at 800°C growth temperature. Some amount of Ag and TiO_2 bulk materials source

material still had not changed into nanomaterials. In contrast, nanomaterials exhibit in zone 2 and zone 3 at 1000°C and 1200°C growth temperature. The nanoparticle size ranges from 700 to 1416 nm.

Figure 6 shows that the majority of silver nanomaterials were detected after Ag/TiO_2 evaporated in zone 1, zone 2, and zone 3. The particles were exhibited on the inner surface of the silica tubes. It also indicates that the majority of the Ag/TiO_2 deposit appeared at zone 2 of the tube. EDX spectroscopy in Figure 7 shows the majority of the material consisting silver exhibits in zone 2 of the tube at 1200°C growth temperature and 6 hours baking time. This phenomenon occurred due to inadequate growth temperature for the evaporation of TiO_2 .

Figure 8 shows the SEM images of the Ag/TiO_2 nanocomposite materials. The results indicate that the majority of materials appear to be nanoparticles and nanorods. The diameter of the nanocomposites varies and has different shapes with different baking time. The results show that the smallest diameter of nanocomposites in all combinations occurred at 8 hours baking time and 1000°C growth temperature with a range of 361 nm–382 nm. In this combination, especially at zone 2, the silver nanorods are extended with sharp end and covered by nanocotton-like titanium dioxide.

The average diameters of the micro- and nanocomposites concerning the parameters of the study which are baking time and growth temperature are shown in Table 3. The material measurements based on SEM image and EDX results were evaluated from 3 different points as shown in Figure 9(a). The measurement method was performed by manual calculation. The results show the diameter of nanocomposites can be predicted statistically [17]. The results show that the smallest average diameter of micro-nanocomposite occurred at the 1000°C growth temperature and 8 hours baking time.

Size, shape, and surface of the nanocomposites are the several critical aspects in determining their interaction behavior with cells. The study proved that the smaller the nanocomposites size, the higher the antimicrobial efficiency of the nanocomposites due to their direct interaction with the interface of the bacteria (membrane). Furthermore, the shape of the nanocomposites could directly influence the

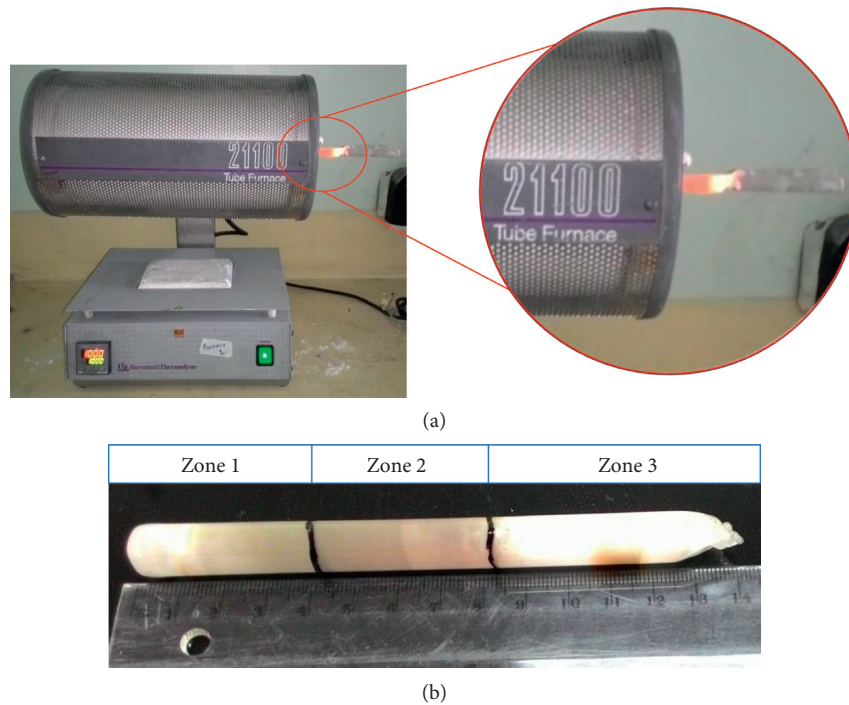


FIGURE 1: (a) Horizontal furnace. (b) Quartz tube after baking.

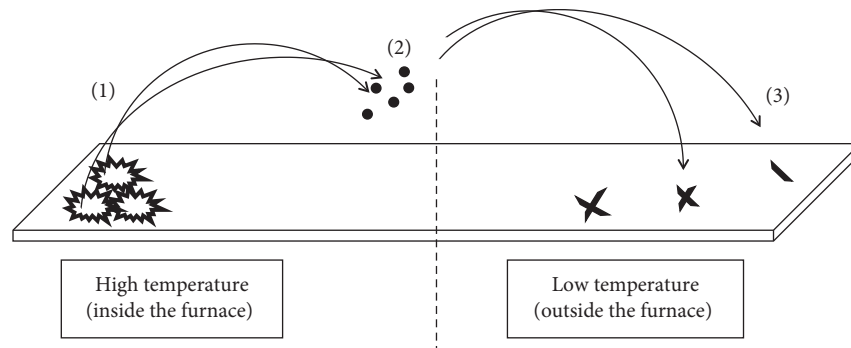


FIGURE 2: HVPG schematics: (1) source macromaterials placed at the end of the tube inside the furnace, (2) the materials changing to particles, and (3) the nanocomposite materials depositing on the parts of the tube outside the furnace.

available contact area required to facilitate the interactions of nanocomposites with the bacterial membrane [41]. Silver nanoplates and silver nanorods showed higher antimicrobial activity towards bacteria compared to other silver nano-shapes [10]. The silver nanorods were capable of inhibiting all viable *S. aureus* cells within 4 hours by using 5 ppm silver nanorods solution and 3.5 hours by using 10 pp solution, respectively [42]. Moreover, based on Table 3 and images from SEM, 8 hours of baking time followed by 1000°C growth temperature could be an effective way to achieve high antimicrobial efficacy. The results show the nanocomposites diameter is from 300 nm to 600 nm with the majority of nanomaterials form as nanorods.

Figure 9 shows Ag/TiO₂ nanorods with diameters around 300 nm to 400 nm (Figure 9(a)). Other forms of the synthesized nanocomposite include strand-like or

cotton-like structures with bigger diameters that addressed to Ag/TiO₂ micro-nanocomposites (Figure 9(b)). EDX analysis (Figure 9(c)) revealed appropriate amounts of Ag, Ti, and O in the nanocomposites along with Si likely from the quartz tube and Au from the coating material.

Figure 9 shows the typical Ag/TiO₂ nanorods synthesized via HVPG technique. It is shown that silver nanomaterials are grown with the titanium dioxide covered on the surface. By using EDX spectroscopy, the nanorods come from silver nanomaterials, and cotton-like nanomaterials are from titanium dioxide nanomaterials. Furthermore, the results show that combination of silver and titanium dioxide can be fabricated with a controllable diameter as explained in the previous study by Muflikhun et al. [17]. To ensure Ag/TiO₂ is capable of eradicating bacteria, the antibacterial test

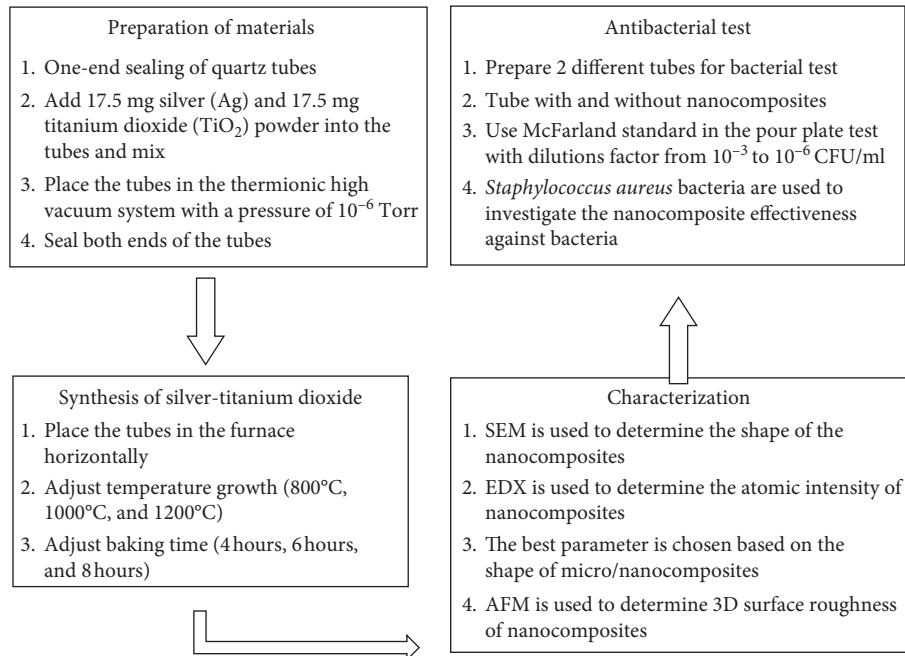


FIGURE 3: A detailed flowchart of the study.

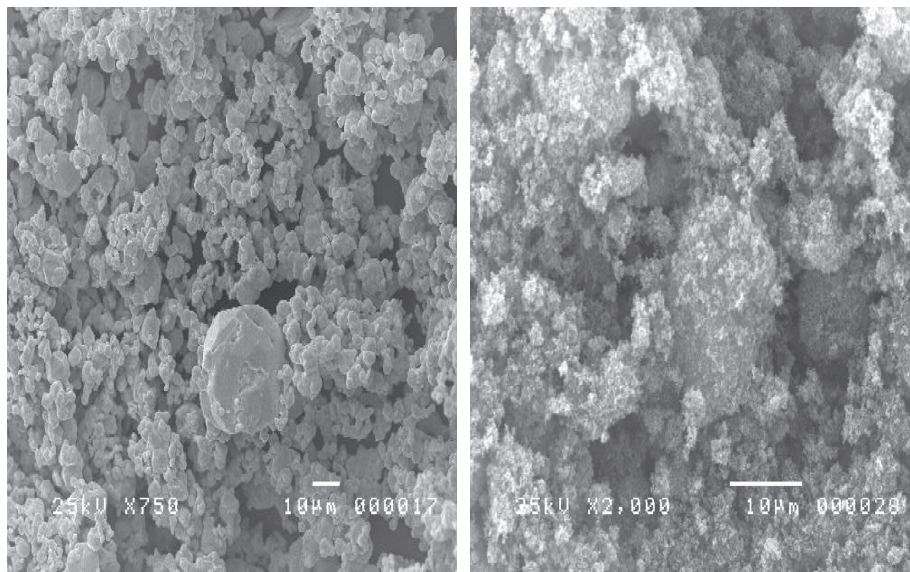


FIGURE 4: Silver material (a) and titanium dioxide material (b).

was conducted by using a combination tube with 8 hours baking time and 1000°C growth temperature.

3.2. Investigation of Antibacterial Property. The antibacterial property of the Ag/TiO₂ nanocomposites were tested against *S. aureus* colonies. The standard analysis was conducted through the 0.5 McFarland standard (approximately 1.5×10^8 CFU/mL). Serial dilution was performed with dilution factors from 10^{-3} to 10^{-6} . Figures 10 and 11 show the colonies grown at dilution factors 10^{-5} and 10^{-6} , with and without the nanocomposites.

Figures 10 and 11 show that treatment with the Ag/TiO₂ nanocomposites resulted in curbing the growth of *S. aureus* colonies. The result and images are presented as the significant capability of Ag/TiO₂ nanocomposite to eradicate the *S. aureus* in terms of the amount of *S. aureus* with the nanocomposites. The antibacterial efficacy of the nanocomposite treatment is computed, and the complete data collected from counting bacterial colony growth in the different setups are compiled in Table 4.

Table 4 shows the bacterial test by using the Ag/TiO₂ nanocomposite material (nanorods). The results show the

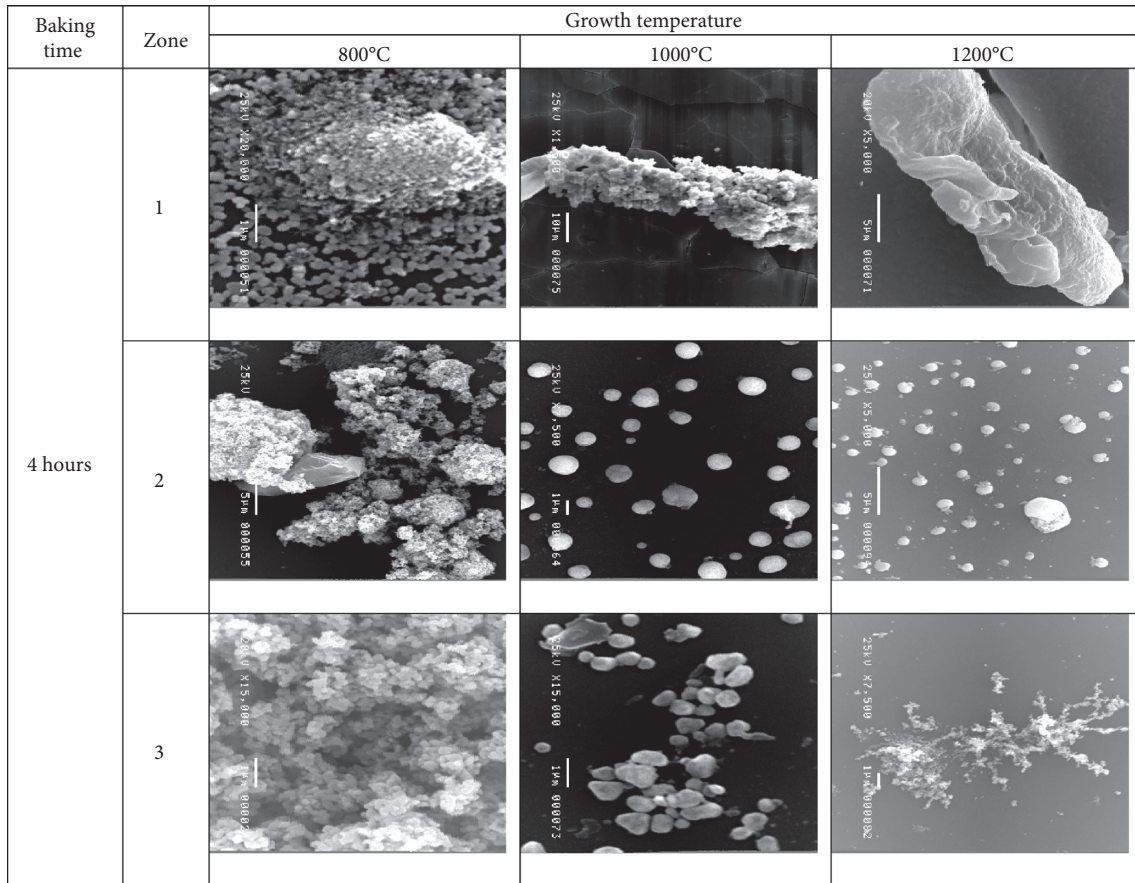


FIGURE 5: SEM image after 4 hours of baking time.

nanocomposite materials are successfully capable of reducing bacterial growth with approximately 75% efficiency. It can be noted that the test is based on the dilution factor by using a 0.5 McFarland standard. The solution that contains bacterial colony was placed inside the tube that consists of nanomaterials. The tube that did not contain nanomaterials was used as the control plate. The tubes were rotated and shaken for around 5 minutes by using a Vertex machine to mix the bacterial colony with nanocomposite materials. The bacterial colony attached Ag/TiO₂ nanorods when the rotation occurred. Since there is no standard for shaking and rotating the tubes by using the Vertex machine, the efficiency of the treatment can be improved by increasing the amount of nanocomposite material and the rotating time. Presumably, the more the nanorods formed and the longer the shaking time, the faster the bacteria eradication.

3.3. Nanocomposite Growth Mechanism. The synthesis of nanomaterials by using the HVPG technique is based on the thermal method where the material is changed at different stages as shown in Figure 12. The conversion depends on the temperature wherein, at low temperature, the material becomes solid. At high temperature, the material becomes liquid (at melting point) and gas (at boiling point) before it condenses in lower temperature and becomes solid again. In

the case of Ag/TiO₂ nanocomposite material, the shape of the nanocomposite depends on the growth temperature and baking time. The higher temperature will fasten the material conversion from liquid to gas and move from zone 1 (inside the furnace) to zone 2 and zone 3. Longer baking time will speed up the material deposit mostly in the bigger size (micro and nano) at zone 2 and zone 3, and lower baking time will create the smaller size of nanocomposite materials in zone 2 and zone 3.

3.4. Antibacterial Mechanism. Modification of silver nanomaterials with specific shape combined with titanium dioxide nanomaterials gives significant results in effectiveness against *S. aureus*. To understand the mechanism of how nanorods can eradicate the bacteria, some relevant papers discussed the nanomaterials contacted to bacteria should be considered. The previous studies conducted by Hajipour et al. [35] and Salata [9] show that nanomaterials have higher efficiency in eradicating bacteria. Bacteria are a robust organism that its cell wall is designed to provide strength and can protect its cell from osmotic rupture and physical damages. As a result, there are two common ways to eradicate bacteria, by the toxicity mechanism and by breaking the membrane of bacteria by the mechanical process. By toxicity, nanoparticles can attach to the membrane of bacteria by

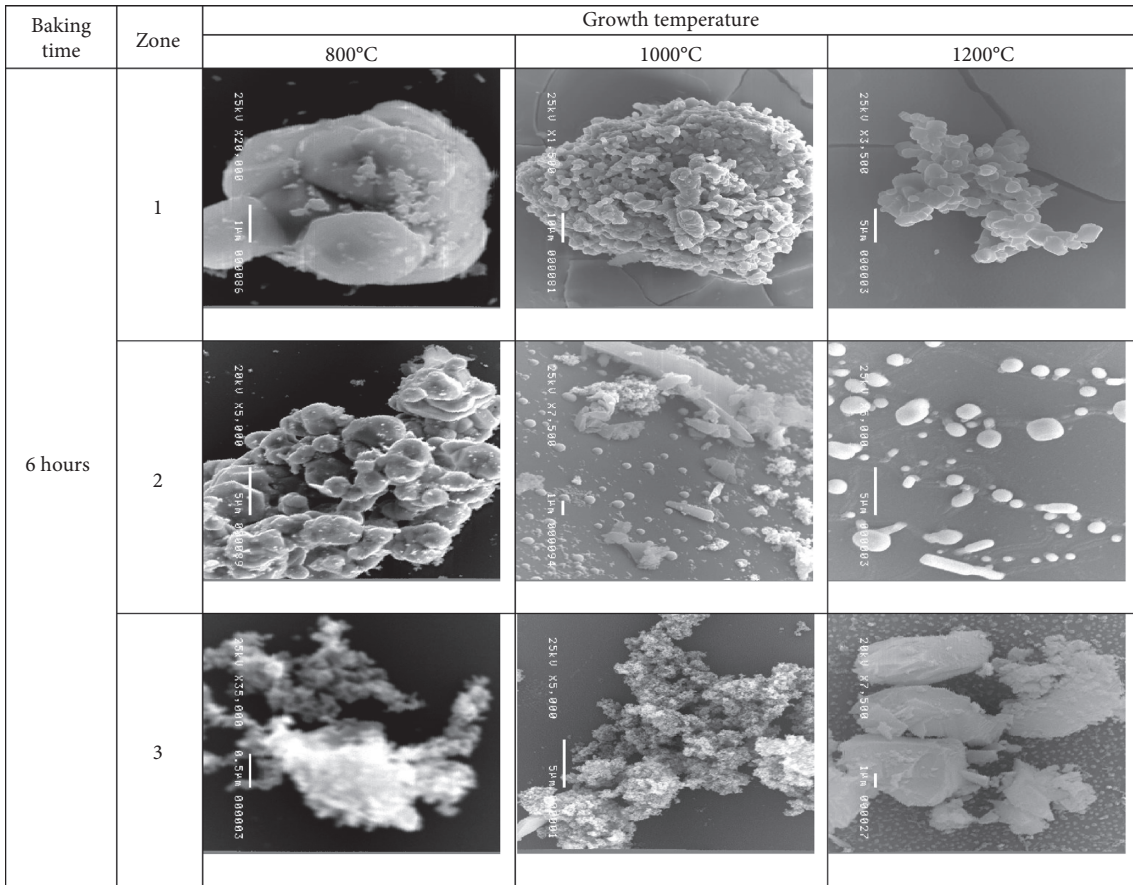


FIGURE 6: SEM image from 6 hours of baking time.

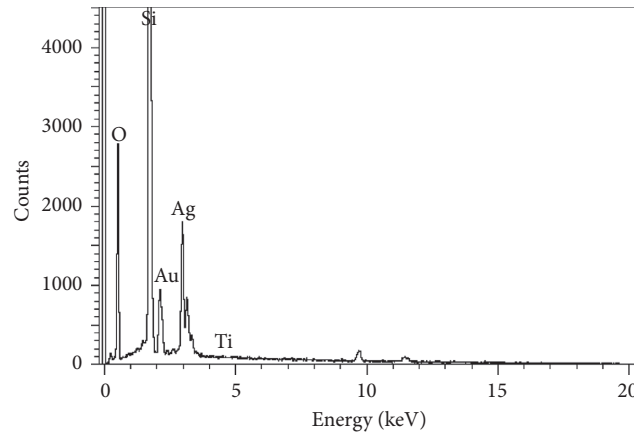


FIGURE 7: EDX result from zone 2 of the sample at 1200°C growth temperature and 6 hours baking time.

electrostatic interaction and disturb the integrity of it. For example, TiO₂ nanomaterials are toxic to the bacterial only under ultraviolet (UV) illumination. The effectiveness of TiO₂ under UV light was able to eradicate the bacteria in 1 hour. The mechanism of TiO₂ to eradicate the bacteria can increase peroxidation of the polyunsaturated phospholipid component in the lipid membrane. This condition can disturb cell respiration. The Ag nanomaterials can eradicate bacteria by

penetrating their membrane and increasing the toxicity in the presence of external magnetic field, electrostatic interaction, and physical damage of the bacteria [9, 35].

In this study, the nanocomposite materials are reported with the unique ability of Ag/TiO₂ to eradicate bacteria caused by physical damage due to its shape. The present study shows that silver nanomaterials can be fabricated with a different shape depending on the baking time and growth temperature. Among the various shapes of nanomaterials,

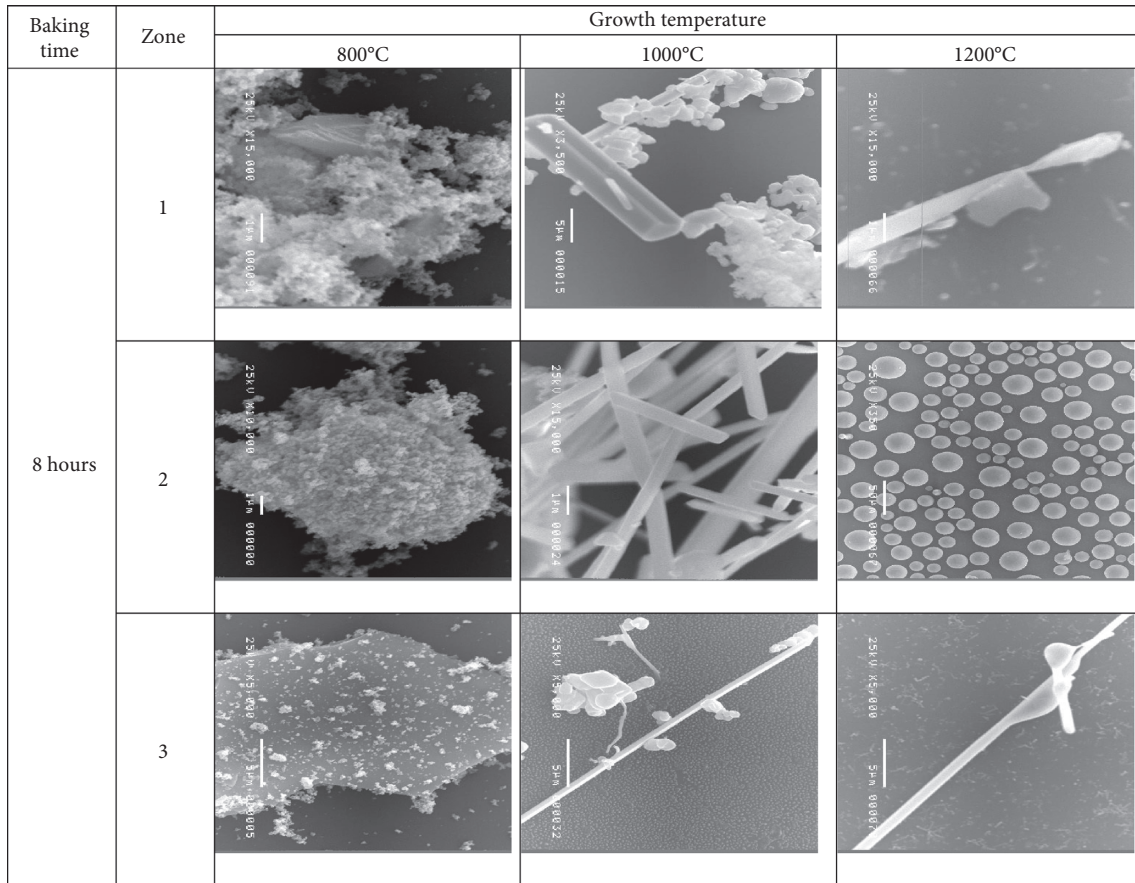


FIGURE 8: SEM image from 8 hours of baking time.

TABLE 3: Average diameters of micro-nanocomposite synthesized at each zone for all parameter settings.

Baking time	Zone	Growth temperature		
		800°C	1000°C	1200°C
4 hours	1	0.177 μm	19.133 μm	7.547 μm
	2	7.010 μm	1.416 μm	0.863 μm
	3	1.604 μm	0.707 μm	1.066 μm
6 hours	1	0.313 μm	2.689 μm	2.012 μm
	2	3.501 μm	0.477 μm	9.406 μm
	3	0.904 μm	1.233 μm	0.541 μm
8 hours	1	3.226 μm	0.651 μm	0.617 μm
	2	0.832 μm	0.382 μm	8.354 μm
	3	1.212 μm	0.562 μm	0.706 μm

nanorods are the one candidate that can be used to eradicate bacteria by using its geometry. The shape of nanorods was sharp at the top of it, and this shape can break the membrane of the bacteria. The *S. aureus* membrane size has been investigated by Touhami et al. [43], and Lee et al. [44] show that the bacterial cell wall and plasma membrane are around 10–20 nm thickness. By using the nanorods that have sharp end on the top of it, the bacterial membrane can be broken, and it caused physical damage to the bacteria. The schematic of bacterial eradication (not to scale) and AFM test are shown in Figure 13.

4. Conclusion

The HVPG technique was successfully used to synthesize silver-titanium dioxide micro-nanocomposites, with the desired optimal nanorods structures fabricated at 1000°C for 8 hours. The SEM and EDX analyses were used to characterize the material. The pour plate technique was used to grow *S. aureus* colonies to determine the antibacterial activity.

The SEM and EDX analyses revealed that the micro- and nanoparticles, nanorods, triangular nanomaterials, and nanotubes were successfully produced in high proportions. Antibacterial treatment with the Ag/TiO₂ nanocomposites was able to reduce bacterial growth by approximately 75%. This result indicated that the bacteria were successfully eradicated with Ag/TiO₂ nanocomposites. In general, the effect of adding Ag/TiO₂ will give more significant effect on the performance of nanocomposite materials to eradicate *S. aureus*. The result is strongly dependent on the growth temperature and baking time to produce and increase the amount of nanorods that have been proven more effective to eradicate bacteria. Furthermore, the study was capable of controlling the structures and morphology of micro- and nanomaterials based on growth temperature and baking time. In the future, the effect of Ag/TiO₂ nanocomposites

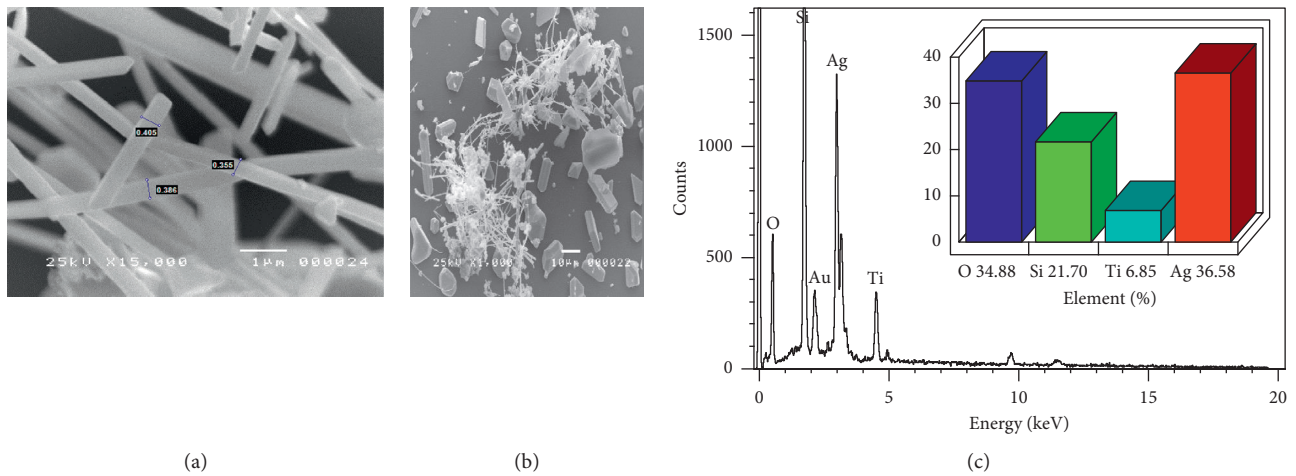


FIGURE 9: (a) Ag/TiO₂ nanorods grown at 1000°C for 8 hours; (b) other spots in the same tube shows different results, including cotton-like growths. (c) EDX results of Ag/TiO₂ from (a) [17].

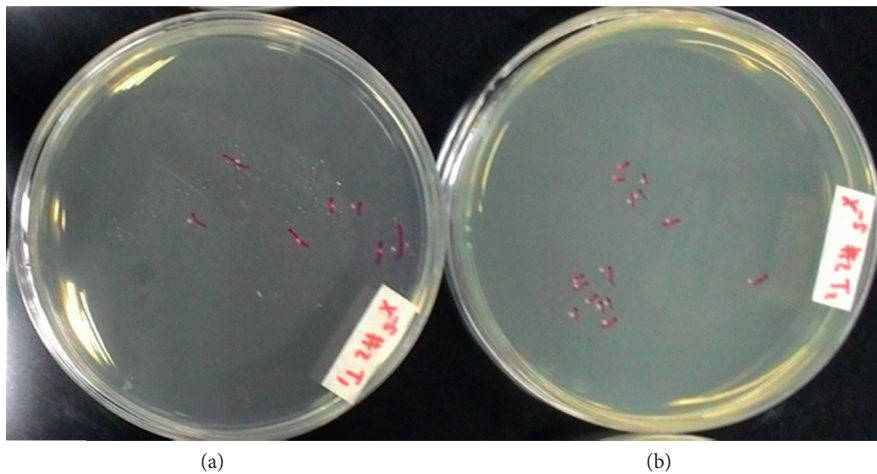


FIGURE 10: *S. aureus* colonies diluted 10⁻⁵ grown (a) with and (b) without the Ag/TiO₂ nanocomposites.

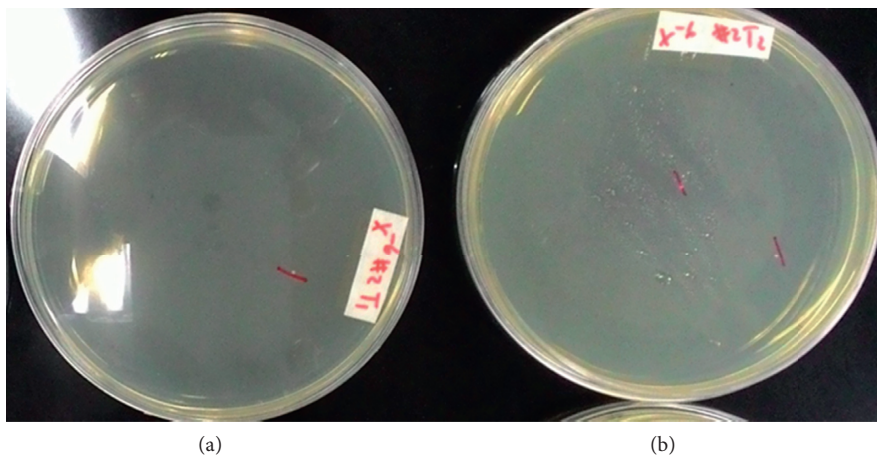


FIGURE 11: *S. aureus* colonies diluted 10⁻⁶ grown (a) with and (b) without the Ag/TiO₂ nanocomposites.

TABLE 4: The number of bacterial colonies for each setup, at each dilution factor.

Tube	Materials	Dilution factor (number of colonies)														
		10^{-3}				10^{-4}				10^{-5}				10^{-6}		
		#1	#2	#3	Ave.	#1	#2	#3	Ave.	#1	#2	#3	Ave.	#1	#2	Ave.
1	Zero (control tube)	>100	>100	>100	>100	>100	>100	>100	>100	12	15	14	14	2	2	2
2	50% Ag, 50% TiO ₂	>100	>100	>100	>100	>100	>100	>100	>100	6	7	7	6.3	1	0	0.5
3	50% Ag, 50% TiO ₂	>100	>100	>100	>100	>100	>100	>100	>100	10	12	10	10,7	0	1	0.5

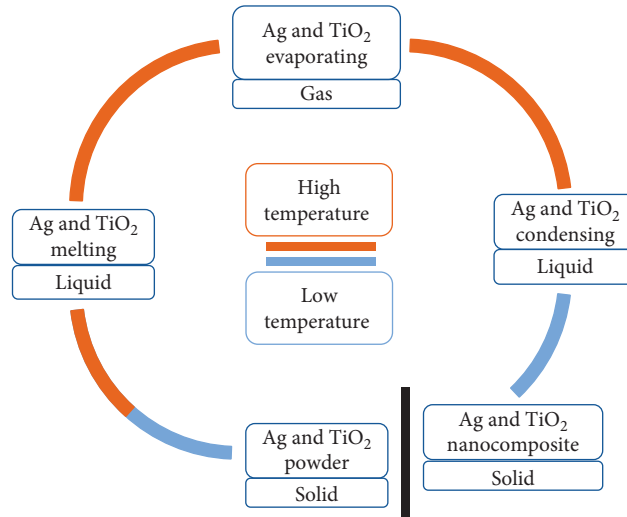
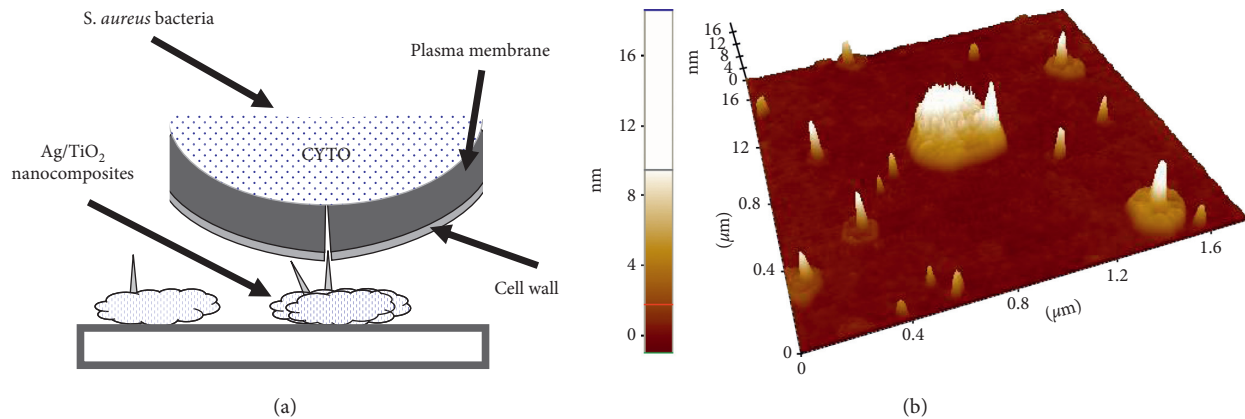


FIGURE 12: Material conversion.

FIGURE 13: (a) Schematic of nanocomposites eradicating bacteria (not to scale) and (b) AFM image of Ag/TiO₂ nanocomposite materials.

will be studied for their antibacterial property with different types of bacteria and will be tested against fungi as well as bacteria.

Data Availability

No data were used to support this study.

Conflicts of Interest

The authors declare that there are no conflicts of interest in this study.

Acknowledgments

The study was supported by the Solid State Physics Lab, Mechanical Engineering Department of De La Salle University, and AUN SEED NET Project JICA Funding. The authors would also thank Siwat Manomaisantiphap for reviewing the manuscript and Gwen Castillon for assisting during the experiment.

References

- [1] F.-C. Yang, K.-H. Wu, J.-W. Huang, D.-N. Horng, C.-F. Liang, and M.-K. Hu, "Preparation and characterization

- of functional fabrics from bamboo charcoal/silver and titanium dioxide/silver composite powders and evaluation of their antibacterial efficacy,” *Materials Science and Engineering: C*, vol. 32, no. 5, pp. 1062–1067, 2012.
- [2] F. Baghbani-arani, R. Movagharnia, A. Sharifian, S. Salehi, S. A. S. Shandiz, and S. Shandiz, “Photo-catalytic, antibacterial, and anti-cancer properties of phyto-mediated synthesis of silver nanoparticles from artemisia tournefortiana Rchb extract,” *Journal of Photochemistry and Photobiology B: Biology*, vol. 173, pp. 640–649, 2017.
 - [3] S. J. Lee, M. Heo, D. Lee et al., “Preparation and characterization of antibacterial orthodontic resin containing silver nanoparticles,” *Applied Surface Science*, vol. 432, pp. 317–323, 2018.
 - [4] H. Cao, X. Liu, F. Meng, and P. K. Chu, “Biological actions of silver nanoparticles embedded in titanium controlled by micro-galvanic effects,” *Biomaterials*, vol. 32, no. 3, pp. 693–705, 2011.
 - [5] S. Sarkar, A. D. Jana, S. K. Samanta, and G. Mostafa, “Facile synthesis of silver nano particles with highly efficient antimicrobial property,” *Polyhedron*, vol. 26, no. 15, pp. 4419–4426, 2007.
 - [6] M. B. Faiz, R. Amal, C. P. Marquis et al., “Nanosilver and the microbiological activity of the particulate solids versus the leached soluble silver,” *Nanotoxicology*, vol. 12, no. 3, pp. 263–273, 2018.
 - [7] A. Llorens, E. Lloret, P. A. Picouet, R. Trbojevich, and A. Fernandez, “Metallic-based micro and nanocomposites in food contact materials and active food packaging,” *Trends in Food Science & Technology*, vol. 24, no. 1, pp. 19–29, 2012.
 - [8] A. Besinis, T. De Peralta, and R. D. Handy, “The antibacterial effects of silver, titanium dioxide and silica dioxide nanoparticles compared to the dental disinfectant chlorhexidine on *Streptococcus mutans* using a suite of bioassays,” *Nanotoxicology*, vol. 8, no. 1, pp. 1–16, 2014.
 - [9] O. Salata, “Applications of nanoparticles in biology and medicine,” *Journal of Nanobiotechnology*, vol. 2, no. 1, p. 3, 2004.
 - [10] K. Zheng, M. I. Setyawati, D. T. Leong, and J. Xie, “Antimicrobial silver nanomaterials,” *Coordination Chemistry Reviews*, vol. 357, pp. 1–17, 2018.
 - [11] N. K. Rajendran, S. S. D. Kumar, N. N. Houreld, and H. Abrahamse, “A review on nanoparticle based treatment for wound healing,” *Journal of Drug Delivery Science and Technology*, vol. 44, pp. 421–430, 2018.
 - [12] Z. Khan, S. A. Al-Thabaiti, A. Y. Obaid, and A. O. Al-Youbi, “Preparation and characterization of silver nanoparticles by chemical reduction method,” *Colloids and Surfaces B: Biointerfaces*, vol. 82, no. 2, pp. 513–517, 2011.
 - [13] O. Beier, A. Pfuch, K. Horn, J. Weisser, M. Schnabelrauch, and A. Schimanski, “Low temperature deposition of antibacterially active silicon oxide layers containing silver nanoparticles, prepared by atmospheric pressure plasma chemical vapor deposition,” *Plasma Processes and Polymers*, vol. 10, no. 1, pp. 77–87, 2013.
 - [14] G. R. Nasretidnova, R. R. Fazleeva, R. K. Mukhitova et al., “Electrochemical mediated synthesis of silver nanoparticles in solution,” *Russian Journal of Electrochemistry*, vol. 51, no. 11, pp. 1029–1040, 2015.
 - [15] S. Patra, S. Mukherjee, A. K. Barui, A. Ganguly, B. Sreedhar, and C. R. Patra, “Green synthesis, characterization of gold and silver nanoparticles and their potential application for cancer therapeutics,” *Materials Science and Engineering: C*, vol. 53, pp. 298–309, 2015.
 - [16] M. A. Muflikhun, G. N. Santos, and A. Y. Chua, “Synthesis and characterization of silver-titanium nanocomposite via horizontal vapor phase growth (HVPG) technique,” in *Proceedings of the DLSU Research Congress*, pp. 1–5, Manila, Philippines, March 2015.
 - [17] M. A. Muflikhun, A. Y. Chua, and G. N. C. Santos, “Statistical design analysis of silver-titanium dioxide nanocomposite materials synthesized via horizontal vapor Phase growth (HVPG),” *Key Engineering Materials*, vol. 735, pp. 210–214, 2017.
 - [18] J. C. Briones, G. Castillon, M. P. Delmo, and G. N. C. Santos, “Magnetic-field-enhanced morphology of tin oxide nanomaterials for gas sensing applications,” *Journal of Nanomaterials*, vol. 2017, Article ID 4396723, 11 pages, 2017.
 - [19] X. Hong, J. Wen, X. Xiong, and Y. Hu, “Shape effect on the antibacterial activity of silver nanoparticles synthesized via a microwave-assisted method,” *Environmental Science and Pollution Research*, vol. 23, no. 5, pp. 4489–4497, 2016.
 - [20] J. S. Gabriel, V. A. M. Gonzaga, A. L. Poli, and C. C. Schmitt, “Photochemical synthesis of silver nanoparticles on chitosans/montmorillonite nanocomposite films and antibacterial activity,” *Carbohydrate Polymers*, vol. 171, pp. 202–210, 2017.
 - [21] Y. Liu, S. Chen, L. Zhong, and G. Wu, “Preparation of high-stable silver nanoparticle dispersion by using sodium alginate as a stabilizer under gamma radiation,” *Radiation Physics and Chemistry*, vol. 78, no. 4, pp. 251–255, 2009.
 - [22] R. A. Salkar, P. Jeevanandam, S. T. Aruna, Y. Koltypin, and A. Gedanken, “The sonochemical preparation of amorphous silver nanoparticles,” *Journal of Materials Chemistry*, vol. 9, no. 6, pp. 1333–1335, 1999.
 - [23] F. Martinez-Gutierrez, P. L. Olive, A. Banuelos et al., “Synthesis, characterization, and evaluation of antimicrobial and cytotoxic effect of silver and titanium nanoparticles,” *Nanomedicine Nanotechnology, Biology and Medicine*, vol. 6, no. 5, pp. 681–688, 2010.
 - [24] M. V. Liga, E. L. Bryant, V. L. Colvin, and Q. Li, “Virus inactivation by silver doped titanium dioxide nanoparticles for drinking water treatment,” *Water Research*, vol. 45, no. 2, pp. 535–544, 2011.
 - [25] A. L. Motlagh, S. Bastani, and M. M. Hashemi, “Investigation of synergistic effect of nano sized Ag/TiO₂ particles on antibacterial, physical and mechanical properties of UV-curable clear coatings by experimental design,” *Progress in Organic Coatings*, vol. 77, no. 2, pp. 502–511, 2014.
 - [26] D.-H. Song, S.-H. Uhm, S.-B. Lee, J.-G. Han, and K.-N. Kim, “Antimicrobial silver-containing titanium oxide nanocomposite coatings by a reactive magnetron sputtering,” *Thin Solid Films*, vol. 519, no. 20, pp. 7079–7085, 2011.
 - [27] S. Mei, H. Wang, W. Wang et al., “Antibacterial effects and biocompatibility of titanium surfaces with graded silver incorporation in titania nanotubes,” *Biomaterials*, vol. 35, no. 14, pp. 4255–4265, 2014.
 - [28] J. Wang, W. Liu, H. Li et al., “Preparation of cellulose fiber-TiO₂ nanobelt-silver nanoparticle hierarchically structured hybrid paper and its photocatalytic and antibacterial properties,” *Chemical Engineering Journal*, vol. 228, pp. 272–280, 2013.
 - [29] E. Shimizu, G. N. Santos, and D. E. Yu, “Nanocrystalline axially bridged iron phthalocyanine polymeric conductor: (μ -thiocyanato)(phthalocyaninato)iron(III),” *Journal of Nanotechnology*, vol. 2016, Article ID 5175462, 7 pages, 2016.
 - [30] W. V. Espulgar and G. N. C. Santos, “Antimicrobial silver nanomaterials synthesized by HVPG technique,”

- International Journal of Scientific & Engineering Research*, vol. 2, no. 8, pp. 8–11, 2011.
- [31] A. C. Quitaneg and G. N. C. Santos, “Cadmium selenide quantum dots synthesized by HVPC growth technique for sensing copper ion concentrations,” *International Journal of Scientific & Engineering Research*, vol. 2, no. 12, pp. 1–4, 2011.
- [32] R. D. L. Reyes and G. N. C. Santos, “Growth mechanism of SnO₂ nanomaterials derived from backscattered electron image and EDX observations,” *International Journal of Scientific & Engineering Research*, vol. 2, no. 12, pp. 1–4, 2011.
- [33] R. M. N. Buot and G. N. C. Santos, “Synthesis and characterization of C-Ag nanomaterials for battery electrode application,” *International Journal of Scientific & Engineering Research*, vol. 3, no. 2, pp. 1–3, 2012.
- [34] M. A. Muflikhun, G. B. Castillon, G. N. C. Santos, and A. Y. Chua, “Micro and nano silver-graphene composite manufacturing via horizontal vapor Phase growth (HVPG) technique,” *Materials Science Forum*, vol. 901, pp. 3–7, 2017.
- [35] M. J. Hajipour, K. M. Fromm, A. Akbar Ashkarran et al., “Antibacterial properties of nanoparticles,” *Trends in Biotechnology*, vol. 30, no. 10, pp. 499–511, 2012.
- [36] W. G. I. U. Rathnayake, H. Ismail, A. Baharin, A. G. N. D. Darsanasiri, and S. Rajapakse, “Synthesis and characterization of nano silver based natural rubber latex foam for imparting antibacterial and anti-fungal properties,” *Polymer Testing*, vol. 31, no. 5, pp. 586–592, 2012.
- [37] S. K. Ray, D. Dhakal, C. Regmi, T. Yamaguchi, and S. W. Lee, “Inactivation of *Staphylococcus aureus* in visible light by morphology tuned α -NiMoO₄,” *Journal of Photochemistry and Photobiology A: Chemistry*, vol. 350, pp. 59–68, 2018.
- [38] E. Goldman and E. G. L. H. Green, *Practical Handbook of Microbiology*, CRC Press, Boca Raton, FL, USA, 1990.
- [39] D. Burdass, J. Grainger, and J. Hurst, “Part 1: the basics an introduction to microbiology, aseptic technique and safety,” in *Basic Practical Microbiology A Manual*, pp. 1–40, Society for General Microbiology (SGM), London, UK, 2006.
- [40] M. A. Muflikhun, M. C. Frommelt, M. Farman, A. Y. Chua, and G. N. C. Santos, “Structures, mechanical properties and antibacterial activity of Ag/TiO₂ nanocomposite materials synthesized via HVPG technique for coating application,” *Heliyon*, vol. 5, no. 4, pp. 1–21, 2019.
- [41] L. Shang, K. Nienhaus, and G. Nienhaus, “Engineered nanoparticles interacting with cells: size matters,” *Journal of Nanobiotechnology*, vol. 12, no. 1, p. 5, 2014.
- [42] B. Sadeghi, F. S. Garmaroudi, M. Hashemi et al., “Comparison of the anti-bacterial activity on the nanosilver shapes: nanoparticles, nanorods and nanoplates,” *Advanced Powder Technology*, vol. 23, no. 1, pp. 22–26, 2012.
- [43] A. Touhami, M. H. Jericho, and T. J. Beveridge, “Atomic Force microscopy of cell growth and division in *Staphylococcus aureus*,” *Journal of Bacteriology*, vol. 186, no. 11, pp. 3286–3295, 2004.
- [44] E.-Y. Lee, D.-Y. Choi, D.-K. Kim et al., “Gram-positive bacteria produce membrane vesicles: proteomics-based characterization of *Staphylococcus aureus*-derived membrane vesicles,” *Proteomics*, vol. 9, no. 24, pp. 5425–5436, 2009.

Research Article

Mechanical Properties, Failure Mode, and Microstructure of Soil-Cement Modified with Fly Ash and Polypropylene Fiber

Xue-lei Duan ^{1,2} and Jing-shuang Zhang ^{1,2}

¹Engineering Research Center of Underground Mine Construction, Ministry of Education, Anhui University of Science and Technology, Huainan 232001, Anhui, China

²School of Civil Engineering and Architecture, Anhui University of Science and Technology, Huainan 232001, Anhui, China

Correspondence should be addressed to Jing-shuang Zhang; hnaust@163.com

Received 27 February 2019; Revised 3 April 2019; Accepted 16 April 2019; Published 6 May 2019

Guest Editor: Alena Šišková

Copyright © 2019 Xue-lei Duan and Jing-shuang Zhang. This is an open access article distributed under the Creative Commons Attribution License, which permits unrestricted use, distribution, and reproduction in any medium, provided the original work is properly cited.

In order to investigate the effects of fly ash and polypropylene fiber on mechanical properties, failure mode, and microstructure of soil-cement, the unconfined compression test, splitting tension test, and scanning electron microscopy (SEM) test of soil-cement with different polypropylene fiber contents (0%, 0.1%, 0.2%, 0.3%, 0.4%, and 0.5% by weight of dry soil) and fly ash contents (0%, 4%, 8%, and 12% by weight of dry soil) were carried out. The compressive and tensile strengths, deformation characteristics, failure mode, and microstructure of soil-cement modified with fly ash and polypropylene fiber were analyzed. The results show that the unconfined compressive strength and splitting tensile strength of soil-cement show a trend of increasing first and then decreasing with the increase of polypropylene fiber and fly ash content. Under the condition of 0.4% polypropylene fiber and 8% fly ash, the unconfined compressive strength and the splitting tensile strength are 4.90 MPa and 0.91 MPa, respectively, which increased by 32.79% and 51.67% as compared with the plain soil-cement, respectively. When 8% fly ash was used in the experiment, the unconfined compressive peak strain and the splitting tensile peak strain of the inclusion of 0.4% polypropylene fiber were 0.0410 and 0.0196, respectively. The corresponding peak strains were increased by 20.94% and 68.97% as compared with non-fiber-stabilized soil-cement, respectively. The stress-strain curve of fly ash soil-cement modified with polypropylene fiber can be divided into compaction phase, linear rise phase, nonlinear rise phase, and failure phase. Polypropylene fiber constrains the lateral deformation of fly ash soil-cement, which improves the peak strain and the failure mode of soil-cement.

1. Introduction

Soil-cement is a kind of composite material composed of cement, soil, and other components. Due to the rapid development of global economy, as an environmentally friendly material, soil-cement has been widely used in soft soil foundation reinforcement, slope support, and channel lining in construction projects (roads, bridges, ports, etc.) [1–4]. Soil-cement has the advantages of easy access to draw materials, low price, and convenient construction. However, soil-cement material tends to have lower mechanical properties (e.g., unconfined compressive strength, shear strength, and triaxial compressive strength) and greater deformation in engineering projects [5–7], which might lead to the damage of building structures.

In order to lenify the disease in engineering projects, stabilization method that is a technique to treat soil-cement has been widely applied in infrastructure construction. Researchers tried to add chemical additives (fly ash, lime, and silicon powder) in soil-cement for improving its mechanical properties [8–10]. As one kind of stabilizers, fly ash that is the main solid waste discharged from coal-fired power plants has been widely employed to increase its strength. Yang et al. [11] studied the incorporation of cement and fly ash for improving the strength of cement-stirred saturated loess and pointed out that the suitable ratio between fly ash and cement was 0.5, which was more economical and reasonable. Jia et al. [12] utilized cement and fly ash to strengthen soft clay and found that the inclusion of 6% fly ash and 16% cement could excellently improve its

compressive strength. According to statistics, fly ash has reached 620 million tons in 2015, and every 10,000 tons of fly ash occupy four to five acres of land [13], which not only occupies a large amount of land resources but also causes serious environmental pollution. Therefore, the use of fly ash is getting more and more attention. Adding fly ash to soil-cement could solve the problems of land occupation and environmental pollution.

Fiber-reinforced soil has attracted the attention of modern researchers, which makes contribution to not only the reduction in the amount of used cement but also the improvement of strength and deformation [14–20]. Chen [16] investigated the effect of basalt fiber on the tensile strength of soil-cement and revealed that the inclusion of 1.5% basalt fiber could attain a maximum tensile strength. Zhang et al. [17] added the asbestos fiber into fly ash soil-cement and obtained that the strength of 6% asbestos fiber-reinforced fly ash soil-cement increased by 140% as compared with fiber unreinforced fly ash soil-cement. Tran et al. [18] studied the toughness of waste cornsilk fiber in soil-cement and found that 0.25%–0.5% fibers were recommended to use in soil-cement. Due to the degradation of natural fiber in soil, synthetic fibers (e.g., glass fiber, nylon fiber, and polypropylene fiber) are employed as the inclusion [21–25]. Li et al. [21] added the glass fiber into the soil-cement and found that under the condition of 0.6% glass fiber, the soil particles and mineral particles can be in maximum contact with the fiber, showing the excellent mechanical performance. Park [22] studied the effect of the polyvinyl alcohol fiber on cemented sand and found that 2% polyvinyl alcohol fiber could improve the compressive strength of 2.5 times as compared with non-fiber-stabilized cemented soil. In these fibers, polypropylene fiber that can enhance the soil strength and reduce the shrinkage is widely used. Tang and Gu [23] studied the addition of polypropylene fiber in soil-cement to reduce the brittleness of soil-cement and revealed that bond strength and friction at the interface seem to be the dominant mechanism controlling the reinforcement benefit. Consoli et al. [24] investigated that the inclusion of polypropylene fiber in the soil-cement increased the unconfined compressive strength and proposed a porosity/volumetric cement content for predicting the unconfined compressive strength. Some scholars had also studied the effects of mixing different fibers on the strength and deformation of soil-cement [26, 27]. Zhang et al. [26] analyzed that the unconfined compressive strength of both sisal fiber and polypropylene fiber into soil-cement could increase by 40.5%–54.1% as compared with plain soil-cement. Gutiérrez-Orrego et al. [27] found that soil-cement blocks reinforced with mineral wool and sisal fiber increased both bending strength and compression strength. The previous investigations primarily concentrated on macroscopic mechanical properties of soil-cement, and limited studies are available on microstructure analysis of stabilized soil-cement. The experiment of microstructure reflects the internal structure mechanism [28, 29].

The primary objective of this paper is to explore the effects of polypropylene fiber and fly ash content on

unconfined compressive strength, splitting tensile strength, deformation characteristics, failure mode, and microstructure of soil-cement. To achieve this purpose, a series of unconfined compression test, splitting tension test, and SEM test were carried out.

2. Experiment Materials and Sample Preparation

2.1. Materials. The soil employed in the experiment was taken from the foundation pit of a construction site, located in east region of China in Huainan city. The depth of the soil was from the underground of 5 m. The physical properties of soil are listed in Table 1. The fly ash used in this research was grade II and its chemical composition is listed in Table 2. In addition, particle size distribution of clayey soil and fly ash is shown in Figure 1. The cement used in the study was P·O 42.5 ordinary Portland cement, which was produced by Huainan Cement Corporation. The polypropylene fiber (Figure 2) was chosen as reinforcement material due to its high tensile strength, low cost, easy to mix with soil, and nonpolluting property for environment. The main physical and mechanical parameters are shown in Table 3. The water for mixing was tap water.

2.2. Sample Preparation. In the experiment, cement content was incorporated 15% by weight of dry soil and between water and cementitious materials was 0.5. Additionally, in order to investigate the effects of fly ash and polypropylene fiber content on strength properties (unconfined compressive strength and splitting tensile strength) and failure mode of the soil-cement, four percentages of fly ash contents (0%, 4%, 8%, and 12% by weight of dry soil) and six percentages of polypropylene fiber contents (0%, 0.1%, 0.2%, 0.3%, 0.4%, and 0.5% by weight of dry soil) were adopted in this study. In order to activate the active ingredient of the fly ash, calcium hydroxide (1% by weight of soil-cement) with a purity of more than 95% was employed [30].

In accordance with the standard for soil test method (GB/T 50123-1999), the test procedure was as follows. (1) The soil was dried, crushed, and passed through a 2 mm sieve. (2) Water was added to the dry soil to natural moisture content, which was made of soil sample. Then, sealed soil sample settled for at least 24 hours to ensure uniform moisture distribution. (3) After this time, according to the design to weigh various materials, cement was added to the soil sample and mixed well, which was made of soil-cement sample. (4) Fly ash, calcium hydroxide, and polypropylene fiber were added to soil-cement sample in sequence. (5) The prepared samples were divided into three parts for placement in the molds. Every layer interface was roughed up to ensure good surface-to-surface contact, which made it possible to more accurately manufacture soil-cement samples. In this experiment, the unconfined compressive strength samples were prepared with the cube of 70.7 mm, and splitting tensile strength samples were prepared with a diameter of 50 mm and a height of 50 mm. To prevent moisture loss, the samples were sealed with plastic film for at

TABLE 1: Physical properties of clay.

Parameter	Value
Natural moisture content (%)	23.80
Severe (kN/m^3)	19.20
Pore ratio	0.74
Liquid limit (%)	41.60
Plastic limit (%)	22.00
Plasticity index	19.60

TABLE 2: Chemical composition of fly ash.

Compound	Percent by weight
SiO_2	54.18
Al_2O_3	22.35
Fe_2O_3	12.36
CaO	0.40
MgO	0.06
K_2O	3.88
Na_2O	2.62
TiO_2	4.13
Other oxides	0.02

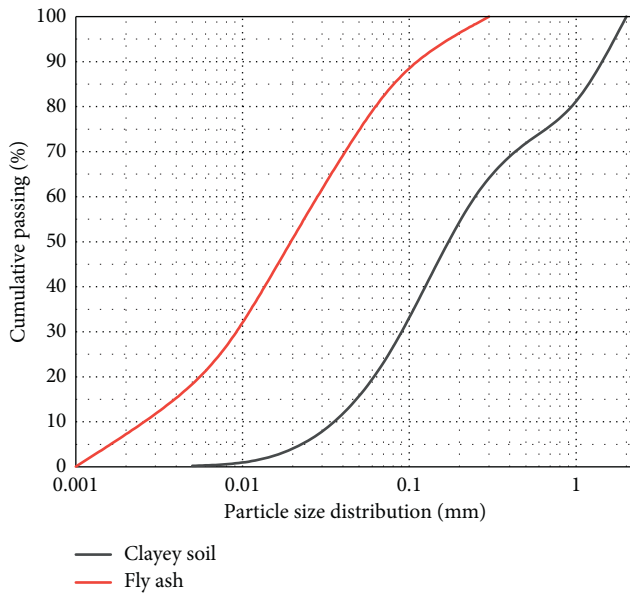


FIGURE 1: Particle size distribution of clayey soil and fly ash.



FIGURE 2: Photograph of polypropylene fibers.

TABLE 3: Physical properties of polypropylene fibers.

Parameter	Value
Fiber type	Single fiber
Density ($\text{g}\cdot\text{cm}^{-3}$)	0.91
Length (mm)	12.00
Diameter (μm)	48.00
Elongation at break (%)	15.00
Modulus of elasticity (GPa)	4.80
Breaking tensile strength (MPa)	486.00

least 24 h, and then the demoulded samples were placed into sealed plastic bag. According to the standard of curing method stabilized soil (JTG E51-2009) [31], samples were placed into a standard moisture room with temperature maintained at $(20 \pm 2)^\circ\text{C}$ and relative moisture above 95% for curing. The curing duration was determined to be twenty-eight days.

There are 24 groups of samples in the research, and three sets of parallel specimens for the unconfined compressive strength and splitting tensile strength were prepared to control the accuracy of the result. For abbreviating, the samples are numbered by some symbols, and the meaning of abbreviations is explained later. The samples FA8-PP0.4 were on behalf of the sample which has 8% fly ash content and 0.4% polypropylene fiber content. WDW-20 microcomputer-controlled electronic universal testing machine with a maximum load sense of 100 kN was employed to conduct the unconfined compression test and splitting tension test. Loading was applied on the sample at a constant displacement rate of 1 mm per minute and continued until sample failure. The microscopic experiment of soil-cement blocks were investigated through scanning electron microscopy (SEM) method, which observed the internal changes in the microstructure. The SEM observations were conducted on blocks taken from a cylindrical sample with a height of 50 mm and a diameter of 50 mm. The blocks removed from soil-cement sample were immersed in ethanol for half an hour and then placed in an oven for drying. In addition, the SEM samples were gold coated by a sputtering technique to make them conductive after drying process. The SEM examinations were performed by using Hitachi S-3400N scanning electron microscope. Figure 3 shows preparation of soil-cement for unconfined compression test, splitting tension test, and SEM test.

3. Experimental Results

3.1. Unconfined Compression Test. Effect of fly ash content on unconfined compressive strength of soil-cement is presented in Figure 4. In order to better describe the influence of polypropylene fiber and fly ash content on the unconfined compressive strength, the strength growth rate η is defined:

$$\eta = \frac{\sigma_n - \sigma_0}{\sigma_0} \times 100\%, \quad (1)$$

where σ_n is the unconfined compressive strength of soil-cement with different polypropylene fiber and fly ash

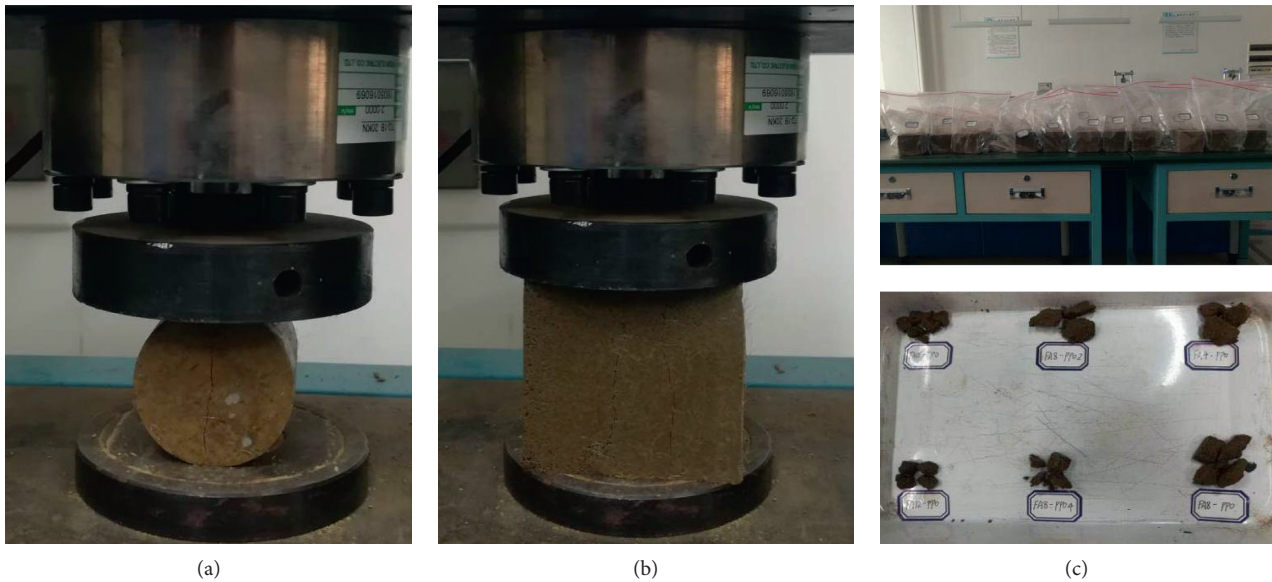


FIGURE 3: Preparation of soil-cement for unconfined compression test, splitting tension test, and SEM test. (a) Splitting tension test. (b) Unconfined compression test. (c) The prepared samples.

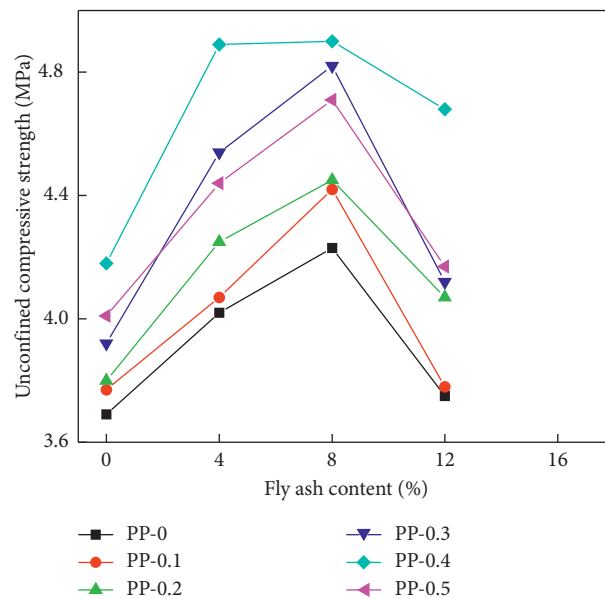


FIGURE 4: Relationship between unconfined compressive strength and fly ash content.

contents and σ_0 is the unconfined compressive strength of plain soil-cement.

It can be seen from Figure 4 that fly ash content plays an important role in unconfined compressive strength of soil-cement. In the same polypropylene fiber content, the unconfined compressive strength of soil-cement increases with the increase of fly ash content from 0% to 8%; however, further increasing fly ash content from 8% to 12% results in the decrease of unconfined compressive strength in general. Hence, the suitable inclusion of fly ash on unconfined compressive strength of soil-cement is 8% in this experiment. This experimental result is consistent with the previous study performed by He and Shen [32]. Figure 4 also shows that

under the condition of 0, 0.1%, 0.2%, 0.3%, 0.4%, and 0.5% fiber inclusion, unconfined compressive strength of soil-cement with 8% fly ash content increases by 14.63%, 17.24%, 17.11%, 22.96%, 17.22%, and 17.46% as compared with that of soil-cement without fly ash inclusion. At the inclusion of 12% fly ash, unconfined compressive strength decreases by 11.35%, 14.48%, 8.54%, 14.52%, 4.49%, and 11.46% as compared with that of soil-cement 8% fly ash with fiber from 0 to 0.5%. Under the condition of 8% fly ash inclusion, the maximum of unconfined compressive strength of soil-cement reinforced with 0.4% fiber is 4.90 MPa, increasing by 16.08% as compared with that of soil-cement without fiber inclusion.

It is likely that fly ash can fill the fine pores between soil particles, and glass bead structure of fly ash can make the soil and fly ash mix uniformly, which makes the hydration reaction more sufficient [4]. The active substances (e.g., silica, alumina, and calcium oxide) in the fly ash react with the hydration reaction products of the cement, which forms a gel material (e.g., hydrated calcium silicate, hydrated calcium aluminate, and calcium meteorite) that is interlaced and wrapped with earthy particles. The internal bonding capacity of soil-cement is greatly enhanced, and the strength of fly ash soil-cement is improved. However, the amount of fly ash exceeds the suitable content (8% in the test), correspondingly reducing the amount of soil and cement, which results in the decrease of main strength provided by the particle size structure of the soil.

Figure 5 shows the variation of unconfined compressive strength of soil-cement specimens with polypropylene fiber content. From Figure 5, it can be seen that polypropylene fiber content has a significant influence on improving unconfined compressive strength for soil-cement specimens. In the same fly ash content, the unconfined compressive strength of soil-cement specimens increases with the increase of polypropylene fiber content from 0% to 0.4%; however, by further increasing polypropylene fiber content from 0.4% to 0.5%, the unconfined compressive strength begins to show a downward trend. Hence, the suitable inclusion of polypropylene fiber content on unconfined compressive strength of reinforced specimens is 0.4%. The results are different from that of Mei and Xu [33], and their results presented that the optimum content of polypropylene fiber is 0.3% by weight of dry soil, which might be due to the difference of soil properties. In addition, the inclusion of fly ash that is glass bead structure increases the fluidity of soil-cement, improving the dispersion of fiber. Under the condition of 0, 4%, 8%, and 12% fly ash inclusion, the unconfined compressive strength of soil-cement with 0.4% polypropylene fiber increases by 13.28%, 21.64%, 15.84%, and 24.80% as compared with the fiber unreinforced samples. At the inclusion of 0.5% fiber, unconfined compressive strength decreases by 4.07%, 9.20%, 3.88%, and 10.88% as compared with that of 0.4% polypropylene fiber soil-cement with fly ash from 0 to 12%. Under the condition of 0.4% polypropylene fiber inclusion, the maximum of unconfined compressive strength of soil-cement reinforced with 8% fly ash is 4.90 MPa, increasing by 17.22% as compared with that of soil-cement without fly ash inclusion. The effect of fiber on unconfined compressive strength might be due to the following reasons:

- (i) The root of the fiber is wrapped with the gel material that is the hydration reaction product of the cement, which forms an anchoring effect on the fiber.
- (ii) Infiltration of hydration reaction products between fibers produces more hydrated gel material on the fiber surface [34], which increases the bonding strength between fibers and soil particles, strengthens the lateral constraint of the wrapped fiber, and improves the deformability of the fiber soil-cement.

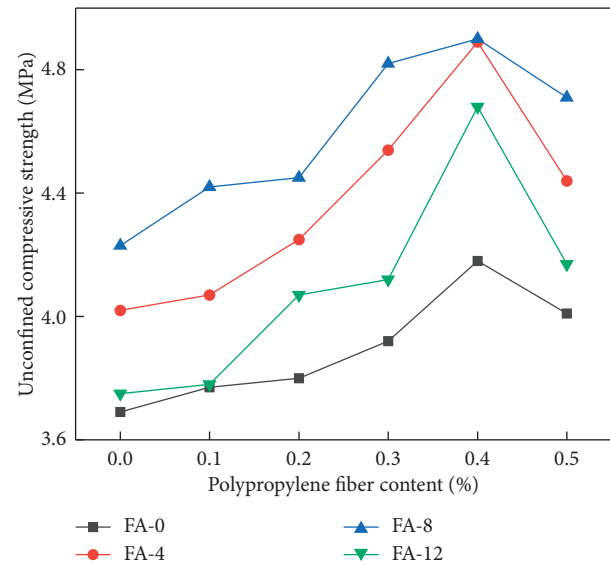


FIGURE 5: Relationship between unconfined compressive strength and polypropylene fiber content.

- (iii) However, when the polypropylene fiber exceeds the optimum content (0.4% in the test), the agglomeration of some fibers leads to a decrease in the bonding interface between fibers and soil particles. The frictional resistance and gripping force of fiber interfaces are smaller than that of fiber, soil particles, and hydration product interface [16], which greatly reduced the reinforcement of fiber.

The addition of both polypropylene fiber and fly ash tends to greatly improve unconfined compressive strength. When 8% fly ash is used, the unconfined compressive strength increased by 15.84%, from 4.23 MPa to 4.90 MPa, as polypropylene fiber increased from 0.1% to 0.4%. It can be seen that the double inclusion of polypropylene fiber and fly ash can effectively improve the unconfined compressive strength of soil-cement.

3.2. Splitting Tension Test. The relationship between polypropylene fiber content, fly ash content, and splitting tensile strength of the soil-cement based on the experimental data is given in Figures 6 and 7.

Figure 6 represents the effect of polypropylene fiber on splitting tensile strength of samples. It can be observed from Figure 3 that the fiber inclusion makes contribution to the enhancement of the splitting tensile strength of soil-cement. In the same fly ash content, the splitting tensile strength increases with the increase of polypropylene fiber content from 0% to 0.4%, further increasing with polypropylene fiber result in the reduction of splitting tensile strength. The result is mainly attributed to the following reasons:

- (i) The tensile strength of polypropylene fiber is much greater than the tensile strength of soil-cement after the tensile cracks formed, and the interaction

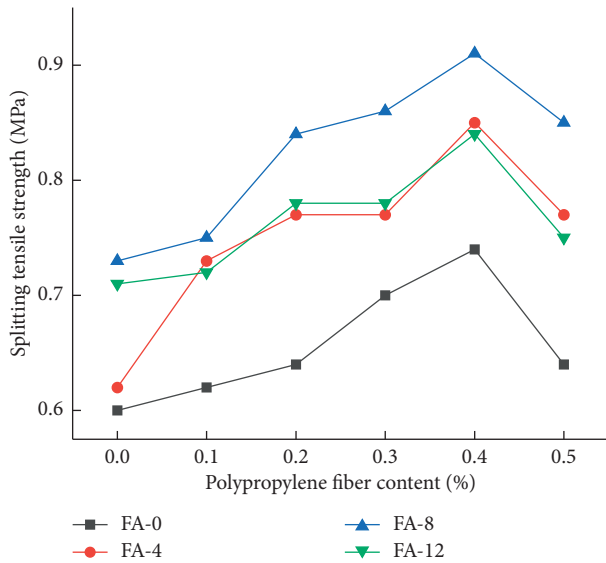


FIGURE 6: Relationship between splitting tensile strength and polypropylene fiber content.

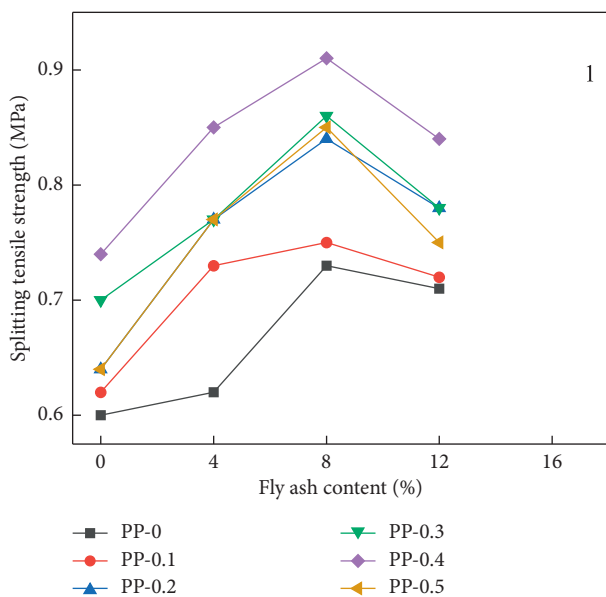


FIGURE 7: Relationship between splitting tensile strength and fly ash content.

between fibers and soil particles provided the tensile resistance.

- (ii) The combined action between fiber and soil particles can efficiently prevent and delay the development of tensile failure plane. Under the condition of the crack further expanding, the bridging effect of polypropylene fiber reduces the stress concentration at the crack tip and bears most of the tensile stress [27].

Under the condition of 0% fly ash inclusion, the splitting tensile strength increases at a relatively slow rate within 0.2%

fiber content. As the fiber content increases from 0.2% to 0.4%, the splitting tensile strength increases rapidly. The splitting tensile strength of soil-cement reinforced with 0.4% fiber is the highest, which increased by 23.33% (0.74 MPa) as compared with that of the plain soil-cement (0.60 MPa). The polypropylene fiber can effectively improve the splitting tensile strength of the soil-cement. Under the condition of 4%, 8%, and 12% fly ash content, splitting tensile strength of soil-cement modified with 0.4% fiber increases by 37.10%, 24.66%, and 18.31% as compared with that of soil-cement without fiber, and splitting tensile strength of soil-cement modified with 0.5% fiber decreases by 9.41%, 6.59%, and 10.71% as compared with that of soil-cement with 0.4% fiber.

Figure 7 shows the variation of splitting tensile strength of soil-cement with fly ash content. As can be seen from Figure 7, in the same polypropylene fiber content, the splitting tensile strength increases with the increase of fly ash content from 0% to 8%. However, further increasing the fly ash content results in the reduction of splitting tensile strength. This is similar to the result of unconfined compressive strength. Under the condition of 0, 0.1%, 0.2%, 0.3%, 0.4%, and 0.5% fiber inclusion, splitting tensile strength of soil-cement modified with 8% fly ash content increases by 21.67%, 20.97%, 31.25%, 22.86%, 22.97%, and 32.81% as compared with that of soil-cement without fly ash inclusion, and splitting tensile strength of soil-cement modified with 12% fly ash decreases by 2.74%, 4.00%, 7.14%, 9.30%, 7.69%, and 11.76% as compared with that of soil-cement modified with 8% fly ash. Under the condition of 8% fly ash inclusion, the maximum of splitting tensile strength of soil-cement modified with 0.4% fiber is 0.91 MPa, increasing by 24.66% as compared with that of soil-cement without fiber inclusion. This indicates that the combined action of fly ash and polypropylene fiber can effectively increase the splitting tensile strength of soil-cement.

4. Deformation and Failure Mode

4.1. Deformation Characteristics. The stress-strain behaviors provide a better understanding of the deformation characteristics of soil-cement. Through the unconfined compressive strength test, the stress-strain curve of soil-cement under different polypropylene fiber and fly ash contents is obtained, as shown in Figures 8 and 9. Figure 8 presents stress-strain curve for plain soil-cement, while Figure 9 shows stress-strain curves for soil-cement with 8% fly ash and different polypropylene fiber contents. It can be seen from the figures that the stress-strain curves of polypropylene fiber-modified fly ash soil-cement and plain soil-cement can be roughly divided into four stages: compaction stage (OA), linear rise stage (AB), nonlinear rise stage (BC), and destruction stage (CD).

OA is a compact phase of the stress-strain curve because the pores between soil particles are compacted, which shows that the compressive strain is independent of polypropylene fiber content. At this stage, the strain growth rate is fast, and the strain of plain soil-cement and soil-cement modified with polypropylene fiber and fly ash are about 0.0110~0.0130.

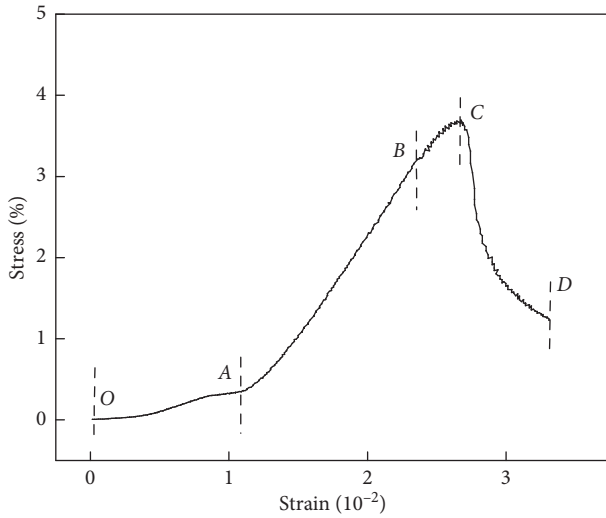


FIGURE 8: Stress-strain curve of plain soil-cement.

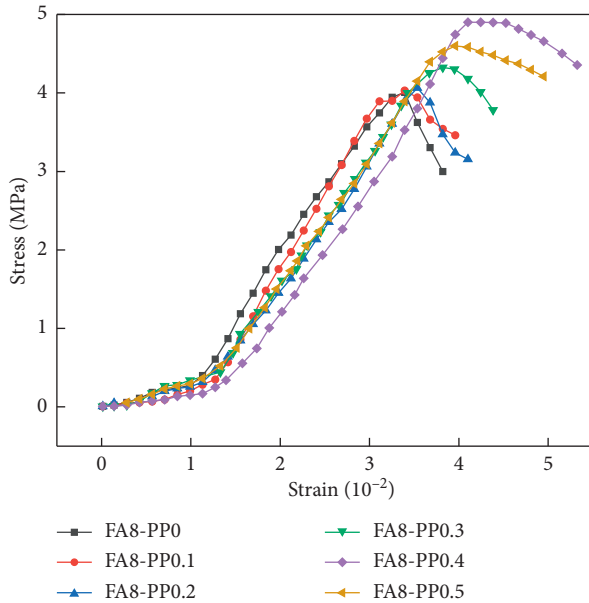


FIGURE 9: Stress-strain curve of soil-cement reinforced with different polypropylene fiber and 8% fly ash contents.

AB is a linear rise phase of the stress-strain curve, which is mainly the stable development stage of soil-cement cracks. The compressive strain is related to the polypropylene fiber content. At this stage, the slope of the curve is large and the strain growth rate is reduced as compared with that of *OA*. The slope of the soil-cement with fiber inclusion is smaller than that of the plain soil-cement, and the maximum linear strain of the plain soil-cement is about 0.0233. Under the condition of 8% fly ash, the maximum linear strains of the soil-cement modified with 0.1%, 0.2%, 0.3%, 0.4%, and 0.5% fiber are approximately 0.0297, 0.0311, 0.0325, 0.0356, 0.0382, and 0.0367. It can be found that the inclusion of fiber can increase the maximum linear strain. However, when the fiber content exceeds 0.4%, the maximum linear strain

decreases. At this stage, the soil-cement with fiber inclusion mainly plays a lateral restraining role in delaying the development of internal cracks in soil-cement and increasing the maximum linear strain. When the fiber content is appropriate (0.1%–0.4% in this test), the maximum linear strain increases with the increase of fiber content due to fiber restriction effect. However, when the fiber exceeds the critical amount (0.4% in this test), the fiber causes a decrease in lateral restraint due to agglomeration, which in turn reduces the maximum linear strain.

BC is a nonlinear rising phase of the stress-strain curve, which is mainly the accelerated expansion stage of soil-cement cracks. At this stage, the stress and strain are nonlinear and the strain growth rate is faster as compared with that of *AB*. The peak strain of plain soil-cement is about 0.0267, and the peak strain of soil-cement modified with 0.1%, 0.2%, 0.3%, 0.4%, and 0.5% fiber is 0.0342, 0.0354, 0.0382, 0.0410, and 0.0396 under the condition of 8% fly ash. It can be found that the inclusion of fibers can increase the peak strain. The fiber mainly acts as a bridging effect to lower the stress concentration at the crack tip, which inhibits the crack development and increases the peak strain. However, when the fiber exceeds the critical content (0.4% in this test), the fiber bridging effect is lowered, which causes the decrease of the peak strain.

CD is the failure stage of the stress-strain curve. After the strain reaches the peak value, the curve shows a downward trend, which shows that the bearing capacity decreases. At this stage, the stress-strain curve is bent downward, and the plain soil-cement exhibits obvious brittle failure characteristics. The postpeak strain of the fiber modified soil-cement is flatter than that of the plain soil-cement, showing a certain ductility characteristic. In addition, the curve gradually flattens with the increase of the fiber content.

4.2. Elastic Modulus. Modulus is employed to evaluate the ability of soil to resist deformation [35]. Modulus of soil based on the unconfined compression test has been investigated by many researchers. As can be seen from Figure 9, the stress-strain curves of soil-cement modified with different polypropylene fibers and 8% fly ash change non-linearly. The elastic modulus *E* is also different due to the difference of intercepted line segment on the curve. According to the literature written by Tang et al. [36], modulus can be obtained from the linear portion of stress-strain curve. From Figure 9, the connecting line segments of *AB* are selected as the research object in the experiment. Elastic modulus can be expressed by following formula:

$$E = \frac{\Delta\sigma}{\Delta\varepsilon} = \frac{\sigma_B - \sigma_A}{\varepsilon_B - \varepsilon_A}, \quad (2)$$

where σ_A and σ_B are the stress of *A* and *B* corresponding to the strain ε_A and ε_B from Figures 8 and 9.

Figure 10 shows that there is a certain fluctuation in the elastic modulus. Under the condition of 0.1% fiber, elastic modulus increases by 11.78% (192.8 MPa) as compared with the fiber unreinforced soil-cement (172.4 MPa). Elastic modulus, with increasing fiber content from 0.1% to 0.3%,

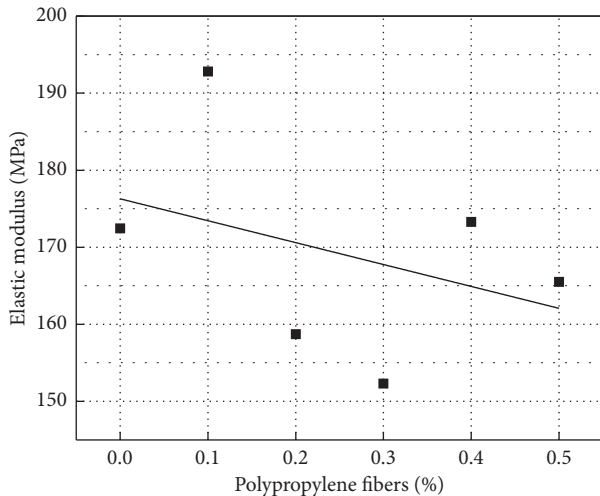


FIGURE 10: Elastic modulus diagram of soil-cement reinforced with different polypropylene fiber and 8% fly ash contents.

ranges from 192.8 MPa to 152.3 MPa. Compared with the fiber from 0.1% to 0.3%, elastic modulus has a smaller fluctuation with the fiber from 0.3% to 0.5%. It is known by curve fitting that the elastic modulus decreases with the increase of fiber in general. The result is similar to the conclusions drawn by Park [22], Gullu and Khudir [25], and Li et al. [37]. The main reason may be that the fiber reduces the contact behaviors between cement and soil particles.

4.3. Peak Strain. The peak strain diagram of soil-cement modified with different polypropylene fibers and 8% fly ash contents, as shown in Figure 11, is obtained by the splitting tension test. It can be seen from Figure 11 that the splitting tensile peak strains of soil-cement modified with 0.1%, 0.2%, 0.3%, 0.4%, and 0.5% polypropylene fibers are 0.0140, 0.0156, 0.0168, 0.0196, and 0.0172, respectively, which increases by 20.69%, 34.48%, 44.83%, 68.97%, and 48.28% as compared with that without fibers inclusion. Due to the reinforcement of the fiber, the splitting tensile peak strain was significantly improved. From Figure 11, it can also be concluded that 0.4% polypropylene fiber in the test has the best ability to resist deformation.

4.4. Failure Mode. The failure mode of soil-cement was studied by unconfined compression test. The final failure mode of soil-cement samples with different polypropylene fiber contents is shown in Figure 12.

The damage of the plain soil-cement is cracked from the diagonal, gradually expanding to the middle, which results in the surface clod of soil-cement falling off and the soil-cement sample destroyed, as shown in Figure 12(a). When the fiber content is from 0.1% to 0.4%, the crack width becomes thinner with the increase of fiber content, and the crack failure changes from coarse and small to fine and dense, as shown in Figures 12(b), 12(c), 12(d), and 12(e). Because the fiber can be uniformly dispersed into the soil-cement, the mesh constraint on soil particles is gradually

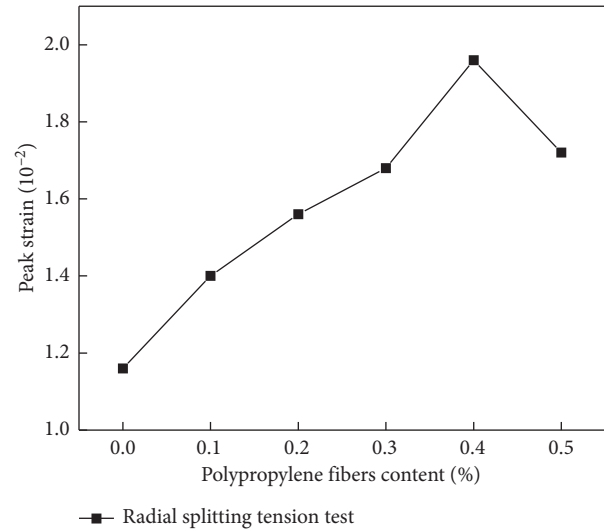


FIGURE 11: Peak strain diagram of soil-cement reinforced with different polypropylene fiber and 8% fly ash contents.

increased as the fiber content increases, inhibiting the development of the crack initiation. When the fiber content reaches 0.5%, the fiber agglomerates in the soil-cement. Because the frictional resistance between fibers is smaller as compared with that between fiber and soil particle, the crack develops and gradually destroys from the fiber agglomeration, as shown in Figure 12(f). From the point of view of the failure mode, the reasonable content of fiber is 0.4% in the experiment.

5. Analysis of SEM Images of Specimens

5.1. Effect of Fly Ash Content. Figure 13 shows SEM images of soil-cement samples modified with different fly ash contents. It can be seen from Figures 13(a), 13(b), 13(c), and 13(d) that specimens exhibit cracks and pores in the soil-cement matrix, which were probably caused during the mechanical test. Cement creates strong bonds between soil particles. In addition, there are many fine threads (Figures 13(c) and 13(h)) on the soil-cement matrix surface, which corresponds to ettringite products and calcium silicate hydrates (C-S-H) gel formed from the hydration reactions of cement [34]. C-S-H gel has a larger specific surface area as compared with soil particles wrapped by C-S-H gel, which gives rise to have a larger specific energy and adsorption energy. The effect of fly ash on soil-cement samples is shown in Figure 13(c). The glass bead structure of the fly ash is clearly observed, which can fill the internal voids of the soil-cement and make the internal structure denser. Figures 13(e), 13(f), and 13(g) show that the connection between soil particles is changed from contact connection to glue connection. The pores between soil particles are decreasing and the structure changes from chaotic disorder to a regularly arranged flaky. However, the excessive fly ash (12%) cannot react with soil particles completely. Given that fly ash is a nonstick material, the unreacted fly ash particles of soil-cement will reduce the



FIGURE 12: The final failure mode of soil-cement with different polypropylene fiber contents. (a) FA-0%, PP-0%. (b) FA-0%, PP-0.1%. (c) FA-0%, PP-0.2%. (d) FA-0%, PP-0.3%. (e) FA-0%, PP-0.4%. (f) FA-0%, PP-0.5%.

interparticle connection and the bonding force between soil particles, which decreases the unconfined compressive strength of soil-cement modified with fly ash (12%) accordingly in previous tests, as shown in Figure 13(i).

5.2. Effect of Polypropylene Fiber Content. Figure 14 shows SEM images of the effect of soil-cement reinforced with polypropylene fiber. Figure 14(a) depicts SEM image of specimens unreinforced with polypropylene fiber, which exhibits pores and cracks in the soil-cement matrix and appears disordered. Figures 14(b), 14(c), and 14(d) show SEM images of specimens reinforced with 0.4% polypropylene fiber under different magnifications. It can be seen from Figures 14(b), 14(c), and 14(d) that the polypropylene fibers having a rough surface are tightly wrapped by the remains of affixed material on the fiber surface, which presents better adhesion between matrix and fibers. The pores between matrix and polypropylene fiber could be generated during the mechanical test.

Figure 15 shows the schematic diagram of the friction between polypropylene fiber and soil-cement. It is supposed that the length of polypropylene fiber is dl and the weights of fiber and soil-cement are ignored. The fiber is subjected to axial tension F_1 , F_2 from external loads and normal stress N from soil particles and hydration products. The tension dF on the microsegment is defined as

$$dF = F_1 - F_2. \quad (3)$$

The friction dT between the fiber and the soil and the hydration product is defined as

$$dT = 2N \cdot \mu \cdot ds, \quad (4)$$

where μ is the coefficient of friction and ds is microsection area corresponding to the length of dl .

As can be seen from the above formula, if $dT > dF$, that is, the friction between the fiber and the soil, the hydration products can resist fiber tension caused by external loads. Polypropylene fiber has high elastic modulus and excellent tensile strength, which prevents the fiber from being pulled

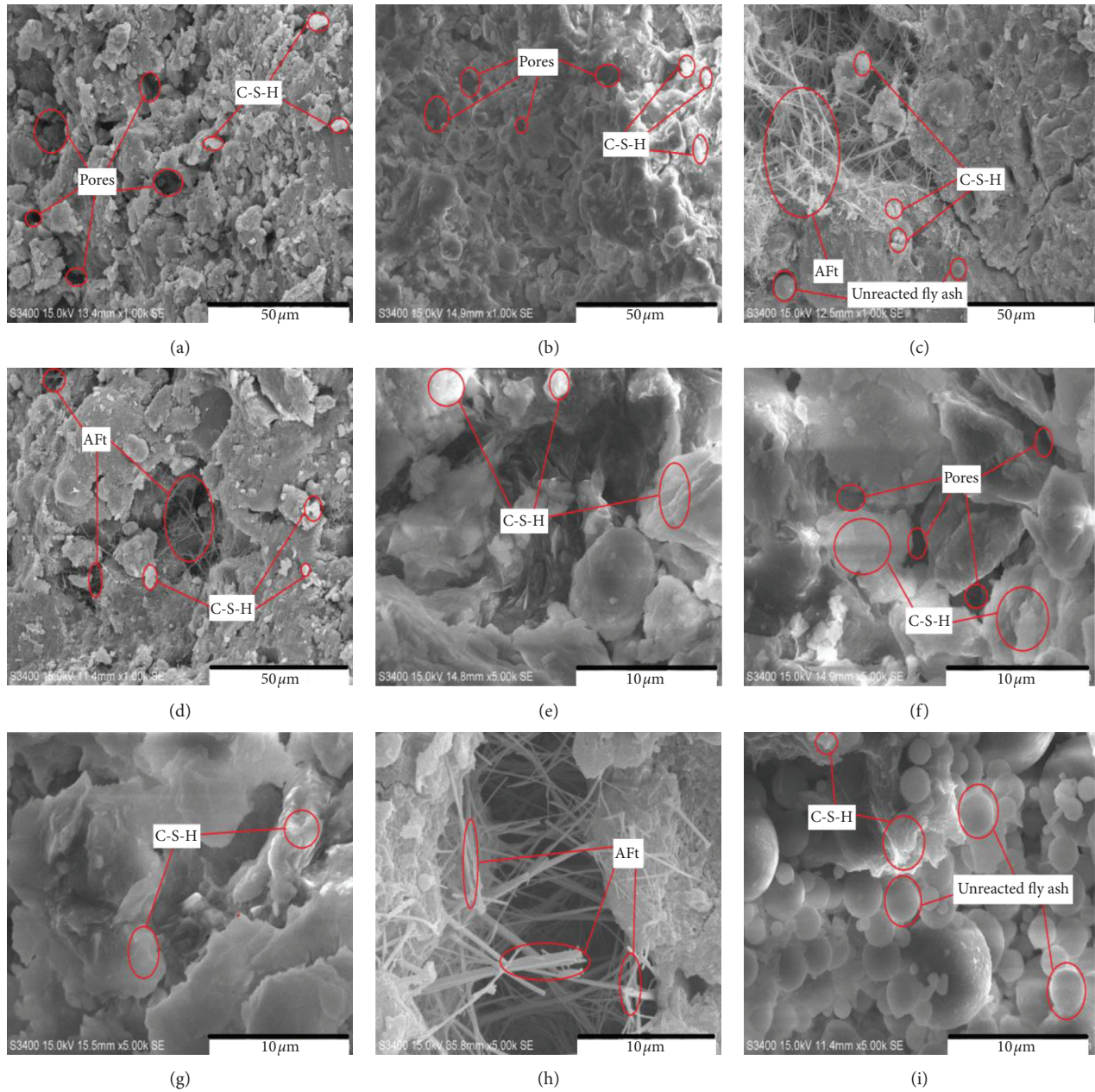


FIGURE 13: SEM images of soil-cement samples reinforced with different fly ash contents. (a) 0% fly ash ($\times 1000$). (b) 4% fly ash ($\times 1000$). (c) 8% fly ash ($\times 1000$). (d) 12% fly ash ($\times 1000$). (e) 0% fly ash ($\times 5000$). (f) 4% fly ash ($\times 5000$). (g) 8% fly ash ($\times 5000$). (h) 12% fly ash ($\times 5000$). (i) 12% fly ash ($\times 5000$).

off under external loads. The fiber is wrapped by the hydration products, increasing the friction between the fiber and the soil and hydration products. The above theory explains the reason why fiber improves the strength of soil-cement from the perspective of friction [38, 39].

Figure 16 shows interface diagram of soil-cement reinforced with fibers. According to the interface wetting theory [34], the fibers and the soil particles are mainly infiltrated and mechanically connected. It can be seen from Figure 16 that the polypropylene fibers are randomly distributed in the soil-cement, and the roots of the fibers are wrapped by the hydration products, which forms an

anchoring effect. The infiltration of the fiber causes more hydration gel material on the surface, and the infiltration of the hydration products between the fibers increases the strong bonds between soil particles, increasing the lateral constraint on fibers. This theory explains the reason why fiber increases the strength of soil-cement from the perspective of interface theory.

6. Conclusions

In this article, unconfined compression test, splitting tension test, and SEM test are conducted to investigate mechanical

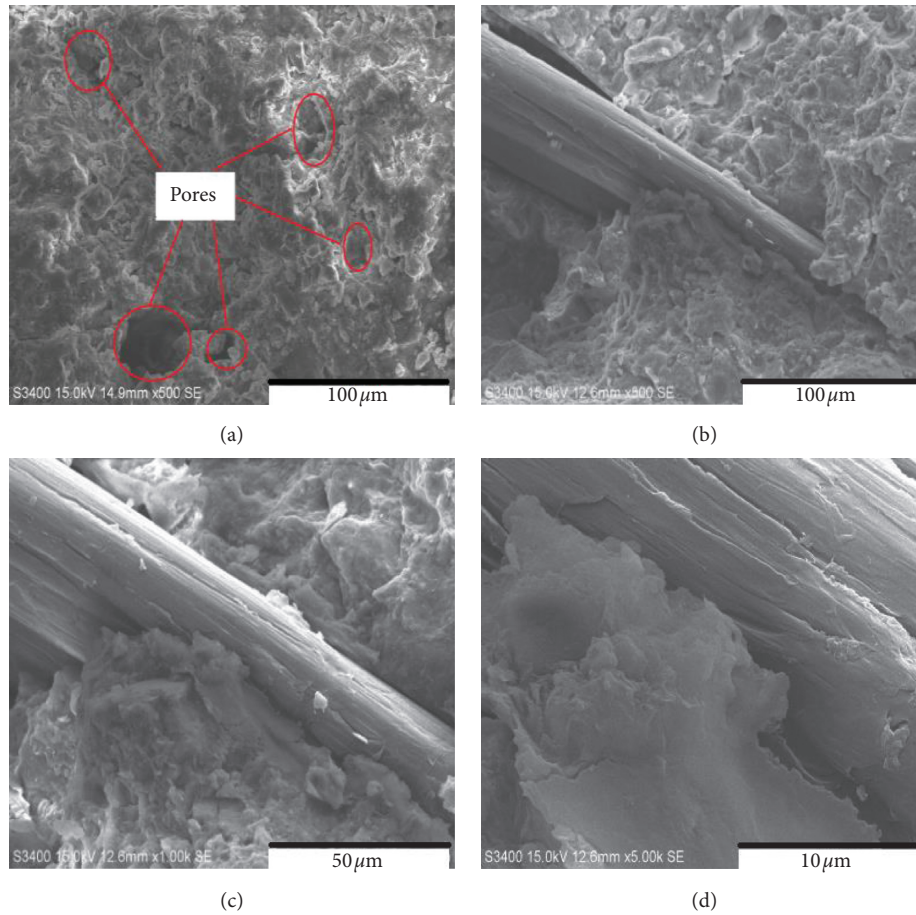


FIGURE 14: Effect of fiber reinforcement on microstructure of stabilized soil-cement. (a) Without polypropylene fiber ($\times 500$). (b) With 0.4% polypropylene fiber ($\times 500$). (c) With 0.4% polypropylene fiber ($\times 1000$). (d) With 0.4% polypropylene fiber ($\times 5000$).

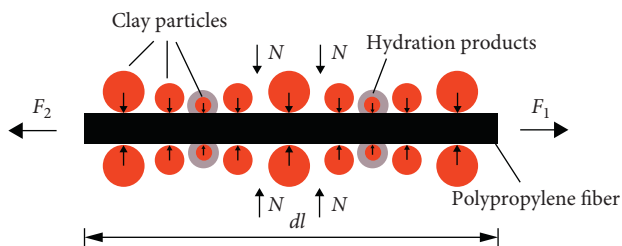


FIGURE 15: The schematic diagram of the friction between polypropylene fiber and soil-cement.

properties, deformation characteristic, failure mode, and microstructure of soil-cement modified with fly ash and polypropylene fiber. The main findings based on the study results can be summarized as follows:

- (1) With the increase of fly ash content and polypropylene fiber content, the unconfined compressive strength and splitting tensile strength of soil-cement modified polypropylene fiber and fly ash increased first and then decreased. Under the conditions of 0.4% polypropylene fiber and 8% fly ash content, the unconfined compressive strength and splitting tensile strength of the soil-cement are the maximum,

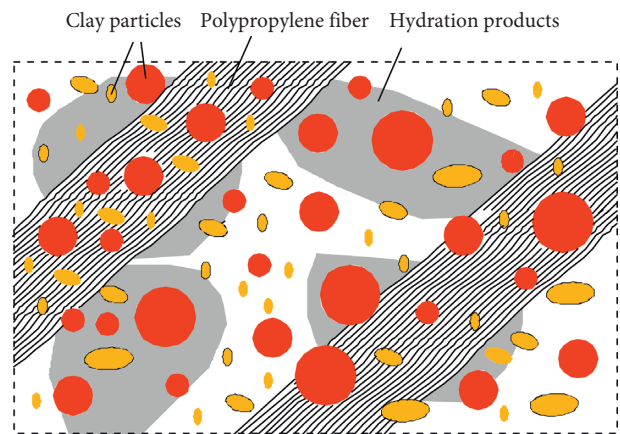


FIGURE 16: Interface diagram of soil-cement reinforced with fibers.

- which is 32.8% and 51.7% higher than that of the plain soil-cement.
- (2) Polypropylene fiber can effectively improve the peak strain of fly ash soil-cement. Under the conditions of 0.4% polypropylene fiber and 8% fly ash content, the unconfined compressive peak strain and splitting tensile peak strain compared to that of without fibers

inclusion were increased by 20.94% and 68.97%, respectively.

- (3) The stress-strain curve of soil-cement modified with polypropylene fiber and fly ash can be divided into compaction stage, linear rising stage, nonlinear rising stage, and failure stage. The transverse reinforcement of polypropylene fiber restrains the fiber soil-cement deformation ability and improved the failure mode of fiber soil-cement.

Data Availability

The data used to support the findings of this study are available from the corresponding author upon request.

Conflicts of Interest

The authors declare that they have no conflicts of interest regarding the publication of this paper.

Acknowledgments

This research was funded by the Natural Science Research Project of Colleges and Universities in Anhui Province (no. KJ2015A135). The authors are grateful to the Engineering Research Center of Underground Mine Construction, Ministry of Education, and Anhui University of Science and Technology for providing the experiment conditions.

References

- [1] Y. Liu, J. Hu, Y.-P. Li, and L.-H. Li, "Statistical evaluation of the overall strength of a soil-cement column under axial compression," *Construction and Building Materials*, vol. 132, pp. 51–60, 2017.
- [2] K. Yao, Q. Chen, J. Ho, H. Xiao, and F. H. Lee, "Strain-dependent shear stiffness of cement-treated marine clay," *Journal of Materials in Civil Engineering*, vol. 30, no. 10, article 04018255, 2018.
- [3] T. Zhang, G. Cai, and S. Liu, "Reclaimed lignin-stabilized silty soil: undrained shear strength, atterberg limits, and microstructure characteristics," *Journal of Materials in Civil Engineering*, vol. 30, no. 11, article 04018277, 2018.
- [4] P. Kumar and S. P. Singh, "Fiber-reinforced fly ash subbases in rural roads," *Journal of Transportation Engineering*, vol. 134, no. 4, pp. 171–180, 2008.
- [5] F. Chen, "Strength and deformation characteristics of basalt fiber cement-soil at early age," *Journal of Shenzhen University Science and Engineering*, vol. 34, no. 6, pp. 611–617, 2017, in Chinese.
- [6] J. J. Li and R. W. Liang, "Experimental study on compressive strength and deformation modulus of cement soil," *Rock and Soil Mechanics*, vol. 30, no. 2, pp. 473–477, 2009, in Chinese.
- [7] R. N. Yong and V. R. Ouhadi, "Cemented sands under static loading," *Journal of Geotechnical Engineering Division*, vol. 107, no. 6, pp. 799–817, 1981.
- [8] M. Khemissa and A. Mahamedi, "Key parameters for strength control of artificially cemented soil," *Journal of Geotechnical and Geoenvironmental Engineering*, vol. 133, no. 2, pp. 197–205, 2007.
- [9] R. Yong and V. Ouhadi, "Experimental study on instability of bases on natural and lime/cement-stabilized clayey soils," *Applied Clay Science*, vol. 35, no. 3–4, pp. 238–249, 2007.
- [10] M. Khemissa and A. Mahamedi, "Cement and lime mixture stabilization of an expansive overconsolidated clay," *Applied Clay Science*, vol. 95, pp. 104–110, 2014.
- [11] Y. H. Yang, Y. H. Liu, and X. Ren, "Experimental study on factors affecting the strength of cement-stirred saturated loess," *Journal of Railway Engineering*, vol. 33, no. 31, pp. 21–25+64, 2016, in Chinese.
- [12] C. Q. Jia, M. S. Huang, and H. Yao, "Experimental study on soft clay strengthened in the minjiang estuary by cement-fly ash," *Journal of Tongji University (Natural Science)*, vol. 32, no. 7, pp. 884–888, 2004, in Chinese.
- [13] X. J. Liu, W. Wang, and L. L. Liu, "Utilization of fly ash resources and industrial development," *Inorganic Chemicals Industry*, vol. 50, no. 5, pp. 12–14, 2018, in Chinese.
- [14] H. Danso, D. B. Martinson, M. Ali, and J. B. Williams, "Physical, mechanical and durability properties of soil building blocks reinforced with natural fibres," *Construction and Building Materials*, vol. 101, pp. 797–809, 2015.
- [15] V. Sharma, H. K. Vinayak, and B. M. Marwaha, "Enhancing compressive strength of soil using natural fibers," *Construction and Building Materials*, vol. 93, pp. 943–949, 2015.
- [16] F. Chen, "Experiment research on tensile strength of basalt fiber cement-soil," *Journal of Shenzhen University Science and Engineering*, vol. 33, no. 2, pp. 188–193, 2016, in Chinese.
- [17] Y. J. Zhang, S. X. Yu, F. Ling, W. P. Yan, X. Liu, and P. Chen, "Experimental study on soft soil reinforced by asbestos fiber fly ash cement," *Journal of Engineering Geology*, vol. 23, no. 5, pp. 982–988, 2015, in Chinese.
- [18] K. Q. Tran, T. Satomi, and H. Takahashi, "Improvement of mechanical behavior of cemented soil reinforced with waste cornsilk fibers," *Construction and Building Materials*, vol. 178, no. 30, pp. 204–210, 2018.
- [19] D. Maskell, A. Heath, and P. Walker, "Inorganic stabilisation methods for extruded earth masonry units," *Construction and Building Materials*, vol. 71, pp. 602–609, 2014.
- [20] P. Zak, T. Ashour, A. Korjenic, S. Korjenic, and W. Wu, "The influence of natural reinforcement fibers, gypsum and cement on compressive strength of earth bricks materials," *Construction and Building Materials*, vol. 106, pp. 179–188, 2016.
- [21] L. H. Li, C. Wan, L. F. Mei et al., "Study on unconfined compressive strength of glass fiber soil-cement," *Journal of Wuhan University (Engineering Science Edition)*, vol. 51, no. 3, pp. 252–256, 2018, in Chinese.
- [22] S.-S. Park, "Unconfined compressive strength and ductility of fiber-reinforced cemented sand," *Construction and Building Materials*, vol. 25, no. 2, pp. 1134–1138, 2011.
- [23] Z. S. Tang and K. Gu, "Strength characteristics of soft soil reinforced by polypropylene fiber and cement," *China Civil Engineering Journal*, vol. 44, no. S2, pp. 5–8, 2011.
- [24] N. C. Consoli, R. R. de Moraes, and L. Festugato, "Parameters controlling tensile and compressive strength of fiber-reinforced cemented soil," *Journal of Materials in Civil Engineering*, vol. 25, no. 10, pp. 1568–1573, 2013.
- [25] H. Gullu and A. Khudir, "Effects of freeze-thaw cycles on mechanical properties of polypropylene fiber and cement stabilized clay," *Cold Regions Science and Technology*, vol. 154, pp. 155–165, 2018.
- [26] P. Y. Zhang, B. Bai, and S. C. Jiang, "Unconfined compressive strength of polyacrylamide modified sand-mixed hybrid fiber

- soil-cement," *China Railway Science*, vol. 35, no. 6, pp. 7–14, 2014.
- [27] D. A. Gutiérrez-Orrego, E. F. Garcia-Aristizabal, and M. A. GomezBotero, "Mechanical and physical properties of soil-cement blocks reinforced with mineral wool and sisal fiber," *Journal of Materials in Civil Engineering*, vol. 29, no. 3, article 04016225, 2016.
- [28] S. Horpibulsuk, R. Rachan, A. Chinkulkijniwat, Y. Raksachon, and A. Suddepong, "Analysis of strength development in cement-stabilized silty clay from microstructural considerations," *Construction and Building Materials*, vol. 24, no. 10, pp. 2011–2021, 2010.
- [29] M. Al-Mukhtar, S. Khattab, and J.-F. Alcover, "Microstructure and geotechnical properties of lime-treated expansive clayey soil," *Engineering Geology*, vol. 139-140, pp. 17–27, 2012.
- [30] W. T. Pang, *Blending Fly Ash Compound Cement Soil Mechanical Properties and Durability Research*, Inner Mongolia Agricultural University, Hohhot, China, 2013.
- [31] Ministry of Transport of the People's Republic of China, *Test Methods of Materials Stabilized with Inorganic Binder for Highway Engineering (JTG E51-2009)*, China Communications Press, Beijing, China, 2009, in Chinese.
- [32] W. X. He and X. D. Shen, "Mechanical properties of glass fiber fly ash cement soil," *Journal of Highway and Transportation Research and Development*, vol. 29, no. 3, pp. 12–16, 2012, in Chinese.
- [33] L. F. Mei and G. L. Xu, "Preparation and mechanical properties of light polystyrene foam particles light soil," *Journal of Composite Materials*, vol. 33, no. 10, pp. 2355–2362, 2016, in Chinese.
- [34] F. Lu, *Study on Mix Design and Mechanism of Fiber Asphalt Crushed Stone Stress Absorption Layer*, Chang'an University, Xi'an China, 2011.
- [35] B. R. Phanikumar and R. S. Sharma, "Volume change behavior of fly ash-stabilized clays," *Journal of Materials in Civil Engineering*, vol. 19, no. 1, pp. 67–74, 2007.
- [36] L. Tang, S. Cong, L. Geng, X. Ling, and F. Gan, "The effect of freeze-thaw cycling on the mechanical properties of expansive soils," *Cold Regions Science and Technology*, vol. 145, pp. 197–207, 2018.
- [37] L. Li, W. Shao, Y. Li, and B. Cetin, "Effects of climatic factors on mechanical properties of cement and fiber reinforced clays," *Geotechnical and Geological Engineering*, vol. 33, no. 3, pp. 537–548, 2015.
- [38] M. Ding, F. Zhang, X. Ling, and B. Lin, "Effects of freeze-thaw cycles on mechanical properties of polypropylene fiber and cement stabilized clay," *Cold Regions Science and Technology*, vol. 154, pp. 155–165, 2018.
- [39] Y. Z. Cao, *Experimental Study on Mechanical Properties of Polypropylene Fiber Silica Fume Cement Soil*, Inner Mongolia Agricultural University, Hohhot, China, 2011.

Research Article

Development, Performance, and Microscopic Analysis of New Anchorage Agent with Heat Resistance, High Strength, and Full Length

Xiaohu Liu ¹, Zhishu Yao ¹, Weipei Xue ^{1,2}, and Xiang Li ¹

¹School of Civil Engineering and Architecture, Anhui University of Science and Technology, Huainan 232001, China

²Post-Doctoral Research Station of Safety Science and Engineering, Anhui University of Science and Technology, Huainan 232001, China

Correspondence should be addressed to Zhishu Yao; zsyao@aust.edu.cn

Received 3 February 2019; Revised 23 March 2019; Accepted 27 March 2019; Published 24 April 2019

Guest Editor: Alena Šišková

Copyright © 2019 Xiaohu Liu et al. This is an open access article distributed under the Creative Commons Attribution License, which permits unrestricted use, distribution, and reproduction in any medium, provided the original work is properly cited.

To solve the difficult problems of failure of pretensioned bolt supports under high ground pressure and temperature, a new kind of anchorage agent with excellent performance is developed. First, the selection and compounding of raw materials were conducted. The new anchorage agent was obtained by modifying the PET resin by mixing with a phenolic epoxy vinyl ester resin (FX-470 resin) and adding a KH-570 silane coupling agent. Then, the viscosity, thermal stability, compressive strength under different temperatures, and anchorage capacity of the new anchorage agent were tested. Moreover, the best proportion ratio of anchorage agent by mixing resin : coarse stone powder : fine stone powder : accelerator : curing agent : KH-570 = 100 : 275 : 275 : 1 : 32.5 : 1 is obtained. The test results showed that, with the addition of a KH-570 silane coupling agent, the viscosity decreased significantly, thereby solving the difficult technical problems of pretensioned bolt supports in full-length anchorage support. Compared with the conventional anchorage agent, the compressive strength of the new anchorage agent increased by 20.4, 82.5, 118.2, and 237.5% at 10, 50, 80, and 110°C, respectively, and the anchorage capacity increased by 4.7, 8.7, 40.2, and 62.9% at 30, 50, 80, and 110°C, respectively. Finally, the enhancement in compressive strength and heat-resistant mechanism are revealed through microanalysis.

1. Introduction

With the increase in mining depth and crustal stress every year, the quantity of broken rock mass increases, which leads to a series of problems such as difficulty in roadway maintenance, cost increase, and safety issues [1, 2]. Full-length anchorage support can maintain the roadways well [3–5]. However, the emerging technology of full-length anchorage support is not yet popular, and with an increase in mining depth, the ground temperature increases, and the anchoring force of the resin anchor becomes lower than the theoretical value [6]; therefore, the anchoring safety decreases.

Many scholars have studied the effect of full-length anchor support and temperature on the anchoring force. Zhou et al. studied the shear stress distribution and load

transfer at the interface of a full-length bonded bolt and deduced the constitutive model of double exponential curve and the exponential form of the load-displacement curve at the top of the bolt. He established that load-displacement distribution at the interface of the bolt and anchor could be a solution [7]. In Nemcik's study, the nonlinear bond-slip constitutive model is combined with FLAC2D to simulate the failure transmission law of a full-length anchored rock under tension [8]. Hu reported a low-viscosity and high-strength anchoring agent using fine stone powder as an aggregate, increasing the amount of resin to improve the consistency of the anchoring agent and compensating for the decrease in resin strength due to a lack of coarse aggregates by increasing the degree of polymerization of the resin [9]. Fan studied the feasibility of introducing a bisphenol A structural reinforcement resin as an anchorage agent into an

unsaturated polyester resin to induce high-temperature stability [10]. Lin carried out optimization test and resin simulation research on the shape and size of a full-length anchor bolt and optimized the height, width, and spacing of the cross-ribs of the bolt [11]. Zhang et al. simulated the resin anchor-hold at different temperatures and obtained the temperature around the drill hole can influence the resin anchor-hold [12]. Hu used a combination of laboratory tests and numerical simulation to study the effect of temperature on the anchoring properties of resin anchors [13]. To solve the problem of adaptability of the full-length anchorage agent technology and ensure the strength of the anchoring support in high ground temperatures, it is urgent to develop a new type of heat-resistant, high-strength, and full-length anchoring agent.

Based on the commonly used full-length anchoring agent comprising unsaturated polyester resins as a binder, the optimum raw materials were selected and samples were prepared. The new type of heat-resistant, high-strength, and full-length anchoring agent was developed by mixing a phenolic epoxy vinyl ester resin (FX-470) with modified PET and adding a silane coupling agent (KH-570). Finally, the physical and mechanical properties of the new anchorage agent were tested.

2. Test

2.1. Test Materials

2.1.1. Resin. The unsaturated polyester resins used in an anchoring agent can be classified into the following types: o-phthalate, phenylene, m-phthalate, and PET. According to Hu and Wang [14], PET resin is widely used in the production of mine-support materials because of its excellent performance, inexpensiveness, and short gelling time. The liquid index of PET unsaturated polyester resin is shown in Table 1.

In this study, polyblend modification was used to improve the poor temperature resistance of the PET resin and the blend system was solidified under the existing solidifying system of unsaturated polyester resin. Vinyl ester resin combines the advantages of unsaturated polyester resin and epoxy resin. Its epoxy framework imparts excellent heat resistance and corrosion resistance to the resin, which can be solidified using the peroxide curing system [15]. Therefore, a phenol epoxy vinyl ester resin was used to modify the PET resin. The chemical formula of the phenol epoxy vinyl ester resin is shown in Figure 1, and the liquid index is shown in Table 1.

2.1.2. Aggregate. The aggregate in an anchorage agent significantly affects the consistency, strength, and thermal stability of the anchoring agent. In this study, river sand, quartz sand, cement, and stone powder were chosen to carry out the proportion test. It was found that river sand and quartz sand fillers decrease the polymer strength and cause fragmentation, while cement fillers rapidly increase the viscosity of polymer and lower the thermal stability. However, stone powder fillers imparted better strength and

TABLE 1: Liquid index of resin.

Type	Acid value (KOH mg/g)	Viscosity (25°C, mPa·s)	Heat distortion temperature (°C)
PET	10–20	550–650	50–55
FX-470	6–18	300–500	165–170

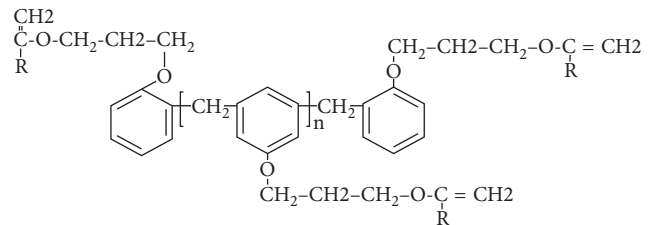


FIGURE 1: Phenol-aldehyde-epoxy-type vinyl ester resin.

viscosity to the anchorage agent. The main components and grain composition of stone powder are selected as shown in Tables 2 and 3. Because wet aggregates can destroy the bonding between the binder and aggregate and reduce the strength of the anchoring agent, the aggregate must be dried to 0.1% or less water content [16].

2.1.3. Curing Agent and Accelerator. As per the requirements of the existing anchoring agent preparation technology, the curing agent used in this study was a mixture of benzoyl peroxide (BPO), calcium carbonate, and ethylene glycol. The content of BPO in the mixture was fixed at 6%, and the amount of curing agent used in the experiment was 5% of the total weight of the anchoring agent cement. The accelerator used was *N,N*-dimethylaniline (DMA), and the amount was 1% of the resin mass in the anchoring agent cement.

2.1.4. Silane Coupling Agents. The silane coupling agent is a kind of organosilicon compound that contains both carbon and silicon functional groups. It is an organic polymer composite that plays the role of an auxiliary for reinforcing, increasing the viscosity, compatibilizing, and imparting moisture resistance. In this paper, the polymer is unsaturated polyester and a silane coupling agent (KH-570) is selected [17]. The compatibility and reinforcement of this silane coupling agent are mainly used to increase the amount of stone powder in the anchoring cement and reduce the consistency of anchoring cement. However, there is an ideal amount of coupling agent to produce the ideal effect [17, 19]. The amount of silane coupling agent (KH-570) in this test ranges from 0.5 to 2% by weight of the resin.

2.2. Test Method. The existing conventional full-length anchoring agent is composed of the resin, stone powder, accelerator, and curing agent. Its composition ratio is PET resin/coarse stone powder/fine stone powder/accelerator/

TABLE 2: Main composition of stone powder.

CaO (%)	SiO ₂ (%)	Al ₂ O ₃ (%)	MgO (%)	Fe ₂ O ₃ (%)
50.7	19.9	5.6	2.5	0.6

TABLE 3: Screening of stone powder particles.

	10–50 mesh	50–100 mesh	100–150 mesh	150–200 mesh	200–325 mesh
Coarse stone powder (%)	95.1	2.53	1.83	0.48	0.06
Fine stone powder (%)	10.7	17.2	10.6	44.1	17.4

curing agent = 100 : 200 : 200 : 1 : 25. In order to adapt to the full-length anchorage construction technology and reduce the pushing resistance of the anchor during construction, the method of reducing the content of stone powder is usually used to reduce the self-consistency of the anchoring agent. On the other hand, with the increase in the amount of resin, the compressive strength of the anchoring agent decreases after solidification. In addition, the heat resistance of the PET resin in the anchoring agent is generally poor, and it deteriorates with the increase in the amount of the resin.

In view of the existing problems of the conventional full-length anchoring agent, FX-470 resin and silane coupling agent KH-570 are introduced to improve the performance of conventional anchoring agent. The design and test scheme are shown in Table 4. Based on the China coal industry standard MT146.1.2011 [20] and GB/T 2567.2008 [21], the viscosity, thermal stability, compressive strength, and anchorage capacity of capsule resin are tested.

3. Experimental Analysis of Physical and Mechanical Properties of Anchoring Agent

3.1. Viscosity Test. Full-length anchoring support technology requires that the anchorage agent fills the whole anchor hole. If the anchorage agent has a high viscosity, the anchorage resistance will be large, which will lead to the anchorage of the anchor not reaching the required depth and thus greatly reducing the support. Therefore, a reasonable viscosity of the anchorage agent is necessary.

Test Method. The hollow cone for determining the standard consistency of cement and the circular mould for determining the setting time of cement according to MT 146.1-2011 are used [20]. Record the sinking depth of the hollow cone within 1 min. The experimental results are shown in Figure 2.

As shown in Figure 2, A1 is a conventional full-length anchoring agent. The proportion of stone powder in group B and group C is increased, and KH-570 is added at the same time. Compared to the viscosity of B1–B3 or B5–B7 in group B, it can be concluded that when the ratio of resin to stone powder is fixed, the consistency of the anchoring agent decreases with the increase in the amount of KH-570. By comparing B1 and B5 with the condition of the same amount coupling agent, the higher the content of the stone powder, the smaller is the consistency value; compared to the viscosity of C1–C6 in group C, it can be concluded that with the

increase in the proportion of FX-470 resin in the mixed resin, the consistency of the anchoring agent decreases because FX-470 resin has a lower viscosity than PET resin; therefore, with increasing FX-470 resin content with the same ratio of resin to stone powder, the consistency deteriorates. By adjusting the amount of silane coupling agent KH-570, the proportion of stone powder in the anchoring agent can be increased while the consistency of the anchorage agent can be reduced at the same time. The consistency value of full-length anchoring agent should be 50–60 mm. The test results show that B2, B6, B7, and C1–C4 in group B are suitable for full-length anchoring support.

3.2. Thermal Stability Test. As supporting material, the storage period of the anchorage agent should not be less than three months. The thermal stability directly affects the storage time of the anchoring agent at room temperature, so it is an important index of anchoring agent performance. The test method is as follows [20]: the anchorage agent is heated in a 101A-2 electric drying oven with forced convection and maintained for 20 h at $(80 \pm 2)^\circ\text{C}$. After removal, it is placed for 4 h at $(22 \pm 1)^\circ\text{C}$. The consistency value of the observed specimens, which is greater than 16 mm, is normal.

Because the influence of the aggregate on the thermal stability was considered and determined at the material selection stage, the new anchoring agent is mainly used to test the influence of FX-470 resin and KH-570 on the thermal stability of anchorage agent. In this paper, B6, C3, and C6 are selected to carry out the thermal stability test. As shown in Table 5, the viscosity is greater than 16 mm and the thermal stability performance is qualified. It can be seen that the introduction of FX-470 resin and KH-570 does not affect the thermal stability of the anchoring agent.

3.3. Compressive Strength Test. In the full-length anchoring support system, the anchoring agent acts as the bond between the bolt and the rock, and its own strength affects the stability of the anchor. The stability of the anchorage agent's strength under different temperatures is verified by performing the compressive strength test. The test method is as follows: three 40 mm cube blocks were prepared using a standard mould, as shown in Figure 3. After curing at a standard temperature for more than 24 h, the specimen was placed in a 101A-2 electric drying oven with forced convection. The test blocks were heated at different temperatures for more than 6 h to ensure that the temperatures

TABLE 4: Test proportion of new resin anchorage agent.

Type	PET	FX-470	Coarse stone powder	Fine stone powder	KH-570	Accelerator	Curing agent
A1	100	0	200	200	0	1	25
B1	100	0	250	250	0.5	1	30
B2	100	0	250	250	1	1	30
B3	100	0	250	250	1.5	1	30
B4	100	0	250	250	2	1	30
B5	100	0	275	275	0.5	1	32.5
B6	100	0	275	275	1	1	32.5
B7	100	0	275	275	1.5	1	32.5
B8	100	0	275	275	2	1	32.5
C1	80	20	275	275	1	1	32.5
C2	70	30	275	275	1	1	32.5
C3	50	50	275	275	1	1	32.5
C4	30	70	275	275	1	1	32.5
C5	20	80	275	275	1	1	32.5
C6	0	100	275	275	1	1	32.5

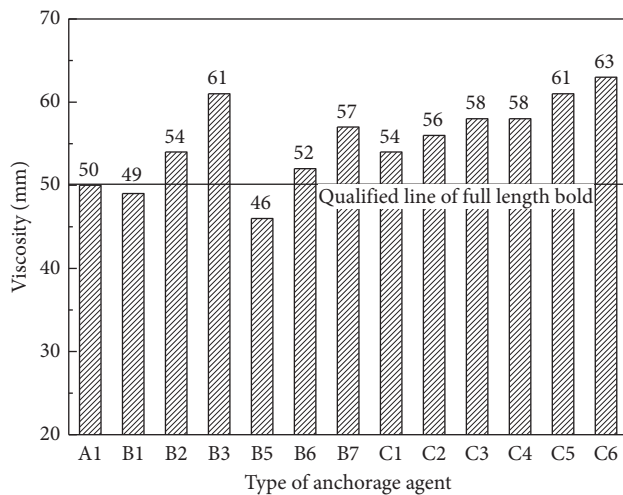


FIGURE 2: Variation in viscosity for different types of anchorage agents.

TABLE 5: Thermal stability test.

Type	B6	C3	C6
Viscosity (80°C/16 h) mm	35	37	38

inside and outside of the specimen were the same. The compressive strength was measured on a universal material testing machine immediately after removing the specimen from the oven so that the specimen temperature does not change by more than 3°C. The temperature of the test piece was measured using an F8380 infrared thermometer. The test results are shown in Figures 4 and 5.

As shown in Figure 4, when the coupling agent KH-570 is added to the group B anchorage agent, the proportion of stone powder becomes higher than that of conventional full-length anchorage agent A1 and the compressive strength significantly increases. Compared to the compressive strength of B1–B4 or B5–B8, with the increase in the amount of the silane coupling agent KH-570 in the anchorage agent,

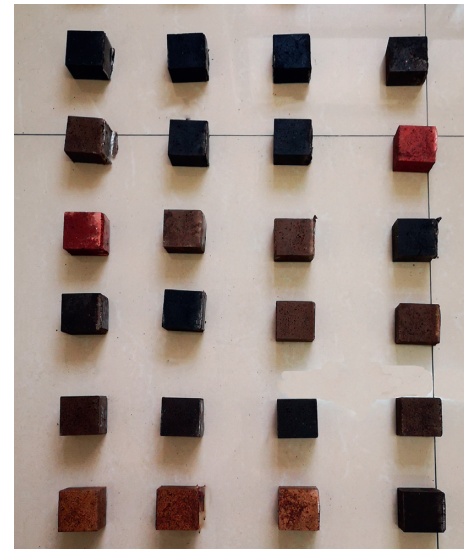


FIGURE 3: Cube blocks.

the compressive strength increased slightly first at a rate of 3–4%. Then, when the content of silane coupling agent reach 1.0% of the resin mass, the strength of the anchoring agent did not increase. It can be seen that adding 0.5%–1.0% coupling agent can improve the bonding between the resin and stone powder in the anchoring agent, and the addition of an excessive amount will not improve the compressive strength of the anchoring agent. Therefore, adding an appropriate coupling agent in the anchoring agent can not only adjust the consistency of the cement and optimize the resin ratio but also improve the compressive strength of the anchoring agent itself.

From Figure 5, it can be concluded that the compressive strength of A1 is 64.4 MPa at 10°C. The compressive strength decreases by 38.8% at 50°C, 57.3% at 80°C, and 76.7% at 110°C. It can be seen that the compressive strength of the A1 anchoring agent is strongly affected by temperature. The B6 anchoring agent is based on A1 ratio to increase the proportion of stone powder and adding KH-570 silane coupling

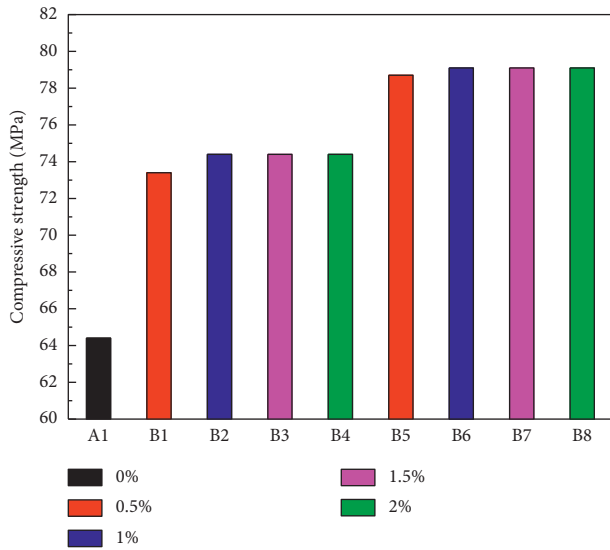


FIGURE 4: Compressive strength corresponding to different coupling agent contents.

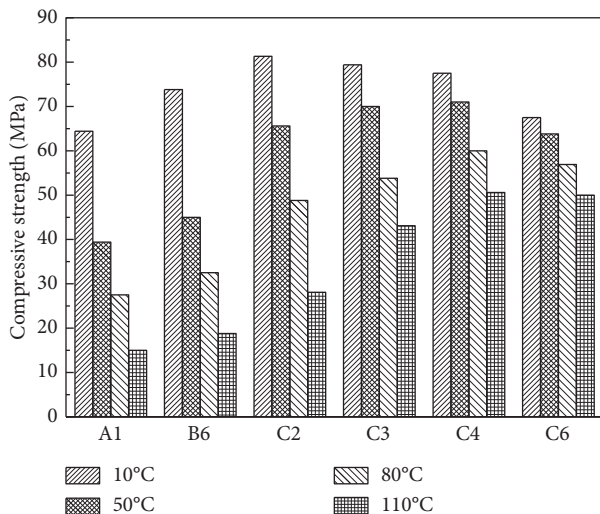


FIGURE 5: Variation of compressive strength with temperature for anchorage agent with different proportions.

agent; thus, the consistency of B6 anchoring agent meets the requirements of full-length anchoring and improves the strength of the anchoring agent at room temperature. However, due to the poor temperature resistance of the PET resin, the performance of the B6 anchoring agent decreases by 74.6% at 110°C. The C6 anchoring agent is composed of FX-470 resin instead of PET resin. The strength of the anchoring agent at room temperature is 67.5 MPa, and its performance remains unchanged up to 50°C and decreases by 25.9% at 110°C. Samples C2–C4 are mixed modified resin anchoring agents that comprise the FX-470 resin, and their compressive strengths at room temperature are higher than that of the conventional resin anchoring agent. Further, with an increase in the proportion of FX-470 resin, the temperature resistance of the anchoring agent gradually improved. The temperature resistance and compressive

strength of the C4 anchoring agent are excellent. The compressive strength at 10°C is 77.5 MPa, which decreases by 7.3% at 50°C, 22.6% at 80°C and 34.6% at 110°C. The compressive strength of C4 increases by 20.4, 82.5, 118.2, and 237.5% over that of A1 at 10, 50, 80, and 110°C, respectively. It can be seen that the temperature resistance of the C4 anchoring agent greatly improved after the FX-470 resin was mixed and modified.

3.4. Anchorage Capacity Test. The anchorage force is the most intrinsic parameter to measure the bonding performance of the anchoring agent. In this study, universal material testing machine and temperature-controlled silicone rubber heating belt are used to draw specimens at different temperatures; the test specimens and setup are shown in Figures 6 and 7, respectively. A steel pipe with an outer diameter of 42 mm, inner diameter of 30 mm, and length of 400 mm and a MSGLW-355 bolt with a diameter of 22 mm and 450 mm length were selected for specimen preparation. The anchoring agent is used to seal one end of the steel pipe, and the amount of the anchoring agent is calculated so that the depth of the plug was 50 mm. After the plug was solidified, the anchor bolt was anchored into the steel pipe with a hand-held pneumatic drill. The anchoring depth is 350 mm. After solidification, the specimen is cured at a standard temperature (22°C) for more than 24 h. Then, the specimen is wrapped with a temperature-controlled silicone rubber heating belt and heated for 2 h to ensure that the temperatures inside and outside the specimen are the same.

The tests of viscosity, thermal stability, and compressive strength show that the group C anchorage agents have a good consistency and thermal stability, especially in a high-temperature environment. Among group C specimens, the comprehensive performance of C4 anchorage agent is outstanding. Therefore, C4 type and A1 type anchorage agents are selected to test the anchorage force at different temperatures. The experimental results are shown in Figure 8.

As shown in Figure 8, A1 and C4 anchorage specimens are pulled apart at 10°C, and their anchorage forces are 186 kN. Further, the anchorage forces of A1 are 172 kN, 161 kN, 117 kN, and 97 kN at 30°C, 50°C, 80°C, and 110°C, respectively, while those of C4 are 180 kN, 175 kN, 164 kN, and 158 kN at 30°C, 50°C, 80°C, and 110°C, respectively. The anchorage capacity of C4 was thus higher than that of A1 by 4.7, 8.7, 40.2, and 62.9% at 30°C, 50°C, 80°C, and 110°C, respectively. Further, the difference in the anchorage capacity between C4 and A1 increases substantially with the temperature. Therefore, C4 is a heat-resistant anchoring agent with superior performance.

In summary, according to the results of tests for the viscosity, thermal stability, compressive strength, and anchoring force, it is concluded that C4 is a heat-resistant, high-strength, and full-length anchoring agent. It has a mixed resin/coarse stone powder/fine stone powder/accelerator/curing agent/KH-570 resin ratio of 100:275:275:1:32.5:1, and the ratio of mixed resin is PET/FX-470



FIGURE 6: Test pieces for testing anchoring force.

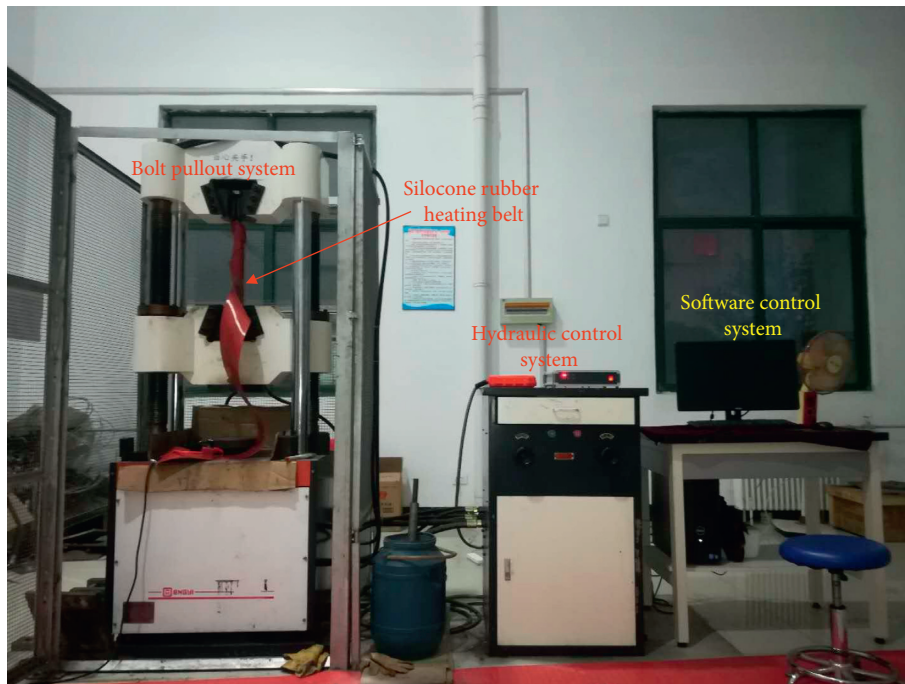


FIGURE 7: Test system for testing anchoring force.

resin = 30:70. The new anchorage agent has excellent thermal stability, suitable consistency, and high compressive strength. The compressive strength and anchorage force at a high temperature are obviously superior to those of the existing full-length anchorage agent.

4. Microscopic Test and Mechanism Analysis of New Resin Anchorage Agent

Compared with the conventional full-length anchorage agent, the C4 anchorage agent shows excellent performance in physical and mechanical tests. The reasons for this are investigated by performing contact angle test and scanning electron microscopy (SEM) imaging.

4.1. Test of Contact Angle between Resin and Stone Powder.

In this study, the contact angle between the PET resin and stone powder was measured using a contact angle tester (SL2000C, Corno Company). Figure 9(a) shows the contact angle between the PET resin and stone powder, and Figure 9(b) shows the contact angle between the stone powder and the PET resin with 1% silane coupling agent KH-570 added into it. As can be seen, the contact angle decreases by about 20° from 120.81° to 101.03° after the addition of KH-570, and the wettability of the resin and stone powder improved with the addition of the coupling agent. It is explained that when KH-570 is added to the anchorage agent of groups B and C, the proportion of stone powder is increased and the viscosity of anchorage agent is decreased.

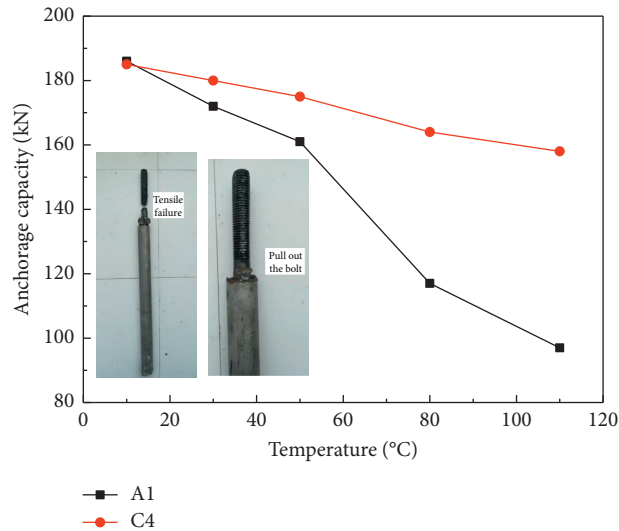


FIGURE 8: Variation in anchorage capacity with temperature for resin capsule.

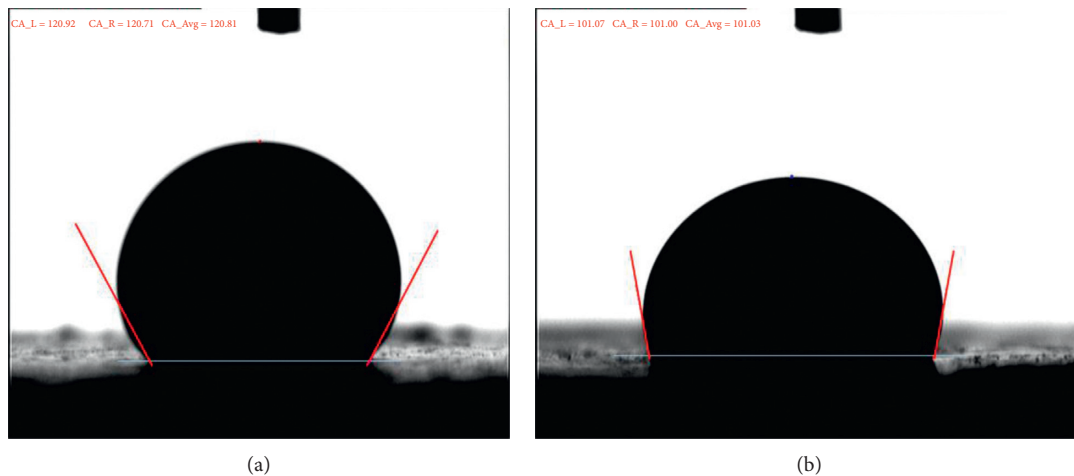


FIGURE 9: Contact angle. (a) Without adding KH-570 and after adding. (b) 1% KH-570 into resin anchoring agent.

4.2. SEM Analysis. In this study, SEM is performed to observe the internal fracture surface of the A1 and C4 anchoring agents after the compressive strength tests. The images are shown in Figure 10.

Figure 10(a) shows a conventional A1 full-length anchorage agent. The filling of fine particles and resin between the coarse particles in the anchoring agent is not compact. The smooth surface of the coarse particles on the shear fracture surface indicates that the resin and particles are not closely bonded. Figure 10(b) shows the C4 anchoring agent, and the resin is closely bound to fine stone powder and is densely packed around coarse grains. The shear fracture surface is rough, and the resin is adsorbed tightly on the surface of the stone powder particles.

4.3. Mechanism Analysis. The wetting effect and chemical bonding of KH-570 between resin and stone powder are verified by performing contact angle measurement and SEM

imaging [22]. The contact angle decreased, and the bonding between the resin and stone powder increased with the addition of the coupling agent. The proportion of stone powder in the anchorage agent increased while meeting the viscosity requirement of full-length anchorage support technology, which makes the new anchorage agent more compact and improves its compressive strength.

FX-470 phenolic epoxy vinyl ester resin itself contains unsaturated double bonds and a high-temperature-resistant epoxy skeleton. Under the catalysis of curing agent free radicals, the unsaturated double bonds break to form a solid network with the PET resin. At the same time, the epoxy skeleton itself is embedded in it, which enhances the heat resistance of the anchorage agent after curing. Therefore, on the basis of the original full-length anchorage agent ratio, the heat-resistant full-length anchorage agent with the appropriate strength and consistency can be prepared by adding KH-570 and FX-470 resins.

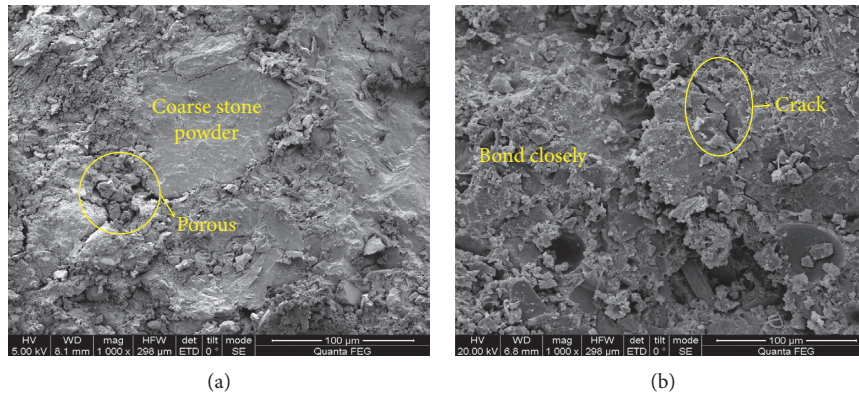


FIGURE 10: SEM micrographs: the ratio of resin to stone powder is (a) 1 : 4 (A1) and (b) 1 : 5.5 (C4).

5. Conclusions

- (1) A new type of anchoring agent with heat resistance, high strength, and full length has been successfully developed. The optimum ratio is mixed resin/coarse stone powder/fine stone powder/accelerator/curing agent/KH-570 = 100 : 275 : 275 : 1 : 32.5 : 1, and the ratio of mixed resin is PET/FX-470 = 30 : 70. The viscosity, thermal stability, compressive strength, and anchorage force results prove that the new anchorage agent has superior physical and mechanical properties, especially in high-temperature environments compared with the conventional anchorage agent.
- (2) Experiments show that adding the KH-570 coupling agent in the new anchorage agent has an infiltration effect, which can reduce the amount of resin in the anchorage agent and the viscosity of the anchorage agent. This makes it more suitable for the full-length anchorage support technology and improves the compressive strength of the anchorage agent itself. The reason why the KH-570 coupling agent optimizes the anchorage agent performance is investigated by performing contact angle measurement and SEM imaging.
- (3) The results of compressive strength test and anchorage force test under different temperatures show that the introduction of the FX-470 resin into the new anchorage agent to modify the original PET resin can greatly improve the thermomechanical properties of the cured anchorage agent. The compressive strength of the new resin anchorage agent increased by 20.4%, 82.5%, 118.2%, and 237.5% at 10°C, 50°C, 80°C, and 110°C, respectively, while the anchorage strength increased by 4.7%, 8.7%, 40.2%, and 62.9% at 30°C, 50°C, 8°C, and 110°C, respectively. The results show that the heat-resistant epoxy group in the FX-470 resin molecule is embedded in the polymer cured by the anchoring agent through the interpolymer reaction between the mixed resins, which improves the overall heat resistance of the anchorage agent.

Data Availability

The data used to support the findings of this study are included within the article.

Conflicts of Interest

The authors declare that there are no conflicts of interest regarding the publication of this paper.

Acknowledgments

This study was supported by the National Natural Science Foundation of China (Nos. 51674006 and 51804006), Anhui Province University disciplines (professional) top-notch talent-funded projects (gxbjZD09), Anhui Provincial College of Natural Science Research Key Project (KJ2018A0098), project funded by the China Postdoctoral Science Foundation (2018M642502), Science Research Foundation for Young Teachers in the Anhui University of Science and Technology (QN2017211), and Science Research for Young and Middle-Aged Academic Backbones in Anhui University of Science and Technology.

References

- [1] S.-Q. Yang, M. Chen, H.-W. Jing, K.-F. Chen, and B. Meng, "A case study on large deformation failure mechanism of deep soft rock roadway in Xin'an coal mine, China," *Engineering Geology*, vol. 217, pp. 89–101, 2017.
- [2] H. Wang, P.-Q. Zheng, W.-J. Zhao, and H.-M. Tian, "Application of a combined supporting technology with U-shaped steel support and anchor-grouting to surrounding soft rock reinforcement in roadway," *Journal of Central South University*, vol. 25, no. 5, pp. 1240–1250, 2018.
- [3] X. G. Su, X. J. Du, H. H. Yuan et al., "Research of the thermal stability of structure of resin anchoring material based on 3D CT," *International Journal of Adhesion & Adhesives*, vol. 68, pp. 161–168, 2016.
- [4] A. Q. Liu and W. J. Ju, "Analysis of shear resisting action of full-length anchored bolt with pre-stress," *Coal mining Technology*, vol. 17, no. 1, pp. 45–47, 2012.

- [5] C. A. You, "Stress analysis of full-length bonded anchor," *Chinese Journal of Rock Mechanics and Engineering*, vol. 19, no. 3, pp. 339–341, 2000.
- [6] X. W. Feng, *Failure Mechanism and Durability Exploration for Fully Bonded Bolting System*, China University of Mining and Technology, Xuzhou, China, 2017.
- [7] B. S. Zhou, B. T. Wang, C. Y. Yang et al., "Study on load transfer characteristics of wholly grouted bolt," *Chinese Journal of Rock Mechanics and Engineering*, vol. 36, no. 2, pp. 3774–3780, 2017.
- [8] J. Nemcik, S. Ma, N. Aziz, T. Ren, and X. Geng, "Numerical modelling of failure propagation in fully grouted rock bolts subjected to tensile load," *International Journal of Rock Mechanics and Mining Sciences*, vol. 71, pp. 293–300, 2014.
- [9] B. Hu, *Study on Mechanical Properties of Resin Capsules for Full-Length Pre-stressed Anchor Bolts*, China Coal Research Institute, Beijing, China, 2011.
- [10] S. P. Fan, Y. Y. Chen, D. Cui et al., "Study on load transfer characteristics of wholly grouted bolt," *Coal Science and Technology*, vol. 25, no. 9, pp. 17–19, 1997.
- [11] J. Lin, S. Ren, and J. H. Yang, "Laboratory research of resin full-length anchoring bolts dimension optimization," *Journal of China Coal Society*, vol. 39, no. 6, pp. 1009–1015, 2014.
- [12] S. Zhang, P. F. Gou, and H. Fan, "Influence of water and temperature on resin anchor-hold," *Journal of Southeast University (Natural Science Edition)*, vol. 35, pp. 50–54, 2005.
- [13] B. Hu, H. P. Kang, J. Lin et al., "Study on influence of temperature on anchorage performance of resin anchored bolt," *Journal of Mining & Safety Engineering*, vol. 29, no. 5, pp. 644–649, 2012.
- [14] Z. Y. Hu and S. M. Wang, "Systematic study on influencing factors of main performance indexes of resin anchoring agent," *Science and Technology Economic Guide*, vol. 19, pp. 78–79, 2017.
- [15] H. Y. Shi, P. Li, Z. M. Xue et al., "Study on the curing of vinyl ester resin composites," *Journal of Materials Engineering*, vol. 1, pp. 300–303, 2006.
- [16] J. J. Nan, J. Yeon, I. Seung et al., "Effects of curing temperature and hardener type on the mechanical properties of bisphenol F-type epoxy resin concrete," *Construction and Building Materials*, vol. 156, pp. 933–943, 2017.
- [17] L. Chen, Y. Wang, Zia-ud-Din et al., "Enhancing the performance of starch-based wood adhesive by silane coupling agent (KH570)," *International Journal of Biological Macromolecules*, vol. 104, pp. 137–144, 2017.
- [18] X. L. Zhang, H. D. Tang, J. Liao et al., *Principles, Synthesis and Application of Silane Coupling Agent*, Chemical Industry Press, Beijing, China, 2012.
- [19] S. Hu and Z. B. Zeng, "Study on unsaturate polyester resins filled with coupling agent-modified wollastonite," *New Chemical Materials*, vol. 30, pp. 30–32, 2002.
- [20] China Standards Publication, *Resin Anchor Bolts-Part 1: Capsules MT 146.1-2011*, Standard Press of China, Beijing, China, 2011.
- [21] China Standards Publication, *Test Methods for Properties of Resin Casting Boby GB/T 2567-2008*, Standard Press of China, Beijing, China, 2008.
- [22] C. Wang, G. S. Jiao, L. Peng et al., "Influences of surface modification of nano-silica by silane coupling agents on the thermal and frictional properties of cyanate ester resin," *Results in Physics*, vol. 9, pp. 886–896, 2018.

Research Article

Effects of High-Density Pulse Currents on the Solidification Structures of Cu-SiC_p/AZ91D Composites

Xi Hao,^{1,2} Weixin Hao ,³ Guihong Geng ,⁴ Teng Ma ,³ Chen Wang,^{1,2} Fuqiang Zhao ,^{1,2} Hao Song,^{1,2} and Yugui Li ^{1,2,3}

¹The Coordinative Innovation Center of Taiyuan Heavy Machinery Equipment, Taiyuan University of Science and Technology, Taiyuan 030024, China

²Shanxi Provincial Key Laboratory of Metallurgical Equipment Design and Technology, Taiyuan University of Science and Technology, Taiyuan 030024, China

³School of Materials Science and Engineering, Taiyuan University of Science and Technology, Taiyuan 030024, China

⁴School of Materials Science and Engineering, North Minzu University, Yinchuan 750000, China

Correspondence should be addressed to Weixin Hao; wxhao@vip.sina.com and Yugui Li; liyugui2008@163.com

Received 11 December 2018; Revised 21 February 2019; Accepted 11 March 2019; Published 3 April 2019

Guest Editor: Alena Šišková

Copyright © 2019 Xi Hao et al. This is an open access article distributed under the Creative Commons Attribution License, which permits unrestricted use, distribution, and reproduction in any medium, provided the original work is properly cited.

In this study, Cu-SiC_p/AZ91D composites were prepared with high-density pulse currents. The wettability between SiC_p and matrix during solidification was improved by coating 0.095- μm thick copper film on the surface of SiC_p. By comparing the composites prepared with/without pulse currents, the solidification structure and its formation mechanism of Cu-SiC_p/AZ91D composites were analyzed under different conditions. The Cu-SiC_p/AZ91D composites prepared without high-density pulse currents were mainly composed of α -Mg, β -Mg₁₇Al₁₂, and a small amount of Mg₂Si phases, with coarse grains and uneven structures. Under the action of high-density pulse currents, the structures of Cu-SiC_p/AZ91D composites were transformed into α -Mg and Mg₂Si phases with refined grain, and the homogeneity of the structures was improved significantly.

1. Introduction

Magnesium matrix composites are widely used in aerospace, construction, marine, and mineral processing industries due to their low density, good mechanical properties, and good corrosion resistance [1–3]. However, the performance of traditional magnesium alloys can no longer meet the needs of social development, and people are committed to the preparation of high-performance magnesium alloys. At present, the commonly used preparation methods of magnesium matrix composites include powder metallurgy, stirring casting, in situ synthesis, and melt infiltration methods [4–6]. After treatment, the reinforced particles are evenly distributed, and the properties of alloys are improved. However, these preparation methods require strict pretreatment procedures, high manufacturing costs, and complex operation. As a new technology, the treatment of alloy melt by using

high-density pulsed current has attracted the attention of researchers, and some research results have been achieved. Especially under the action of high-density pulsed current, it can effectively inhibit the segregation of the second phase and refine the solidification structure. At the same time, this technology has the characteristics of in situ synthesis technology for some composite materials [7–9].

SiC particles are often used as reinforcing phase for magnesium matrix composites. However, the surface activity of micron and nano-SiC particles is easy to agglomerate, and the wettability of SiC particles is poor [10]. The wettability can generally be improved by increasing the surface energy of the reinforcing phase to lower the surface tension of the melt. Preheat treatment of reinforcing particles, addition of appropriate elements to melt, surface coating, and ultrasonic dispersion can be adopted. Therefore, the modification of the SiC surface is beneficial to

promote the wettability of interface and the uniform distribution of reinforcing particles in the process of liquid casting. At present, the volume fraction of SiC reinforcing phase added by the full liquid stirring casting method is 5 vol.%~10 vol.% [11]. In this paper, a new type of full liquid treatment device under the condition of electric pulse is used. SiC particles coated with copper film are added into the AZ91D matrix as reinforcing phase to improve the wettability of the matrix and reinforcing phase. The Cu-SiC_p/AZ91D composites prepared under different conditions are studied. The microstructures of AZ91D composites and the strengthening mechanism are discussed, which provides a new design concept and method for future research.

2. Experimental

Cu-SiC_p/AZ91D composites contain 10 vol.% Cu-SiC_p, in which a layer of 0.095 μm copper film is deposited on the surface of SiC_p. The mass of Cu is 17.3% of that of Cu-SiC_p. The sample size of AZ91D magnesium alloy is 16 mm × 16 mm × 30 mm. The chemical composition of the AZ91D alloy is shown in Table 1 [12]. The magnesium alloy was used as the matrix in the experiment, and 10 μm SiC particles were chosen as the reinforcer to prepare Cu-SiC_p/AZ91D composites.

Figure 1 shows the schematic diagram of the electric pulse melting device used in this study. The preparation process is described as follows. Firstly, magnesium alloy samples were placed in the boron nitride crucible, and then, SiC_p was placed on the surface of magnesium alloys. The pressure in the vacuum box was pumped to 2×10^{-4} Pa, and then, argon gas was filled to the pressure of 50 kPa. Then turning on the high-frequency induction power supply, the samples were heated to 700°C in the vacuum box, and all the samples were melted in the crucible. Then, the metal melt was heated for 10 min. Finally, the electric pulse was applied to the metal melt for 5 min. The electric pulse treatment process of the metal melt was provided as follows. First, set the pulse width 10 μs, the frequency is 30 Hz, and start the power, then read the required current peak on the oscilloscope by adjusting the voltage, and finally the heating device was closed to start the cooling process in the furnace. When the body was completely solidified, the pulse power supply was turned off.

The structure and composition of the samples were analyzed by SS-550 Shimadzu scanning electron microscope, Phoenix EDAX-2000 energy dispersive spectrometer, and X-ray diffractometer (6000×).

3. Results and Discussion

3.1. XRD Analysis of Solidification Structures. XRD analysis was carried out with the prepared magnesium matrix composites (Figure 2). As shown in Figure 2, the Cu-SiC_p/AZ91D magnesium matrix composites prepared under conventional conditions mainly consist of three phases: α-Mg, β-Mg₁₇Al₁₂, and Mg₂Si. The composites prepared under pulse currents mainly consist of two phases: α-Mg and Mg₂Si, and the diffraction peaks of Mg₂Si are enhanced.

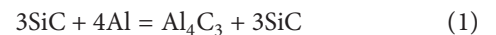
TABLE 1: Chemical composition of AZ91D alloy.

ω (%)					
Cu	Al	Zn	Mn	Si	Mg
0.015	9	0.67	0.25	0.05	Bal.

Note: reproduced from Zhang et al. [12], under the Creative Commons Attribution License/public domain.

3.2. SEM Analysis of Solidification Structures. In order to further analyze the tissue changes, the samples were photographed at a high solution for elemental scanning. The scanning results are listed in Table 2. The XRD spectrum of Figure 2 and Table 2 indicated that the material was composed of α-Mg phase (Spectrogram 1 and Spectrogram 4). The black skeletal dendrite is α-Mg₁₇Al₁₂ phase (Spectrogram 2). The new phase Mg₂Si is formed on the dendrite of β-Mg₁₇Al₁₂ (Spectrogram 3). The gray-white structure near Mg₂Si is composed of α-Mg and Al₄C₃ as well as less attached Cu (Spectrogram 5).

Figure 3 shows high-resolution SEM photographs of AZ91D magnesium alloy, Cu-SiC_p/AZ91D magnesium matrix composite, and Cu-SiC_p/AZ91D composite in pulsed electric fields. The AZ91D magnesium alloy is mainly composed of gray-black α-Mg and dark-black skeletal eutectic β-Mg₁₇Al₁₂ (Figure 3(a)). The phase of β-Mg₁₇Al₁₂ grows along the grain boundary. Figures 3(b) and 3(c) show that the hard strengthening phase Mg₂Si grows along the β-phase after adding Cu-SiC_p, and the Mg₂Si phase replaces the β-Mg₁₇Al₁₂ phase after applying pulsed electric fields. This is consistent with the bright white structure shown in Figures 4(b) and 4(c), the formation of Mg₂Si diffraction peaks in Figure 2, and the disappearance of Mg₁₇Al₁₂ diffraction peaks. The results show that Mg₂Si precipitates as a heterogeneous nucleation point at the grain boundary. SiC and Mg₁₇Al₁₂ peaks were not observed in the XRD spectra (Figure 2). It was inferred that the formation of Mg₂Si was ascribed to the reaction of SiC_p and Al [6]:



SiC_p in the copper-SiC_p was depleted, and Cu was distributed among the dendrites. Formed Al₄C₃ was dispersed in the vicinity of Mg₂Si [2]. Al₄C₃ was mixed with the matrix α-Mg, thus changing the color from gray to gray-white (red circle in Figure 3(c)), which was consistent with Spectrogram 5 in Table 2. The color change in Figure 3(b) was not obvious because SiC_p was not mixed evenly, and the content of Al₄C₃ was too small. As a heterogeneous nucleation point, Al₄C₃ increased the nucleation rate and refined grains [13, 14].

Copper-SiC_p used in this study could effectively change the wettability between particles and melt, but segregation of copper-SiC_p still occurred, and a large number of copper-SiC_p had not yet reacted with Al in the melt. Dendrites in the structure were mainly composed of β-Mg₁₇Al₁₂ and Mg₂Si phases. Al₄C₃ had fewer heterogeneous nucleation points and poor homogeneity, and the grain refinement effect was

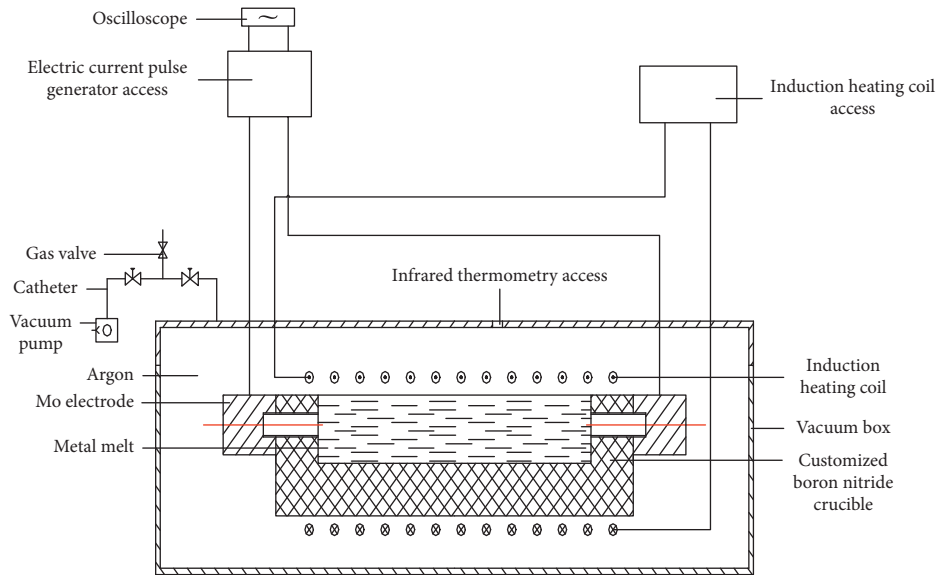
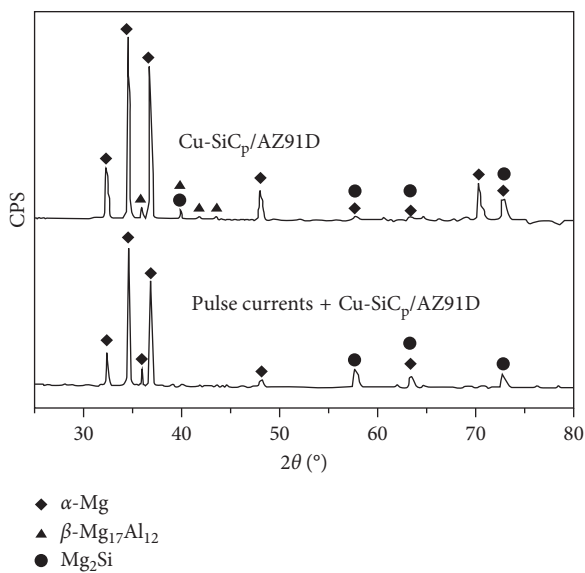


FIGURE 1: Schematic diagram of the electric pulse melting device.

FIGURE 2: XRD spectrum of Cu-SiC_p/AZ91D magnesium matrix composites.TABLE 2: AZ91D and Cu-SiC_p/AZ91D magnesium matrix composite element scanning atomic content table.

Elemental atomic percentage	C	Mg	Al	Si	Zn	Cu
Spectrogram 1	—	90.97	8.27	—	0.76	—
Spectrogram 2	—	60.48	39.52	—	—	—
Spectrogram 3	—	66.71	—	33.29	—	—
Spectrogram 4	—	93.78	5.68	—	0.54	—
Spectrogram 5	21.94	51.23	23.84	—	—	2.99

not observed (Figure 3(b)). When high-density pulse currents were applied, the Lorentz force was produced by the metal melt under the action of electric fields [15], and the

first cyclotron force of the Lorentz force formed strong convection together with the melt, thus resulting in the decreased temperature gradient, widened two-phase zone in the melt. Therefore, the segregation of Cu-SiC_p was effectively restrained, and Cu-SiC_p was allowed to join the melt and maintained in the uniformly mixing state. Due to the wetting effect and the increase in the contact area, Cu-SiC_p reacted with Mg₁₇Al₁₂ sufficiently, thus resulting in phase replacement of β-Mg₁₇Al₁₂ phase by the vermicular Mg₂Si (Figure 3(c)). In addition, the formation of a large number of heterogeneous nucleation points Al₄C₃ increased the nucleation rate, promoted heterogeneous nucleation, obtained uniform structures, and further refined the grains [16] (Figure 4(c)).

In the magnesium alloy of AZ91D, α-Mg formed the matrix, and the β-Mg₁₇Al₁₂ phase was distributed along the crystal boundary with the large crystal grain. In the Cu-SiC_p/AZ91D composite material obtained under conventional conditions, the tissue was mainly composed of three phases: β-Mg₁₇Al₁₂, Mg₂Si, and a small amount of Al₄C₃ phase. Under pulsed electric fields, the composite material showed the uniform structure, and the vermicular Mg₂Si phase replaced the β-Mg₁₇Al₁₂ phase. In the vicinity of the Mg₂Si phase, α-Mg was mixed with Al₄C₃ to form the gray-white zone. When a high-density pulse current is applied, the Lorentz force is generated in the melt under the electric field [16], and the melt is strongly convected by the Lorentz force, resulting in a decrease in the temperature gradient inside the melt and a widening of the two-phase region. In this way, the nucleation rate of Cu-SiC_p/AZ91D increased, and crystal grains were refined. After adding Cu-SiC_p particles, the Al₄C₃ phase was not detected because the following hydrolysis reaction occurred in the sampling preparation process [6]:



3.3. Refinement Mechanism of Solidification Structures. Figure 3 shows the metallographic pictures of AZ91D magnesium alloy, Cu-SiC_p/AZ91D magnesium matrix

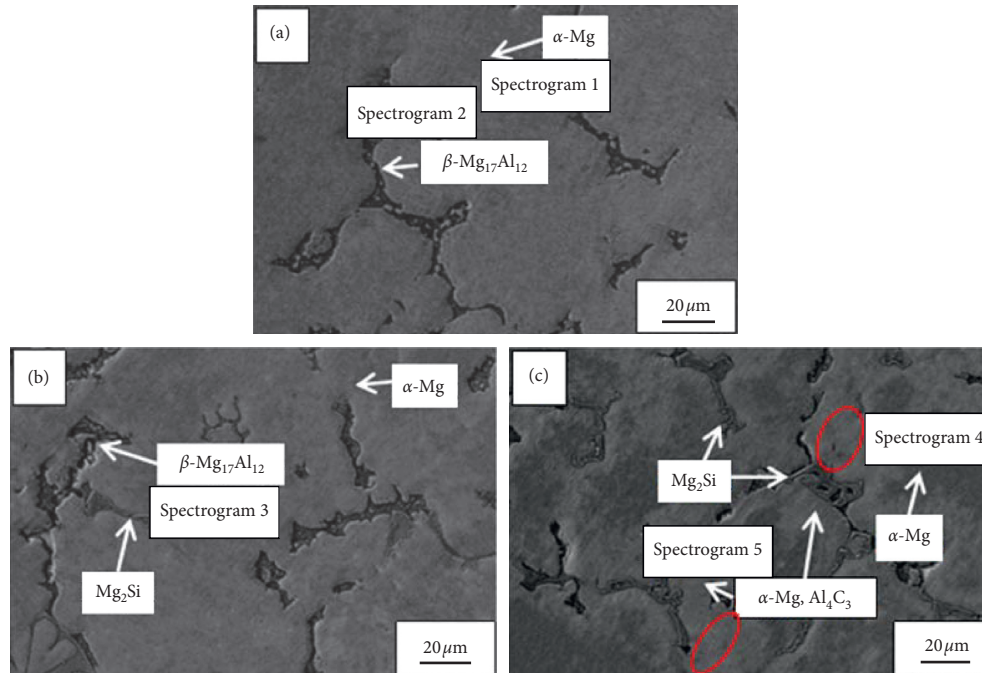


FIGURE 3: High times SEM of AZ91D magnesium alloy and Cu-SiC_p/AZ91D magnesium matrix composites: (a) AZ91D, (b) Cu-SiC_p/AZ91D, and (c) pulsed electric field+Cu-SiC_p/AZ91D).

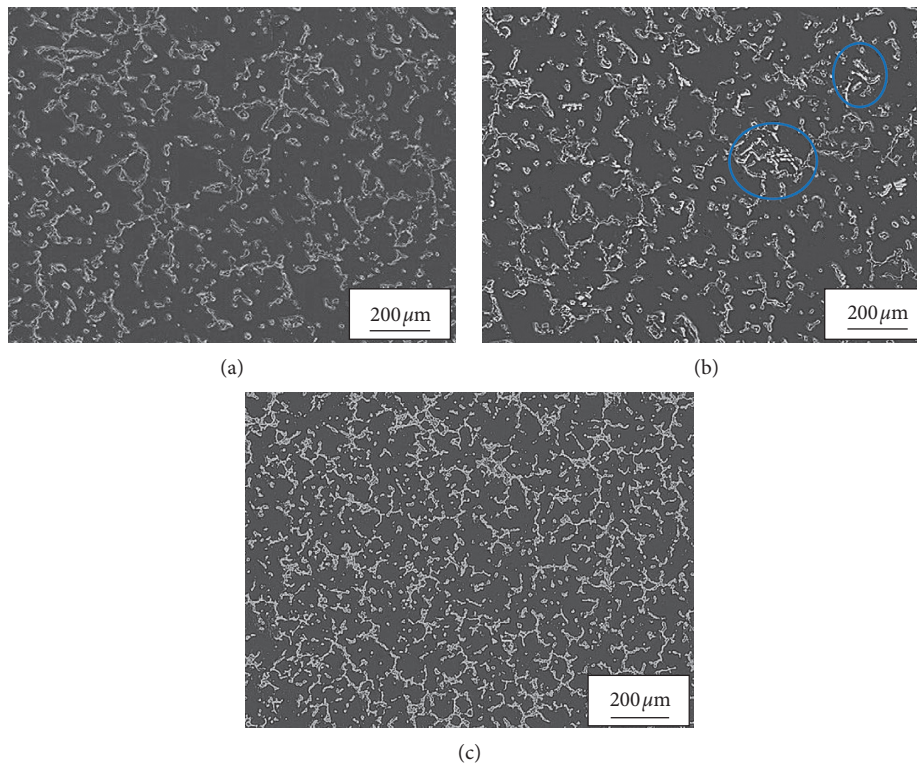


FIGURE 4: Photos of AZ91D magnesium alloy and Cu-SiC_p/AZ91D magnesium matrix composites: (a) AZ91D, (b) Cu-SiC_p/AZ91D, and (c) pulsed electric field +Cu-SiC_p/AZ91D.

composite, and Cu-SiC_p/AZ91D composite under pulsed electric fields. As shown in Figure 4(a), AZ91D magnesium alloy is composed of black matrix and gray reticulated

structure, and its grain size is relatively large. As shown in Figure 3(b), after adding Cu-SiC_p, a little bright white fine structure occurs in the gray-white reticulated structure

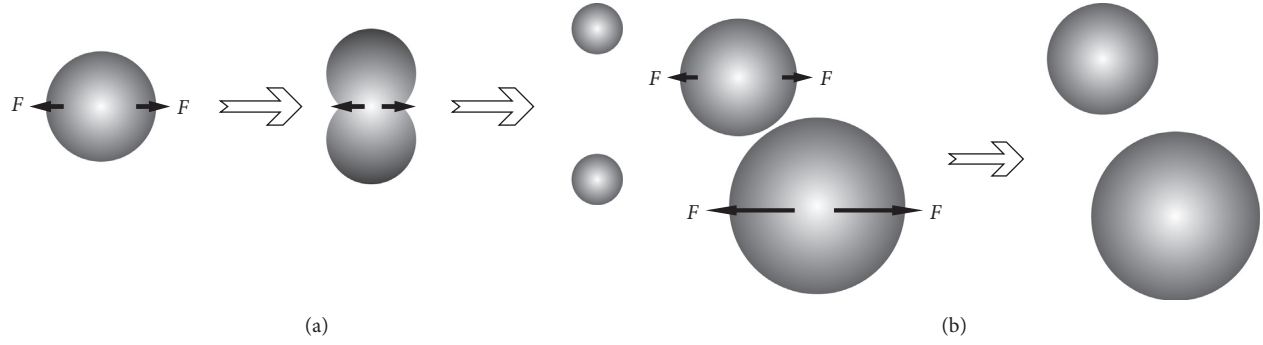


FIGURE 5: Particle condensation process under the influence of electromagnetic force.

(marked by the blue ellipse), and the grains near the bright white structure are refined Cu-SiC_p that can provide potential nucleation points for the melt, thus increasing the number of fine grains in the composites. The copper-SiC_p particles have the pinning effect on grain boundaries and inhibit the grain growth [17]. As shown in Figure 4(c), after applying pulsed electric fields and adding Cu-SiC_p, all the gray-white reticulated structures become the finer bright white structures with dense dendrites and fine grains.

According to the theory of electromagnetic field dynamics, under the action of pulse currents, the particles and the whole melt are affected by the changing electromagnetic force. This vibration will produce the following effects on the aggregation of particles in the melt. Firstly, the vibration of the electromagnetic force can break coagulated Cu-SiC_p into smaller particles, as shown in Figure 5(a). Secondly, under the action of pulse currents, the SiC particles of different sizes are also affected by inertial force, which results in the relative motion between them. The effect of relative motion also weakens the coagulation effect of Cu-SiC_p, as shown in Figure 5(b). Furthermore, under the action of pulsed electric fields, the undercooling of the alloy melt increases, thus leading to the increase in the viscosity of the alloy melt and weakening the coagulation effect of Cu-SiC_p particles [10, 18].

In order to study the effect of pulse currents on the nucleation rate of alloy melt, the nucleation rate of classical nucleation theory [15] is expressed as follows:

$$N = \frac{nKT}{h} \exp\left(-\frac{16\pi\sigma_{sl}^3 T_m^2}{3L_m^2 \Delta T^2 KT}\right) \cdot \exp\left(-\frac{\Delta G_A}{KT}\right), \quad (4)$$

where h is the Planck constant; n is the number of atoms per unit volume; K is the Boltzmann constant; T is the absolute temperature; σ_{sl} is the surface free energy; T_m is the melting point; $\Delta T = (\Delta T_m - T)$ is the undercooling of the alloy melt; L_m is the latent heat of melting; ΔG_A is the liquid atom nucleation barrier. When the axisymmetric current $\vec{j} = j(r)\vec{e}_z$ passes through a cylindrical conductive melt, the magnetic field $\vec{B} = B(r)\vec{e}_\theta$ is formed. Pulse currents usually affect the undercooling of the alloy melt through the generated Joule heat and electromagnetic force. In addition, when pulse currents are applied during the melt solidification process, more solute atoms are stimulated to break the energy barrier and enter the matrix due to the effect of

instantaneous discharge. At the same time, pulse currents enhance the vibration of atoms deviating from the equilibrium position, reduce the energy barrier, and change the nucleation barrier. Therefore, in the original nuclear rate equation (1), $\Delta G_A = (\Delta G_0 + \Delta G_E)$, where G_0 is the thermodynamic barrier for the nucleation without applying an external field and G_E is the thermodynamic barrier for the nucleation after applying an external field. Then, we get

$$\Delta G_A = (\Delta G_0 + \Delta G_E) = \Delta G_0 + K_1 \cdot j_2 \cdot \xi_2 \cdot V, \quad (5)$$

$$\xi = (\sigma_0 - \sigma_n) \cdot (\sigma_n - 2\sigma_0)^{-1}.$$

Among them, K_1 is a parameter related to materials; J is the pulsed current density; σ_0 is the conductivity of disordered dielectrics; σ_n is the conductivity of nuclei; V is the volume of nuclei; and K is the Boltzmann constant. For the crystalline melt, if $\sigma_n > \sigma_0$, then $\xi > 0$. Therefore, it can be concluded that the pulse currents reduce the nucleation barrier in the alloy melt. The effect of pulse currents increases the nucleation rate in the alloy melt, and the increase in the nucleation rate leads to the grain refinement in the alloy melt. When EPT is applied after heat preservation, the pulse currents contact directly with the melt and the nucleation growth stops, thus forming an equiaxed region, which can effectively improve the nucleation rate of liquid metal and semisolid metal and trigger the heterogeneous nucleation mechanism [19]. Fine structures were obtained during the rapid solidification because the increase in the undercooling promoted the nucleation rate. The mechanism of dendrite breakage induced by Loren magnetic force under electric pulse treatment allowed the grain refinement [16, 20].

4. Conclusion

Cu-SiC_p/AZ91D composites prepared without high-density pulse currents mainly consisted of three phases: α -Mg, β -Mg₁₇Al₁₂, and Mg₂Si. By applying high-density pulse currents, the structures of Cu-SiC_p/AZ91D composites were transformed into the phases of α -Mg and Mg₂Si.

Cu-SiC_p/AZ91D composites were prepared by different testing methods. The results showed that the Cu-SiC_p/AZ91D composites under high-density pulse currents had uniform structures, and the grains were significantly refined. The nucleation barrier was reduced, and the nucleation rate

was effectively increased by applying high-density pulse currents. Therefore, the fine structure was obtained.

The microstructures of Cu-SiC_p/AZ91D composites were transformed into α -Mg, Al₄C₃ and Mg₂Si phases under the action of high-density pulse currents. Al₄C₃ and Mg₂Si phases as heterogeneous nucleation points increased the nucleation rate of the composites. The Al₄C₃ phase was not detected in the obtained tissues due to the hydrolysis reaction.

Data Availability

The data used to support the findings of this study are available from the corresponding author upon request.

Conflicts of Interest

The authors declare that there are no conflicts of interest regarding the publication of this paper.

Acknowledgments

This work was supported by the National Natural Science Foundation of China (51561001, 51574171, and 51641406), the Natural Science Foundation of Shanxi Province of China (no. 201601D011012), Key Project of Shanxi Key Research and Development Program “Development of Ultra High Strength and Composite Wide and Heavy Plate Large Rolling Equipment” (201703D111003), Shanxi Province Science and Technology Major Project “Research on High Temperature, Corrosion and Wear Resistant Metal Composite Plate/Tube Material Technology”: (MC2016-01), and NSFC-Shanxi Coal-Based Low-Carbon Joint Fund Support Project “Research on the Evolution and Performance of Key Materials in Ultra-Supercritical Boilers under Preparation and Service Conditions” (U610256).

References

- [1] W.-J. Li, K.-K. Deng, X. Zhang et al., “Microstructures, tensile properties and work hardening behavior of SiC_p/Mg-Zn-Ca composites,” *Journal of Alloys and Compounds*, vol. 695, pp. 2215–2223, 2017.
- [2] T. J. Chen, X. D. Jiang, Y. Ma, Y. D. Li, and Y. Hao, “Grain refinement of AZ91D magnesium alloy by SiC,” *Journal of Alloys and Compounds*, vol. 496, no. 1-2, pp. 218–225, 2010.
- [3] S.-Y. Liu, F.-P. Gao, Q.-y. Zhang, X. Zhu, and W.-Z. Li, “Fabrication of carbon nanotubes reinforced AZ91D composites by ultrasonic processing,” *Transactions of Nonferrous Metals Society of China*, vol. 20, no. 7, pp. 1222–1227, 2010.
- [4] Y. Wu, W. Du, Y. Nie et al., “Research status of particulate reinforced magnesium matrix composite,” *Rare Metal Materials and Engineering*, vol. 36, no. 1, pp. 184–188, 2007.
- [5] A. Noguchi, I. Ezawa, J. Kaneko, and M. Sugamata, “SiC/Mg-Ce and Mg-Ca alloy composites obtained by spray forming,” *Journal of Japan Institute of Light Metals*, vol. 45, no. 2, pp. 64–69, 1995.
- [6] T. J. Chen, Y. Ma, W. B. Lv, Y. D. Li, and Y. Hao, “Grain refinement of AM60B magnesium alloy by SiC particles,” *Journal of Materials Science*, vol. 45, no. 24, pp. 6732–6738, 2010.
- [7] B. T. Zi, K. F. Yao, W. J. Liu, J. Z. Cui, and Q. X. Ba, “Effect of higher density pulsed current on solidification structures of 2024 Al alloy,” *Rare Metal Materials and Engineering*, vol. 32, no. 1, pp. 9–12, 2003.
- [8] S. Xiaosi, H. Weixin, M. Teng, and G. Geng, “Control of the solidification structure of hypermonotecticCu-40 wt.% Pb alloy melt by pulse currents,” *AIP Advances*, vol. 8, no. 10, article 105019, 2018.
- [9] M. Teng, H. Weixin, S. Xiaosi, J. Zhang, and G. Geng, “Effects of high-density electric current pulse on the undercooling of Fe-B eutectic alloy melt,” *Advances in Materials Science and Engineering*, vol. 2018, Article ID 9721508, 6 pages, 2018.
- [10] R. Wu, Q. Li, L. Guo, and Y. Ma, “Fabrication and characterization of bimodal size Al₂O_{3p} reinforced 7075 aluminium matrix composites,” *Materials Science*, vol. 23, no. 4, pp. 317–321, 2017.
- [11] Q. Yan, S. Li, and X. Wang, “Research progress on SiC_p reinforced AZ91 magnesium matrix composites,” *Foundry Technology*, vol. 34, no. 12, pp. 1608–1611, 2013.
- [12] L. Zhang, Q. Wang, W. Guo, W. au, W. Li, and H. Ding, “Microstructure and mechanical properties of the carbon nanotubes reinforced AZ91D magnesium matrix composites processed by cyclic extrusion and compression,” *Materials Science and Engineering: A*, vol. 689, pp. 427–434, 2017.
- [13] E. Yano, Y. Tamura, T. Motegi, and E. Sato, “Effect of pure carbon powder on grain refining of cast magnesium alloy AZ91,” *Journal of Japan Institute of Light Metals*, vol. 51, no. 11, pp. 599–603, 2001.
- [14] S. Chen, C. Cai, H. Yu et al., “Effect of SiC content on refining efficiency and morphology of AZ91D magnesium alloys,” *Special Casting & Nonferrous Alloys*, vol. 33, no. 10, pp. 976–979, 2013.
- [15] D. Rábiger, Y. Zhang, V. Galindo, S. Franke, B. Willers, and S. Eckert, “The relevance of melt convection to grain refinement in Al-Si alloys solidified under the impact of electric currents,” *Acta Materialia*, vol. 79, pp. 327–338, 2014.
- [16] H. Z. Liu, Z. L. Zhao, and L. H. Ma, “Influence of high density pulse electric current on solidified aluminum structure and undercooling degree,” *Foundry Technology*, vol. 29, no. 10, pp. 1354–1358, 2008.
- [17] Y. Huang, K. U. Kainer, and N. Hort, “Mechanism of grain refinement of Mg-Al alloys by SiC inoculation,” *Scripta Materialia*, vol. 64, no. 8, pp. 793–796, 2011.
- [18] X. Zhang, S. Wang, and X. Na, “Effect of magnetic field on the solidification of metallic materials,” *Journal of Iron and Steel Research*, vol. 26, no. 5, pp. 1–7, 2014.
- [19] M. Sugamata, K. Shiina, M. Kubota, and J. Kaneko, “Properties of mechanically alloyed P/M composites of Al-Mg₂Si-oxide systems,” *Journal of Alloys and Compounds*, vol. 483, no. 1-2, pp. 350–354, 2009.
- [20] M. J. Abou-Khalil, R. J. Gauthier Jr., T. C. Lee et al., “Structures, methods and applications for electrical pulse anneal processes,” U.S. Patent 9,881,810, 2018.

Review Article

Recent Advances in Characterization Techniques for the Interface in Carbon Nanotube-Reinforced Polymer Nanocomposites

Junjie Chen , Xuhui Gao , and Deguang Xu 

Department of Energy and Power Engineering, School of Mechanical and Power Engineering, Henan Polytechnic University, Jiaozuo, Henan, China

Correspondence should be addressed to Junjie Chen; cjj@hpu.edu.cn

Received 6 December 2018; Revised 24 February 2019; Accepted 6 March 2019; Published 1 April 2019

Guest Editor: Alena Šišková

Copyright © 2019 Junjie Chen et al. This is an open access article distributed under the Creative Commons Attribution License, which permits unrestricted use, distribution, and reproduction in any medium, provided the original work is properly cited.

The current state of characterization techniques for the interface in carbon nanotube-reinforced polymer nanocomposites is reviewed. Different types of interfaces that exist within the nanocomposites are summarized, and current efforts focused on understanding the interfacial properties and interactions are reviewed. The emerging trends in characterization techniques and methodologies for the interface are presented, and their strengths and limitations are summarized. The intrinsic mechanism of the interactions at the interface between the carbon nanotubes and the polymer matrix is discussed. Special attention is given to research efforts focused on chemical functionalization of carbon nanotubes. The benefits and disadvantages associated with covalent and noncovalent functionalization methods are evaluated, respectively. Various techniques used to characterize the properties of the interface are extensively reviewed. How the mechanical and thermal properties of the nanocomposites depend on the physical and chemical nature of the interface is also discussed. Better understanding and design of the interface at the atomic level could become the forefront of research in the polymer community. Potential problems going to be solved are finally highlighted.

1. Introduction

Since the discovery of carbon nanotubes and, in particular, the realization of their unique performance [1–4], much effort has been devoted to develop advanced nanocomposites with carbon nanotubes as reinforcement [5–10]. Full understanding of the excellent behavior of carbon nanotube-reinforced nanocomposites requires knowledge of the interactions at the interface between the carbon nanotubes and the matrix [11–16]. There are no essential differences between such a requirement and that for conventional fiber-reinforced composites, but the characteristic length scale of the reinforcement varies from micrometer to nanometer. The fundamental challenge for applied research on carbon nanotube-reinforced nanocomposites can be illustrated by the electron microscope images shown in Figure 1, where multiwalled carbon nanotubes (decade nanometers in diameter) are deposited on the surface of carbon fibers (a few microns in

diameter) in yarn bundles (a few millimeters in diameter) [17, 18]. The variation in the characteristic length scale of the reinforcement presents both new challenges and significant advantages in the development of fabrication techniques for carbon nanotube-reinforced nanocomposites [19–22] and the development of characterization techniques for such nanocomposites [23–28]. The nanometer scale of the reinforcement represents a significant challenge in the fundamental research of mechanics, since the interfacial interactions at the atomic-scale must be accounted for [29–32].

Various attempts have been made in recent years to develop ceramic-matrix and metal-matrix nanocomposites with carbon nanotubes as reinforcement [33–36], but much more attention has been focused on the development of carbon nanotube-reinforced polymer nanocomposites [37–40]. The outstanding physical and mechanical properties of this new form of carbon have led to significant advances in the development of such nanocomposites for

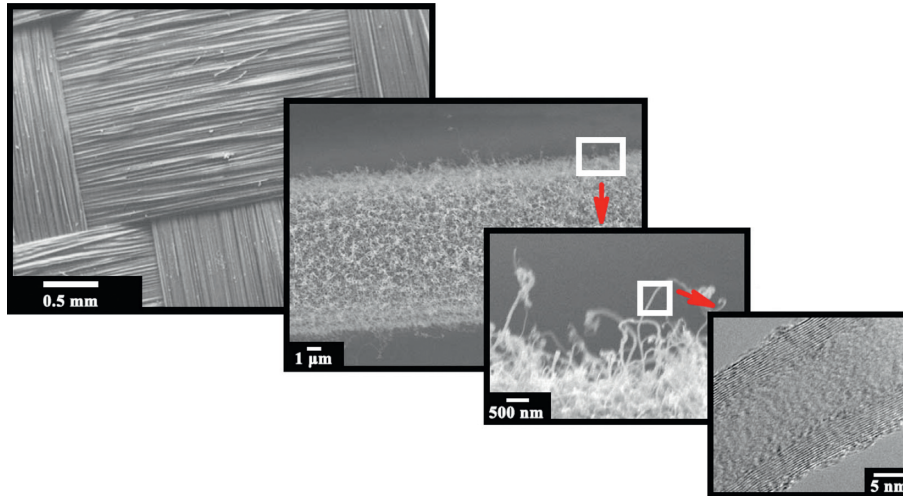


FIGURE 1: Evolution of the characteristic length scale of reinforcement from millimeters to nanometers: (from upper left to lower right corner) from woven fabric of yarn bundles, to an individual carbon fiber with multiwalled carbon nanotubes grown and entangled on its surface, to such a carbon nanotube (adapted with permission from references [17, 18]; copyright 2005, Elsevier Ltd. and copyright 2002, AIP Publishing LLC).

both functional and structural applications [41–44]. However, the potential of carbon nanotubes as reinforcement for polymers has not yet been fully realized, especially in the resulting mechanical properties [17, 20]. The application of carbon nanotube-reinforced polymer nanocomposites depends strongly on how to effectively address the issues and challenges associated with the fundamental properties of the interface between the carbon nanotubes and the polymer matrix [45, 46].

Increasing attention is focused on the properties of the interface in carbon nanotube-reinforced polymer nanocomposites. From the point of view of micromechanics, stress is transferred across such an interface [47, 48]. In addition, the mechanical performance of the nanocomposites depends critically on both the stress transfer across the interface and the shear strength of the interface [49–52]. Furthermore, the thermal resistance of the interface is the most critical factor influencing the thermal performance of the nanocomposites [53–56]. Consequently, knowledge of the properties of the interface becomes particularly essential to the development of carbon nanotube-reinforced polymer nanocomposites. To unlock the full potential of carbon nanotubes and to further improve the overall performance of such nanocomposites, it is important to understand the fundamental properties of the interface [57–60].

Research on carbon nanotube-reinforced polymer nanocomposites is an emerging area, which was first introduced by Ajayan and coworkers [61, 62]. Their work certainly represents a significant milestone towards the development of the nanocomposites and, together with other early work [63, 64], clearly demonstrates that the extraordinary properties inherent to carbon nanotubes can be transferred into the polymer matrix efficiently. Since then, the literature related to the nanocomposites is growing explosively, always accompanied by scientific debates [65–70]. Significant insights have been gained through

nanotechnology research, with over 20 papers each day currently appearing in relation to carbon nanotube-reinforced polymer nanocomposites alone, as shown in Figure 2. One of the most interesting avenues of research involves manipulation of the chemistry of carbon nanotubes [71–74], which offers great opportunities for developing multifunctional polymer nanocomposites with the ability to tailor the properties of the interface [75, 76]. As yet, the physical and chemical nature of the interface, along with its influence on the bulk properties of carbon nanotube-reinforced polymer nanocomposites, remains a poorly understood area of research.

Significant progress has been made in understanding the nature of the interface in carbon nanotube-reinforced polymer nanocomposites. Unfortunately, there are only several review articles focused on the topic available in the literature. Chen et al. [77] have provided an overview of the current state of the properties of the interface in carbon nanotube-reinforced polymer nanocomposites. However, full understanding of the nature of the interface requires knowledge of both interfacial properties and characterization techniques [78]. Both complement each other naturally, be short of one cannot, making it easier to understand the nature of the interface. It is therefore of great significance to provide a literature review about the characterization techniques for the interface, in addition to interfacial properties. This review is devoted to characterization techniques for the interface in carbon nanotube-reinforced polymer nanocomposites. Particular emphasis is placed on how to determine the properties of the interface at the nanometer scale for such nanocomposites.

2. Techniques for Interface Characterization

Measurement and control of the strength of the interface are important for developing carbon nanotube-reinforced polymer nanocomposites with tailored interfacial structures and

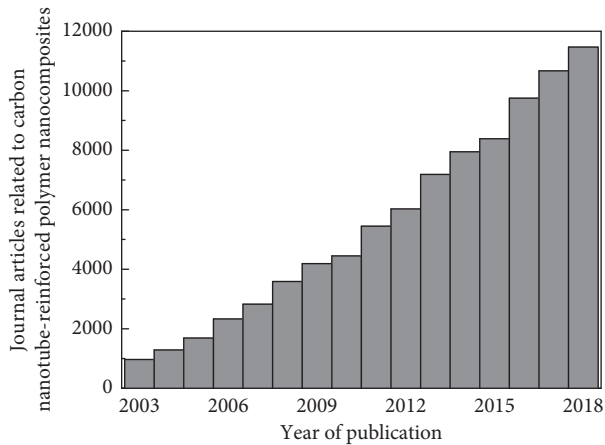


FIGURE 2: Refereed journal articles published in English related to carbon nanotube-reinforced polymer nanocomposites. Data collected from Web of Science by the end of 2018.

properties [79, 80]. To fully realize the benefits of carbon nanotubes and to further improve the overall performance of the nanocomposites, it is essential to obtain accurate information about the microscopic structure and properties of the interface [81, 82]. Electron microscope techniques such as scanning electron microscopy [83, 84] and transmission electron microscopy [85, 86] have been extensively used for the general visual identification of carbon nanotube-reinforced polymer nanocomposites. Additionally, optical microscope techniques such as confocal laser scanning microscopy are effective in evaluating the quality of the dispersion of carbon nanotube in a polymer matrix [87–90]. However, the above microscope techniques are usually not sufficient enough to characterize the properties of the interface at the atomic level. High-resolution transmission electron microscopy could achieve the atomic resolution and is being used widely in the field of the nanocomposites to provide more information about the microscopic structure of the interface [91–94].

Atomic force microscopy [95, 96] and Raman spectroscopy [97, 98] have served to quantitatively characterize the properties of the interface. Atomic force microscopy may be the preferred technique for characterization of the interface due to its advantages for high-precision and high-sensitivity measurements [99, 100]. This microscope technique can also serve as a means to elucidate the properties of the interface in polymer nanocomposites [101, 102]. Two particularly powerful approaches to characterize the properties of the interface are the pull-out method [103] and the peeling method [104]. Attempts have also been made in recent years to develop more convenient ways such as Raman spectroscopy to directly assess the properties of the interface [97, 98].

2.1. Atomic Force Microscopy. In developing carbon nanotube-reinforced polymer nanocomposites, it is essential to focus on the properties of the interface, as they determine the efficiency of interfacial load transfer [41–44] and can significantly influence the resulting mechanical performance

[1–4]. The strength of the interface can serve as a quantitative indicator in evaluating the mechanical properties of the nanocomposites. This physical parameter is usually measured through individual carbon nanotube pull-out tests using atomic force microscopy [99, 100]. Individual carbon nanotube pull-out tests are ideal measurements to quantitatively characterize the interfacial load transfer between carbon nanotubes and the polymer matrix. Such experiments involve the use of the probes of atomic force microscopy *ex situ*, or are carried out *in situ* within a chamber of scanning electron microscopy. Based on such nano-pull-out test technology, several nanomechanical methods are being developed and tested for the nanocomposites [58, 99, 103, 105–112]. For example, carbon nanotubes can be bonded to the probe of an atomic force microscopy, embedded in a polymer melt, and then pulled out from the matrix after solidification [103, 105, 106], as shown in Figure 3. Partially embedded carbon nanotubes were observed on the fatigue fracture surface in a polymer matrix and pulled out by a nanomanipulator [58, 99, 107].

Barber et al. [103, 105, 106] attached an individual multiwalled carbon nanotube to the sharp tip of an atomic force microscope. The carbon nanotube was then pulled from a polymer matrix, while the critical force necessary to remove such a carbon nanotube was recorded by the atomic force microscope. Shear strength of the interface [103] and fracture energy for the interface [105] were predicted by measuring the critical pull-out force and the carbon nanotube embedment length. Poggi et al. [113, 114] measured the interfacial adhesion between specific functional groups and the outer surface of an individual single-walled carbon nanotube using a chemically modified chemical force microscope, where the tip of the cantilever of an atomic force microscope was chemically modified. The interaction characteristics of the interface were then measured using this chemical force microscopy [113, 114].

However, there are still some critical issues that need to be addressed before performing such an individual carbon nanotube pull-out test using atomic force microscopy [108]. Images may be limited by misalignment during the cantilever-tip assembly load. Additionally, the intensity of the force signal recorded by atomic force microscopy is based on the assessment of cantilever stiffness as well as the determination of cantilever deflection from low-resolution scanning electron microscope images, both of which may eventually lead to considerable errors [103, 105, 106]. Finally, the embedment depth of an individual carbon nanotube cannot be controlled and measured easily using this nano-pull-out test technology. To observe the embedded portion of such a carbon nanotube after the process of a nano-pull-out test, Nie et al. [101] developed a carbon nanotube-polymer nanobridge structure in a polymer film, as described below.

The strength of the interface can serve as an indicator of interfacial load transfer for the nanocomposites, as it can greatly affect their effective mechanical performance. Unfortunately, inevitable entanglement or kinks of carbon nanotubes inside a polymer matrix would complicate the characterization of the interface as probed and measured by

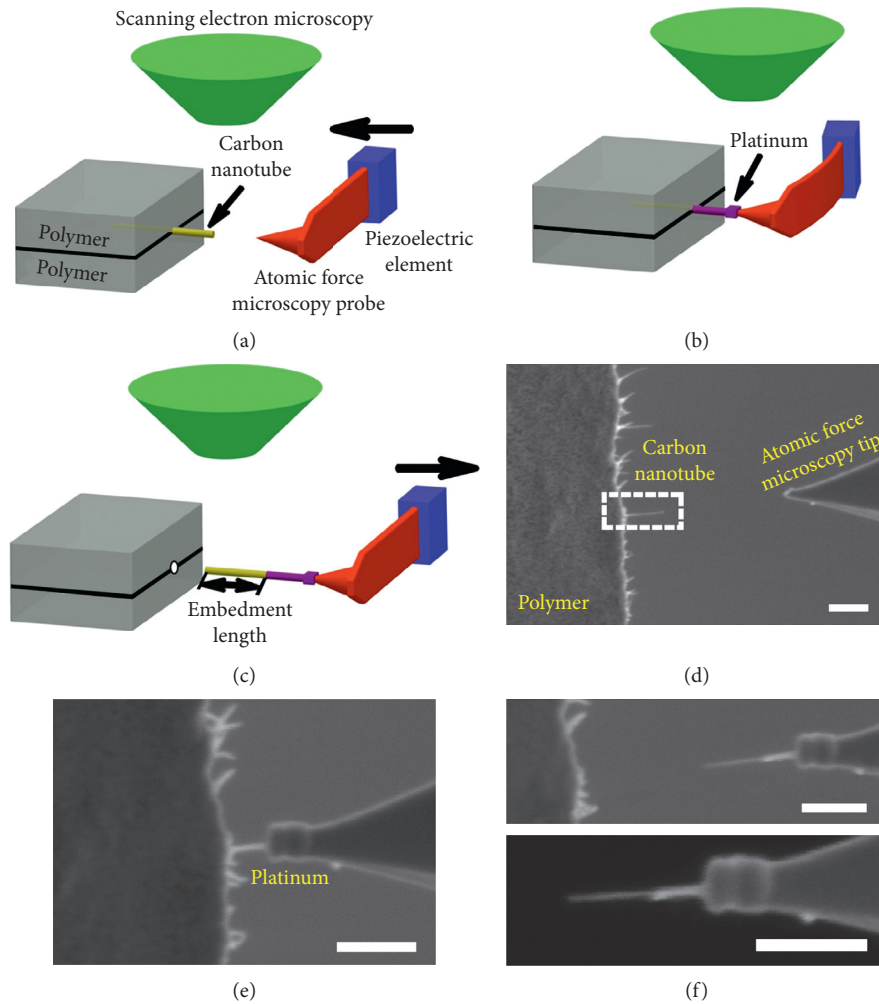


FIGURE 3: Schematic diagram of an individual carbon nanotube pull-out experiment and scanning electron microscope images of one representative individual carbon nanotube pull-out test: (a) a tip fixed to the cantilever of an atomic force microscope approaches the free end of an individual carbon nanotube embedded within a polymer matrix in a controlled way, (b) such a free end has been attached to the tip of the cantilever by means of electron beam-induced deposition of platinum, (c) the carbon nanotube has been pulled out from the polymer matrix completely, and (d)–(f) three scanning electron microscope images of the individual carbon nanotube pull-out test, corresponding to the schematic diagrams illustrated in (a)–(c), respectively. The lower right image in (f) is a zoom-in view of the carbon nanotube after being pulled out. Each of the scale bars represents 500 nm (adapted with permission from reference [99]; copyright 2015, Elsevier Ltd).

individual carbon nanotube pull-out tests. To observe an embedded carbon nanotube before or during the process of a nano-pull-out test, there is a need for a beam of electrons with high energy in a transmission electron microscope or a scanning electron microscope [115–118], which may damage or cross-link the polymer matrix and the interface. To address this issue, Nie et al. [101] developed a controllable method to measure the strength of the interface with the help of an individual nanobridge in a suspended polymer film and proposed an effective way to evaluate the efficiency of interfacial load transfer, as illustrated in Figure 4. Such a microscopic structure is constructed on the basis of the self-assembly of multiwalled carbon nanotubes in liquid flow and the phase separation of polymer blends and the ductile fracture of such blends after thermal and chemical treatment, as shown in Figure 5(a). The microscopic structure of such a nanobridge can be characterized

by a nanomechanical method, by which the force applied to the individual multiwalled carbon nanotube in a suspended state in the transverse direction leads to the pull-out force in the axial direction, as shown in Figures 5(b)–5(d). An atomic force microscope is used to apply such transverse force in a controlled way to the suspended carbon nanotube to produce the force in the axial direction. Such axial force can be applied to pull a segment of the embedded part of an individual carbon nanotube out of a polymer matrix. The pull-out force in the axial direction can be obtained through the control signal recorded by the deflection of the cantilever. The average strength of the interface formed by an individual multiwalled carbon nanotube and a poly(-methyl methacrylate) matrix is about 48 MPa, measured by using this method [101]. Such a controllable method can be used to measure the strength of the interface for the nanocomposites due to the ability to form an image of the

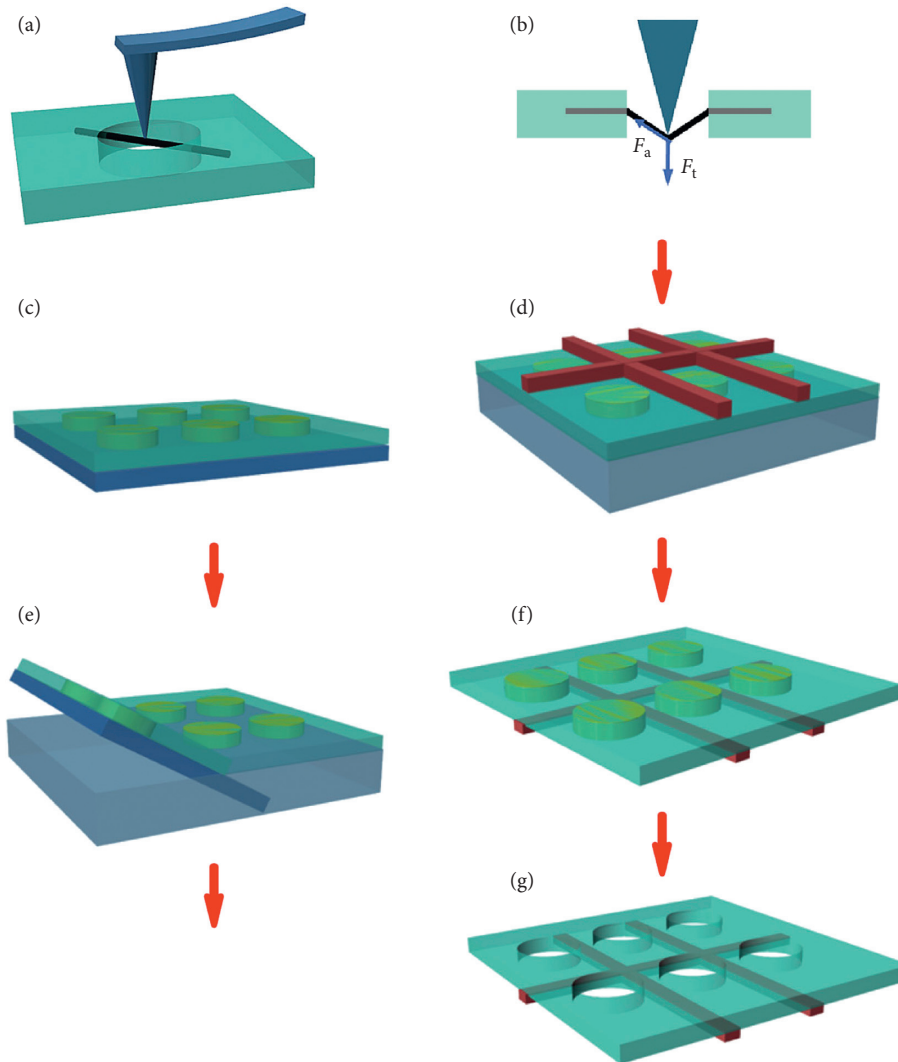


FIGURE 4: (a and b) Schematic diagram of the pull-out process applied to an individual carbon nanotube suspended within a free-standing polymer thin film using an atomic force microscope. Schematic diagram of the fabrication process of a suspended holey film as being formed from a polymer blend: (c) a hydrophobic polymer thin film coated on the surface of a hydrophilic glass slide using a dip-coating method, (d) release of such a film from the glass slide by water, (e and f) transfer of the film to a grid made of copper, and (g) hole-opening using cyclohexane as a solvent and then using a heat treatment method (adapted with permission from reference [101]; copyright 2017, Elsevier Ltd).

embedded portion of an individual carbon nanotube and to the high-resolution imaging during the loading process [101]. It is important to note that this technique is only applicable to the polymers with the ability to form a phase separation structure.

Atomic force microscopy also provides an efficient way to gain insight into the adhesive mechanics of an individual carbon nanotube peeled from a polymer matrix by means of the peeling method described in the literature [104]. Strus et al. [104] used such a method to attach an individual multiwalled carbon nanotube to the peeling probe of an atomic force microscope, as illustrated in Figure 6. The critical force required to peel the multiwalled carbon nanotube off the surface of a polymer matrix was recorded, and the fracture energy of the interface was then quantitatively measured. This method has the ability to measure the

properties of the interface, but it is incapable of measuring the interfacial energy per unit area [104].

2.2. Raman Spectroscopy. Raman spectroscopy can serve as a powerful tool to characterize the properties of the interface by utilizing the unique electronic and vibrational structure of carbon nanotube-reinforced polymer nanocomposites [119–130]. This spectroscopic technique was found to be more effective in revealing the level of disorder and defect sites on the surface of carbon nanotubes [129, 130]. Raman spectroscopy is one of the most effective techniques used to analyze the microscopic mechanism of interfacial load transfer for the nanocomposites [63]. There is a shift in Raman frequency with the stress or strain applied to the nanocomposites [131, 132]. If such a stress is transferred to

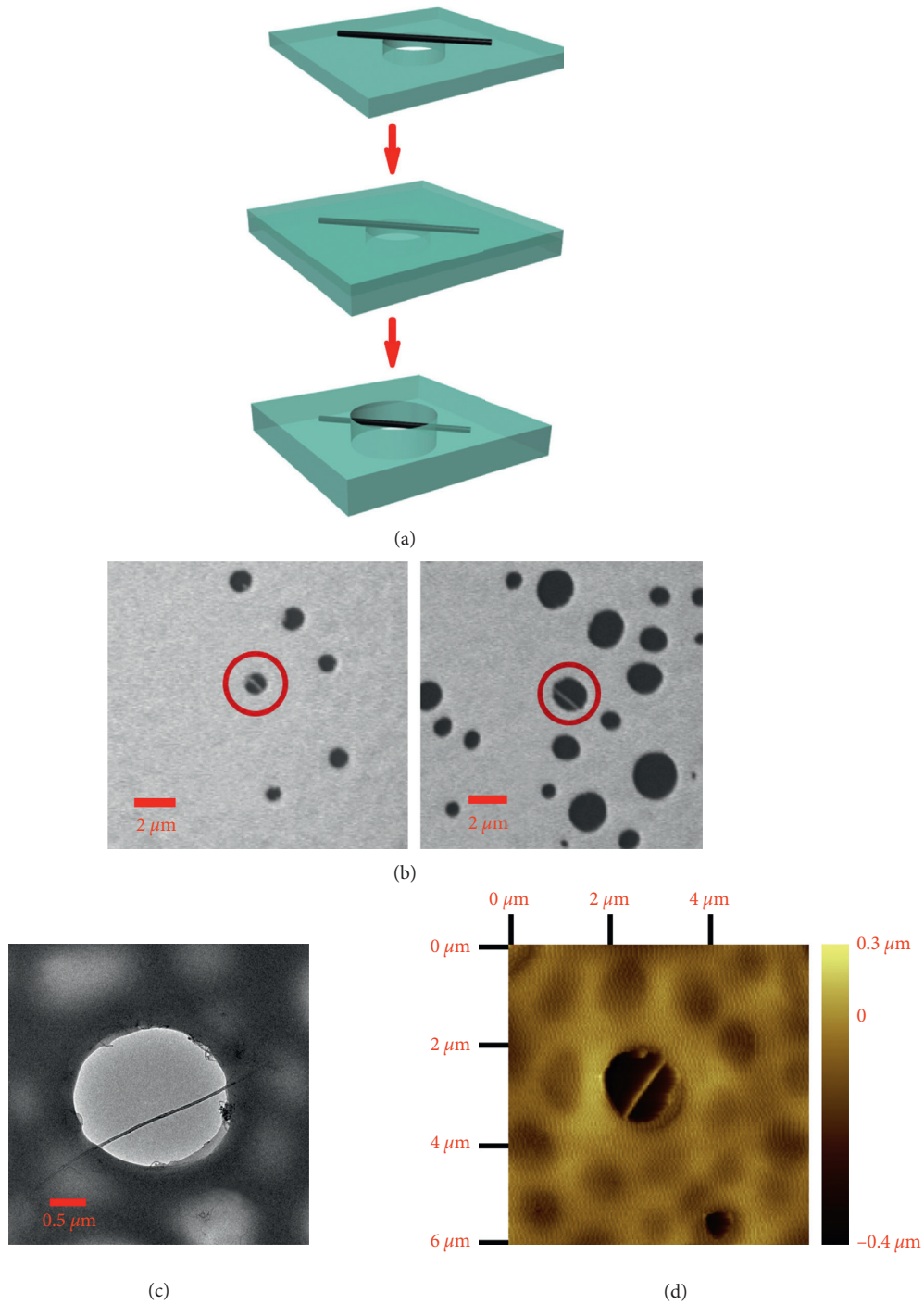


FIGURE 5: (a) Schematic diagram of the formation and evolution process of a nanobridge structure for an individual carbon nanotube-polymer nanocomposite, (b) scanning electron microscope images of such a carbon nanotube suspended across a hole in a layer of the polymer blend film made of poly(methyl methacrylate) and polystyrene using a self-assembly method (left) and the holes opened by using thermal and solvent treatment techniques after adding a second layer of poly(methyl methacrylate) film (right), (c) transmission electron microscope image of the nanobridge structure in a polymer film, and (d) atomic force microscope image of an individual, suspended carbon nanotube with two ends embedded in a poly(methyl methacrylate) matrix (adapted with permission from reference [101]; copyright 2017, Elsevier Ltd).

the carbon nanotubes across the interface, the Raman peak shifts by a few cm^{-1} . The shift in Raman frequency is linear with the strain applied to the nanocomposites, and the slope of the Raman shift-strain response curve is dependent on the

properties of the polymer matrix as well as the degree of alignment of carbon nanotubes [133, 134].

Raman spectroscopy can provide information about the elastic modulus of polymer-based nanocomposites, alignment

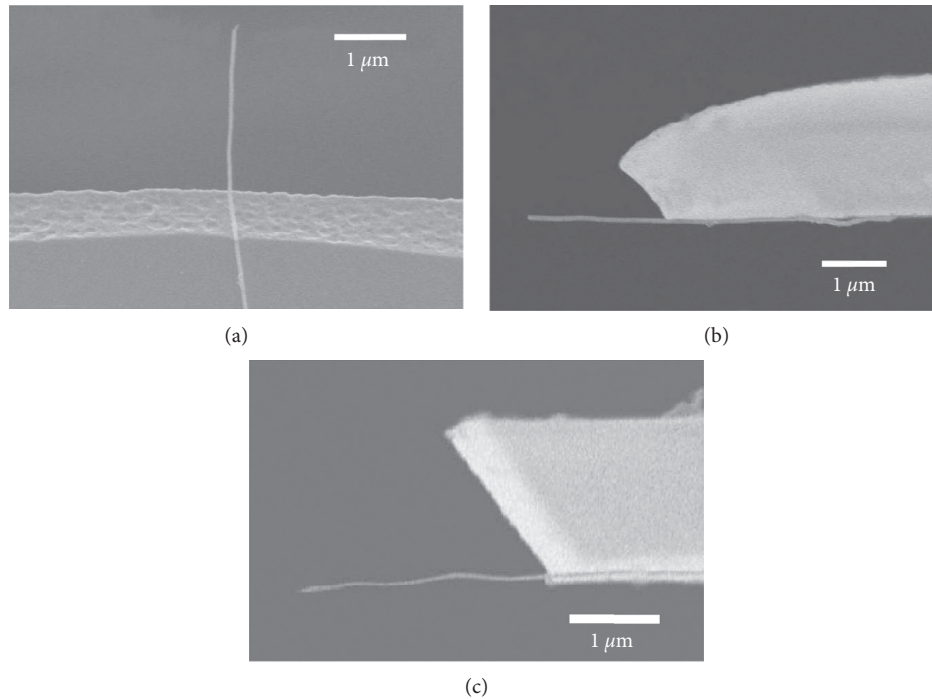


FIGURE 6: Scanning electron microscopy images of the (a) bottom and (b) side of a peeling atomic force microscope probe with a length of $2.2\ \mu\text{m}$ and of the (c) side of a peeling atomic force microscope probe with a length of $2.5\ \mu\text{m}$. The individual carbon nanotube used to attach such probes is $10 \pm 2\ \text{nm}$ in inner diameter and $40 \pm 6\ \text{nm}$ in outer diameter, respectively (adapted with permission from reference [104]; copyright 2009, Elsevier Ltd).

and dispersion of carbon nanotubes, interfacial load transfer, and interfacial interaction characteristics [135–140]. Such interactions are usually reflected by a shift in Raman frequency or a peak width change [91, 141]. However, there are some disadvantages associated with this spectroscopic technique [135–140]. For example, since the diameter of the Raman laser spot is much larger than that of an individual carbon nanotube, the Raman signal is averaged over carbon nanotubes in all directions [91, 141].

Earlier publications associated a shift in Raman frequency to a lower frequency or to a higher frequency from the peak about $2700\ \text{cm}^{-1}$ with tensile strain and compressive strain in a carbon nanotube-reinforced polymer nanocomposite [64, 142]. Ruan et al. [143, 144] monitored load transfer across the interface from an ultrahigh molecular weight polyethylene matrix to multiwalled carbon nanotubes, with a shift in Raman frequency at $2691\ \text{cm}^{-1}$. They also suggested four regimes of strain behavior, as outlined in Table 1. Another work [145] related a shift in Raman frequency at $1594\ \text{cm}^{-1}$ with the compressive strain in single-walled carbon nanotubes embedded in an epoxy matrix.

3. Interactions at the Interface

It is of great significance to understand the interactions at the interface [146–149]. Knowledge of such interactions is necessary to gain insight into the properties of the nanocomposites [146]. An optimum interfacial interaction is a critical step in achieving the full potential of carbon nanotubes [147], which has become a primary goal of this emerging area of research [146–149].

Chemical functionalization of carbon nanotubes has proved effective in improving the characteristics of interfacial interactions and the performance of the resulting nanocomposites [150–153]. Chemical functionalization of carbon nanotubes, such as wrapping of polymer around carbon nanotubes [154], as illustrated schematically in Figure 7, or introducing covalent interfacial bonding [155], has been achieved. In general, covalent and noncovalent interfacial interactions [156–159] are the two main chemical functionalization methods.

3.1. Covalent Interactions. Covalent chemical functionalization of carbon nanotubes involves the covalent attachment of functional groups onto either the sidewalls or ends of carbon nanotubes [160, 161]. The open ends of carbon nanotubes can be stabilized by hydroxide and carboxylic acid groups, and the sidewalls of carbon nanotubes can be chemically modified by reactive elements [42]. For example, nitric acid treatment was reported to successfully oxidize the surface of carbon nanotubes as detected by Fourier transform infrared spectroscopy [162, 163]. Covalent chemical functionalization of carbon nanotubes can also be accomplished through diazonium salts [164] or Diels–Alder reactions [165].

Recently, an extensive review of various covalent functionalization methods of nanoparticles by means of tailoring surface properties to improve their wettability and compatibility with polymer matrices has been made by Mosnáčková et al. [166]. Different methods of surface modification by polymer chains have been described in

TABLE 1: Shift in Raman frequency (2691 cm^{-1}) as a function of the tensile strain applied to an ultrahigh molecular weight polyethylene nanocomposite reinforced with multiwalled carbon nanotubes.

Regime*	Tensile strain	Shift	Interpretation
Regime (i): elastic region	0–1%	Clear shift to a lower frequency	Elastic response; tensile loading of multiwalled carbon nanotubes
Regime (ii): viscoelastic and plastic deformation occurs	1–10%	Much less apparent shift to a lower frequency	Slip and stick at the interface
Regime (iii): strain hardening occurs	10–15%	Somewhat more apparent shift to a lower frequency	Multiwalled carbon nanotube knots preventing further stretching of the chain of the polymer; tensile loading of multiwalled carbon nanotubes
Regime (iv): partial failure occurs in the polymer matrix at the microscopic level	Larger than 15%	Shift to a higher frequency	Elastic recovery from local failure occurred in the polymer matrix; compressive loading of multiwalled carbon nanotubes

*Four regimes of behavior are available for a shift in Raman frequency when different tensile strains are applied to an ultrahigh molecular weight polyethylene nanocomposite reinforced with multiwalled carbon nanotubes. Interpretation of data is available in reference [143].

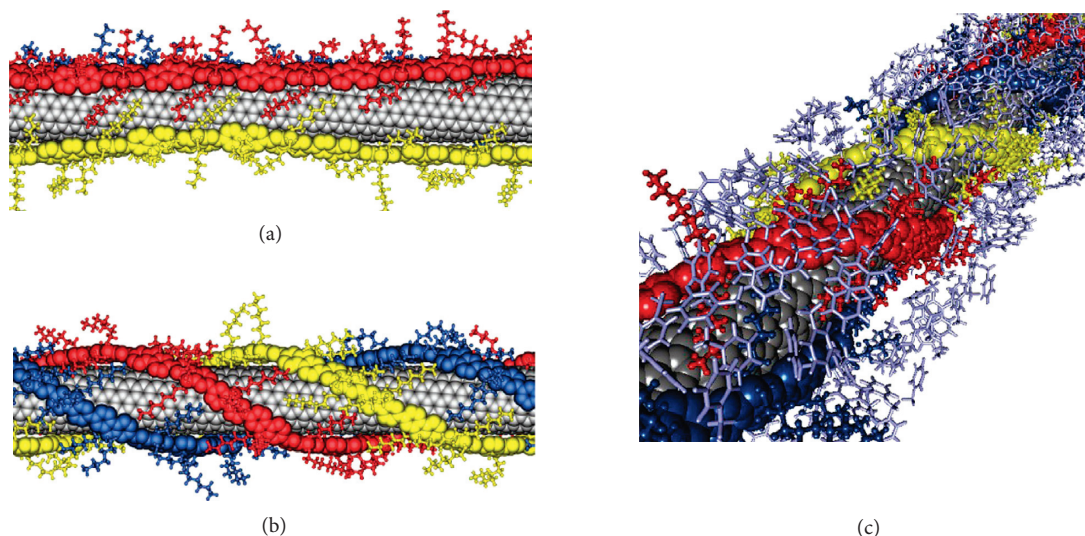


FIGURE 7: Single-walled carbon nanotube wrapped by three poly(9,9-dioctylfluorenyl-2,7-diyl) chains with different geometries: (a) polymer chains aligned to the axis of the carbon nanotube and (b) periodic helical conformation. The polymer chains are represented by different colors: red, blue, and yellow. (c) The side chains of the polymer covered by the solvent system that contains enough toluene molecules. The toluene molecules are represented by light gray (adapted with permission from reference [154]; copyright 2011, American Chemical Society).

detail with some examples of functionalization of various types of nanoparticles to obtain advanced properties of polymer nanocomposites. Various polymerization mechanisms have been discussed in detail. The current state of various grafting methods has also been summarized. The effect of introduced functional groups on the properties of carbon nanotubes and polymer nanocomposites has recently been reviewed by Wei et al. [167].

Covalent functionalization can enhance the interactions at the interface effectively, making it possible to significantly improve the performance of the resulting nanocomposites [16, 42, 49]. Gojny et al. [168, 169] gave direct evidence of significant interactions existed at the interface, as illustrated

in Figure 8. Amino acids were successfully used to modify carbon nanotubes by heating the oxidized carbon nanotubes with excess triethylenetetramine. Their works clearly demonstrated that a covalent bond was formed at the interface through introducing functional groups [168, 169]. The chemically modified carbon nanotubes were completely covered with an epoxy matrix, as indicated by the transmission electron microscope images of functionalized carbon nanotubes in the polymer matrix in Figure 8. Upon the expansion of the crack formed in the polymer matrix heated by a beam of electrons from a transmission electron microscope, the outer layer of an individual, functionalized multiwalled carbon nanotube was fractured and embedded

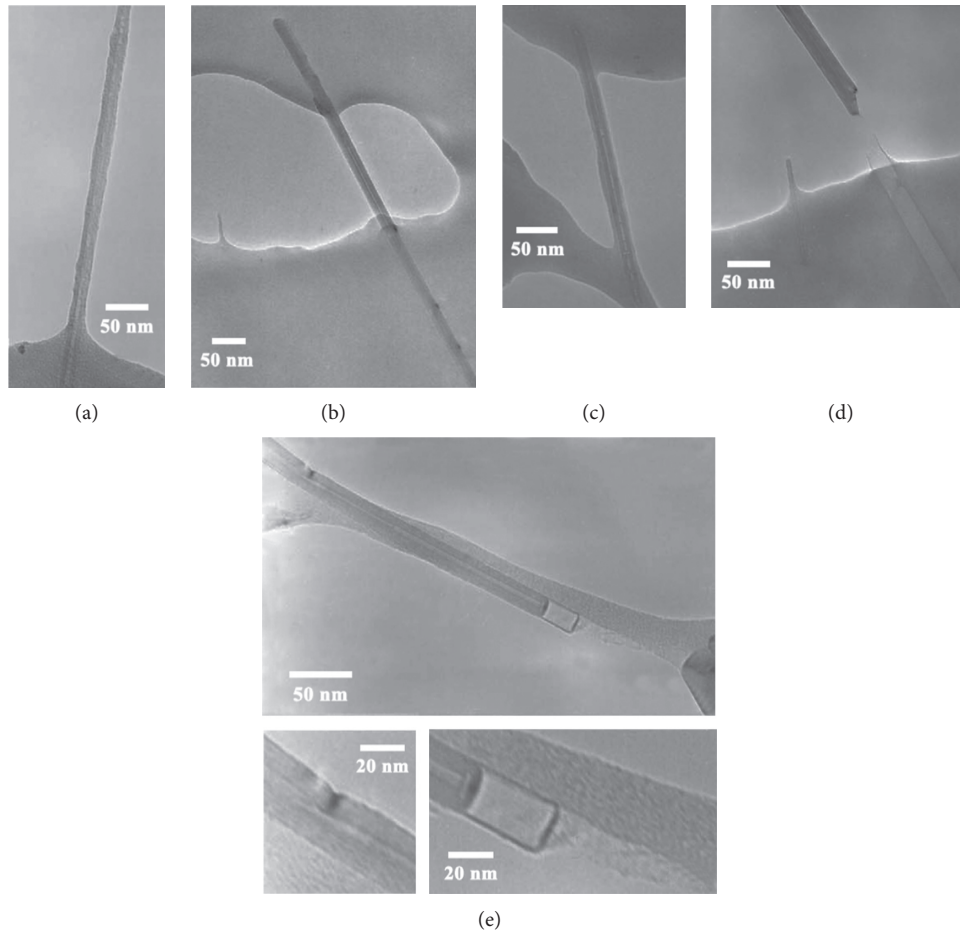


FIGURE 8: Transmission electron microscope images of an individual, functionalized multiwalled carbon nanotube in an epoxy matrix. (a) Chemically modified carbon nanotube covered by the polymer matrix completely, indicating improved interactions at the interface through a covalent chemical functionalization method. (b and c) Fracture toughness improved by such carbon nanotubes through bridging microcracks and pores in the polymer matrix. (d and e) Evidence of improved interactions at the interface through pull-out tests (adapted with permission from references [168, 169]; copyrights 2003 and 2004, Elsevier Ltd).

in an epoxy matrix, as shown in Figure 8(d). In contrast, the inner shells of the functionalized multiwalled carbon nanotube, which were bounded together by the relatively weak van der Waals forces between these shells, were pulled out from the polymer matrix through a sword-in-sheath mechanism [168, 169].

Covalent chemical functionalization has been proved to be an effective way for improving the properties of the interface [168, 169], such as the efficiency of interfacial load transfer, making it possible to significantly improve the properties of carbon nanotube-reinforced polymer nanocomposites [168, 169]. However, this functionalization method would introduce structural defects into the surface of carbon nanotubes, thus lowering their intrinsic properties [170, 171]. As a consequence, there is often a tradeoff between the properties of carbon nanotubes and those of the interface. In addition, covalent functionalization may cause severe disruption of the electronic network and structure of carbon nanotubes [170, 171], which may lead to decreased performance of the final nanocomposites.

3.2. Noncovalent Interactions. Alternatively, noncovalent functionalization of carbon nanotubes can serve to improve the properties of the interface. This functionalization method utilizes $\pi-\pi$ interactions and van der Waals forces by adsorption of polymers [172–175]. Noncovalent functionalization of carbon nanotubes is particularly attractive, since it does not deteriorate their intrinsic properties [176–179]. This functionalization method mainly involves the polymer wrapping of carbon nanotubes. Wrapping is typically denoted as the enveloping of the surface of carbon nanotubes by polymers. Three possible multihelical wrapping conformations can be found in the work of O’Connell et al. [175], as shown in Figure 9. Recent studies demonstrated that single-walled carbon nanotubes can be wrapped in a number of adsorbing polymers, such as biopolymers such as DNA [180, 181], block copolymers [182, 183], and semiconjugated polymers [184, 185].

Polymer wrapping of carbon nanotubes has proven to be quite effective in improving the properties of the interface, making it possible to greatly improve the properties of

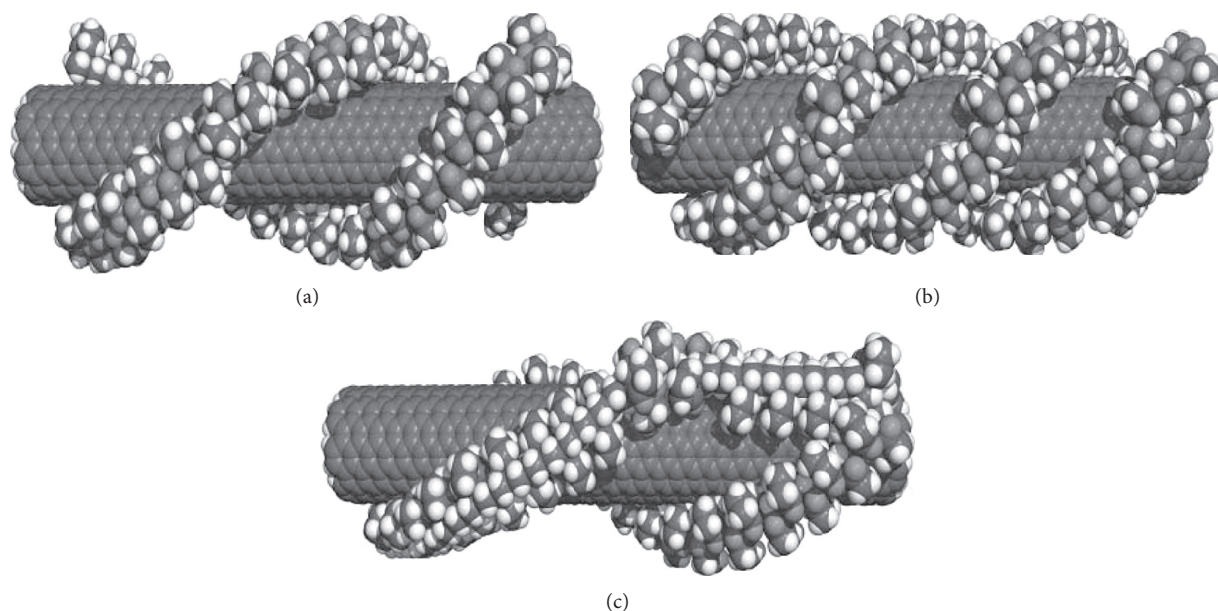


FIGURE 9: Three possible multihelical wrapping conformations of polyvinyl pyrrolidone around an individual single-walled carbon nanotube. (a) A double helix and (b) a triple helix. (c) Backbone bond rotations can cause a sharp bend, which allows multiple parallel wrapping strands to come from the same chain of the linear polymer. Low-backbone strain with high-surface area coverage is allowed for multihelical wrapping (adapted with permission from reference [175]; copyright 2001, Elsevier Ltd).

carbon nanotube-reinforced polymer nanocomposites [186, 187]. For example, interfacial interactions can be significantly improved by using conjugated polymers with a specific molecular configuration [187]. Yang et al. [187] utilized molecular dynamics to investigate the physical interactions at the interface for different polymer matrices. Their modeling work suggested that polymers with a main chain containing aromatic functionalities hold great promise for the noncovalent binding of carbon nanotubes into the structure of the nanocomposites, as shown in Figure 10, since these aromatic rings are able to provide strong interactions at the interface. Such polymers could serve as a building block for amphiphilic copolymers not only to enhance the interactions at the interface but also to improve the mechanical performance of the resulting nanocomposites. Polymer wrapping of carbon nanotubes also holds great promise for the manipulation and organization of carbon nanotubes into ordered structures and even for their noncovalent functionalization [187].

Unfortunately, the possible mechanisms underlying the noncovalent interactions have not yet been fully understood [146]. It has been found that wrapping of single-walled carbon nanotubes by polymers is a general interfacial phenomenon [175]. Furthermore, recent molecular dynamics studies suggested that such interactions depend strongly on the specific structure of polymer matrices, and the effect of polymer affinity and flexibility is important [188–193]. For example, stiff-chain polymers tend to wrap around single-walled carbon nanotubes in a more distinct conformation than polymers with a high degree of flexibility in the backbone structure [188, 189], as shown in Figure 11, making it possible to improve the interfacial properties, such

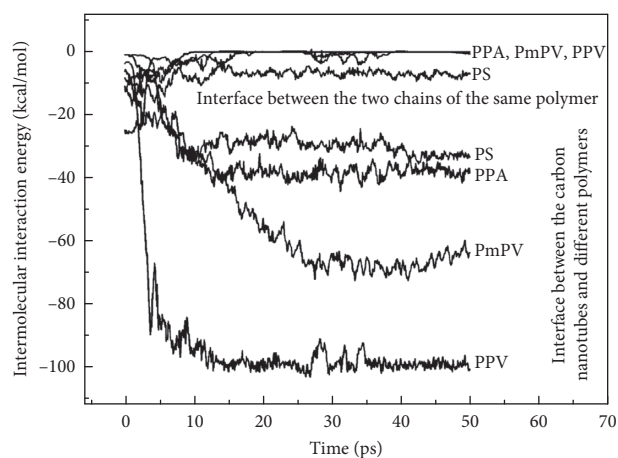


FIGURE 10: Time evolution of the intermolecular interaction energy at the interface between single-walled carbon nanotubes and different polymer matrices as well as between the two chains of the same polymer during the wrapping procedure for polystyrene (PS), poly(*p*-phenylenevinylene) (PPV), poly(*m*-phenylenevinylene-co-2,5-dioctyloxy-*p*-phenylenevinylene) (PmPV), and poly(phenylacetylene) (PPA) (adapted with permission from reference [187]; copyright 2005, American Chemical Society).

as the intermolecular interaction energy at the interface, for the resulting nanocomposites.

Noncovalent functionalization offers a number of advantages for improving the properties of the interface and the performance of the resulting nanocomposites, without affecting the intrinsic properties of carbon nanotubes [194–197]. However, it is often difficult to achieve the

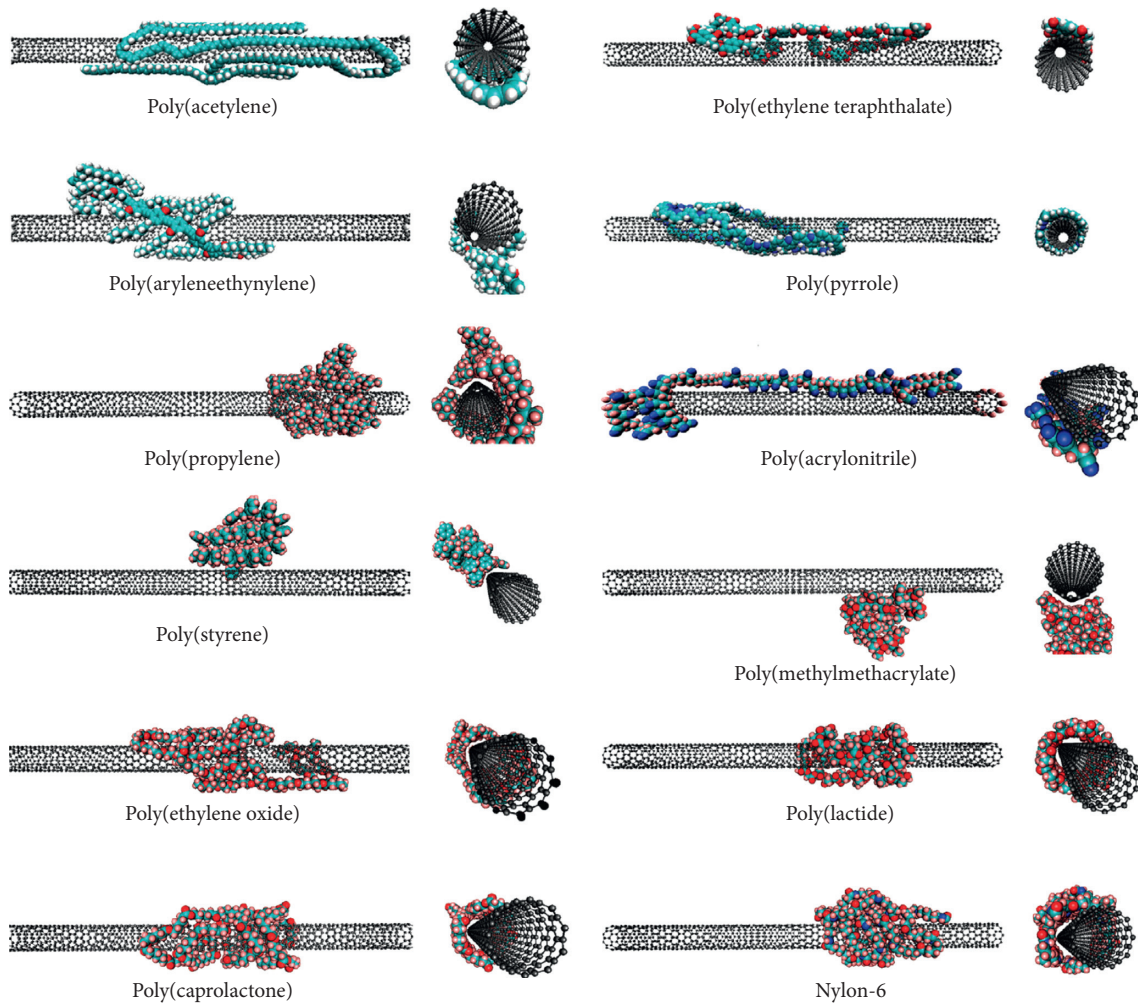


FIGURE 11: Possible wrapping conformations obtained from a model used to illustrate potential interactions at the interface between single-walled carbon nanotubes and different polymer matrices at the 3.2 ns time step in molecular dynamics simulations. The polymers have different degrees of flexibility in the structure of their respective backbone (adapted with permission from references [188, 189]; copyright 2010, American Chemical Society).

desirable strength of the interface so as to ensure the load transfer across the interface with high efficiency for carbon nanotube-reinforced nanocomposites [198–201].

4. Characterization of Interfacial Mechanical Properties

The nature of the interface is of particular importance to the interfacial stress transfer and the consequent improvement in the mechanical properties for the nanocomposites [202, 203]. For example, good interfacial bonding is necessary to ensure the load transfer across the interface with high efficiency, which is a necessary condition for further development of the nanocomposites with high mechanical performance [204, 205]. Over the past few decades, it has become increasingly clear that considerable modification of the properties of the interface can be an effective way to improve the overall mechanical performance for the nanocomposites [206–209].

The work of Wong et al. [204] has shown that the interfacial shear stress measured for multiwalled carbon nanotube-reinforced polymer nanocomposites is larger than that measured for conventional microfiber-reinforced composites by orders of magnitude. Furthermore, there were no broken carbon nanotubes based on an analysis of the interfacial morphology measured by both transmission electron microscopy and scanning electron microscopy for carbon nanotube-reinforced epoxy nanocomposites [204], indicating that the load transfer across the interface was not sufficient to fracture the multiwalled carbon nanotubes. In contrast, recent experiments have demonstrated that the failure of multiwalled carbon nanotube-reinforced polymer nanocomposites appears to arise from mechanical fracture of the polymer matrix and from the pull-out of such carbon nanotubes from the polymer matrix [106, 210, 211].

Qian et al. [212] characterized the properties of the polystyrene nanocomposites reinforced with multiwalled carbon nanotubes to investigate the behavior of the load transfer across the interface and deformation mechanisms of

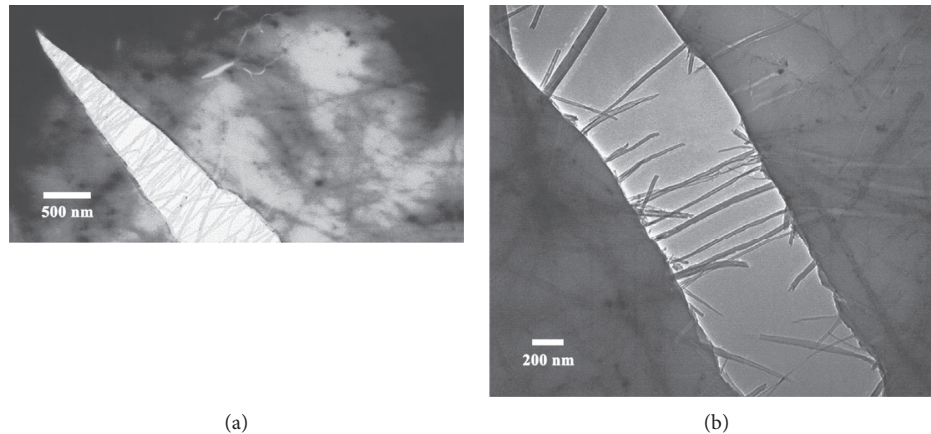


FIGURE 12: *In situ* transmission electron microscopy images of crack nucleation and propagation induced by thermal stresses in a polystyrene thin film reinforced with multiwalled carbon nanotubes. (a) Such a crack propagates along relatively low density regions of carbon nanotubes or along weak interfaces. (b) The multiwalled carbon nanotubes tend to align and bridge the crack wake, and subsequently to break and/or pull out from the polymer matrix (adapted with permission from reference [212]; copyright 2000, American Institute of Physics).

the nanocomposites. *Ex situ* mechanical tensile tests on films of the nanocomposites shown that after adding 1.0% by weight of carbon nanotubes, the tensile strength is improved by about 25.0% and the elastic stiffness is increased by about 36–42%, indicating that there are considerable load transfer across the interface and significant improvement in the mechanical performance of the polymer. In this context, an external load can be transferred from the polymer matrix to carbon nanotubes effectively. Furthermore, *in situ* transmission electron microscopy provided essential information about the interfacial bonding and deformation mechanisms of the nanocomposites described above, as illustrated in Figure 12. As for commercial carbon fiber-reinforced polymer composites, a fracture of carbon nanotubes and crack bridging by carbon nanotubes were observed during pull-out tests. In contrast, multiwalled carbon nanotubes pulled out from the polymer matrix, while less fracture was observed, as shown in Figure 12. Furthermore, there are strong interactions at the interface [212], as evidenced by the significant improvement in the mechanical performance of the nanocomposites given above. Qian et al. [212] also demonstrated that 10% by weight of carbon fibers in the previous work of Tibbetts and McHugh [213] was required to achieve the same effectiveness of the improvement in the elastic modulus of the nanocomposites containing only 1.0% by weight of multiwalled carbon nanotubes by utilizing short-fiber composite theory.

The force required to pull an individual multiwalled carbon nanotube out from a polyethylenebutene matrix was measured by atomic force microscopy [103]. The mean interfacial shear strength of 47 MPa was sufficiently high, indicating that there exists covalent bonding at the interface. Furthermore, the chain of the polymer close to the interface behaved differently from its bulk. A sheathing layer of a polymer on pulled out multiwalled carbon nanotubes, i.e., an interfacial region, was imaged [107], as shown in Figure 13, which gave direct evidence of significant interfacial interactions. In addition, an additional increase was observed in the diameter of the polymer sheathing layer after chemical functionalization of carbon

nanotubes, possibly indicating chemical augmentation of interfacial bonding. Chemically functionalized carbon nanotubes could improve the interactions at the interface [214, 215]. Orders of magnitude improvement in interfacial shear strength would be required to achieve more efficient reinforcement for the nanocomposites [216]. While optimization of the interfacial properties for the mechanical reinforcement is still poorly understood at the nanoscale, the recent evidence available clearly suggests that chemical functionalization can be effective for such reinforcement [217], as shown in Figure 14, and this method appears to be a major focus of improvement in the performance of the nanocomposites.

Strong interfacial interactions are usually necessary to ensure successful stress transfer across such an interface. An effective strategy for the improvement in the interactions at the interface is chemical functionalization by which polymer chains are attached onto the surface of carbon nanotubes. However, the unique mechanical performance of carbon nanotubes is dependent on their specific chemical structure [218, 219]. Covalent functionalization would introduce internal stresses and atomic defects into the surface of carbon nanotubes [220, 221], thereby deteriorating their inherent mechanical properties. On the other hand, noncovalent functionalization offers an alternative strategy for regulating the properties of the interface [222, 223]. Such a strategy does retain the intrinsic properties of carbon nanotubes, but, unfortunately, interfacial stress transfer might not be so effective in the treatment for the nanocomposites. It is usually difficult for this modification strategy to improve the interfacial properties efficiently [224, 225], and considerable improvements remain to be exploited.

5. Characterization of Interfacial Thermal Properties

The thermal resistance of the interface, also known as Kapitza resistance, plays an important role in determining

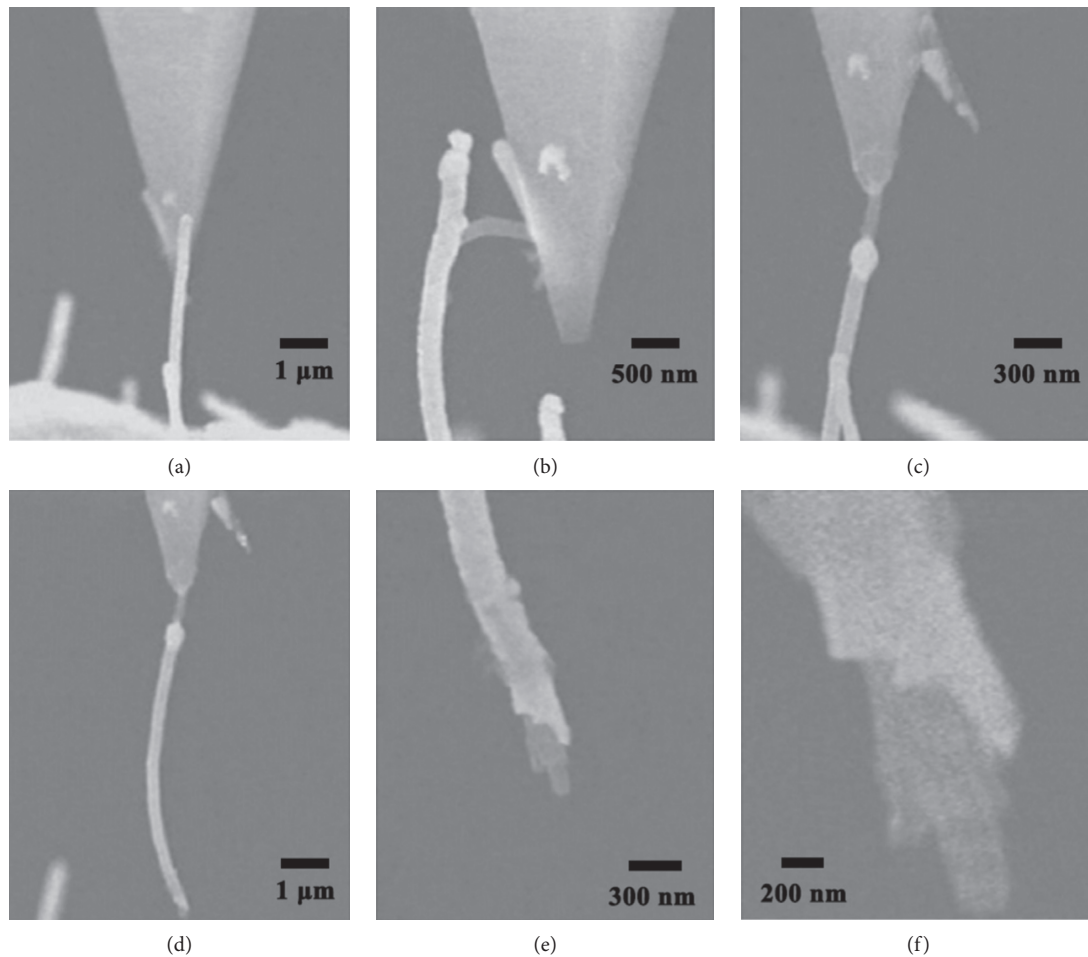


FIGURE 13: Direct evidence of multiple polymer sheathing layers in a polycarbonate nanocomposite reinforced with multiwalled carbon nanotubes, confirmed by the nanomanipulation contact experiments carried out under a scanning electron microscope. (a) Initial contact with an individual, protruding multiwalled carbon nanotube by a tip of the cantilever of an atomic force microscope. (b) The inner structure of the nanocomposite has become detached partially from the outer polymer sheathing layer in the process of bending. (c) Such a structure is clamped to a tip of the cantilever of an atomic force microscope by electron beam-induced deposition, and the outer polymer sheathing layer balls up. (d) The inner structure has been broken close to the fracture surface of the nanocomposite during tensile loading. (e) The fracture broken end of the coated multiwalled carbon nanotube provides clear evidence of a double polymer sheathing layer. (f) Higher magnification image of the fracture broken end of the coated multiwalled carbon nanotube (adapted with permission from reference [107]; Copyright 2003, American Chemical Society).

the thermal properties of the nanocomposites [226, 227]. The interfacial thermal resistance has been investigated both experimentally and theoretically [228–237]. The recent results measured and predicted for the interfacial thermal resistance of the nanocomposites are summarized in Table 2. Such resistance is typically on the order of magnitude of $10^{-8} \text{ m}^2 \cdot \text{K}/\text{W}$.

Since transport of heat in carbon nanotube-reinforced polymer nanocomposites is by way of elastic vibrations of the lattice, heat transfer based on this mechanism is limited by the elastic scattering of acoustic phonons at lattice defects [238, 239]. As a consequence, the interfacial thermal resistance is caused by the scattering of acoustic phonons across the interface [238, 239]. It is therefore of great significance to gain insight into such a thermal property for the nanocomposites, making it possible to further improve their overall thermal

performance [53, 54]. To address issues associated with the interfacial thermal resistance, it is usually necessary to use the method of molecular dynamics simulations to understand the interfacial thermal resistance and to evaluate the benefits and disadvantages associated with new ways to reduce such resistance [227, 229, 231].

Large thermal resistance at the interface has emerged as a significant challenge, and such a technical issue has not been addressed yet. Much effort has been devoted to estimate the interfacial thermal resistance [227], as well as to evaluate the effect of chemical functionalization and the role of interfacial interactions [240, 241]. Unfortunately, the influence of interfacial properties on the thermal conductivity of the nanocomposites has not yet been fully understood. Chemically functionalized multiwalled carbon nanotubes were found to have the potential to realize carbon nanotube-

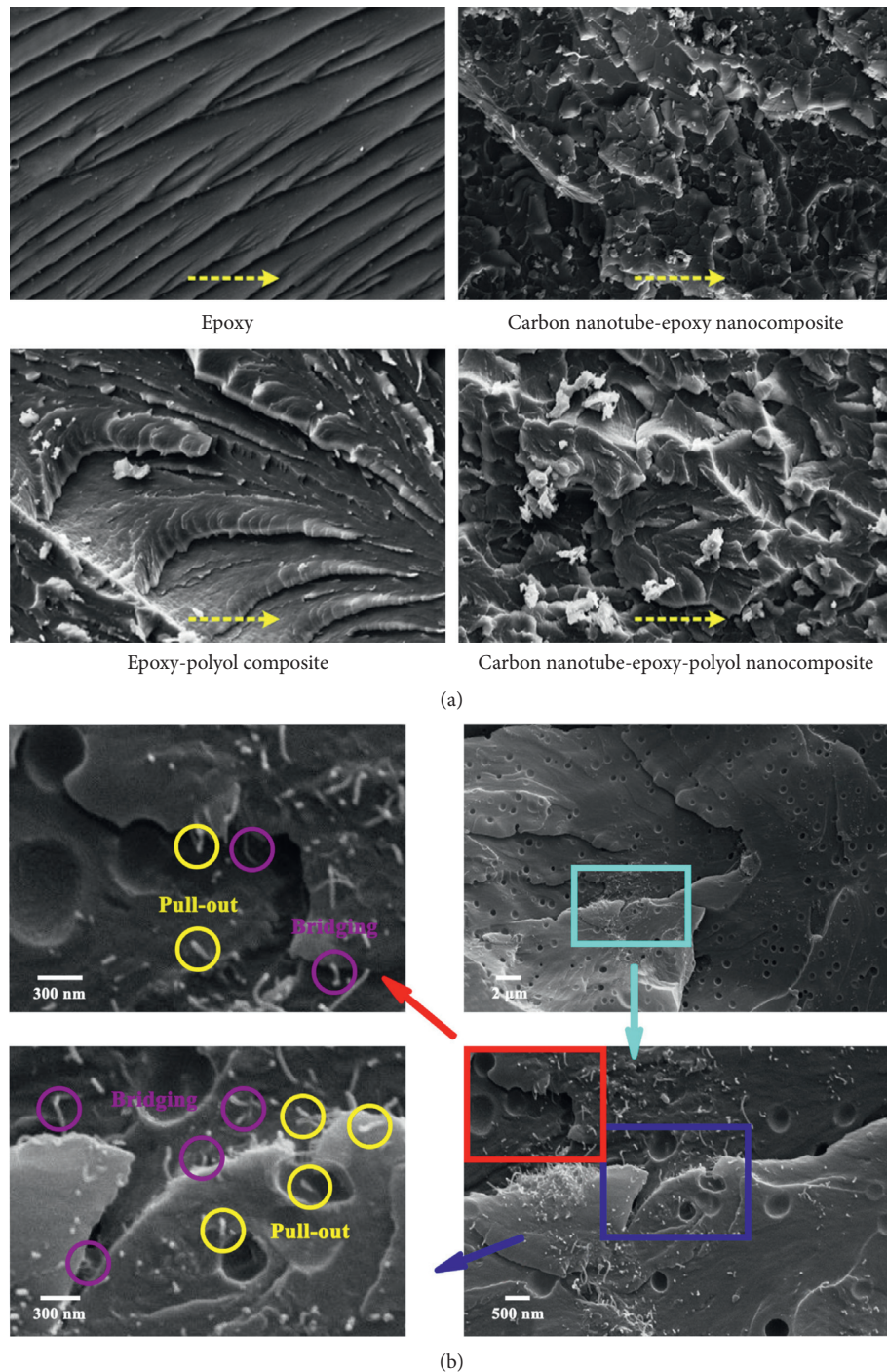


FIGURE 14: (a) Morphology of the quasistatically fractured surfaces characterized by a scanning electron microscope for neat epoxy and chemically modified epoxy composites. (b) Morphology of the quasistatic fracture surface characterized by a scanning electron microscope for an epoxy-polyol hybrid nanocomposite reinforced with multiwalled carbon nanotubes, illustrating a bridging phenomenon as well as the pull-out process of multiwalled carbon nanotubes from the polymer matrix (adapted with permission from reference [217]; copyright 2014, Elsevier Ltd).

reinforced polymer nanocomposites with improved thermal properties because this type of carbon nanotubes can provide unique structure advantages [240, 241].

Covalent functionalization of carbon nanotubes have proven to be very effective in improving the interfacial thermal conductance for carbon nanotube-reinforced polymer nanocomposites [242, 243], eventually leading to

their improved overall thermal performance [228]. For example, a significant improvement in interfacial thermal conductance was reported as large as one order of magnitude for the nanocomposites by means of this chemical method [229]. Molecular dynamics simulations can serve as a powerful tool to explore the effect of covalent functionalization of carbon nanotubes on the thermal properties of the

TABLE 2: Thermal resistance of the interface in carbon nanotube-reinforced polymer nanocomposites.

Nanocomposites	Interfacial thermal resistance	Method	Reference
Carbon nanotube-octane	$3.3 \times 10^{-8} \text{ m}^2 \cdot \text{K/W}$	Simulation	[226]
Carbon nanotube-octane	$4.0 \times 10^{-8} \text{ m}^2 \cdot \text{K/W}$	Simulation	[227]
Carbon nanotube-EVA*	$(0.2-9.6) \times 10^{-8} \text{ m}^2 \cdot \text{K/W}$	Simulation	[229]
Carbon nanotube-epoxy	$(0.24-2.6) \times 10^{-8} \text{ m}^2 \cdot \text{K/W}$	Experimental	[230]
Carbon nanotube-epoxy	$(0.77-2.5) \times 10^{-8} \text{ m}^2 \cdot \text{K/W}$	Simulation	[231]
Carbon nanotube-polyimide	$1.58 \times 10^{-8} \text{ m}^2 \cdot \text{K/W}$	Theoretical	[232]

*EVA: poly(ethylene vinyl acetate).

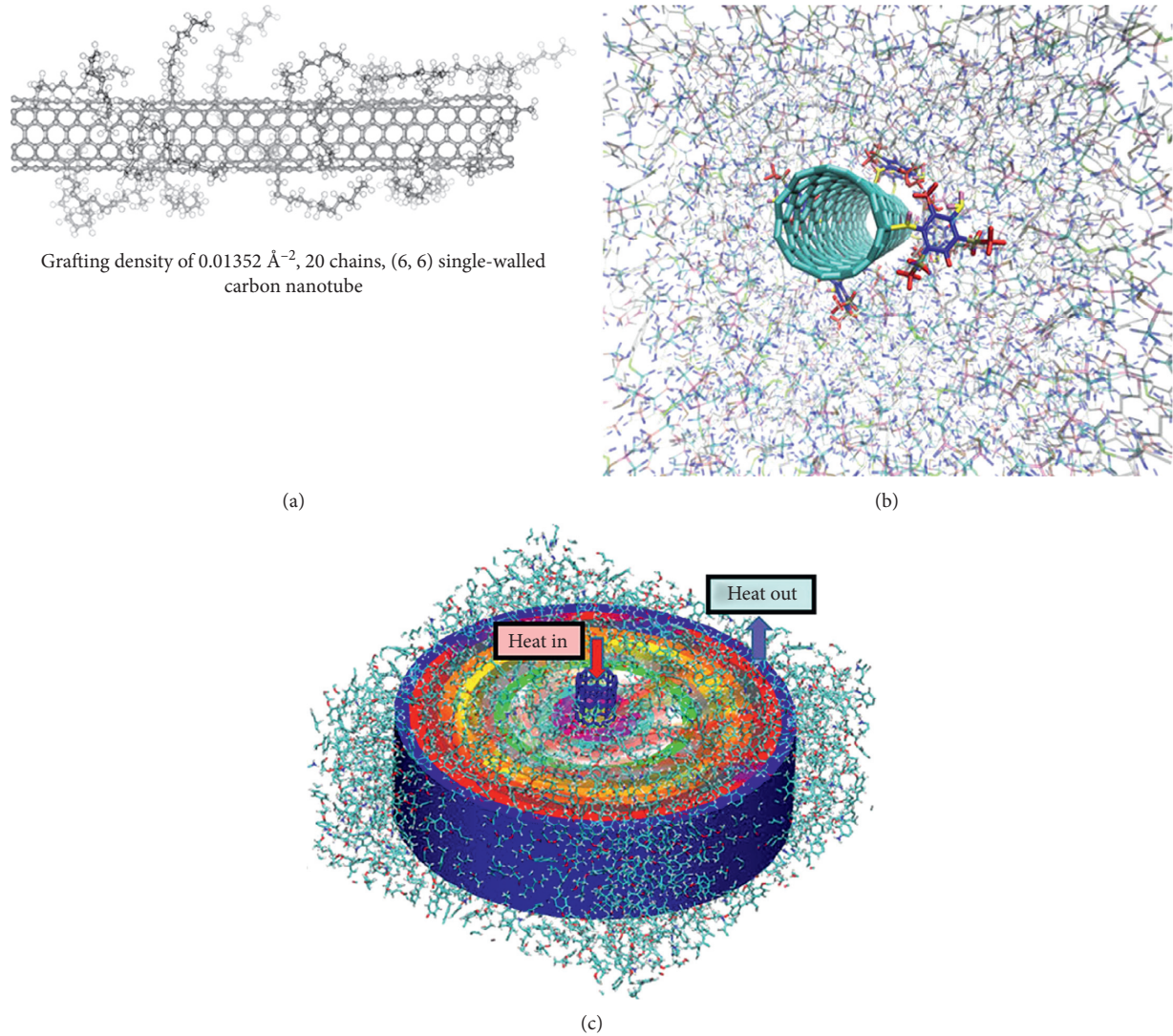


FIGURE 15: (a) An individual single-walled carbon nanotube with short end-grafted chains. (b) Schematic diagram of an individual single-walled carbon nanotube functionalized with crosslinker diethylenetriamine and embedded in an epoxy matrix. Carbon nanotubes are rendered in cyan. The color scheme for the functionalized diethylenetriamine molecule (red: hydrogen and carbon atoms contained in methyl groups, yellow: nitrogen atoms, and blue: carbon atoms contained in benzene rings). (c) Schematic diagram of a single-walled carbon nanotube-epoxy nanocomposite with different interfacial thicknesses. The nanocomposite exists in an epoxy environment, with the carbon nanotube as heat source and the interfacial region close to the polymer matrix as heat sink (adapted with permission from references [229, 231]; copyright 2006, Elsevier Ltd. Copyright 2012, TMS).

resulting nanocomposites [229, 231], as particularly well illustrated in Figure 15. Covalent functionalization can significantly improve the overall thermal performance for carbon nanotube-reinforced polymer nanocomposites due

to a great increase in the thermal conductance of the interface [229, 231]. However, excessive chemical functionalization will damage the intrinsic thermal properties of carbon nanotubes [244–247].

6. Concluding Remarks

Characterization is a fundamental process in the field of materials science, without which no scientific understanding of engineering materials could be ascertained. Characterization of the interface in carbon nanotube-reinforced polymer nanocomposites has been reviewed. Special emphasis is placed on how to determine the properties of the interface at the nanometer scale.

Tremendous research efforts are ongoing to characterize the properties of the interface in the polymer community. The state of research on the chemical functionalization of carbon nanotubes has been presented, followed by considerable details given over to the mechanical and thermal properties being pursued or envisioned in this emerging area. Various emerging characterization techniques used to determine the microscopic structure and properties of the interface are summarized.

New characterization techniques and methodologies are constantly emerging. In particular, the advent of atomic force microscopy in recent decades has revolutionized the field of carbon nanotube-reinforced polymer nanocomposites, allowing the imaging and analysis of the structures of the interface on much smaller scales than was previously possible, resulting in a significant increase in the level of understanding as to why different carbon nanotube-polymer interfaces show different bulk properties and behaviors. Atomic force microscopy can be combined with a variety of optical microscopy and spectroscopy techniques, thus further expanding its applicability.

Progress towards carbon nanotube-reinforced polymer nanocomposites will require continued development of characterization techniques, providing potential for tailoring the properties of the interface. The characteristic scale of the carbon nanotube reinforcement presents significant challenges to the development of methods for characterizing the properties of the interface. To address the issues associated with interfacial properties, it will be essential to understand the critical nature of the interface, develop accurate nanomechanics-based models, elucidate the interactions at the interface, and acquire knowledge of the relationship between nanocomposite properties and interfacial optimization, aiming at improving the performance of the nanocomposites effectively.

Carbon nanotubes pose both tremendous opportunities and significant new challenges for the development of fundamentally new polymer-based nanocomposites. Understanding the essence of the nanometer-scale reinforcement mechanism for the nanocomposites certainly warrants further experimental and theoretical research. Multidisciplinary research efforts will be required to bridge the gap in the existing knowledge between technological developments and fundamental understanding. There has never been a more exciting time to be involved in the field with new fundamental discoveries to be made regularly. It is hoped that this review would contribute to the development of this emerging area in some small way and would stimulate new research enthusiasm to enrich the content of an increasingly exciting discipline.

Conflicts of Interest

The authors declare that they have no conflicts of interest.

Acknowledgments

This work was supported by the National Natural Science Foundation of China (no. 51506048).

References

- [1] S. Iijima, "Helical microtubules of graphitic carbon," *Nature*, vol. 354, no. 6348, pp. 56–58, 1991.
- [2] S. Iijima and T. Ichihashi, "Single-shell carbon nanotubes of 1-nm diameter," *Nature*, vol. 363, no. 6430, pp. 603–605, 1993.
- [3] D. S. Bethune, C. H. Kiang, M. S. de Vries et al., "Cobalt-catalysed growth of carbon nanotubes with single-atomic-layer walls," *Nature*, vol. 363, no. 6430, pp. 605–607, 1993.
- [4] K. Tanaka and S. Iijima, *Carbon Nanotubes and Grapheme*, Elsevier Ltd., Amsterdam, Netherlands, 2nd edition, 2014.
- [5] K. M. Liew, M. F. Kai, and L. W. Zhang, "Carbon nanotube reinforced cementitious composites: an overview," *Composites Part A: Applied Science and Manufacturing*, vol. 91, no. 1, pp. 301–323, 2016.
- [6] R. Bhatia, K. Kumari, R. Rani, A. Suri, U. Pahuja, and D. Singh, "A critical review of experimental results on low temperature charge transport in carbon nanotubes based composites," *Reviews in Physics*, vol. 3, pp. 15–25, 2018.
- [7] D. Janas and B. Liszka, "Copper matrix nanocomposites based on carbon nanotubes or graphene," *Materials Chemistry Frontiers*, vol. 2, no. 1, pp. 22–35, 2018.
- [8] D. R. Paul and L. M. Robeson, "Polymer nanotechnology: nanocomposites," *Polymer*, vol. 49, no. 15, pp. 3187–3204, 2008.
- [9] D. Han, H. Mei, S. Xiao, K. G. Dassios, and L. Cheng, "A review on the processing technologies of carbon nanotube/silicon carbide composites," *Journal of the European Ceramic Society*, vol. 38, no. 11, pp. 3695–3708, 2018.
- [10] A. Azarniya, A. Azarniya, S. Sovizi et al., "Physicomechanical properties of spark plasma sintered carbon nanotube-reinforced metal matrix nanocomposites," *Progress in Materials Science*, vol. 90, pp. 276–324, 2017.
- [11] M. Ding, Y. Tang, and A. Star, "Understanding interfaces in metal-graphitic hybrid nanostructures," *Journal of Physical Chemistry Letters*, vol. 4, no. 1, pp. 147–160, 2013.
- [12] G. A. Rance, D. H. Marsh, S. J. Bourne, T. J. Reade, and A. N. Khlobystov, "van der Waals interactions between nanotubes and nanoparticles for controlled assembly of composite nanostructures," *ACS Nano*, vol. 4, no. 8, pp. 4920–4928, 2010.
- [13] Z. P. Michael, W. Shao, D. C. Sorescu, R. W. Euler, S. C. Burkert, and A. Star, "Probing biomolecular interactions with gold nanoparticle-decorated single-walled carbon nanotubes," *Journal of Physical Chemistry C*, vol. 121, no. 38, pp. 20813–20820, 2017.
- [14] K. Bhattacharya, S. P. Mukherjee, A. Gallud et al., "Biological interactions of carbon-based nanomaterials: from coronation to degradation," *Nanomedicine: Nanotechnology, Biology and Medicine*, vol. 12, no. 2, pp. 333–351, 2016.
- [15] J. Gao, B. Zhao, M. E. Itkis et al., "Chemical engineering of the single-walled carbon nanotube-nylon 6 interface," *Journal of the American Chemical Society*, vol. 128, no. 23, pp. 7492–7496, 2006.

- [16] Y. Ni, H. Han, S. Volz, and T. Dumitrică, “Nanoscale azide polymer functionalization: a robust solution for suppressing the carbon nanotube-polymer matrix thermal interface resistance,” *Journal of Physical Chemistry C*, vol. 119, no. 22, pp. 12193–12198, 2015.
- [17] E. T. Thostenson, C. Li, and T.-W. Chou, “Nanocomposites in context,” *Composites Science and Technology*, vol. 65, no. 3-4, pp. 491–516, 2005.
- [18] E. T. Thostenson, W. Z. Li, D. Z. Wang, Z. F. Ren, and T. W. Chou, “Carbon nanotube/carbon fiber hybrid multiscale composites,” *Journal of Applied Physics*, vol. 91, no. 9, pp. 6034–6037, 2002.
- [19] A. Alshaghel, S. Parveen, S. Rana, and R. Fanguero, “Effect of multiscale reinforcement on the mechanical properties and microstructure of microcrystalline cellulose-carbon nanotube reinforced cementitious composites,” *Composites Part B: Engineering*, vol. 149, pp. 122–134, 2018.
- [20] S. I. Yengejeh, S. A. Kazemi, and A. Öchsner, “Carbon nanotubes as reinforcement in composites: a review of the analytical, numerical and experimental approaches,” *Computational Materials Science*, vol. 136, pp. 85–101, 2017.
- [21] A. M. Beese, X. Wei, S. Sarkar et al., “Key factors limiting carbon nanotube yarn strength: exploring processing-structure-property relationships,” *ACS Nano*, vol. 8, no. 11, pp. 11454–11466, 2014.
- [22] V. M. Candelario, R. Moreno, Z. Shen, F. Guiberteau, and A. L. Ortiz, “Liquid-phase assisted spark-plasma sintering of SiC nanoceramics and their nanocomposites with carbon nanotubes,” *Journal of the European Ceramic Society*, vol. 37, no. 5, pp. 1929–1936, 2017.
- [23] V. Lutz, J. Duchet-Rumeau, N. Godin, F. Smail, F. Lortie, and J. F. Gérard, “Ex-PAN carbon fibers vs carbon nanotubes fibers: from conventional epoxy based composites to multiscale composites,” *European Polymer Journal*, vol. 106, pp. 9–18, 2018.
- [24] H. Deng, J. Yi, C. Xia, and Y. Yi, “Mechanical properties and microstructure characterization of well-dispersed carbon nanotubes reinforced copper matrix composites,” *Journal of Alloys and Compounds*, vol. 727, pp. 260–268, 2017.
- [25] A. E. Moumen, M. Tarfaoui, and K. Lafdi, “Mechanical characterization of carbon nanotubes based polymer composites using indentation tests,” *Composites Part B: Engineering*, vol. 114, pp. 1–7, 2017.
- [26] T. K. Truong, Y. Lee, and D. Suh, “Multifunctional characterization of carbon nanotube sheets, yarns, and their composites,” *Current Applied Physics*, vol. 16, no. 9, pp. 1250–1258, 2016.
- [27] H. S. Bedi, M. Tiwari, and P. K. Agnihotri, “Quantitative determination of size and properties of interphases in carbon nanotube-based multiscale composites,” *Carbon*, vol. 132, pp. 181–190, 2018.
- [28] H. Wang, Z.-H. Zhang, H.-M. Zhang, Z.-Y. Hu, S.-L. Li, and X.-W. Cheng, “Novel synthesizing and characterization of copper matrix composites reinforced with carbon nanotubes,” *Materials Science and Engineering: A*, vol. 696, pp. 80–89, 2017.
- [29] B. D. Jensen, G. M. Odegard, J.-W. Kim, G. Sauti, E. J. Siochi, and K. E. Wise, “Simulating the effects of carbon nanotube continuity and interfacial bonding on composite strength and stiffness,” *Composites Science and Technology*, vol. 166, pp. 10–19, 2018.
- [30] X. Chen, J. Tao, J. Yi et al., “Enhancing the strength of carbon nanotubes reinforced copper matrix composites by optimizing the interface structure and dispersion uniformity,” *Diamond and Related Materials*, vol. 88, pp. 74–84, 2018.
- [31] H. Wang, Z.-H. Zhang, Z.-Y. Hu et al., “Improvement of interfacial interaction and mechanical properties in copper matrix composites reinforced with copper coated carbon nanotubes,” *Materials Science and Engineering: A*, vol. 715, pp. 163–173, 2018.
- [32] C. Yi, S. Bagchi, C. M. Dmuchowski et al., “Direct nanomechanical characterization of carbon nanotubes–titanium interfaces,” *Carbon*, vol. 132, pp. 548–555, 2018.
- [33] A. R. Boccaccini, J. Cho, T. Subhani, C. Kaya, and F. Kaya, “Electrophoretic deposition of carbon nanotube-ceramic nanocomposites,” *Journal of the European Ceramic Society*, vol. 30, no. 5, pp. 1115–1129, 2010.
- [34] E. Zapata-Solvas, D. Gómez-García, and A. Domínguez-Rodríguez, “Towards physical properties tailoring of carbon nanotubes-reinforced ceramic matrix composites,” *Journal of the European Ceramic Society*, vol. 32, no. 12, pp. 3001–3020, 2012.
- [35] S. R. Bakshi, D. Lahiri, and A. Agarwal, “Carbon nanotube reinforced metal matrix composites—a review,” *International Materials Reviews*, vol. 55, no. 1, pp. 41–64, 2010.
- [36] A. V. Radhamani, H. C. Lau, and S. Ramakrishna, “CNT-reinforced metal and steel nanocomposites: a comprehensive assessment of progress and future directions,” *Composites Part A: Applied Science and Manufacturing*, vol. 114, pp. 170–187, 2018.
- [37] H. Wang and Z. Bao, “Conjugated polymer sorting of semiconducting carbon nanotubes and their electronic applications,” *Nano Today*, vol. 10, no. 6, pp. 737–758, 2015.
- [38] P. S. Goh, A. F. Ismail, and B. C. Ng, “Directional alignment of carbon nanotubes in polymer matrices: contemporary approaches and future advances,” *Composites Part A: Applied Science and Manufacturing*, vol. 56, pp. 103–126, 2014.
- [39] X. Wang, S.-C. Wong, Y. J. Jung, and K.-T. Wan, “Measuring interfacial adhesion of carbon nanotube bundles and electrospun polymer fibers,” *Langmuir*, vol. 33, no. 44, pp. 12592–12595, 2017.
- [40] O. A. Bãrsan, G. G. Hoffmann, L. G. J. van der Ven, and G. de With, “Single-walled carbon nanotube networks: the influence of individual tube-tube contacts on the large-scale conductivity of polymer composites,” *Advanced Functional Materials*, vol. 26, no. 24, pp. 4377–4385, 2016.
- [41] Z. Spitalsky, D. Tasis, K. Papagelis, and C. Galiotis, “Carbon nanotube-polymer composites: chemistry, processing, mechanical and electrical properties,” *Progress in Polymer Science*, vol. 35, no. 3, pp. 357–401, 2010.
- [42] V. D. Punetha, S. Rana, H. J. Yoo et al., “Functionalization of carbon nanomaterials for advanced polymer nanocomposites: a comparison study between CNT and graphene,” *Progress in Polymer Science*, vol. 67, pp. 1–47, 2017.
- [43] C. Pramanik, D. Nepal, M. Nathanson et al., “Molecular engineering of interphases in polymer/carbon nanotube composites to reach the limits of mechanical performance,” *Composites Science and Technology*, vol. 166, pp. 86–94, 2018.
- [44] Y. Liu and S. Kumar, “Polymer/carbon nanotube nano composite fibers—A review,” *ACS Applied Materials & Interfaces*, vol. 6, no. 9, pp. 6069–6087, 2014.
- [45] S. K. Kumar, B. C. Benicewicz, R. A. Vaia, and K. I. Winey, “50th anniversary perspective: are polymer nanocomposites practical for applications?,” *Macromolecules*, vol. 50, no. 3, pp. 714–731, 2017.
- [46] J. Winey, J. F. Douglas, F. W. Starr et al., “Current issues in research on structure-property relationships in polymer

- nanocomposites,” *Polymer*, vol. 51, no. 15, pp. 3321–3343, 2010.
- [47] J. N. Coleman, U. Khan, W. J. Blau, and Y. K. Gun’ko, “Small but strong: a review of the mechanical properties of carbon nanotube-polymer composites,” *Carbon*, vol. 44, no. 9, pp. 1624–1652, 2006.
- [48] J. N. Coleman, U. Khan, and Y. K. Gun’ko, “Mechanical reinforcement of polymers using carbon nanotubes,” *Advanced Materials*, vol. 18, no. 6, pp. 689–706, 2006.
- [49] K. S. Khare, F. Khabaz, and R. Khare, “Effect of carbon nanotube functionalization on mechanical and thermal properties of cross-linked epoxy-carbon nanotube nanocomposites: role of strengthening the interfacial interactions,” *ACS Applied Materials & Interfaces*, vol. 6, no. 9, pp. 6098–6110, 2014.
- [50] N. Ning, T. Mi, G. Chu et al., “A quantitative approach to study the interface of carbon nanotubes/elastomer nanocomposites,” *European Polymer Journal*, vol. 102, pp. 10–18, 2018.
- [51] M. Yoonessi, M. Lebrón-Colón, D. Scheiman, and M. A. Meador, “Carbon nanotube epoxy nanocomposites: the effects of interfacial modifications on the dynamic mechanical properties of the nanocomposites,” *ACS Applied Materials & Interfaces*, vol. 6, no. 19, pp. 16621–16630, 2014.
- [52] P. Katti, S. Bose, and S. Kumar, “Tailored interface resulting in improvement in mechanical properties of epoxy composites containing poly(ether ether ketone) grafted multiwall carbon nanotubes,” *Polymer*, vol. 102, pp. 43–53, 2016.
- [53] Z. Han and A. Fina, “Thermal conductivity of carbon nanotubes and their polymer nanocomposites: a review,” *Progress in Polymer Science*, vol. 36, no. 7, pp. 914–944, 2011.
- [54] H. Chen, V. V. Ginzburg, J. Yang et al., “Thermal conductivity of polymer-based composites: fundamentals and applications,” *Progress in Polymer Science*, vol. 59, pp. 41–85, 2016.
- [55] M. K. Hassanzadeh-Aghdam and M. J. Mahmoodei, “Micromechanical modeling of thermal conducting behavior of general carbon nanotube-polymer nanocomposites,” *Materials Science and Engineering: B*, vol. 229, pp. 173–183, 2018.
- [56] S. Hida, T. Hori, T. Shiga, J. Elliott, and J. Shiomi, “Thermal resistance and phonon scattering at the interface between carbon nanotube and amorphous polyethylene,” *International Journal of Heat and Mass Transfer*, vol. 67, pp. 1024–1029, 2013.
- [57] R. E. Gorga, K. K. S. Lau, K. K. Gleason, and R. E. Cohen, “The importance of interfacial design at the carbon nanotube/polymer composite interface,” *Journal of Applied Polymer Science*, vol. 102, no. 2, pp. 1413–1418, 2006.
- [58] X. Chen, M. Zheng, C. Park, and C. Ke, “Direct Measurements of the mechanical strength of carbon nanotube-poly(methyl methacrylate) interfaces,” *Small*, vol. 9, no. 19, pp. 3345–3351, 2013.
- [59] P.-H. Wang, S. Sarkar, P. Gulgunje, N. Verghese, and S. Kumar, “Fracture mechanism of high impact strength polypropylene containing carbon nanotubes,” *Polymer*, vol. 151, pp. 287–298, 2018.
- [60] K. K. Ghuman and T. Fujigaya, “Electronic structure of a polybenzimidazole-wrapped single-wall carbon nanotube,” *Journal of Physical Chemistry C*, vol. 122, no. 28, pp. 15979–15985, 2018.
- [61] P. M. Ajayan, O. Stephan, C. Colliex, and D. Trauth, “Aligned carbon nanotube arrays formed by cutting a polymer resin-nanotube composite,” *Science*, vol. 265, no. 5176, pp. 1212–1214, 1994.
- [62] P. M. Ajayan, “Aligned carbon nanotubes in a thin polymer film,” *Advanced Materials*, vol. 7, no. 5, pp. 489–491, 1995.
- [63] H. D. Wagner, O. Lourie, Y. Feldman, and R. Tenne, “Stress-induced fragmentation of multiwall carbon nanotubes in a polymer matrix,” *Applied Physics Letters*, vol. 72, no. 2, pp. 188–190, 1998.
- [64] L. S. Schadler, S. C. Giannaris, and P. M. Ajayan, “Load transfer in carbon nanotube epoxy composites,” *Applied Physics Letters*, vol. 73, no. 26, pp. 3842–3844, 1998.
- [65] S. V. Ahir, Y. Y. Huang, and E. M. Terentjev, “Polymers with aligned carbon nanotubes: active composite materials,” *Polymer*, vol. 49, no. 18, pp. 3841–3854, 2008.
- [66] M. J. Green, N. Behabtu, M. Pasquali, and W. W. Adams, “Nanotubes as polymers,” *Polymer*, vol. 50, no. 21, pp. 4979–4997, 2009.
- [67] M. T. Byrne and Y. K. Gun’ko, “Recent advances in research on carbon nanotube-polymer composites,” *Advanced Materials*, vol. 22, no. 15, pp. 1672–1688, 2010.
- [68] T. Ji, Y. Feng, M. Qin, and W. Feng, “Thermal conducting properties of aligned carbon nanotubes and their polymer composites,” *Composites Part A: Applied Science and Manufacturing*, vol. 91, no. 1, pp. 351–369, 2016.
- [69] G. Pal and S. Kumar, “Modeling of carbon nanotubes and carbon nanotube-polymer composites,” *Progress in Aerospace Sciences*, vol. 80, pp. 33–58, 2016.
- [70] M. Kaseem, K. Hamad, and Y. G. Ko, “Fabrication and materials properties of polystyrene/carbon nanotube (PS/CNT) composites: a review,” *European Polymer Journal*, vol. 79, pp. 36–62, 2016.
- [71] D. Tasis, N. Tagmatarchis, A. Bianco, and M. Prato, “Chemistry of carbon nanotubes,” *Chemical Reviews*, vol. 106, no. 3, pp. 1105–1136, 2006.
- [72] S. W. Kim, T. Kim, Y. S. Kim et al., “Surface modifications for the effective dispersion of carbon nanotubes in solvents and polymers,” *Carbon*, vol. 50, no. 1, pp. 3–33, 2012.
- [73] K. Adachi and Y. Tsukahara, “Surface modification of carbon nanotubes by anionic approach,” *Current Opinion in Chemical Engineering*, vol. 11, pp. 106–113, 2016.
- [74] M. Adamska and U. Narkiewicz, “Fluorination of carbon nanotubes—a review,” *Journal of Fluorine Chemistry*, vol. 200, pp. 179–189, 2017.
- [75] S. B. Jagtap, V. D. Patil, K. Suresh et al., “Functionalized carbon nanotube reinforced polymer nanocomposite microcapsules with enhanced stiffness,” *Colloids and Surfaces A: Physicochemical and Engineering Aspects*, vol. 550, pp. 82–89, 2018.
- [76] R. Vijayan, A. Ghazinezami, S. R. Taklimi, M. Y. Khan, and D. Askari, “The geometrical advantages of helical carbon nanotubes for high-performance multifunctional polymeric nanocomposites,” *Composites Part B: Engineering*, vol. 156, pp. 28–42, 2019.
- [77] J. Chen, L. Yan, W. Song, and D. Xu, “Interfacial characteristics of carbon nanotube-polymer composites: a review,” *Composites Part A: Applied Science and Manufacturing*, vol. 114, pp. 149–169, 2018.
- [78] S. Bagchi, A. Harpale, and H. B. Chew, “Interfacial load transfer mechanisms in carbon nanotube-polymer nanocomposites,” *Proceedings of the Royal Society A: Mathematical, Physical and Engineering Sciences*, vol. 474, no. 2216, article 20170705, 2018.
- [79] J. Chen, Y.-Y. Shi, J.-H. Yang, N. Zhang, T. Huang, and Y. Wang, “Improving interfacial adhesion between

- immiscible polymers by carbon nanotubes,” *Polymer*, vol. 54, no. 1, pp. 464–471, 2013.
- [80] N. Taloub, L. Liu, N. Rahoui, M. Hegazy, and Y. Huang, “Grafting multi-walled carbon nanotubes (MWCNTs) into PIPD fiber for enhancing mechanical and interfacial performance,” *Polymer Testing*, vol. 75, pp. 344–349. In Press, 2019.
- [81] Y. Li and G. D. Seidel, “Multiscale modeling of the interface effects in CNT-epoxy nanocomposites,” *Computational Materials Science*, vol. 153, pp. 363–381, 2018.
- [82] R. Chawla and S. Sharma, “Molecular dynamics simulation of carbon nanotube pull-out from polyethylene matrix,” *Composites Science and Technology*, vol. 144, pp. 169–177, 2017.
- [83] J. Z. Kovacs, K. Andresen, J. R. Pauls et al., “Analyzing the quality of carbon nanotube dispersions in polymers using scanning electron microscopy,” *Carbon*, vol. 45, no. 6, pp. 1279–1288, 2007.
- [84] W. Li, S. T. Buschhorn, K. Schulte, and W. Bauhofer, “The imaging mechanism, imaging depth, and parameters influencing the visibility of carbon nanotubes in a polymer matrix using an SEM,” *Carbon*, vol. 49, no. 6, pp. 1955–1964, 2011.
- [85] D. Qian and E. C. Dickey, “In-situ transmission electron microscopy studies of polymer-carbon nanotube composite deformation,” *Journal of Microscopy*, vol. 204, no. 1, pp. 39–45, 2001.
- [86] B. A. Newcomb, L. A. Giannuzzi, K. M. Lyons et al., “High resolution transmission electron microscopy study on polyacrylonitrile/carbon nanotube based carbon fibers and the effect of structure development on the thermal and electrical conductivities,” *Carbon*, vol. 93, pp. 502–514, 2015.
- [87] M. Ilčíková, M. Danko, M. Doroshenko et al., “Visualization of carbon nanotubes dispersion in composite by using confocal laser scanning microscopy,” *European Polymer Journal*, vol. 79, pp. 187–197, 2016.
- [88] F. Zhou, D. Xing, B. Wu, S. Wu, Z. Ou, and W. R. Chen, “New insights of transmembranal mechanism and sub-cellular localization of noncovalently modified single-walled carbon nanotubes,” *Nano Letters*, vol. 10, no. 5, pp. 1677–1681, 2010.
- [89] T. Kashiwagi, J. Fagan, J. F. Douglas et al., “Relationship between dispersion metric and properties of PMMA/SWNT nanocomposites,” *Polymer*, vol. 48, no. 16, pp. 4855–4866, 2007.
- [90] B. E. Smith, H. Yazdani, and K. Hatami, “Three-dimensional imaging and quantitative analysis of dispersion and mechanical failure in filled nanocomposites,” *Composites Part A: Applied Science and Manufacturing*, vol. 79, pp. 23–29, 2015.
- [91] Y. Gao, L. Li, P. Tan, L. Liu, and Z. Zhang, “Application of Raman spectroscopy in carbon nanotube-based polymer composites,” *Chinese Science Bulletin*, vol. 55, no. 35, pp. 3978–3988, 2010.
- [92] F. Solá, Z. H. Xia, M. Lebrón-Colón, and M. A. Meador, “Transmission electron microscopy of single wall carbon nanotube/polymer nanocomposites: a first-principles study,” *Physica Status Solidi (RRL)–Rapid Research Letters*, vol. 6, no. 8, pp. 349–351, 2012.
- [93] Z. Jin, X. Sun, G. Xu, S. H. Goh, and W. Ji, “Nonlinear optical properties of some polymer/multi-walled carbon nanotube composites,” *Chemical Physics Letters*, vol. 318, no. 6, pp. 505–510, 2000.
- [94] T.-M. Wu and Y.-W. Lin, “Doped polyaniline/multi-walled carbon nanotube composites: preparation, characterization and properties,” *Polymer*, vol. 47, no. 10, pp. 3576–3582, 2006.
- [95] O. A. Bârsan, G. G. Hoffmann, L. G. J. van der Ven, and G. de With, “Quantitative conductive atomic force microscopy on single-walled carbon nanotube-based polymer composites,” *ACS Applied Materials & Interfaces*, vol. 8, no. 30, pp. 19701–19708, 2016.
- [96] M. Rahmat, K. Das, and P. Hubert, “Interaction stresses in carbon nanotube-polymer nanocomposites,” *ACS Applied Materials & Interfaces*, vol. 3, no. 9, pp. 3425–3431, 2011.
- [97] W. A. Chapkin, D. Q. McNerny, M. F. Aldridge et al., “Real-time assessment of carbon nanotube alignment in a polymer matrix under an applied electric field via polarized Raman spectroscopy,” *Polymer Testing*, vol. 56, pp. 29–35, 2016.
- [98] M. Baibarac, I. Baltog, and S. Lefrant, “Raman spectroscopic evidence for interfacial interactions in poly(bithiophene)/single-walled carbon nanotube composites,” *Carbon*, vol. 47, no. 5, pp. 1389–1398, 2009.
- [99] X. Chen, L. Zhang, M. Zheng, C. Park, X. Wang, and C. Ke, “Quantitative nanomechanical characterization of the van der Waals interfaces between carbon nanotubes and epoxy,” *Carbon*, vol. 82, pp. 214–228, 2015.
- [100] M. Rahmat and P. Hubert, “Interaction stress measurement using atomic force microscopy: a stepwise discretization method,” *Journal of Physical Chemistry C*, vol. 114, no. 35, pp. 15029–15035, 2010.
- [101] M. Nie, D. M. Kalyon, K. Pochiraju, and F. T. Fisher, “A controllable way to measure the interfacial strength between carbon nanotube and polymer using a nanobridge structure,” *Carbon*, vol. 116, pp. 510–517, 2017.
- [102] D. Wang and T. P. Russell, “Advances in atomic force microscopy for probing polymer structure and properties,” *Macromolecules*, vol. 51, no. 1, pp. 3–24, 2018.
- [103] A. H. Barber, S. R. Cohen, and H. D. Wagner, “Measurement of carbon nanotube-polymer interfacial strength,” *Applied Physics Letters*, vol. 82, no. 23, pp. 4140–4142, 2003.
- [104] M. C. Strus, C. I. Cano, R. Byron Pipes, C. V. Nguyen, and A. Raman, “Interfacial energy between carbon nanotubes and polymers measured from nanoscale peel tests in the atomic force microscope,” *Composites Science and Technology*, vol. 69, no. 10, pp. 1580–1586, 2009.
- [105] A. H. Barber, S. R. Cohen, S. Kenig, and H. D. Wagner, “Interfacial fracture energy measurements for multi-walled carbon nanotubes pulled from a polymer matrix,” *Composites Science and Technology*, vol. 64, no. 15, pp. 2283–2289, 2004.
- [106] A. H. Barber, S. R. Cohen, A. Eitan, L. S. Schadler, and H. D. Wagner, “Fracture transitions at a carbon-nanotube/polymer interface,” *Advanced Materials*, vol. 18, no. 1, pp. 83–87, 2006.
- [107] W. Ding, A. Eitan, F. T. Fisher et al., “Direct observation of polymer sheathing in carbon nanotube-polycarbonate composites,” *Nano Letters*, vol. 3, no. 11, pp. 1593–1597, 2003.
- [108] Y. Ganesan, C. Peng, Y. Lu et al., “Interface toughness of carbon nanotube reinforced epoxy composites,” *ACS Applied Materials & Interfaces*, vol. 3, no. 2, pp. 129–134, 2011.
- [109] M. P. Manoharan, A. Sharma, A. V. Desai, M. A. Haque, C. E. Bakis, and K. W. Wang, “The interfacial strength of carbon nanofiber epoxy composite using single fiber pullout experiments,” *Nanotechnology*, vol. 20, no. 29, article 295701, 2009.

- [110] T. Tsuda, T. Ogasawara, F. Deng, and N. Takeda, "Direct measurements of interfacial shear strength of multi-walled carbon nanotube/PEEK composite using a nano-pullout method," *Composites Science and Technology*, vol. 71, no. 10, pp. 1295–1300, 2011.
- [111] S.-Y. Fu, Z.-K. Chen, S. Hong, and C. C. Han, "The reduction of carbon nanotube (CNT) length during the manufacture of CNT/polymer composites and a method to simultaneously determine the resulting CNT and interfacial strengths," *Carbon*, vol. 47, no. 14, pp. 3192–3200, 2009.
- [112] Y.-N. Liu, M. Li, Y. Gu et al., "The interfacial strength and fracture characteristics of ethanol and polymer modified carbon nanotube fibers in their epoxy composites," *Carbon*, vol. 52, pp. 550–558, 2013.
- [113] M. A. Poggi, L. A. Bottomley, and P. T. Lillehei, "Measuring the adhesion forces between alkanethiol-modified AFM cantilevers and single walled carbon nanotubes," *Nano Letters*, vol. 4, no. 1, pp. 61–64, 2004.
- [114] M. A. Poggi, P. T. Lillehei, and L. A. Bottomley, "Chemical force microscopy on single-walled carbon nanotube paper," *Chemistry of Materials*, vol. 17, no. 17, pp. 4289–4295, 2005.
- [115] I. Y. Phang, T. Liu, W.-D. Zhang, H. Schönherr, and G. J. Vancso, "Probing buried carbon nanotubes within polymer-nanotube composite matrices by atomic force microscopy," *European Polymer Journal*, vol. 43, no. 10, pp. 4136–4142, 2007.
- [116] H. T. Thompson, F. Barroso-Bujans, J. G. Herrero, R. Reifenger, and A. Raman, "Subsurface imaging of carbon nanotube networks in polymers with DC-biased multifrequency dynamic atomic force microscopy," *Nanotechnology*, vol. 24, no. 13, article 135701, 2013.
- [117] W. Wang, P. Ciselli, E. Kuznetsov, T. Peijs, and A. H. Barber, "Effective reinforcement in carbon nanotube-polymer composites," *Philosophical Transactions of the Royal Society A: Mathematical, Physical and Engineering Sciences*, vol. 366, no. 1870, pp. 1613–1626, 2008.
- [118] M. Rahmat, H. Ghiasi, and P. Hubert, "An interaction stress analysis of nanoscale elastic asperity contacts," *Nanoscale*, vol. 4, no. 1, pp. 157–166, 2012.
- [119] S. Lefrant, M. Baibarac, and I. Baltog, "Raman and FTIR spectroscopy as valuable tools for the characterization of polymer and carbon nanotube based composites," *Journal of Materials Chemistry*, vol. 19, no. 32, pp. 5690–5704, 2009.
- [120] M. Mu, S. Osswald, Y. Gogotsi, and K. I. Winey, "An *in situ* Raman spectroscopy study of stress transfer between carbon nanotubes and polymer," *Nanotechnology*, vol. 20, no. 33, article 335703, 2009.
- [121] A. Rasheed, H. G. Chae, S. Kumar, and M. D. Dadmun, "Polymer nanotube nanocomposites: correlating intermolecular interaction to ultimate properties," *Polymer*, vol. 47, no. 13, pp. 4734–4741, 2006.
- [122] T. E. Chang, L. R. Jensen, A. Kisliuk, R. B. Pipes, R. Pyrz, and A. P. Sokolov, "Microscopic mechanism of reinforcement in single-wall carbon nanotube/polypropylene nanocomposite," *Polymer*, vol. 46, no. 2, pp. 439–444, 2005.
- [123] A. de la Vega, I. A. Kinloch, R. J. Young, W. Bauhofer, and K. Schulte, "Simultaneous global and local strain sensing in SWCNT-epoxy composites by Raman and impedance spectroscopy," *Composites Science and Technology*, vol. 71, no. 2, pp. 160–166, 2011.
- [124] L. Bokobza, J.-L. Bruneel, and M. Couzi, "Raman spectroscopic investigation of carbon-based materials and their composites. Comparison between carbon nanotubes and carbon black," *Chemical Physics Letters*, vol. 590, pp. 153–159, 2013.
- [125] L. Bokobza, J.-L. Bruneel, and M. Couzi, "Raman spectroscopy as a tool for the analysis of carbon-based materials (highly oriented pyrolytic graphite, multilayer graphene and multiwall carbon nanotubes) and of some of their elastomeric composites," *Vibrational Spectroscopy*, vol. 74, pp. 57–63, 2014.
- [126] A. Y. Glamazda, A. M. Plokhotnichenko, V. S. Leontiev, and V. A. Karachevtsev, "DNA-wrapped carbon nanotubes aligned in stretched gelatin films: polarized resonance Raman and absorption spectroscopy study," *Physica E: Low-dimensional Systems and Nanostructures*, vol. 93, pp. 92–96, 2017.
- [127] D. Roy, S. Bhattacharyya, A. Rachamim, A. Plati, and M.-L. Saboungi, "Measurement of interfacial shear strength in single wall carbon nanotubes reinforced composite using Raman spectroscopy," *Journal of Applied Physics*, vol. 107, no. 4, article 043501, 2010.
- [128] N. Lachman, C. Bartholome, P. Miaudet, M. Maugey, P. Poulin, and H. D. Wagner, "Raman response of carbon nanotube/PVA fibers under strain," *Journal of Physical Chemistry C*, vol. 113, no. 12, pp. 4751–4754, 2009.
- [129] X. Yan, H. Sato, and Y. Ozaki, "Raman and tip-enhanced Raman scattering spectroscopy studies of polymer nanocomposites," in *Spectroscopy of Polymer Nanocomposites*, S. Thomas, D. Rouxel, and D. Ponnamma, Eds., William Andrew Publishing, Kidlington, Oxford, UK, pp. 88–111, 2016.
- [130] H. D. Wagner, "Raman spectroscopy of polymer-carbon nanotube composites," in *Polymer-Carbon Nanotube Composites: Preparation, Properties and Applications, A vol. in Woodhead Publishing Series in Composites Science and Engineering*, T. McNally and P. Pötschke, Eds., Woodhead Publishing Limited., Sawston, Cambridge, UK, pp. 400–427, 2011.
- [131] J. R. Wood and H. D. Wagner, "Single-wall carbon nanotubes as molecular pressure sensors," *Applied Physics Letters*, vol. 76, no. 20, pp. 2883–2885, 2000.
- [132] J. R. Wood, Q. Zhao, M. D. Frogley et al., "Carbon nanotubes: from molecular to macroscopic sensors," *Physical Review B*, vol. 62, no. 11, pp. 7571–7575, 2000.
- [133] J. R. Wood, M. D. Frogley, E. R. Meurs et al., "Mechanical response of carbon nanotubes under molecular and macroscopic pressures," *Journal of Physical Chemistry B*, vol. 103, no. 47, pp. 10388–10392, 1999.
- [134] J. R. Wood, Q. Zhao, and H. D. Wagner, "Orientation of carbon nanotubes in polymers and its detection by Raman spectroscopy," *Composites Part A: Applied Science and Manufacturing*, vol. 32, no. 3-4, pp. 391–399, 2001.
- [135] E. Francis, L. Zhai, H. Chan Kim et al., "Morphology correlated free volume studies of multi-walled carbon nanotube plasticized poly (vinyl chloride) nanocomposites: positronium probes and electrical properties," *Polymer*, vol. 141, pp. 232–243, 2018.
- [136] B. A. Newcomb, H. G. Chae, L. Thomson, J. Luo, J.-B. Baek, and S. Kumar, "Reinforcement efficiency of carbon nanotubes and their effect on crystal-crystal slip in poly(ether ketone)/carbon nanotube composite fibers," *Composites Science and Technology*, vol. 147, pp. 116–125, 2017.
- [137] H. Chang, J. Luo, H. C. Liu, A. A. Bakhtary Davijani, P.-H. Wang, and S. Kumar, "Orientation and interfacial stress transfer of cellulose nanocrystal nanocomposite fibers," *Polymer*, vol. 110, pp. 228–234, 2017.

- [138] B. A. Newcomb, H. G. Chae, P. V. Gulgunje et al., "Stress transfer in polyacrylonitrile/carbon nanotube composite fibers," *Polymer*, vol. 55, no. 11, pp. 2734–2743, 2014.
- [139] J. Cheng, H. Pu, and J. Du, "A processing method with high efficiency for low density polyethylene nanofibers reinforced by aligned carbon nanotubes via nanolayer coextrusion," *Polymer*, vol. 111, pp. 222–228, 2017.
- [140] L. Liu, A. H. Barber, S. Nurriel, and H. D. Wagner, "Mechanical properties of functionalized single-walled carbon-nanotube/poly(vinyl alcohol) nanocomposites," *Advanced Functional Materials*, vol. 15, no. 6, pp. 975–980, 2005.
- [141] Q. Zhao and H. D. Wagner, "Raman spectroscopy of carbon-nanotube-based composites," *Philosophical Transactions of the Royal Society of London. Series A: Mathematical, Physical and Engineering Sciences*, vol. 362, no. 1824, pp. 2407–2424, 2004.
- [142] R. Graupner, "Raman spectroscopy of covalently functionalized single-wall carbon nanotubes," *Journal of Raman Spectroscopy*, vol. 38, no. 6, pp. 673–683, 2007.
- [143] S. L. Ruan, P. Gao, X. G. Yang, and T. X. Yu, "Toughening high performance ultrahigh molecular weight polyethylene using multiwalled carbon nanotubes," *Polymer*, vol. 44, no. 19, pp. 5643–5654, 2003.
- [144] S. Ruan, P. Gao, and T. X. Yu, "Ultra-strong gel-spun UHMWPE fibers reinforced using multiwalled carbon nanotubes," *Polymer*, vol. 47, no. 5, pp. 1604–1611, 2006.
- [145] D. Puglia, L. Valentini, I. Armentano, and J. M. Kenny, "Effects of single-walled carbon nanotube incorporation on the cure reaction of epoxy resin and its detection by Raman spectroscopy," *Diamond and Related Materials*, vol. 12, no. 3–7, pp. 827–832, 2003.
- [146] M. Rahmat and P. Hubert, "Carbon nanotube-polymer interactions in nanocomposites: a review," *Composites Science and Technology*, vol. 72, no. 1, pp. 72–84, 2011.
- [147] N. Ning, D. Cheng, J. Yang et al., "New insight on the interfacial interaction between multiwalled carbon nanotubes and elastomers," *Composites Science and Technology*, vol. 142, pp. 214–220, 2017.
- [148] H. Li, S. Liu, P. Li et al., "Interfacial control and carrier tuning of carbon nanotube/polyaniline composites for high thermoelectric performance," *Carbon*, vol. 136, pp. 292–298, 2018.
- [149] X. Yao, X. Gao, J. Jiang, C. Xu, C. Deng, and J. Wang, "Comparison of carbon nanotubes and graphene oxide coated carbon fiber for improving the interfacial properties of carbon fiber/epoxy composites," *Composites Part B: Engineering*, vol. 132, pp. 170–177, 2018.
- [150] T. Palacin, H. L. Khanh, B. Jusselme et al., "Efficient functionalization of carbon nanotubes with porphyrin dendrons via click chemistry," *Journal of the American Chemical Society*, vol. 131, no. 42, pp. 15394–15402, 2009.
- [151] M. Rafiee, F. Nitzsche, and M. R. Labrosse, "Effect of functionalization of carbon nanotubes on vibration and damping characteristics of epoxy nanocomposites," *Polymer Testing*, vol. 69, pp. 385–395, 2018.
- [152] S. H. Boroushaki, R. Ansari, and S. Ajori, "Molecular dynamics simulations of the thermal conductivity of cross-linked functionalized single- and double-walled carbon nanotubes with polyethylene chains," *Diamond and Related Materials*, vol. 86, pp. 173–178, 2018.
- [153] G. Zamfirova, V. Gaydarov, F. Faraguna, E. Vidović, and A. Jukić, "Influence of carbon nanotubes functionalization on the mechanical properties of polymethacrylate nanocomposites," *Colloids and Surfaces A: Physicochemical and Engineering Aspects*, vol. 510, pp. 169–175, 2016.
- [154] J. Gao, M. A. Loi, E. J. F. de Carvalho, and M. C. dos Santos, "Selective wrapping and supramolecular structures of polyfluorene-carbon nanotube hybrids," *ACS Nano*, vol. 5, no. 5, pp. 3993–3999, 2011.
- [155] L. Wang, Y. Tan, X. Wang, T. Xu, C. Xiao, and Z. Qi, "Mechanical and fracture properties of hyperbranched polymer covalent functionalized multiwalled carbon nanotube-reinforced epoxy composites," *Chemical Physics Letters*, vol. 706, pp. 31–39, 2018.
- [156] C. Min, D. Liu, Z. He, S. Li, K. Zhang, and Y. Huang, "Preparation of novel polyimide nanocomposites with high mechanical and tribological performance using covalent modified carbon nanotubes via Friedel-Crafts reaction," *Polymer*, vol. 150, pp. 223–231, 2018.
- [157] T. Tsafack, J. M. Alred, K. E. Wise, B. Jensen, E. Siochi, and B. I. Yakobson, "Exploring the interface between single-walled carbon nanotubes and epoxy resin," *Carbon*, vol. 105, pp. 600–606, 2016.
- [158] A. A. B. Davijani, H. Chang, H. C. Liu, J. Luo, and S. Kumar, "Stress transfer in nanocomposites enabled by poly(methyl methacrylate) wrapping of carbon nanotubes," *Polymer*, vol. 130, pp. 191–198, 2017.
- [159] Y.-Q. Huang, Y.-Y. Zhong, R. Zhang et al., "Tuning the backbones and side chains of cationic meta-linked poly(phenylene ethynylene)s: different conformational modes, tunable light emission, and helical wrapping of multi-walled carbon nanotubes," *Polymer*, vol. 102, pp. 143–152, 2016.
- [160] Y. Li, D. Yang, A. Adronov, Y. Gao, X. Luo, and H. Li, "Covalent functionalization of single-walled carbon nanotubes with thermoresponsive core cross-linked polymeric micelles," *Macromolecules*, vol. 45, no. 11, pp. 4698–4706, 2012.
- [161] K. M. Lee, L. Li, and L. Dai, "Asymmetric end-functionalization of multi-walled carbon nanotubes," *Journal of the American Chemical Society*, vol. 127, no. 12, pp. 4122–4123, 2005.
- [162] C. Bergeret, J. Cousseau, V. Fernandez, J.-Y. Mevellec, and S. Lefrant, "Spectroscopic evidence of carbon nanotubes' metallic character loss induced by covalent functionalization via nitric acid purification," *Journal of Physical Chemistry C*, vol. 112, no. 42, pp. 16411–16416, 2008.
- [163] K. S. Lee, M. Park, J. M. Ko, and J.-D. Kim, "Electrochemical properties of multi-walled carbon nanotubes treated with nitric acid for a supercapacitor electrode," *Colloids and Surfaces A: Physicochemical and Engineering Aspects*, vol. 506, pp. 664–669, 2016.
- [164] J. Ramirez, M. L. Mayo, S. Kilina, and S. Tretiak, "Electronic structure and optical spectra of semiconducting carbon nanotubes functionalized by diazonium salts," *Chemical Physics*, vol. 413, pp. 89–101, 2013.
- [165] C. M. Q. Le, X. T. Cao, Y. T. Jeong, and K. T. Lim, "Covalent functionalization of multi-walled carbon nanotubes with imidazolium-based poly(ionic liquid)s by Diels-Alder "click" reaction," *Journal of Industrial and Engineering Chemistry*, vol. 64, pp. 337–343, 2018.
- [166] K. Mosnáčková, J. Kollár, Y.-S. Huang, C.-F. Huang, and J. Mosnáček, "Synthesis routes of functionalized nanoparticles," in *Polymer Composites with Functional Nanoparticles: Synthesis, Properties, and Applications, A vol. in Micro and Nano Technologies*, K. Pielichowski and T. M. Majka, Eds., Elsevier Ltd., Amsterdam, Netherlands, 2019.

- [167] C. Wei, B. Akinwolemiwa, L. Yu, D. Hu, and G. Z. Chen, "Polymer composites with functionalized carbon nanotube and graphene," in *Polymer Composites with Functional Nanoparticles: Synthesis, Properties, and Applications, A vol. in Micro and Nano Technologies*, K. Pielichowski and T. M. Majka, Eds., Elsevier Ltd., Amsterdam, Netherlands, 2019.
- [168] F. H. Gojny and K. Schulte, "Functionalisation effect on the thermo-mechanical behaviour of multi-wall carbon nanotube/epoxy-composites," *Composites Science and Technology*, vol. 64, no. 15, pp. 2303–2308, 2004.
- [169] F. H. Gojny, J. Nastalczyk, Z. Roslaniec, and K. Schulte, "Surface modified multi-walled carbon nanotubes in CNT/epoxy-composites," *Chemical Physics Letters*, vol. 370, no. 5-6, pp. 820–824, 2003.
- [170] B. Ruelle, S. Peeterbroeck, C. Bittencourt et al., "Semi-crystalline polymer/carbon nanotube nanocomposites: effect of nanotube surface-functionalization and polymer coating on electrical and thermal properties," *Reactive and Functional Polymers*, vol. 72, no. 6, pp. 383–392, 2012.
- [171] Y. J. Kim, T. S. Shin, H. D. Choi, J. H. Kwon, Y.-C. Chung, and H. G. Yoon, "Electrical conductivity of chemically modified multiwalled carbon nanotube/epoxy composites," *Carbon*, vol. 43, no. 1, pp. 23–30, 2005.
- [172] A. A. B. Davijani and S. Kumar, "Ordered wrapping of poly(methyl methacrylate) on single wall carbon nanotubes," *Polymer*, vol. 70, pp. 278–281, 2015.
- [173] A. Nish, J.-Y. Hwang, J. Doig, and R. J. Nicholas, "Highly selective dispersion of single-walled carbon nanotubes using aromatic polymers," *Nature Nanotechnology*, vol. 2, no. 10, pp. 640–646, 2007.
- [174] X. Tu, S. Manohar, A. Jagota, and M. Zheng, "DNA sequence motifs for structure-specific recognition and separation of carbon nanotubes," *Nature*, vol. 460, no. 7252, pp. 250–253, 2009.
- [175] M. J. O'Connell, P. Boul, L. M. Ericson et al., "Reversible water-solubilization of single-walled carbon nanotubes by polymer wrapping," *Chemical Physics Letters*, vol. 342, no. 3-4, pp. 265–271, 2001.
- [176] S. K. Samanta, M. Fritsch, U. Scherf, W. Gomulya, S. Z. Bisri, and M. A. Loi, "Conjugated polymer-assisted dispersion of single-wall carbon nanotubes: the power of polymer wrapping," *Accounts of Chemical Research*, vol. 47, no. 8, pp. 2446–2456, 2014.
- [177] T. Lei, I. Pochorovski, and Z. Bao, "Separation of semi-conducting carbon nanotubes for flexible and stretchable electronics using polymer removable method," *Accounts of Chemical Research*, vol. 50, no. 4, pp. 1096–1104, 2017.
- [178] J. Ouyang, J. Ding, J. Lefebvre et al., "Sorting of semi-conducting single-walled carbon nanotubes in polar solvents with an amphiphilic conjugated polymer provides general guidelines for enrichment," *ACS Nano*, vol. 12, no. 2, pp. 1910–1919, 2018.
- [179] P. Deria, C. D. Von Bargaen, J.-H. Olivier, A. S. Kumbhar, J. G. Saven, and M. J. Therien, "Single-handed helical wrapping of single-walled carbon nanotubes by chiral, ionic, semiconducting polymers," *Journal of the American Chemical Society*, vol. 135, no. 43, pp. 16220–16234, 2013.
- [180] S. Badaire, C. Zakri, M. Maugey et al., "Liquid crystals of DNA-stabilized carbon nanotubes," *Advanced Materials*, vol. 17, no. 13, pp. 1673–1676, 2005.
- [181] P. V. Jena, M. M. Safaei, D. A. Heller, and D. Roxbury, "DNA-carbon nanotube complexation affinity and photoluminescence modulation are independent," *ACS Applied Materials & Interfaces*, vol. 9, no. 25, pp. 21397–21405, 2017.
- [182] R. Shvartzman-Cohen, Y. Levi-Kalishman, E. Nativ-Roth, and R. Yerushalmi-Rozen, "Generic approach for dispersing single-walled carbon nanotubes: the strength of a weak interaction," *Langmuir*, vol. 20, no. 15, pp. 6085–6088, 2004.
- [183] H. S. Park, B. G. Choi, W. H. Hong, and S.-Y. Jang, "Interfacial interactions of single-walled carbon nanotube/conjugated block copolymer hybrids for flexible transparent conductive films," *Journal of Physical Chemistry C*, vol. 116, no. 14, pp. 7962–7967, 2012.
- [184] N. A. Rice, A. V. Subrahmanyam, B. R. Coleman, and A. Adronov, "Effect of induction on the dispersion of semiconducting and metallic single-walled carbon nanotubes using conjugated polymers," *Macromolecules*, vol. 48, no. 15, pp. 5155–5161, 2015.
- [185] T. Lei, X. Chen, G. Pitner, H.-S. P. Wong, and Z. Bao, "Removable and recyclable conjugated polymers for highly selective and high-yield dispersion and release of low-cost carbon nanotubes," *Journal of the American Chemical Society*, vol. 138, no. 3, pp. 802–805, 2016.
- [186] W. Chung, K. Nobusawa, H. Kamikubo, M. Kataoka, M. Fujiki, and M. Naito, "Time-resolved observation of chiral-index-selective wrapping on single-walled carbon nanotube with non-aromatic polysilane," *Journal of the American Chemical Society*, vol. 135, no. 6, pp. 2374–2383, 2013.
- [187] M. Yang, V. Koutsos, and M. Zaiser, "Interactions between polymers and carbon nanotubes: a molecular dynamics study," *Journal of Physical Chemistry B*, vol. 109, no. 20, pp. 10009–10014, 2005.
- [188] S. S. Tallury and M. A. Pasquinelli, "Molecular dynamics simulations of polymers with stiff backbones interacting with single-walled carbon nanotubes," *Journal of Physical Chemistry B*, vol. 114, no. 29, pp. 9349–9355, 2010.
- [189] S. S. Tallury and M. A. Pasquinelli, "Molecular dynamics simulations of flexible polymer chains wrapping single-walled carbon nanotubes," *Journal of Physical Chemistry B*, vol. 114, no. 12, pp. 4122–4129, 2010.
- [190] J. Gou, B. Minaie, B. Wang, Z. Liang, and C. Zhang, "Computational and experimental study of interfacial bonding of single-walled nanotube reinforced composites," *Computational Materials Science*, vol. 31, no. 3-4, pp. 225–236, 2004.
- [191] I. Kusner and S. Srebnik, "Conformational behavior of semi-flexible polymers confined to a cylindrical surface," *Chemical Physics Letters*, vol. 430, no. 1–3, pp. 84–88, 2006.
- [192] J. Chen, H. Liu, W. A. Weimer, M. D. Halls, D. H. Waldeck, and G. C. Walker, "Noncovalent engineering of carbon nanotube surfaces by rigid, functional conjugated polymers," *Journal of the American Chemical Society*, vol. 124, no. 31, pp. 9034–9035, 2002.
- [193] P. Kelich and A. Asadinezhad, "Molecular dynamics insights into behavior of poly(ethylene succinate) single chain on carbon nanotube surface," *Journal of Physical Chemistry C*, vol. 119, no. 46, pp. 26143–26153, 2015.
- [194] Z. Qi, Y. Tan, H. Wang, T. Xu, L. Wang, and C. Xiao, "Effects of noncovalently functionalized multiwalled carbon nanotube with hyperbranched polyesters on mechanical properties of epoxy composites," *Polymer Testing*, vol. 64, pp. 38–47, 2017.
- [195] A. Mandal and A. K. Nandi, "Noncovalent functionalization of multiwalled carbon nanotube by a polythiophene-based

- compatibilizer: reinforcement and conductivity improvement in poly(vinylidene fluoride) films,” *Journal of Physical Chemistry C*, vol. 116, no. 16, pp. 9360–9371, 2012.
- [196] W. Yuan, W. Li, Y. Mu, and M. B. Chan-Park, “Effect of side-chain structure of rigid polyimide dispersant on mechanical properties of single-walled carbon nanotube/cyanate ester composite,” *ACS Applied Materials & Interfaces*, vol. 3, no. 5, pp. 1702–1712, 2011.
- [197] W. Yuan, J. Feng, Z. Judeh, J. Dai, and M. B. Chan-Park, “Use of polyimide-graft-bisphenol a diglyceryl acrylate as a reactive noncovalent dispersant of single-walled carbon nanotubes for reinforcement of cyanate ester/epoxy composite,” *Chemistry of Materials*, vol. 22, no. 24, pp. 6542–6554, 2010.
- [198] J. Cha, S. Jin, J. H. Shim, C. S. Park, H. J. Ryu, and S. H. Hong, “Functionalization of carbon nanotubes for fabrication of CNT/epoxy nanocomposites,” *Materials & Design*, vol. 95, pp. 1–8, 2016.
- [199] E. Y. Choi, S. C. Roh, and C. K. Kim, “Noncovalent functionalization of multi-walled carbon nanotubes with pyrene-linked nylon66 for high performance nylon66/multi-walled carbon nanotube composites,” *Carbon*, vol. 72, pp. 160–168, 2014.
- [200] J. M. Gonzalez-Dominguez, M. A. Tesa-Serrate, A. Anson-Casaos, A. M. Diez-Pascual, M. A. Gomez-Fatou, and M. T. Martinez, “Wrapping of SWCNTs in polyethylenoxide-based amphiphilic diblock copolymers: an approach to purification, debundling, and integration into the epoxy matrix,” *Journal of Physical Chemistry C*, vol. 116, no. 13, pp. 7399–7408, 2012.
- [201] N. E. Kallmyer, T. Huynh, J. C. Graves, J. Musielewicz, D. Tamiev, and N. F. Reuel, “Influence of sonication conditions and wrapping type on yield and fluorescent quality of noncovalently functionalized single-walled carbon nanotubes,” *Carbon*, vol. 139, pp. 609–613, 2018.
- [202] Q. L. Xiong and S. A. Meguid, “Atomistic investigation of the interfacial mechanical characteristics of carbon nanotube reinforced epoxy composite,” *European Polymer Journal*, vol. 69, pp. 1–15, 2015.
- [203] J. Chen, X. Cui, Y. Zhu, W. Jiang, and K. Sui, “Design of superior conductive polymer composite with precisely controlling carbon nanotubes at the interface of a co-continuous polymer blend via a balance of π - π interactions and dipole-dipole interactions,” *Carbon*, vol. 114, pp. 441–448, 2017.
- [204] M. Wong, M. Paramsothy, X. J. Xu, Y. Ren, S. Li, and K. Liao, “Physical interactions at carbon nanotube-polymer interface,” *Polymer*, vol. 44, no. 25, pp. 7757–7764, 2003.
- [205] J. M. Wernik, B. J. Cornwell-Mott, and S. A. Meguid, “Determination of the interfacial properties of carbon nanotube reinforced polymer composites using atomistic-based continuum model,” *International Journal of Solids and Structures*, vol. 49, no. 13, pp. 1852–1863, 2012.
- [206] G. Zhu, X. Wang, Y. Jiang, and J. Zheng, “In situ construction of dual-noncovalent bonding to prepare enhanced carbon nanotubes/poly(methyl methacrylate) nanocomposites,” *Composites Science and Technology*, vol. 155, pp. 58–63, 2018.
- [207] R. K. Prusty, D. K. Rathore, and B. C. Ray, “CNT/polymer interface in polymeric composites and its sensitivity study at different environments,” *Advances in Colloid and Interface Science*, vol. 240, pp. 77–106, 2017.
- [208] R. Nadiv, R. M. F. Fernandes, G. Ochbaum et al., “Polymer nanocomposites: insights on rheology, percolation and molecular mobility,” *Polymer*, vol. 153, pp. 52–60, 2018.
- [209] C. Ma, H.-Y. Liu, X. Du, L. Mach, F. Xu, and Y.-W. Mai, “Fracture resistance, thermal and electrical properties of epoxy composites containing aligned carbon nanotubes by low magnetic field,” *Composites Science and Technology*, vol. 114, pp. 126–135, 2015.
- [210] C. Bower, R. Rosen, L. Jin, J. Han, and O. Zhou, “Deformation of carbon nanotubes in nanotube-polymer composites,” *Applied Physics Letters*, vol. 74, no. 22, pp. 3317–3319, 1999.
- [211] M. Shtein, R. Nadiv, N. Lachman, H. Daniel Wagner, and O. Regev, “Fracture behavior of nanotube-polymer composites: insights on surface roughness and failure mechanism,” *Composites Science and Technology*, vol. 87, pp. 157–163, 2013.
- [212] D. Qian, E. C. Dickey, R. Andrews, and T. Rantell, “Load transfer and deformation mechanisms in carbon nanotube-polystyrene composites,” *Applied Physics Letters*, vol. 76, no. 20, pp. 2868–2870, 2000.
- [213] G. G. Tibbetts and J. J. McHugh, “Mechanical properties of vapor-grown carbon fiber composites with thermoplastic matrices,” *Journal of Materials Research*, vol. 14, no. 7, pp. 2871–2880, 1999.
- [214] J. Gupta, C. Wan, D. M. Haddleton, and T. McNally, “Plasticisation and compatibilisation of poly(propylene) with poly(lauryl acrylate) surface modified MWCNTs,” *Polymer*, vol. 133, pp. 89–101, 2017.
- [215] D. Roy, N. Tiwari, K. Mukhopadhyay, and A. K. Saxena, “The effect of a doubly modified carbon nanotube derivative on the microstructure of epoxy resin,” *Polymer*, vol. 55, no. 2, pp. 583–593, 2014.
- [216] S. Mallakpour and A. N. Ezhieh, “Preparation and characterization of chitosan-poly(vinyl alcohol) nanocomposite films embedded with functionalized multi-walled carbon nanotube,” *Carbohydrate Polymers*, vol. 166, pp. 377–386, 2017.
- [217] K. C. Jajam, M. M. Rahman, M. V. Hosur, and H. V. Tippur, “Fracture behavior of epoxy nanocomposites modified with polyol diluent and amino-functionalized multi-walled carbon nanotubes: a loading rate study,” *Composites Part A: Applied Science and Manufacturing*, vol. 59, pp. 57–69, 2014.
- [218] A. Kis and A. Zettl, “Nanomechanics of carbon nanotubes,” *Philosophical Transactions of the Royal Society A: Mathematical, Physical and Engineering Sciences*, vol. 366, no. 1870, pp. 1591–1611, 2008.
- [219] A. O. Monteiro, P. B. Cachim, and P. M. F. J. Costa, “Mechanics of filled carbon nanotubes,” *Diamond and Related Materials*, vol. 44, pp. 11–25, 2014.
- [220] N. Karousis, N. Tagmatarchis, and D. Tasis, “Current progress on the chemical modification of carbon nanotubes,” *Chemical Reviews*, vol. 110, no. 9, pp. 5366–5397, 2010.
- [221] Y.-P. Sun, K. Fu, Y. Lin, and W. Huang, “Functionalized carbon nanotubes: properties and applications,” *Accounts of Chemical Research*, vol. 35, no. 12, pp. 1096–1104, 2002.
- [222] T. Wang, X. Hu, X. Qu, and S. Dong, “Noncovalent functionalization of multiwalled carbon nanotubes: application in hybrid nanostructures,” *Journal of Physical Chemistry B*, vol. 110, no. 13, pp. 6631–6636, 2006.
- [223] Y.-L. Zhao and J. F. Stoddart, “Noncovalent functionalization of single-walled carbon nanotubes,” *Accounts of Chemical Research*, vol. 42, no. 8, pp. 1161–1171, 2009.

- [224] P. S. Omurtag, B. Alkan, H. Durmaz, G. Hizal, and U. Tunca, "Indirect functionalization of multiwalled carbon nano tubes through non-covalent interaction of functional polyesters," *Polymer*, vol. 141, pp. 213–220, 2018.
- [225] C.-C. Yang, Y.-C. Lin, P.-I. Wang, D.-J. Liaw, and S.-W. Kuo, "Polybenzoxazine/single-walled carbon nanotube nanocomposites stabilized through noncovalent bonding interactions," *Polymer*, vol. 55, no. 8, pp. 2044–2050, 2014.
- [226] S. Shenogin, L. Xue, R. Ozisik, P. Keblinski, and D. G. Cahill, "Role of thermal boundary resistance on the heat flow in carbon-nanotube composites," *Journal of Applied Physics*, vol. 95, no. 12, pp. 8136–8144, 2004.
- [227] S. T. Huxtable, D. G. Cahill, S. Shenogin et al., "Interfacial heat flow in carbon nanotube suspensions," *Nature Materials*, vol. 2, no. 11, pp. 731–734, 2003.
- [228] S. Shenogin, A. Bodapati, L. Xue, R. Ozisik, and P. Keblinski, "Effect of chemical functionalization on thermal transport of carbon nanotube composites," *Applied Physics Letters*, vol. 85, no. 12, pp. 2229–2231, 2004.
- [229] T. C. Clancy and T. S. Gates, "Modeling of interfacial modification effects on thermal conductivity of carbon nanotube composites," *Polymer*, vol. 47, no. 16, pp. 5990–5996, 2006.
- [230] M. B. Bryning, D. E. Milkie, M. F. Islam, J. M. Kikkawa, and A. G. Yodh, "Thermal conductivity and interfacial resistance in single-wall carbon nanotube epoxy composites," *Applied Physics Letters*, vol. 87, no. 16, article 161909, 2005.
- [231] V. Varshney, A. K. Roy, T. J. Michalak, J. Lee, and B. L. Farmer, "Effect of curing and functionalization on the interface thermal conductance in carbon nanotube-epoxy composites," *JOM*, vol. 65, no. 2, pp. 140–146, 2013.
- [232] L. Gao, X. Zhou, and Y. Ding, "Effective thermal and electrical conductivity of carbon nanotube composites," *Chemical Physics Letters*, vol. 434, no. 4–6, pp. 297–300, 2007.
- [233] N. A. Fasanella and V. Sundararaghavan, "Atomistic modeling of thermal conductivity of epoxy nanotube composites," *JOM*, vol. 68, no. 5, pp. 1396–1410, 2016.
- [234] H. Huang, L. Chen, V. Varshney, A. K. Roy, and S. Kumar, "Investigation of phonon transport and thermal boundary conductance at the interface of functionalized SWCNT and poly (ether-ketone)," *Journal of Applied Physics*, vol. 120, no. 9, article 095102, 2016.
- [235] S. Ju and Z. Y. Li, "Theory of thermal conductance in carbon nanotube composites," *Physics Letters A*, vol. 353, no. 2-3, pp. 194–197, 2006.
- [236] Z. Xu and M. J. Buehler, "Nanoengineering heat transfer performance at carbon nanotube interfaces," *ACS Nano*, vol. 3, no. 9, pp. 2767–2775, 2009.
- [237] S. Y. Kim, H. G. Jang, C.-M. Yang, and B. J. Yang, "Multiscale prediction of thermal conductivity for nanocomposites containing crumpled carbon nanofillers with interfacial characteristics," *Composites Science and Technology*, vol. 155, pp. 169–176, 2018.
- [238] H. Zhong and J. R. Lukes, "Interfacial thermal resistance between carbon nanotubes: molecular dynamics simulations and analytical thermal modeling," *Physical Review B*, vol. 74, no. 12, article 125403, 2006.
- [239] D. Estrada and E. Pop, "Imaging dissipation and hot spots in carbon nanotube network transistors," *Applied Physics Letters*, vol. 98, no. 7, article 073102, 2011.
- [240] F. H. Gojny, M. H. G. Wichmann, B. Fiedler et al., "Evaluation and identification of electrical and thermal conduction mechanisms in carbon nanotube/epoxy composites," *Polymer*, vol. 47, no. 6, pp. 2036–2045, 2006.
- [241] B. Fiedler, F. H. Gojny, M. H. G. Wichmann, M. C. M. Nolte, and K. Schulte, "Fundamental aspects of nano-reinforced composites," *Composites Science and Technology*, vol. 66, no. 16, pp. 3115–3125, 2006.
- [242] S.-Y. Yang, C.-C. M. Ma, C.-C. Teng et al., "Effect of functionalized carbon nanotubes on the thermal conductivity of epoxy composites," *Carbon*, vol. 48, no. 3, pp. 592–603, 2010.
- [243] Y. Kuang and B. Huang, "Effects of covalent functionalization on the thermal transport in carbon nanotube/polymer composites: a multi-scale investigation," *Polymer*, vol. 56, pp. 563–571, 2015.
- [244] C. H. Liu and S. S. Fan, "Effects of chemical modifications on the thermal conductivity of carbon nanotube composites," *Applied Physics Letters*, vol. 86, no. 12, article 123106, 2005.
- [245] C. Baudot and C. M. Tan, "Covalent functionalization of carbon nanotubes and their use in dielectric epoxy composites to improve heat dissipation," *Carbon*, vol. 49, no. 7, pp. 2362–2369, 2011.
- [246] W. Chen, J. Zhang, and Y. Yue, "Molecular dynamics study on thermal transport at carbon nanotube interface junctions: effects of mechanical force and chemical functionalization," *International Journal of Heat and Mass Transfer*, vol. 103, pp. 1058–1064, 2016.
- [247] C. Guo, F. Xin, C. Zhai, and Y. Chen, "Flammability and thermal properties of modified carbon nanotubes in poly(lactic acid)," *Journal of Thermoplastic Composite Materials*, vol. 27, article 089270571878567, 2018, In Press.

Review Article

Microstructure Characteristics of GFRP Reinforcing Bars in Harsh Environment

Hilal El-Hassan  and Tamer El Maaddawy

Department of Civil and Environmental Engineering, UAE University, Al Ain, Abu Dhabi, P.O. Box 15551, UAE

Correspondence should be addressed to Hilal El-Hassan; helhassan@uaeu.ac.ae

Received 15 January 2019; Revised 5 March 2019; Accepted 13 March 2019; Published 1 April 2019

Guest Editor: Alena Šišková

Copyright © 2019 Hilal El-Hassan and Tamer El Maaddawy. This is an open access article distributed under the Creative Commons Attribution License, which permits unrestricted use, distribution, and reproduction in any medium, provided the original work is properly cited.

Fiber reinforced polymer (FRP) composites have been suggested as corrosion-resistant alternatives to traditional steel reinforcement in concrete structures. Within this family of composites, glass fiber reinforced polymers (GFRPs) have been gaining momentum as the primary selection of FRP for construction applications. Despite being advantageous, its wide adoption by the industry has been hindered due to the degradation of its performance in severe environmental conditions. As such, significant studies have been carried out to assess the mechanical properties of GFRP bars subject to different conditioning schemes. However, the inconsistencies and wide variations of results called for more in-depth microstructure evaluation. Accordingly, this paper presents a critical review of existing research on the microstructure of GFRP reinforcing bars exposed to various conditioning regimes. The review analysis revealed that sustained load limits set by codes and standards were satisfactory for nonaggressive environment conditions but should be updated to include different conditioning regimes. It was also found that conditioning in alkaline solutions was more severe than concrete and mortars, where test specimens experienced irreversible chemical degradation, more hydroxyl group formation, and more intense degradation to the microstructure. The progression of hydrolysis was reported correlatively through an increase in hydroxyl groups and a decrease in the glass transition temperature. While moisture uptake was the primary instigator of hydrolysis, restricting it to 1.6% could limit the reduction in tensile strength to 15%. Further, the paper identifies research gaps in the existing knowledge and highlights directions for future research.

1. Introduction

Reinforced concrete structures are designed with certain life expectancy under normal service conditions. However, exposure to severe environments may reduce the design service life due to unanticipated durability problems, including corrosion of steel reinforcement. The corrosion of steel reinforcing bars causes cracking and spalling of concrete, creating major reductions in performance and a significant increase in cost for rehabilitation. In fact, Koch [1] reported that 3-4% of each nation's gross domestic product is dedicated to corrosion-related expenditures. As a form of corrosion management, glass fiber reinforced polymer (GFRP) reinforcing bars have been proposed as a replacement to steel equivalents. This alternative reinforcement is characterized by its light weight, high strength-to-weight ratio, and corrosion

resistance [2-4]. However, conflicting results on the degradation of its properties upon exposure to alkaline or acidic solution, moisture/water, and elevated temperatures have been a major setback in its adoption by the construction industry [2-4].

For the last few years, extensive research has been carried out to investigate the durability performance of GFRP reinforcement exposed to different environmental conditions. Research findings have identified the major contributors to deterioration of GFRP as moisture uptake, alkaline environment, and temperature. Moisture penetrates the matrix by the flow of solution into the microgaps between polymer chains and capillary transport through fiber/matrix interfacial microcracks and in microcracks formed during manufacturing [5]. As a result, the matrix exhibits plasticisation, leading to a reduction in strength and glass

transition temperature. On the other hand, alkaline solutions break the bond between the oxygen and carbon atoms in the molecular chain of the GFRP matrix. This breakage creates microcracks and fractures in the matrix structure, leading to more moisture uptake and a significant reduction in strength. Further, to expedite investigative work conducted on GFRP reinforcing bars, higher temperatures have been employed. Vijay and GangaRao [6] reported that an increase in the conditioning temperature led to an exponential amplification in the actual age. Nevertheless, it should be noted that the elevated temperatures employed in most work may have affected the physical properties of the bars by increasing the coefficient of thermal expansion [7] and, thus, may have altered the behavior of the GFRP bars, rendering the results, in some cases, unrealistic.

With the majority of past work characterizing the durability performance of GFRP bars, several researchers have reviewed and summarized these publications to highlight the gaps in existing knowledge and propose future direction of research. In contrast, much fewer and more recent investigations have correlated the degradation in GFRP to changes in the microstructure. Yet, there is no such review and summary of these in-depth investigations. Accordingly, this paper aims to present an overview of recent studies examining the effect of conditioning on the microstructure of GFRP reinforcing bars. Research findings obtained help to shed light on the morphological and microstructure changes in GFRP bars subject to different exposure conditions using various microstructure characterization techniques, including differential scanning calorimetry (DSC), thermogravimetric analysis (TGA), Fourier transform infrared spectroscopy (FTIR), and scanning electron microscopy (SEM). A correlation among these microstructural evaluation techniques is reported. The influence of moisture uptake on the microstructure of conditioned GFRP bars is also evaluated.

2. Taxonomy

GFRP reinforcing bars are made of glass fibers impregnated with an organic resin or matrix. Typical diameters range between 8 and 20 mm with smooth surfaces for smaller sizes and ribbed and/or sand-coated surfaces for larger counterparts. GFRP reinforcement falls within the family of FRP composites. The taxonomy on the studies of FRP composites is presented in Figure 1. They can be classified based on their fiber type, resin type, and application. Different combinations of fibers and resins have been employed in the production of FRPs, of which composites made with glass fibers and vinylester are the most common. Also, FRPs have been used across many industries, including aerospace, automotive, sports, musical, and construction. In the latter industry, they have been employed in new and existing buildings as internal and external reinforcing bars and for repair, strengthening, and retrofitting purposes. The literature has especially focused on the ability of FRPs to replace steel as the main reinforcement in concrete structures [8–15]. However, before being widely adopted by the construction industry, their durability performance was

rigorously investigated. Accordingly, GFRP reinforcing bars have been conditioned in various media, including acidic and alkaline solutions, concrete, tap water, and seawater. Elevated temperatures were also employed during conditioning to accelerate the degradation process. Further, the validity of the environmental reduction factors and creep rupture stress limits adopted by the current international guidelines and standards were assessed by applying a sustained load to GFRP bars exposed to severe environments. Such specimens were examined for performance retention by measuring the tensile properties after conditioning. Correlations between the properties and microstructural changes were evaluated using DSC, TGA, SEM, FTIR, and moisture uptake.

3. GFRP Reinforcing Bars

The properties of GFRP reinforcing bars and conditions to which they are exposed are primary factors affecting their performance and microstructure. As such, a comprehensive review of the literature on the physical and mechanical properties and conditioning of GFRP bars is presented in the sections below. It should be noted that the literature reviewed in this paper focuses on examining the microstructure characteristics of GFRP bars exposed to different conditioning regimes.

3.1. Physical Properties. Prior to conducting any experimental testing on GFRP reinforcing bars, their physical properties were determined. Various tests, shown in Table 1, were typically carried out to measure the diameter, void content, fiber content, moisture uptake, glass transition temperature, and thermal expansion coefficient. Physical properties reported in past studies are summarized in Table 2. The most commonly used glass and matrix materials were E-glass and vinylester, with 90 and 74% of the conducted research having used this fiber and matrix, respectively, as shown in Figure 2. Epoxy, on the other hand, has been only recently employed as the resin of GFRP reinforcing bars, with 14% of published work having explored its combination with E-glass [8, 10, 11, 23, 41, 42]. The diameter has also been varied between 8 and 44.5 mm, with the majority being approximately 12 mm. Yet, Benmokrane, et al. [24] concluded that the bar diameter had limited influence on the physical and mechanical properties of GFRP reinforcing bars. Furthermore, very limited work reported the thermal expansion coefficients, as it was not typically measured by researchers, but provided by the manufacturer [8, 13, 14, 24–27]. In contrast, the moisture uptake has been essential in characterizing the performance and assessing its retention capacity. It ranged between 0.01 and 1.59%, by mass, for unconditioned/control specimens. The fiber content was measured by volume and mass. However, the latter was more commonly reported with the availability of standardized test procedures (ASTM D3171 and ASTM E1868). Measured values ranged between 70 and 83%. The volumetric fiber content, on the other hand, was mainly provided by the manufacturer and could only be determined at the initial stages of production.

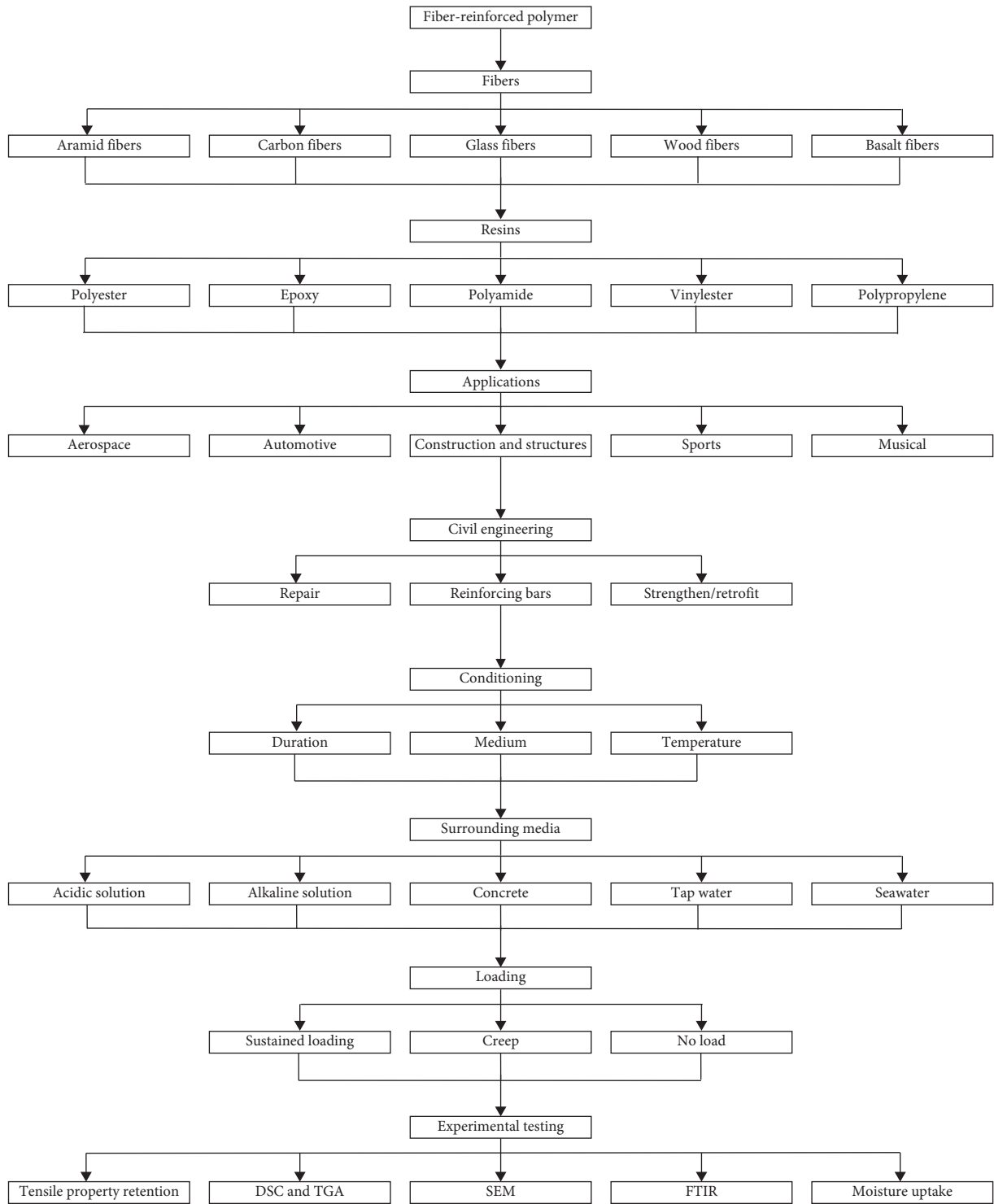


FIGURE 1: Taxonomy on the studies of fiber reinforced polymer composites.

3.2. *Mechanical Properties.* The performance of GFRP reinforcing bars is typically characterized by its ability to retain its mechanical properties. For this reason, as-received and unconditioned specimens were tested for various performance indicators, as summarized in Table 3, including tensile and flexural strength, strain, and modulus. Shear strength was also reported in relevant work. Experimental

results of a number of studies are shown in Table 4. Over 90% of the studies focused on tensile properties, with values of tensile strength, modulus, and strain in the range of 432–1321 MPa, 31–65 GPa, and 1–3%, respectively. Given the large database of results for the former two properties, it was possible to develop a relation between them. Figure 3 presents a correlation between tensile modulus (E_t) and

TABLE 1: Summary of standardized testing for physical properties.

Property (unit)	Standardized test	Reference
Diameter (mm)	ACI 440.3R & ASTM D7205	[3, 16]
Void content (%)	ASTM D3171 & ASTM D2734	[17, 18]
Fiber content, by mass (%)	ASTM D3171 & ASTM E1868	[17, 19]
Moisture uptake (%)	ASTM D570	[20]
Glass transition temperature ($^{\circ}\text{C}$)	ASTM E1356	[21]
Thermal expansion coefficient ($1/^{\circ}\text{C}$)	ASTM E831	[22]

TABLE 2: Physical properties of GFRP reinforcing bars.

Reference	Glass material	Matrix material	Diameter (mm)	Long. thermal expansion coef. ($\times 10^{-6}/^{\circ}\text{C}$)	Trans. thermal expansion coef. ($\times 10^{-6}/^{\circ}\text{C}$)	Moisture absorption (%)	Fiber content (% by volume)	Fiber content (% by mass)
[7]	E-glass	Vinylester	9.5	—	—	0.1	—	74.5
[8]	E-glass	Vinylester polyester epoxy	12	—	17.7–20.8	0.23–1.15	—	78.8–83.9
[9]	Short Glass E-glass	Vinylester	15.0–20.0	—	—	—	—	83
[10]	E-glass	Epoxy	8.0–9.0	—	—	0.1	—	75.5–78.3
[11]	E-glass	Epoxy	8.0–9.0	—	—	0.10	—	75–78
[12]	E-glass E-glass 366 Advantex 366 Advantex 712	Polyester vinylester	9.3–12.0	—	—	0.01–0.05	—	—
[13]	E-glass	Vinylester	19.0	6.1	23.5	0.48	65.4	74.5
[14]	E-glass	Vinylester	12.7	5.5	29.5	0.38	60.3	77.9
[15]	E-glass	Vinylester	9.5	—	—	—	65	—
[23]	E-glass	Vinylester polyester epoxy	12	—	—	0.23–1.15	—	78.8–83.9
[24]	E-glass	Vinylester	9.5–25.4	—	20.5–22.0	0.02–0.15	80.9–83.0	—
[25]	E-glass	Vinylester	12.7	6.7	27.2	0.62	64.3	81.5
[26]	E-glass	Vinylester	12.7	5.5	29.5	0.38	—	77.9
[27]	E-glass	Vinylester polyester	25.4–44.5	6.9–7.8	21.0–27.1	0.05–1.59	—	79.6–81.5
[28]	E-glass	Vinylester	8.0	—	—	—	—	—
[29]	E-glass	Vinylester	9	—	—	—	70	—
[30]	E-glass	Vinylester	12	—	—	—	—	83
[31]	E-glass	Epoxy	14	—	—	0.01	—	—
[32]	E-glass	Vinylester	12	—	—	—	—	83
[33]	E-glass	Vinylester	9.5	—	—	—	—	—
[34]	E-glass	Vinylester	12.7	—	—	0.37	—	81.5
[35]	E-glass	Vinylester	9.5–16.0	—	—	—	75	—
[36]	E-glass	Vinylester	12.7	—	—	—	—	69.1–73.3
[37]	E-glass	Vinylester	12	—	—	—	—	83
[38]	E-glass	Vinylester	—	—	—	—	—	—
[39]	E-glass	Vinylester	10	—	—	0.4	—	—
[40]	E-glass	Vinylester	—	—	—	—	—	—

square root of tensile strength ($\sqrt{f_t}$) of GFRP bars. A linear trend line, in the form of Equation (1) could provide a prediction of tensile modulus from the strength with reasonable accuracy. On the other hand, flexural and shear properties were recorded on few occasions, mainly in research work related to bending and shear testing. Yet, the available data have shown a linear relationship between flexural (f_r) and tensile strength (f_t), as shown in Figure 4 and Equation (2). This linear relation provides a reasonably accurate prediction of the former from the latter without the

need for experimental testing. It is also worth noting that tensile properties of unconditioned GFRP samples made with epoxy as the matrix material seem to be, on average, 14% higher than those of vinylester counterparts. Additionally, a correlation was made between the physical and mechanical properties of GFRP specimens made with E-glass and vinylester. From Figure 5, it is clear that the tensile strength and modulus are generally proportional to the fiber content, up to a maximum value of 83%, by mass. Similarly, Micelli and Nanni [44] reported that GFRP bars

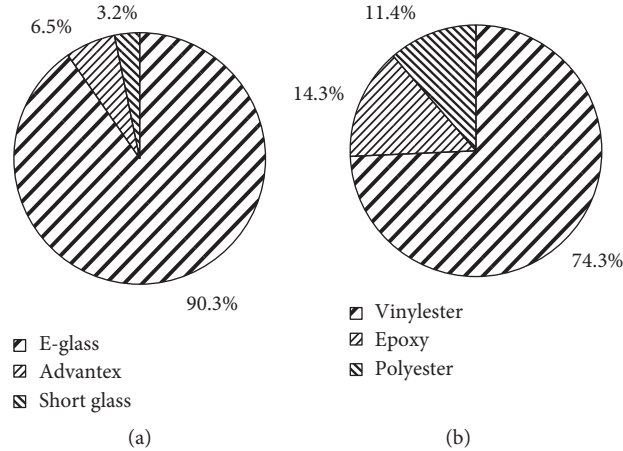


FIGURE 2: Percentage distribution of GFRP components. (a) Glass fiber material. (b) Matrix material.

TABLE 3: Summary of standardized testing for mechanical properties.

Mechanical property (unit)	Standardized test	Reference
Tensile strength (MPa)	ACI 440.3R & ASTM D7205	[3, 16]
Tensile strain (%)	ACI 440.3R & ASTM D7205	[3, 16]
Tensile modulus (MPa)	ACI 440.3R & ASTM D7205	[3, 16]
Flexural strength (MPa)	ASTM D4476	[43]
Flexural strain (%)	ASTM D4476	[43]
Flexural modulus (MPa)	ASTM D4476	[43]
Shear strength (MPa)	ACI 440.3R	[3]

with lower fiber content may experience inferior mechanical performance.

$$E_t = 1.67\sqrt{f_t} \quad (1)$$

$$f_r = 1.28f_t \quad (2)$$

3.3. Conditioning. The durability performance of GFRP reinforcing bars exposed to different environmental conditions has been evaluated using accelerated aging tests. Four main exposure parameters were investigated: surrounding medium, conditioning duration, conditioning temperature, and presence of a sustained load. Table 5 summarizes the exposure conditions employed by various studies on the microstructure of GFRP bars. It should be noted that only one study reviewed in this work, assessing the microstructure, has investigated the effect of acidic solutions on the performance of GFRP. Seawater exposure has also received little attention, although it is critical to assess the properties and microstructure of GFRP bars for employment in offshore structures and bridge decks in coastal cities and seaports [10, 11, 42]. According to Figure 6(a), alkaline and water solutions have been utilized in 39 and 25% of the studies shown herein. It seems that the

ease of preparing such media renders them most favourable among researchers, especially that the former is proposed to simulate concrete alkalinity and behavior. Concrete, on the other hand, has been used by 23% of presented research, even though it better represents real-life scenarios.

The duration of conditioning has been widely altered in research studies and ranged between 0.02 and 7200 days. Figure 6(b) shows that 28, 18, 10, 23, and 21% of studies have conditioned GFRP bars for a maximum of 0–90, 91 to 180, 181 to 240, 241 to 365, and more than 365 days, respectively. Clearly, the majority of research has focused on examining the effects of early age and prolonged conditioning.

The conditioning temperature has been pivotal in accelerating aging of GFRP specimens. Work by Vijay and GangaRao [6] highlighted the relationship between actual age in calendar days at Morgantown, WV, and chamber conditioning days in the form of Equation (3), where T is the temperature in °F. It is worth noting that in their experiments, they [6] placed the specimens in a weathering chamber, i.e., a controlled temperature environment, and in alkaline solutions. Effectively, an increase in chamber conditioning temperature (T) led to an amplification in the actual age. Thus, the conditioning temperature has been altered within and among different studies. In general, they have ranged between 20°C and 90°C, with the exceptions of [25, 32], which investigated the performance of GFRP bars subject to freezing and elevated temperatures. Based on Equation (3), such conditioning temperatures (20°C–90°C) could accelerate the aging by at least four times when specimens are conditioned in alkaline solutions. For instance, alkaline conditioning for 30 days in a chamber at 50°C is equivalent to an actual age of 2660 days (approx. 7 years) at Morgantown, WV. Yet, this equation may not be applicable to specimens encased in concrete or conditioned in regimes other than alkaline solutions. Figure 6(c) highlights the distribution of conditioning temperatures, with 77% of studies utilizing conditioning temperatures above 50°C. Nevertheless, it should be noted that such temperatures may affect the physical properties of the bars by increasing the coefficient of thermal expansion [7] and, thus,

TABLE 4: Mechanical properties of unconditioned GFRP reinforcing bars.

Reference	Tensile strength (MPa)	Tensile modulus (GPa)	Tensile strain (%)	Flexural strength (MPa)	Flexural modulus (GPa)	Flexural strain (%)	Shear strength (MPa)
[7]	653	38.5	—	888	—	—	—
[8]	—	—	—	1150–1573	56.9–663.3	2.02–2.54	250–270
[9]	1105–1184	62.6–64.7	1.71–1.89	—	—	—	—
[10]	816–1321	52–53	—	—	—	—	—
[11]	816–1321	52–53	—	—	—	—	—
[12]	612–958.3	31.6–51.8	—	—	—	—	—
[13]	728	47.6	1.53	—	—	—	—
[14]	786	46.3	1.7	1005	46.8	2.15	212
[15]	644.7	53.4	1.2	—	—	—	—
[23]	1015–1220	—	—	—	—	—	—
[24]	1237.4–1315.3	60.0–62.5	2.1–2.3	1406.3–1757.5	—	—	—
[25]	788	47.2	1.7	1095	52.6	2.15	185
[26]	786	46.3	1.7	—	—	—	—
[27]	—	—	—	759–1324	49.3–54.1	—	151–197
[28]	821	44.4	1.84	—	—	—	—
[29]	1200	42.9	2.8	—	—	—	—
[30]	1478	60.4	2.45	—	—	—	—
[31]	714.6	55	1.62	—	—	—	—
[32]	1478	60.4	2.45	—	—	—	—
[33]	700	40.8	—	—	—	—	—
[34]	854	43.0	—	—	—	—	—
[35]	580–658	40–42	1.4–1.6	—	—	—	—
[36]	660.6–692.8	38.5–42.7	—	—	—	—	36.9–42.3
[37]	432–1478	41.9–60.4	1.04–2.45	—	—	—	—

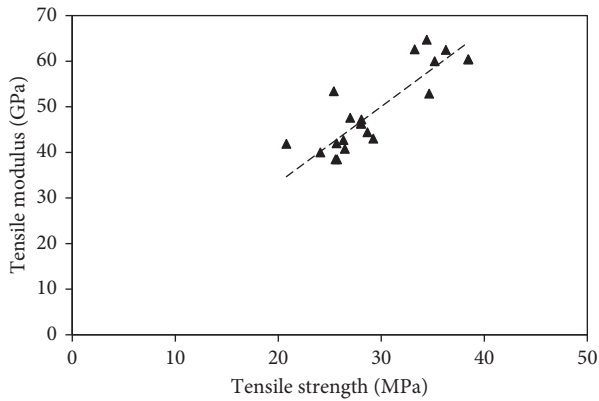


FIGURE 3: Relationship between tensile modulus and strength of GFRP bars.

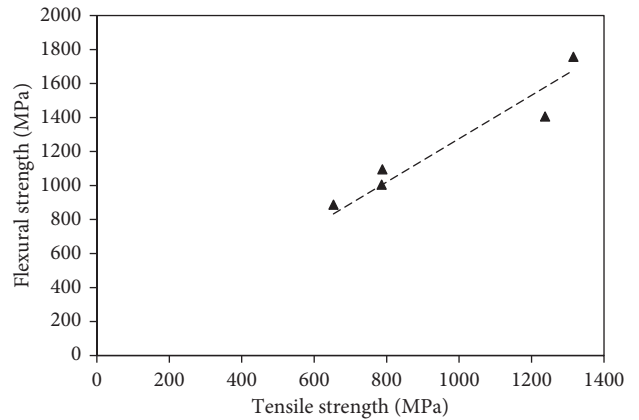


FIGURE 4: Correlation between flexural and tensile strength of GFRP bars.

may alter the behavior of the GFRP bars, rendering unrealistic results.

$$\frac{\text{Age in calendar days}}{\text{Chamber conditioning days}} = 0.098e^{0.0558T} \quad (3)$$

3.4. Loading. The degradation of GFRP reinforcing bars could be intensified in the presence of a sustained load during conditioning [53–55]. ACI 440.1R [2] limits the tensile stress in GFRP under service conditions to 14% of the ultimate tensile strength (UTS), considering the strength reduction factor for environmental exposure. Higher stress levels caused a shift in the degradation mechanism of GFRP from being affected by the rate of diffusion of alkaline

solutions to being controlled by solution transport through resin cracks [56]. Nevertheless, it can be noted from Figure 6(d) that only 27% of investigated microstructure studies applied a sustained load to GFRP bars, with values ranging from 0 to 80% UTS. The objectives of these works, nonetheless, were different. While some researchers applied sustained loads within the limits specified by codes and standards [2, 4, 57–60], others explored the possibility of increasing this allowable limit [11, 12, 28, 33–35, 52]. Some of these latter studies concluded that the limits recommended by codes and standards were conservative for specific reinforcing bars and conditions. In fact, elevated temperatures could accelerate the degradation induced by conditioning. As a result, the limits were found to be

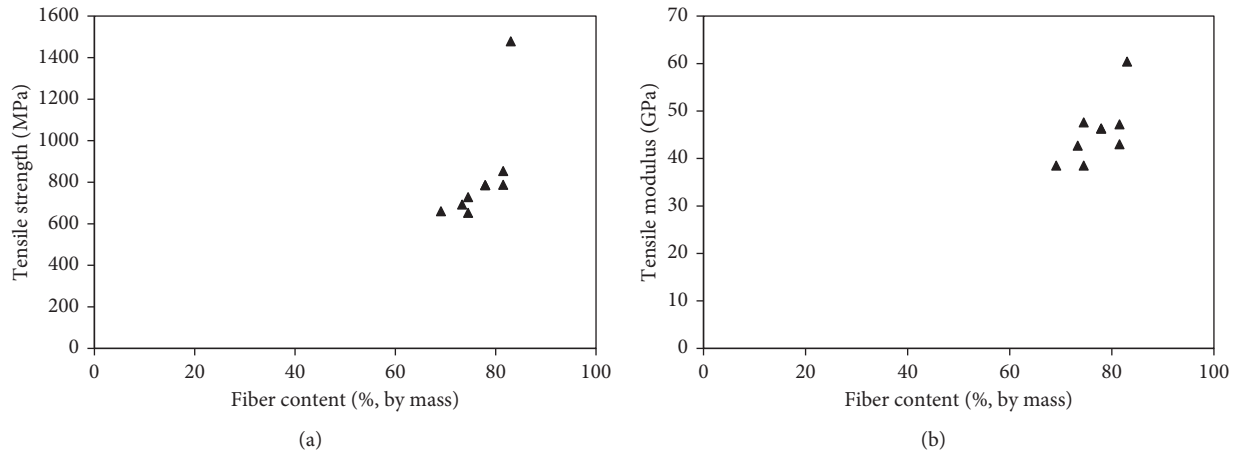


FIGURE 5: Correlation between fiber content and mechanical properties. (a) Tensile strength. (b) Tensile modulus.

TABLE 5: Summary of conditioning regimes in studies investigating the microstructure of GFRP reinforcing bars.

Reference	Surrounding media				Conditioning		Loading		
	Alkaline	Concrete	Water	Seawater	Acidic	Duration (days)	Temperature (°C)	Yes (% UTS ¹)	No
[7]			x			40 to 120	23 to 80		x
[8]	x					41.7 to 208.3	60		x
[9]	x	x				30 to 60	-30 to 60		x
[10]		x		x		150 to 450	20 to 60		x
[11]		x		x		150 to 450	20 to 60	25	
[12]	x	X				Up to 1445	-	20-65	
[13]			x			60 to 180	23 to 50		x
[14]		x	x			60 to 240	23 to 50		x
[15]	x					100 to 660	40		x
[23]	x					41.67 to 208.33	22 to 60		x
[42]				x		90 to 365	23 to 65		x
[24]	x					90	60		x
[25]			x			0.0208 to 0.1285	-100 to 325		x
[26]	x	x				60 to 365	23 to 70		x
[27]	x					30 to 180	23 to 60		x
[28]	x					30 to 270	23	0-25	
[29]	x		x	x	x	28 to 50	60 to 80		x
[30]	x		x	x		180 to 540	23 to 50		x
[31]	x					30 to 720	60		x
[32]		x				0.0417 to 0.125	100 to 300		x
[33]	x	x	x			90 to 730	60	20 & x ²	
[34]		x	x			60 to 240	23 to 50	20-80	
[35]	x		x			30 to 120	20 to 73	19-29	
[36]	x		x	x		30 to 132	-25 to 80		x
[37]		x	x	x		180 to 540	23 to 50		x
[38]		x ²				1825 to 2920	-24 to 30	x ²	
[39]	x					30 to 365	23 to 75		x
[40]	x		x			54.2	22 to 90		x
[44]	x	x				21 to 42	-18 to 49		x
[45]	x		x			15 to 60	60		x
[46]	x		x			42 to 365	20 to 60	15	
[47]		x				30 to 270	20 to 60	10-15	
[48]	x					30 to 180	60		x
[49]	x					41.7	60		x
[50]	x					20 to 120	20 to 70		x
[51]			x	x		41.7	20 to 70		x
[52]	x	x	x			90 to 730	60	20 & x ¹	

¹Ultimate tensile strength. ²Natural weathering conditions.

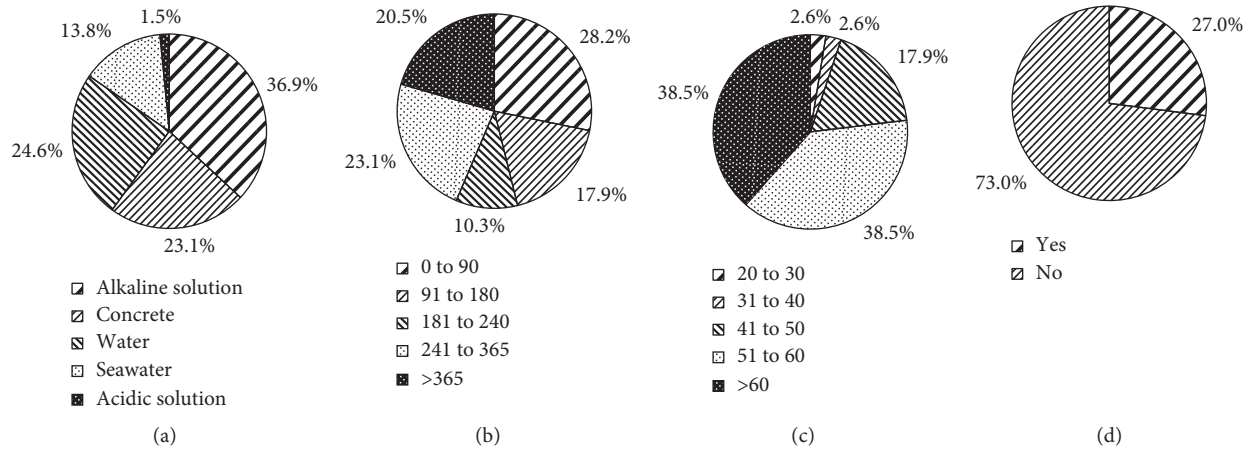


FIGURE 6: Percentage distribution of conditioning parameters. (a) Surrounding media. (b) Maximum conditioning duration (days). (c) Maximum conditioning temperature ($^{\circ}\text{C}$). (d) Presence of sustained loading.

inappropriate and required revision through further research data.

3.5. Reduction Factors. The effects of service time, relative humidity, and temperature are incorporated into an environmental reduction factor for GFRP bars used as internal reinforcement in concrete structures. ACI 440.1R [2] relates the design (f_{fu}^*) and guaranteed tensile strength (f_{fu}) using the proposed reduction factors (C_E). The relationship is shown as Eq. (4). The reduction factors for environmental conditions, shown in Table 6, ranged between 0.3 and 1.0. Lower values were associated with higher relative humidity, service time, and temperature, while a reduction factor of 1 was typically attributed to less severe conditioning [61]. Another load reduction factor was introduced by several researchers and codes to account for the presence of a sustained load [2, 4, 58–60]. Its value ranged between 0.2 and 1.0, with more recent codes suggesting lower reduction factors. This is associated to the wide variations of results reported and somewhat concerning impact of accelerated aging, even though extensive research has been conducted in this area. The combined effect of both factors has also been noted, as shown in the last column of Table 6, to vary between 0.13 and 0.50.

$$f_{fu} = C_E \cdot f_{fu}^* \quad (4)$$

4. Microstructure Evaluation Methods

Microstructural characterization was employed to evaluate changes to GFRP reinforcing bars after conditioning and provide explanations to the degradation in mechanical properties. Of the many procedures available, TGA, SEM, FTIR, and DSC have been the most commonly used. Table 7 summarizes the types of microstructure tests conducted in each of the studies presented herein. While moisture uptake is not a typical microstructure evaluation method, it has been proven pivotal in understanding the causes of degradation in the properties of GFRP specimens [10]. Clearly,

SEM has been the most utilized of all tests. In fact, it has been employed in 92% of the studies reviewed, while DSC, FTIR, and moisture uptake have been used in only 40–43%, as shown in Figure 7. This is mainly due to SEM being able to highlight and identify morphological changes due to conditioning, which are typically characterized by matrix degradation, interfacial deterioration, and/or fiber etching. TGA, on the other hand, has been used in 5% of the studies reviewed herein. Its primary use was to determine the thermal degradation of the polymer matrix [12, 25]. Nevertheless, it is worth noting that the majority of researchers have resorted to more than one microstructure test to confirm experimental results and findings. It should also be noted that the results reported hereafter for conditioned samples are associated to the most severe conditioning scheme utilized in each study.

4.1. Moisture Uptake. Moisture penetrates into a composite material by the flow of solution into the microgaps between polymer chains, capillary transport through fiber/matrix interfacial microcracks, and in microcracks formed during manufacturing [5]. The diffusion process mainly depends on the type of matrix and surrounding environment. It can be measured as per the procedure of ASTM D570 [20]. Typical moisture absorption/uptake tests involve weighing samples before and after immersion. However, the hydrolysis reaction that may have occurred during conditioning could cause mass dissolution and, thus, affect the results. To account for this mass loss, samples are oven-dried for 24 hours at 100°C . This oven-dried mass would then be used to find the moisture uptake:

$$\begin{aligned} & \text{moisture uptake (\%, by mass)} \\ &= \frac{(\text{conditioned mass} - \text{oven dried mass})}{(\text{initial mass})} \times 100. \end{aligned} \quad (5)$$

Figure 8 is a typical moisture uptake curve that presents the increase in mass over conditioning time. Clearly, the diffusion rate of moisture is different for temperatures below

TABLE 6: Summary of reduction factors for GFRP reinforcing bars.

Reference	Country	Year	Reduction factor		
			Environmental	Creep/sustained load	Combined
ACI 440.1R [2]	USA	2015	0.7–0.8	0.2	0.14–0.16
FIB [4]	UK	1999	0.72	0.3	0.216
Ali, et al. [23]	Canada	2018	0.75–1.00	—	—
JSCE [57]	Japan	1997	0.77	—	—
CSA S6 [58]	Canada	2006	0.55	0.25	0.1375
NS 3473 [59]	Norway	1998	0.5	0.80–1.00	0.40–0.50
CSA S806 [60]	Canada	2012	0.75	0.3	0.225
Huang and Aboutaha [61]	USA	2010	0.31–1.00	—	—

TABLE 7: Summary of microstructure tests conducted on GFRP reinforcing bars.

Reference	Microstructure tests				
	Moisture uptake	TGA	SEM	FTIR	DSC
[7]	x				
[8]	x		x	x	x
[9]	x		x	x	
[10]			x	x	x
[11]	x		x	x	x
[12]	x	x	x		
[13]			x		
[14]			x	x	x
[23]	x		x	x	
[42]	x		x		
[24]	x			x	
[25]		x	x		x
[26]			x	x	x
[27]			x	x	x
[28]			x		
[29]			x		
[30]			x		
[31]	x		x	x	x
[32]			x		
[33]			x		
[34]	x		x	x	x
[35]			x	x	x
[36]			x		
[37]			x		
[38]			x	x	x
[39]	x		x	x	
[40]	x			x	
[44]			x		
[45]			x		
[46]	x		x		
[47]			x		
[48]	x			x	x
[49]			x		
[50]			x		
[51]			x		

and above 60°C. At temperatures of 60°C and below, the majority of the uptake occurs within the first 30 days of immersion. At higher temperatures, the uptake increases at a steady rate up to 50 days. Robert, et al. [7] explained that such behavior is owed to the amplification of thermo-mechanical degradation mechanisms at a temperature of 80°C. Further, the moisture uptakes for conditioned and unconditioned GFRP reinforcing bars tested in the past

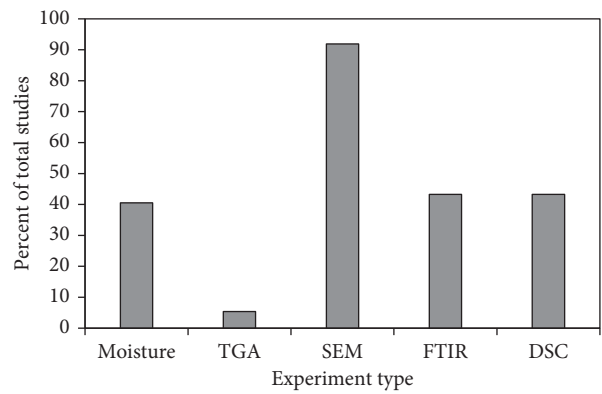


FIGURE 7: Percentage distribution of microstructure tests across investigated past research.

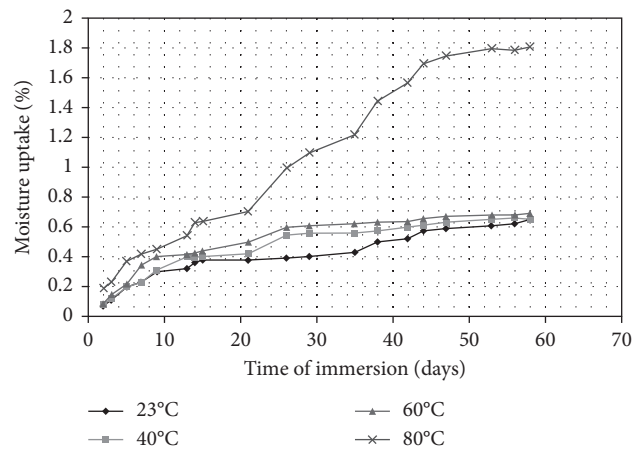


FIGURE 8: Typical moisture uptake curve of GFRP bars (adapted from [7]).

literature are summarized in Table 8. These values correspond to the most severe conditioning regime employed in each study. Results for conditioned samples ranged between 0.06 and 5.1, with vinylester-GFRP presenting the widest variations. Past researchers have discussed several factors that affected the uptake, namely, presence of a sustained load, void content, pH of conditioning medium, conditioning duration, and conditioning temperature [8–11, 24, 30, 32, 35, 38, 47, 56, 64, 65]. Each factor will be discussed in the sections below.

TABLE 8: Results of moisture uptake of GFRP reinforcing bars.

Reference	Unconditioned			Conditioned			Within high durability limits	
	Uptake (%)	Medium	Temperature (°C)	Time (days)	Sustained load	Uptake (%)	ACI 440.6 [62]	CSA S807 [63]
[7]	0.10	Water	80	58		1.80	Not Acceptable	Not Acceptable
[8]	0.23–1.15	Alkaline	50	21		0.25–1.36	Not Acceptable	Not Acceptable
[9]	0.00	Concrete	50	Saturation		0.44	Acceptable	Acceptable
[10]	0.10	Concrete	60	450		1.23–1.50	Not Acceptable	Not Acceptable
[11]	0.10	Concrete	60	288 & 372	x	1.95–2.54	Not Acceptable	Not Acceptable
[12]	0.05	Concrete	60	48.2	x	0.50	Acceptable	Acceptable
[23]	0.23–1.15	Alkaline	60	208.3		0.25–1.36	Not Acceptable	Not Acceptable
[42]	0.00	Seawater	65	365		5.10	Not Acceptable	Not Acceptable
[24]	0.02–0.15	Water	23	Saturation		0.20	Acceptable	Acceptable
[27]	0.05–1.59	Alkaline	50	21		0.06–1.63	Not Acceptable	Not Acceptable
[32]	0.01	Alkaline	60	720		0.74	Acceptable	Not Acceptable
[35]	0.37	Concrete	50	30	x	0.57	Acceptable	Acceptable
[40]	0.40	Alkaline	50	94		1.20	Not Acceptable	Not Acceptable
[44]	0.00	Alkaline	22	16.67		0.55	Acceptable	Acceptable
[46]	0.00	Alkaline	60	360.4	x	1.10	Not Acceptable	Not Acceptable
[48]	0.01	Alkaline	60	176		0.38	Acceptable	Acceptable

The effect of sustained load can be noted by comparing the results of [10, 11]. The only difference between these two researches is the addition of a sustained load of 25% UTS in [11]. Results, presented in Table 8, show that even with an average 26% shorter conditioning durations, the uptake was, on average, 68% higher. It is thus obvious that the addition of a sustained load can aggravate the moisture uptake.

Recent work by El-Hassan, et al. [10] compared two types of GFRP bars under similar exposure conditions. The void contents were measured as 0.10 and 0.23%. The authors reported higher moisture uptake in the latter GFRP bar with higher void content. However, with limited information on the void content or fiber content in the existing literature, it is difficult to create a general conclusion. Further work would be needed to investigate the effect of void content on performance retention and microstructure changes.

To simulate severe environments, researchers have utilized alkaline solutions with different pH. Values of pH ranged between 12 and 13.6. A recent study by D'Antino, et al. [66] reported that higher pH resulted in less tensile strength retention. Yet, immersion in simulated concrete pore (alkaline) solution is not a proper reproduction of real-life concrete. The main difference is the degree of contact of alkaline solution with the GFRP reinforcing bars. In the former case, the surface of the bar is entirely coated by the solution, resulting in maximum contact area, while in the latter case, alkaline solutions remain in the concrete pores, causing limited contact with the imbedded GFRP bar. In the case of moist concrete, representing underwater concrete, the degree of contact is intermediary between the dry concrete and wet alkaline solution.

Conditioning temperature and duration have been widely investigated. Figure 8 shows the effect of each of these conditions on the moisture uptake. It is clear that higher temperatures and longer exposure durations resulted in more uptake. Yet, it is worth noting that the former was the more influential factor of the two, thus, causing a more exacerbated degradation phenomenon. Robert, et al. [7] concluded that a thermomechanical degradation mechanism would occur at

an elevated temperature of 80°C, owing to higher solution diffusion in a more porous resin matrix. Nevertheless, such conditioning temperature does not correspond to service life conditions of GFRP bars, justifying the maximum aging temperature recommended by ACI 440.3 [3] and CSA S806 [60] being 60°C.

ACI 440.6 [62] and CSA S807 [63] propose durability limits in the form of maximum allowable moisture/water uptake. These limits are 1 and 0.75%, by mass, respectively, regardless of the exposure conditions. Table 8 shows the comparison of conditioned GFRP reinforcing bars with each limit. It is clear that more than half of the bars tested were not classified of high durability, based on moisture uptake. In fact, Figure 9 shows that 56 and 62% of bars, tested under the worst conditions in each study, failed to fall within the high durability limits of ACI 440.6 [62] and CSA S807 [63], respectively. In general, samples conditioned in alkaline solution at temperatures beyond 50°C were deemed unacceptable [8, 23, 27, 39, 46]. GFRP bars imbedded in concrete resulted in uptakes within the acceptable range, except for El-Hassan, et al. [11], where a sustained load of 25% UTS was applied, which is higher than the maximum allowable load recommended by ACI 440.1R [2]. A general comparison between alkaline and concrete conditioned GFRPs shows higher uptake in the former case and lower degree of satisfactoriness by the codes. Therefore, it should be noted that the moisture uptake of GFRP bars fell within the acceptable limits if conditioned in concrete and for shorter durations, lower temperatures, and/or without a sustained load. Nevertheless, in real-life scenarios, where GFRP bars are imbedded in concrete, it is possible to limit the moisture uptake by creating an impermeable concrete. This can be achieved by adding supplementary cementitious materials, as fly ash, ground granulated blast furnace slag, silica fume, or others.

4.2. TG Analysis. TG analysis was employed in the past literature to assess the decomposition of the polymer matrix

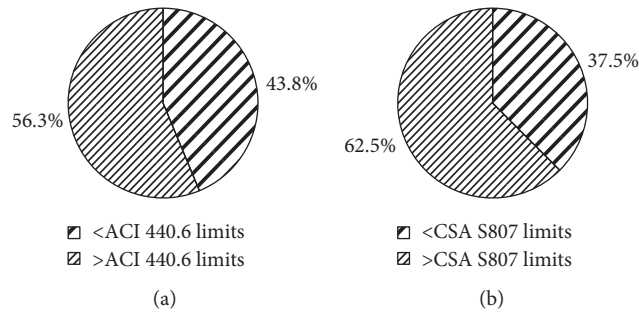


FIGURE 9: Percentage of GFRPs within acceptable durability limits. (a) ACI 440.6. (b) CSA S807.

under heat exposure. ASTM E1868 [19] was used to examine the change in mass as a function of temperature (20°C–800°C) and evaluate the thermal stability of the matrix. A typical mass variation curve as a function of temperature measured by TGA is shown in Figure 10. It is clear that a major mass loss of 18% occurred in the range of 300°C–450°C. This is attributed to the thermal degradation of the polymer matrix, as the molecular chains broke, leading to microcrack formation at the fiber/matrix interface and matrix itself. Such mass loss also indicates a critical loss of mechanical properties due to an irreversible degradation mechanism.

4.3. FTIR Analysis. A number of past studies explored the degradation mechanism of GFRP reinforcing bars using FTIR analysis. Samples were placed in an FTIR spectrometer and analysed from 400 to 4000 cm^{-1} in transmittance or absorbance mode. Figure 11 shows typical FTIR spectra for conditioned and unconditioned samples. Five zones could be identified: 900–1200, 1400–1600, 1600–1800, 2800–3100, and 3200–3600 cm^{-1} . These spectral zones are, respectively, attributed to O–H bending, C–O stretching, C=O stretching, C–H stretching, and O–H stretching. The past literature studies have identified and reported these peaks, as shown in Table 9. It is clear that most conducted research has focused on the O–H and C–H stretching bonds. This is owed to the ability to evaluate the hydrolysis reaction by measuring the peak in the OH band, which increases due to hydrolysis and relating it to the constant peak of CH. As such, the relative quantity of hydroxyl groups is characterized by the ratio of maximum peaks of OH-to-CH [13, 14, 27, 34]. Table 10 presents the OH-to-CH ratio of conditioned and control specimens of numerous studies. It should be noted that the reported ratio for conditioned samples is a result of the most severe conditioning scheme utilized in each study. This is a typical approach adopted by several researchers [8, 9, 13, 14, 24, 26, 31, 34]. The ratio for control GFRP bars ranged between 0.21 and 2.60, while that of conditioned counterparts was between 0.25 and 14.30. With such wide variations in the degradation, i.e., OH-to-CH ratio, the percentage increase was calculated and reported in Table 10. It ranged between 0 and 450%. Thus, to provide a more conclusive interpretation of the results, a more isolated investigation is performed. GFRP bars made with epoxy and vinyl ester are separated and each correlated to its associated moisture

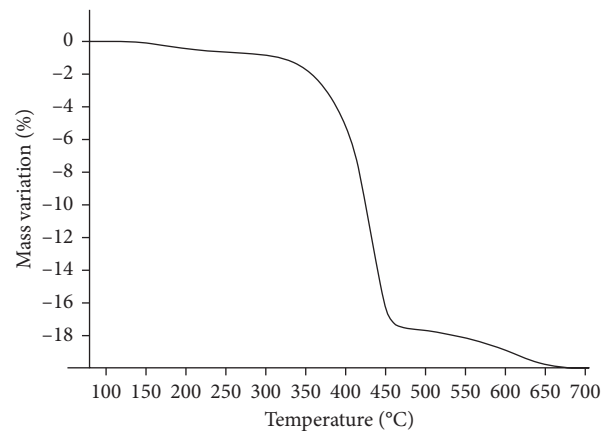


FIGURE 10: Mass variation of GFRP bar specimen when heated between 20°C and 800°C (adapted from [25]).

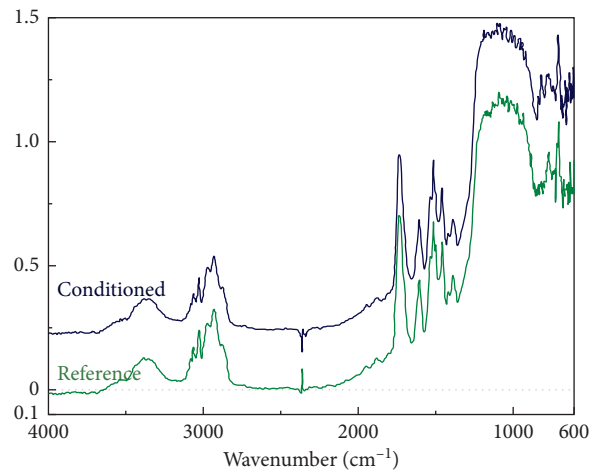


FIGURE 11: Glass transition temperature of conditioned and reference GFRP bars (adapted from [24]).

uptake. Results of Figure 12(a) show that the higher the moisture uptake, the higher the OH/CH increase due to conditioning of epoxy-GFRP bars. These test samples were all conditioned at 60°C, but for different durations. In fact, the left marker (0.74% moisture uptake increase) was conditioned in alkaline solution for up to 720 days, but did not show any increase in OH/CH ratio, indicating no degradation due to hydrolysis reaction [31]. This shows that

TABLE 9: Summary of FTIR wavelengths detected in conditioned GFRP reinforcing bars.

Reference	Wavelength (cm ⁻¹)				
	O-H stretch	C=O stretch	C-H stretch	C-O stretch	O-H bend
[8]	3200-3650	—	2800-3000	—	—
[9]	3300-3600	1600-1800	2800-3100	1400-1600	900-1100
[10]	3200-3600	—	2800-3000	—	—
[11]	3200-3600	—	2800-3000	—	—
[13]	3300-3600	—	2800-3100	—	—
[14]	3300-3600	—	2800-3000	—	—
[23]	3200-3650	—	2800-3000	—	—
[24]	3300-3600	1600-1800	2800-3100	1400-1600	900-1200
[26]	3200-3500	—	2800-3000	—	—
[27]	3300-3600	—	2850-3100	—	—
[31]	3400	—	3026	—	—
[34]	3200-3400	—	2800-3100	—	—
[35]	3430	—	2900	—	—
[38]	3430	—	2900	—	—
[39]	3540	—	2900	—	—
[40]	3334	1557	2900	1420	1019

TABLE 10: Results of OH/CH ratios in control and conditioned GFRP reinforcing bars.

Reference	Resin type	Conditioning				OH/CH		
		Medium	Temperature (°C)	Time (days)	Sustained load	Control	Conditioned	% Increase
[8]	Polyester	Alkaline	60	208.3		2.6 & 1.6	14.3 & 3.5	450 & 118.8
[9]	Vinylester	Concrete	50	60		No change		—
[10]	Epoxy	Concrete	60	450		0.59 & 1.07	1.15 & 1.24	94.9 & 15.9
[11]	Epoxy	Concrete	60	288 & 372	x	0.59 & 1.07	1.27 & 1.27	115.3 & 18.7
[13]	Vinylester	Water	50	180		0.45	0.51	13.3
[14]	Vinylester	Concrete	50	240		0.21	0.25	19.0
[23]	Polyester	Alkaline	60	208.3		2.6 & 1.6	14.3 & 3.5	450 & 118.8
[24]	Vinylester	Water	23	90		No change		—
[26]	Vinylester	Alkaline	70	365		No change		—
[27]	Vinylester polyester	Alkaline	60	180		0.49 & 0.48	0.54 & 0.87	22.7 & 81.3
[31]	Epoxy	Alkaline	60	720		No change		—
[34]	Vinylester	Concrete	50	30	x	0.51	0.53	3.9
[35]	Vinylester	Alkaline	73	120	x	1.05	1.45 & 1.30	38.1 & 23.8
[38]	Vinylester	Concrete	30	2920	x	No change		—
[39]	Vinylester	Alkaline	50	365		1.05	1.18	12.4
[40]	Vinylester	Alkaline	22	16.67		No change		—

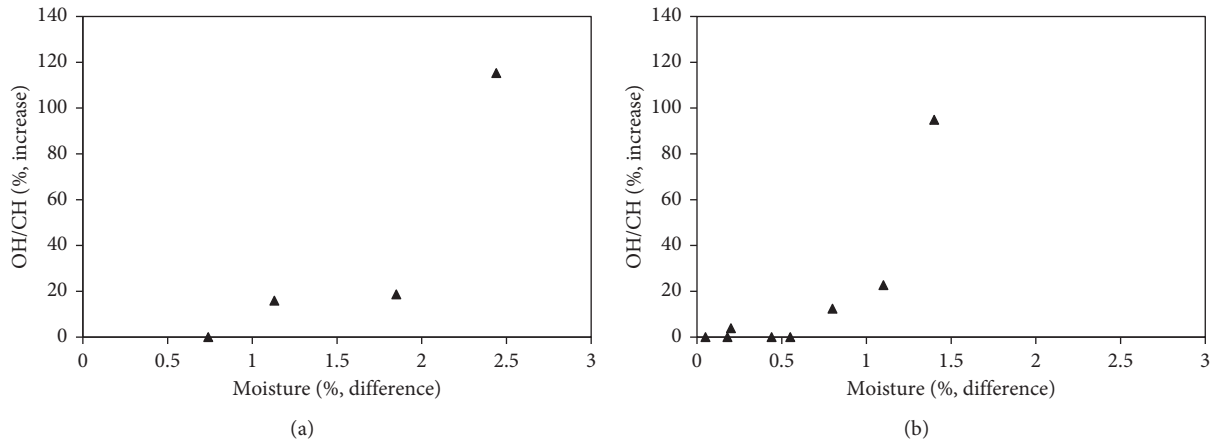


FIGURE 12: Correlation between OH/CH increase (%) and moisture uptake due to conditioning (%). (a) GFRP with epoxy matrix. (b) GFRP with vinylester matrix.

the degradation only initiated after 1% moisture uptake. Further increase in uptake up to 2% did not cause significant impact on the change in OH/CH ratio, after which it dramatically increased up to 115%. Thus, it can be concluded that epoxy-GFRP bars could experience limited degradation if the moisture uptake is maintained below 2%, by mass.

Figure 12(b) presents a relation between OH/CH percent increase and moisture uptake in conditioned GFRP bars made with vinylester matrix. The OH/CH increase remained below 20%, indicating a lower degree of hydrolysis reaction, when the moisture uptake was below 1.5%. Beyond 1.5%, degradation was much more significant due to conditioning, with OH/CH increasing by up to 95% compared to the control samples. In comparison and based on the studies revised in this paper, GFRP bars made with vinylester resin have been found to be more generally susceptible to hydrolysis than their epoxy counterparts.

The effect of the initial tensile strength of unconditioned GFRP bars on their resistance to degradation was investigated in [10, 11]. In these studies, two different types of GFRP bars with dissimilar tensile strengths were compared. FTIR analysis results of [10], presented in Table 10, show that the GFRP bar with lower void content had an increase in OH/CH ratio of 15.9% compared to 94.9% for the sample with the higher void content. Obviously, as the void content increased, the hydrolysis reaction progressed, leading to higher OH/CH ratios. The degradation was further intensified upon the application of a sustained load, as shown in the results of [11].

4.4. DSC Analysis. The thermal behavior and characteristics of conditioned and control GFRP samples is analysed using DSC. The main properties obtained from DSC are glass transition temperature (T_g), curing process, melting temperature, crystallinity, relaxation, and thermal stability [25]. Of these properties, glass transition temperature is the most reported in the past literatures. It is determined by performing two scans, each from 20°C to 250°C, in accordance with ASTM E1356 [21]. The first scan compares the T_g of the conditioned and control samples. A reduction in T_g is indicative of matrix plasticization. The second scan identifies the degradation mechanism, whereby a similar T_g for conditioned and control samples indicates a reversible plasticizing effect, while a lower T_g for the former signifies an irreversible chemical degradation. Figure 13 illustrates typical DSC curves for alkaline-conditioned and unconditioned GFRP reinforcing bars. The step shown in the range of 90°C–110°C is used to find the T_g . While it appeared to be an endothermic or melting peak, there was no melting involved in this work [31]. In fact, the authors associated this peak to “the thermal stress relaxation phenomenon of polymer chains of the GFRP rebar during long-term ageing”.

Furthermore, a summary of T_g temperatures and cure ratio of various studies is presented in Table 11. These temperatures are results of the GFRP samples subject to the most severe conditioning scheme utilized in each study. It is clear that most studies experienced some decrease in the T_g of the first scan, ranging from 0 to 46%. This wide variation

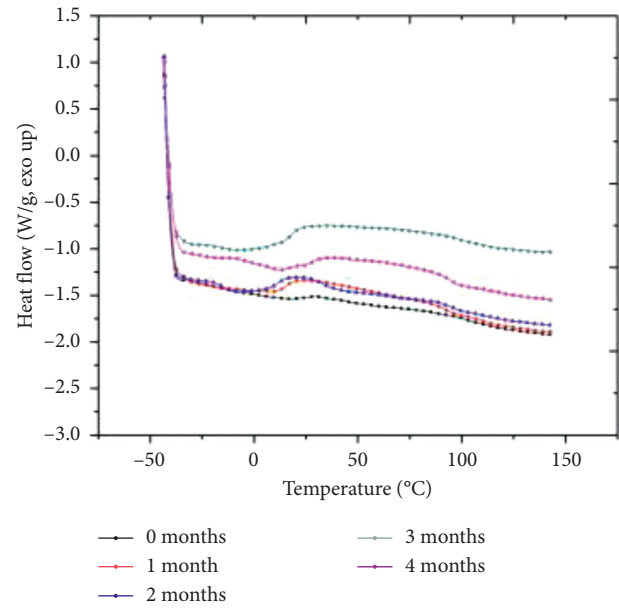


FIGURE 13: Differential scanning calorimetry curve for conditioned and control GFRP bars (adapted from [31]).

in results is owed to the different curing regimes, fiber content, matrix type, and presence of sustained loading, which all contribute to lowering the T_g and the deterioration of the GFRP bars. However, it is possible to isolate some values by selecting GFRP bars made with epoxy matrix and correlating them to other parameters. Figure 14 shows that higher changes in OH/CH ratios led to more intense reductions in the T_g . This shows a clear correlation between results of FTIR and DSC, signifying the progression of a hydrolysis reaction. In other terms, the factors that affect the OH/CH ratios have a similar effect on the T_g .

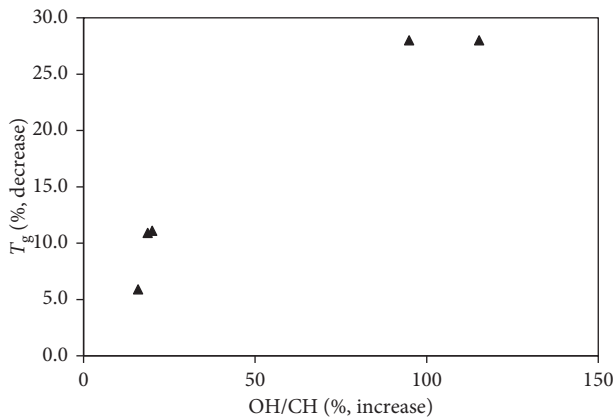
In the second scan, studies that employed concrete as the conditioning medium did not note any change in the T_g between conditioned and control samples [10, 11, 14, 34, 38]. On the other hand, specimens conditioned in alkaline solutions and water showed some signs of irreversible chemical degradation, with the former conditioning scheme being more detrimental [25, 27, 42]. This provides evidence to the severity of conditioning in alkaline solutions, rendering results somewhat unrealistic and unreliable.

Additionally, the cure ratio is shown in Table 11. It is the ratio of the T_g of the first to second scan for the control samples. Other than [13, 14, 34], which are conducted by the same authors and probably using the same GFRP bars, the reported cure ratios were above 95%. Lower values signify that the samples were not fully cured and that postcuring occurred during the second scan.

4.5. SEM Analysis. SEM was employed to evaluate the microstructure and morphological changes to the GFRP reinforcing bars after conditioning. The fiber-matrix interface is considered one of the most vulnerable areas in GFRP reinforcing bars. It is merely a few microns thick and plays a critical role in transfer of the load between fiber and

TABLE 11: Results of T_g temperatures and cure ratio in control and conditioned GFRP reinforcing bars.

Reference	T_g			T_g			Cure ratio (%)
	1 st scan (°C)		Decrease (%)	2 nd scan (°C)		Decrease (%)	
	Control	Conditioned		Control	Conditioned		
[8]	93, 113, 126	98, 100, 112	5.4, 11.5, 11.1	—	—	—	98–100
[9]	145	140	3.4	—	—	—	—
[10]	101 & 125	95 & 90	5.9 & 28	106 & 125	105 & 126	0.0	95.3 & 100
[11]	101 & 125	90 & 90	10.9 & 28	106 & 125	105 & 125	—	95.3 & 100
[13]	110	103	6.4	129	128	0.8	85.3
[14]	105	104	1.0	134	129	3.7	78.4
[42]	116	62	46.6	120	83	30.8	96.7
[24]	105–125	—	—	105–125	—	—	100.0
[25]	112	67	40.2	113	68	39.8	99.1
[26]	116	117	—	117	118	—	99.1
[27]	123, 124, 90	122, 123, 84	0, 0, 6.6	124, 123, 90	123, 122, 85	0, 0, 5.5	100
[31]	105	96	8.6	—	—	—	—
[34]	112	95	15.2	131	130	0.8	85.5
[35]	114	105	7.9	120	120	0.0	95.0
[38]	124	120	3.2	125	120	4.0	99.2
[48]	115–125	112–124	2.4–2.6	—	—	—	—

FIGURE 14: Percent increase of T_g of the first scan as a function of percent increase of OH/CH after conditioning of epoxy-GFRP bars.

matrix [67]. In the presence of moisture and alkalis, the bond between fiber and matrix is weakened, causing damage to the interface itself and the GFRP as a whole.

Micrographs typically highlight different damages or deteriorations that may be induced by conditioning, including matrix degradation, fiber/material interface degradation, microcrack formation, and fiber etching and leaching. Table 12 shows a summary of deteriorations that have been identified in different studies using SEM. Clearly, matrix degradation, fiber/matrix interfacial degradation, and microcrack formation are interlinked, as they are reported simultaneously in multiple studies; they are denoted collectively hereafter as damage A. Fiber etching and leaching, on the other hand, is designated as damage B. Of the literature reviewed in this work, 58, 15, and 27% reported damage A, damage B, and no damage, respectively, as shown in Figure 15. This demonstrates that the matrix and the fiber/matrix interface are indeed the most vulnerable components of GFRP reinforcing bars, with much lesser deterioration of the fiber.

Figure 16(a) shows a micrograph from past work that identified damage A in a conditioned GFRP reinforcing bar [10]. Samples in this study were placed in seawater-contaminated concrete for 15 months at 60°C. Clearly, the fiber/matrix interface weakened to the extent that fiber delamination occurred. This is primarily owed to the progression of hydrolysis reaction.

Fiber etching and leaching were only noticed in research work that examined the durability performance of GFRP reinforcing bars made with E-glass/vinylester and conditioned in alkaline environment; they are represented as damage B. Figure 16(b) presents a micrograph of a GFRP bar that suffered damage B [28] with circumferential damage to the fiber. In this work, GFRP samples were conditioned in an alkaline solution under a 25% UTS sustained load. The severity of the testing conditions resulted in all samples failing within 20 days of conditioning. No tensile strength could be retained at that point. The degree of deterioration was too harsh that it caused matrix degradation, fiber/matrix interfacial debonding, microcrack formation, and fiber damage simultaneously.

In some of the reviewed studies, no damage or deterioration was noticed. Though some degradation may have been reported in the microstructure study, the mechanical properties of GFRP reinforcing bars were not significantly affected. It is thus critical for researchers to correlate the tensile strength, moisture uptake, OH/CH ratio, and SEM micrographs in a distinct study to provide a better understanding of the effect of the microstructure on the mechanical properties. Yet, while the scope of this work is to focus on microstructure characteristics of GFRP bars exposed to different conditioning regimes, a correlation based on the reviewed studies has been developed. For this matter, results from [10, 11, 13, 14, 27, 35] are employed. It is worth noting the GFRP samples were conditioned differently in these studies. The SEM micrographs of Figures 17(a)–17(f) show little to no cracks at the fiber/matrix interface, indicating limited degradation. The GFRPs of [10, 11, 27] are

TABLE 12: Summary of deteriorations identified by SEM in conditioned GFRP reinforcing bars.

Reference	Deterioration/Damages			
	Matrix degradation	Fiber/matrix interface damage	Microcracks	Fiber etching and leaching
[8]	x	x	x	
[9]		No deterioration reported		
[10]	x	x	x	
[11]	x	x	x	
[12]	x	x	x	
[13]		No deterioration reported		
[14]		No deterioration reported		
[15]	x	x	x	x
[23]	x	x	x	
[42]	x	x		
[24]		No deterioration reported		
[25]	x	x	x	
[26]		No deterioration reported		
[27]	x	x	x	
[28]	x	x	x	x
[29]	x	x	x	
[30]	x	x	x	
[31]		No deterioration reported		
[32]	x	x	x	
[33]	x	x	x	
[34]		No deterioration reported		
[35]	x	x	x	
[36]	x	x	x	x
[37]	x	x	x	
[38]		No deterioration reported		
[39]	x	x	x	
[44]	x	x	x	
[45]	x	x	x	
[46]	x	x	x	x
[47]	x	x	x	
[49]	x	x	x	
[50]	x	x	x	x
[51]		No deterioration reported		

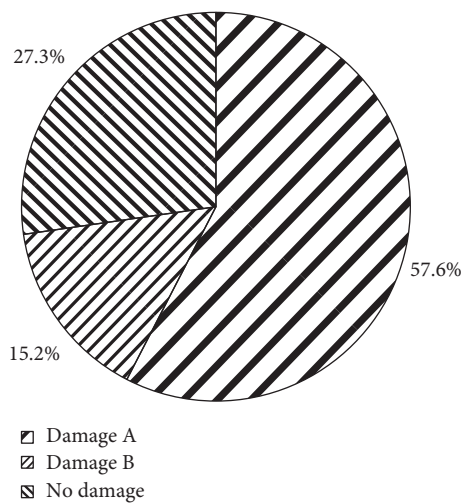


FIGURE 15: Distribution of damage/deterioration in conditioned GFRP reinforcing bars.

associated with moisture uptakes of 1.20, 1.95, and 1.63%, respectively. The respective increases in OH/CH ratios of [10, 11, 13, 14, 27, 35] are 15.9, 18.5, 13.3, 19.0, 22.7, and

3.9%. The strength retention of these samples was 85, 73, 93, 84, 100, and 84%, respectively. Yet, samples in [11, 35] were conditioned under sustained loads. Accordingly, it is possible to accept an increase in moisture uptake and OH/CH ratio up to a threshold of 1.6 and 18%, respectively, while anticipating up to 15% reduction in tensile strength.

5. Conclusions and Remarks

In this paper, studies examining the microstructure of GFRP reinforcing bars exposed to different environmental conditions and sustained loading were reviewed. Experimental results and findings were collected from past literature, analysed, and compared to provide conclusive remarks on the effect of conditioning on the microstructure of GFRP reinforcing bars. Based on the conducted analysis, the following conclusions can be drawn:

- (i) Mechanical properties from the past literature were used to provide correlation equations for unconditioned GFRP bars. Tensile strength and modulus of as-received GFRP bars were correlated in a linear equation. These relationships could

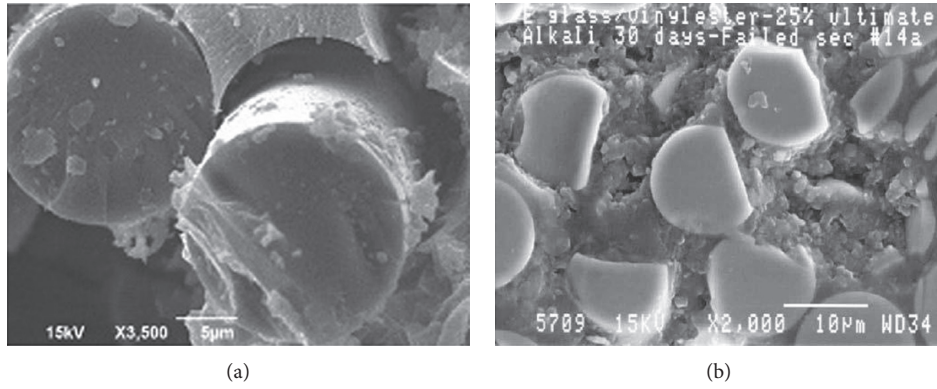


FIGURE 16: Micrograph of conditioned GFRP reinforcing bar. (a) Damage A (adapted from [10]). (b) Damage B (adapted from [28]).

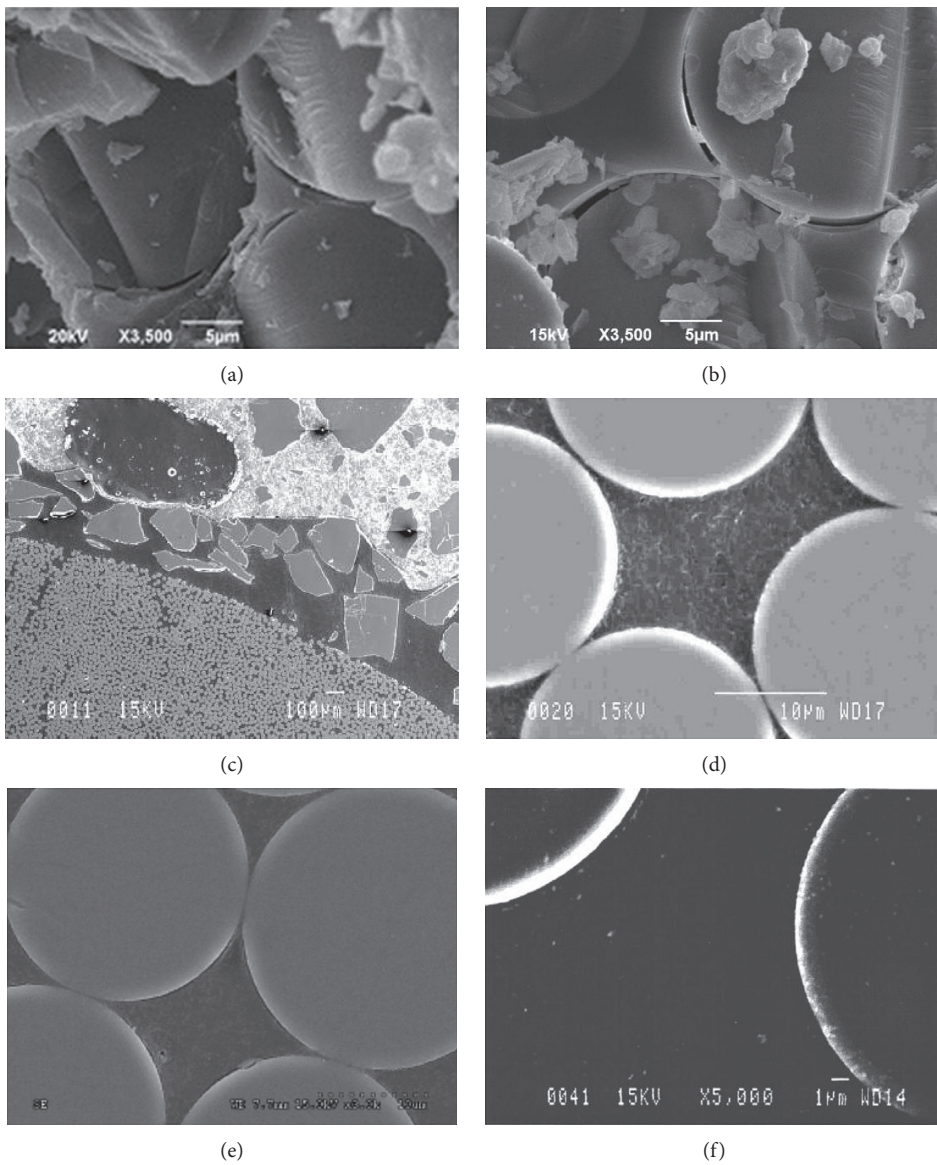


FIGURE 17: Micrograph of conditioned GFRP reinforcing bar with no damage. (a) Adapted from [10]. (b) Adapted from [11]. (c) Adapted from [13]. (d) Adapted from [14]. (e) Adapted from [27]. (f) Adapted from [35].

provide reasonably accurate prediction of the tensile modulus from the tensile strength.

- (ii) Only 14% of reviewed studies investigated the performance and microstructure of GFRP bars made with E-glass and epoxy. On average, the tensile properties of such unconditioned bars seemed to be 14% superior to those of vinylester counterparts. Discrepancies in the testing procedures did not allow for a direct microstructure comparison between the two types. Further testing is needed prior to the adoption of these GFRP reinforcing bars.
- (iii) In the majority of reviewed studies, GFRP specimens were conditioned in alkaline and water solutions due to the ease of the experimental setup. Concrete was only employed in 23% of the studies. Conditioning durations varied greatly, with 0–90 and more than 365 days being most commonly used.
- (iv) The application of a sustained load to GFRP reinforcing bars during conditioning was adopted in 28% of the studies reviewed. Research studies that exceeded the limits stated by codes and standards concluded that the set limits were only valid for specific nonaggressive environment conditions. In fact, elevated temperatures promoted the degradation mechanism. More research is needed to update these limits to include different conditioning regimes.
- (v) Higher temperature, prolonged conditioning, presence of a sustained load, and conditioning in alkaline solution caused an increase in moisture uptake. Most uptake values extracted from the literature exceeded the limits set by ACI 440.6 [62] and CSA S807 [63]. Only specimens that were conditioned in concrete at low temperatures, for short durations, and/or without a sustained load were within the acceptable moisture uptake durability limits. This raises a concern to the aggressiveness of the conditioning utilized in the literature.
- (vi) A correlation was developed between the progression of hydrolysis (OH/CH increase) and the decrease in T_g (%). Within an increase of 20% OH/CH, the T_g decreased by only 10%. However, greater surges in OH/CH caused much more dramatic reductions in the glass transition temperature. Nevertheless, limiting the moisture uptake could control the increase in hydroxyl groups.
- (vii) Conditioning in alkaline solution was found to be too severe and did not accurately represent real-life scenarios. Specimens conditioned in alkaline solutions experienced irreversible chemical degradation, more hydroxyl group formation, and more intense degradation to the microstructure.
- (viii) Four types of damages were reported in conditioned GFRP bars: matrix degradation, fiber degradation, fiber/matrix interface degradation, and

microcrack formation. Most of concrete-encased GFRP specimens did not experience excessive degradation, as opposed to alkaline conditioning that severely damaged the GFRP.

- (ix) The increase in moisture uptake and OH/CH ratio and formation of microcracks does not necessarily have a severe effect on the mechanical performance. In fact, it is possible to allow an increase in moisture uptake and OH/CH ratio up to 1.6 and 18%, respectively, while anticipating up to 15% reductions in tensile strength.

The conclusions presented above were based on the past literature reviewed in this work. Further studies are needed to fill the research gaps before GFRP reinforcing bars could be widely adopted by the construction industry. The following are suggestions for future research direction:

- (i) A standard testing procedure for GFRP reinforcing bars capable of providing consistent and reliable results that represents real-life scenarios
- (ii) Comparative performance and microstructure evaluation of GFRP reinforcing bars in concrete and subjected to different environment conditions and levels of sustained load
- (iii) Microstructure characterization of GFRP bars exposed to acidic solution
- (iv) The effect of void content on performance retention and microstructure changes of GFRP reinforcing bars
- (v) Performance and microstructure comparison between GFRP bars made with different resin, i.e., epoxy and vinylester, subject to the same conditioning schemes
- (vi) Performance and microstructure comparison between concrete-encased GFRP specimens exposed to elevated temperatures with an applied sustained load and actual in-service specimens
- (vii) GFRP reinforcing bars in concretes made with different supplementary cementitious materials to limit the moisture uptake

Conflicts of Interest

The authors declare that there are no conflicts of interest regarding the publication of this paper.

Acknowledgments

This research publication is supported by the Abu Dhabi Department of Education and Knowledge (ADEK) and United Arab Emirates University (UAEU) under grant 21N209.

References

- [1] G. Koch, "1-Cost of corrosion," in *Trends in Oil and Gas Corrosion Research and Technologies*, A. M. El-Sherik, Ed., Woodhead Publishing, Boston, MA, USA, 2017.

- [2] ACI 440.1R, *Guide for the Design and Construction of Concrete Reinforced with FRP Bars*, American Concrete Institute, Farmington Hills, MI, USA, 2015.
- [3] ACI 440.3R, *Guide Test Methods for Fiber-Reinforced Polymers (FRPs) for Reinforcing or Strengthening Concrete Structures*, American Concrete Institute, Farmington Hills, MI, USA, 2012.
- [4] FIB, "FRP reinforcement in RC structures," in *Bulletin 40*, The International Federation for Structural Concrete FIB, Lausanne, Switzerland, 2007.
- [5] H. P. Abeysinghe, W. Edwards, G. Pritchard, and G. J. Swampillai, "Degradation of crosslinked resins in water and electrolyte solutions," *Polymer*, vol. 23, no. 12, pp. 1785–1790, 1982.
- [6] P. V. Vijay and H. V. S. GangaRao, "Accelerated and natural weathering of glass fiber reinforced plastic bars," in *Proceedings of the 4th International Conference on Fibre-Reinforced Plastics for Reinforced Concrete Structures*, Baltimore, MD, USA, 1999.
- [7] M. Robert, P. Wang, P. Cousin, and B. Benmokrane, "Temperature as an accelerating factor for long-term durability testing of FRPS: should there be any limitations?," *Journal of Composites for Construction*, vol. 14, no. 4, pp. 361–367, 2010.
- [8] B. Benmokrane, A. H. Ali, H. M. Mohamed, A. ElSafty, and A. Manalo, "Laboratory assessment and durability performance of vinyl-ester, polyester, and epoxy glass-FRP bars for concrete structures," *Composites Part B: Engineering*, vol. 114, pp. 163–174, 2017.
- [9] B. Benmokrane, H. M. Mohamed, A. Manalo, and P. Cousin, "Evaluation of physical and durability characteristics of new headed glass fiber-reinforced polymer bars for concrete structures," *Journal of Composites for Construction*, vol. 21, no. 2, article 04016081, 2017.
- [10] H. El-Hassan, T. El-Maaddawy, A. Al-Sallamin, and A. Al-Saidy, "Performance evaluation and microstructural characterization of GFRP bars in seawater-contaminated concrete," *Construction and Building Materials*, vol. 147, pp. 66–78, 2017.
- [11] H. El-Hassan, T. El-Maaddawy, A. Al-Sallamin, and A. Al-Saidy, "Durability of glass fiber-reinforced polymer bars conditioned in moist seawater-contaminated concrete under sustained load," *Construction and Building Materials*, vol. 175, pp. 1–13, 2018.
- [12] B. Benmokrane, P. Wang, T. M. Ton-That, H. Rahman, and J.-F. Robert, "Durability of glass fiber-reinforced polymer reinforcing bars in concrete environment," *Journal of Composites for Construction*, vol. 6, no. 3, pp. 143–153, 2002.
- [13] M. Robert and B. Benmokrane, "Effect of aging on bond of GFRP bars embedded in concrete," *Cement and Concrete Composites*, vol. 32, no. 6, pp. 461–467, 2010.
- [14] M. Robert, P. Cousin, and B. Benmokrane, "Durability of GFRP reinforcing bars embedded in moist concrete," *Journal of Composites for Construction*, vol. 13, no. 2, pp. 66–73, 2009.
- [15] H. Roh, C. Park, and D. Y. Moon, "Experimental investigation of the effects of concrete alkalinity on tensile properties of preheated structural GFRP rebar," *Advances in Materials Science and Engineering*, vol. 2017, p. 13, 2017.
- [16] ASTM, *Standard Test Method for Tensile Properties of Fiber Reinforced Polymer Matrix Composite Bars*, D7205, ASTM International, West Conshohocken, PA, USA, 2016.
- [17] ASTM, *Standard Test Methods for Constituent Content of Composite Materials*, D3171, ASTM, West Conshohocken, PA, USA, 2015.
- [18] ASTM, *Standard Test Methods for Void Content of Reinforced Plastics*, D2734, ASTM International, West Conshohocken, PA, USA, 2016.
- [19] ASTM, *Standard Test Methods for Loss-On-Drying by Thermogravimetry*, E1868, ASTM, West Conshohocken, PA, USA, 2015.
- [20] ASTM, *Standard Test Method for Water Absorption of Plastics*, D570, ASTM, West Conshohocken, PA, USA, 2010.
- [21] ASTM, *Standard Test Method for Assignment of the Glass Transition Temperatures by Differential Scanning Calorimetry*, E1356, ASTM, West Conshohocken, PA, USA, 2008.
- [22] ASTM, *Standard Test Method for Linear Thermal Expansion of Solid Materials by Thermomechanical Analysis*, E831, ASTM International, West Conshohocken, PA, USA, 2014.
- [23] A. H. Ali, B. Benmokrane, H. M. Mohamed, A. Manalo, and A. El-Safty, "Statistical analysis and theoretical predictions of the tensile-strength retention of glass fiber-reinforced polymer bars based on resin type," *Journal of Composite Materials*, vol. 52, no. 21, pp. 2929–2948, 2018.
- [24] B. Benmokrane, A. Manalo, J.-C. Bouhet, K. Mohamed, and M. Robert, "Effects of diameter on the durability of glass fiber-reinforced polymer bars conditioned in alkaline solution," *Journal of Composites for Construction*, vol. 21, no. 5, article 04017040, 2017.
- [25] M. Robert and B. Benmokrane, "Behavior of GFRP reinforcing bars subjected to extreme temperatures," *Journal of Composites for Construction*, vol. 14, no. 4, pp. 353–360, 2010.
- [26] M. Robert and B. Benmokrane, "Combined effects of saline solution and moist concrete on long-term durability of GFRP reinforcing bars," *Construction and Building Materials*, vol. 38, pp. 274–284, 2013.
- [27] M. Montaigu, M. Robert, E. A. Ahmed, and B. Benmokrane, "Laboratory characterization and evaluation of durability performance of new polyester and vinylester E-glass GFRP dowels for jointed concrete pavement," *Journal of Composites for Construction*, vol. 17, no. 2, pp. 176–187, 2013.
- [28] G. M. Rajan Sen and S. Tom, "Durability of E-glass/vinylester reinforcement in alkaline solution," *ACI Structural Journal*, vol. 99, no. 3, pp. 369–375, 2002.
- [29] J.-P. Won and C.-G. Park, "Effect of environmental exposure on the mechanical and bonding properties of hybrid FRP reinforcing bars for concrete structures," *Journal of Composite Materials*, vol. 40, no. 12, pp. 1063–1076, 2006.
- [30] Y. A. Al-Salloum, S. El-Gamal, T. H. Almusallam, S. H. Alsayed, and M. Aqel, "Effect of harsh environmental conditions on the tensile properties of GFRP bars," *Composites Part B: Engineering*, vol. 45, no. 1, pp. 835–844, 2013.
- [31] M. A. Sawpan, A. A. Mamun, and P. G. Holdsworth, "Long term durability of pultruded polymer composite rebar in concrete environment," *Materials & Design*, vol. 57, pp. 616–624, 2014.
- [32] S. Alsayed, Y. Al-Salloum, T. Almusallam, S. El-Gamal, and M. Aqel, "Performance of glass fiber reinforced polymer bars under elevated temperatures," *Composites Part B: Engineering*, vol. 43, no. 5, pp. 2265–2271, 2012.
- [33] A. Mukherjee and S. J. Arwika, "Performance of glass fiber-reinforced polymer reinforcing bars in tropical environments—Part II: microstructural tests," *ACI Structural Journal*, vol. 102, no. 6, pp. 816–822, 2005.
- [34] M. Robert and B. Benmokrane, "Physical, mechanical, and durability characterization of preloaded GFRP reinforcing bars," *Journal of Composites for Construction*, vol. 14, no. 4, pp. 368–375, 2010.
- [35] A. S. Debaiky, G. Nkurunziza, B. Benmokrane, and P. Cousin, "Residual tensile properties of GFRP reinforcing bars after loading in severe environments," *Journal of Composites for Construction*, vol. 10, no. 5, pp. 370–380, 2006.

- [36] H.-Y. Kim, Y.-H. Park, Y.-J. You, and C.-K. Moon, "Short-term durability test for GFRP rods under various environmental conditions," *Composite Structures*, vol. 83, no. 1, pp. 37–47, 2009.
- [37] T. H. Almusallam, Y. A. Al-Salloum, S. H. Alsayed, S. El-Gamal, and M. Aqel, "Tensile properties degradation of glass fiber-reinforced polymer bars embedded in concrete under severe laboratory and field environmental conditions," *Journal of Composite Materials*, vol. 47, no. 4, pp. 393–407, 2013.
- [38] A. A. Mufti, N. Banthia, B. Benmokrane, M. Boulfiza, and J. P. Newhook, "Durability of GFRP composite rods," *Concrete International*, vol. 29, no. 2, pp. 37–42, 2007.
- [39] A. S. M. Kamal and M. Boulfiza, "Durability of GFRP rebars in simulated concrete solutions under accelerated aging conditions," *Journal of Composites for Construction*, vol. 15, no. 4, pp. 473–481, 2011.
- [40] J. W. Chin, K. Aouadi, M. R. Haight, W. L. Hughes, and T. Nguyen, "Effects of water, salt solution and simulated concrete pore solution on the properties of composite matrix resins used in civil engineering applications," *Polymer Composites*, vol. 22, no. 2, pp. 282–297, 2001.
- [41] B. Benmokrane, F. Elgabbas, E. A. Ahmed, and P. Cousin, "Characterization and comparative durability study of glass/vinylester, basalt/vinylester, and basalt/epoxy FRP bars," *Journal of Composites for Construction*, vol. 19, no. 6, article 04015008, 2015.
- [42] A.-H. I. Mourad, B. M. Abdel-Magid, T. El-Maaddawy, and M. E. Grami, "Effect of seawater and warm environment on glass/epoxy and glass/polyurethane composites," *Applied Composite Materials*, vol. 17, no. 5, pp. 557–573, 2010.
- [43] ASTM, *Standard Test Method for Flexural Properties of Fiber Reinforced Pultruded Plastic Rods*, D4476, ASTM International, West Conshohocken, PA, USA, 2014.
- [44] F. Micelli and A. Nanni, "Durability of FRP rods for concrete structures," *Construction and Building Materials*, vol. 18, no. 7, pp. 491–503, 2004.
- [45] W. Li, C. Ji, H. Zhu, F. Xing, J. Wu, and X. Niu, "Experimental investigation on the durability of glass fiber-reinforced polymer composites containing nanocomposite," *Journal of Nanomaterials*, vol. 2013, p. 11, 2013.
- [46] H. Fergani, M. Di Benedetti, M. Guadagnini, C. Lynsdale, and C. Mias, "Characterization and durability study of GFRP bars exposed to severe environments and under sustained loads," in *Proceedings of the Fifth International Conference on Durability of Fiber Reinforced Polymer (FRP) Composites for Construction and Rehabilitation of Structures*, QC, Canada, 2017.
- [47] J. F. Davalos, Y. Chen, and I. Ray, "Long-term durability prediction models for GFRP bars in concrete environment," *Journal of Composite Materials*, vol. 46, no. 16, pp. 1899–1914, 2012.
- [48] M. A. Sawpan, P. G. Holdsworth, and P. Renshaw, "Glass transitions of hygrothermal aged pultruded glass fibre reinforced polymer rebar by dynamic mechanical thermal analysis," *Materials & Design*, vol. 42, pp. 272–278, 2012.
- [49] O. Gooranorimi, W. Suaris, E. Dauer, and A. Nanni, "Microstructural investigation of glass fiber reinforced polymer bars," *Composites Part B: Engineering*, vol. 110, pp. 388–395, 2017.
- [50] C.-G. Park, C.-I. Jang, S.-W. Lee, and J.-P. Won, "Microstructural investigation of long-term degradation mechanisms in GFRP dowel bars for jointed concrete pavement," *Journal of Applied Polymer Science*, vol. 108, no. 5, pp. 3128–3137, 2008.
- [51] D. Miller, J. Mandell, D. Samborsky, B. Hernandez-Sanchez, and D. T. Griffith, "Performance of composite materials subjected to salt water environments," in *Proceedings of the 53rd AIAA/ASME/ASCE/AHS/ASC Structures, Structural Dynamics and Materials Conference*, American Institute of Aeronautics and Astronautics, Honolulu, HI, USA, 2012.
- [52] M. Abhijit and S. J. Arwihar, "Performance of glass fiber-reinforced polymer reinforcing bars in tropical environments-Part I: structural scale tests," *ACI Structural Journal*, vol. 102, no. 5, pp. 745–753, 2005.
- [53] C. E. Bakis, A. J. Freimanis, and D. Gremel, "Effect of resin material on bond and tensile properties of unconditioned and conditioned FRP reinforcement rods," in *Proceedings of the 1st International Conference on durability of Fiber Reinforced Polymer (FRP) Composites for Construction*, Sherbrooke, QC, Canada, 1998.
- [54] C. E. Bakis, T. E. Boothby, R. A. Schaut, and C. G. Pantano, "Tensile strength of GFRP bars under sustained loading in concrete beams," *ACI Special Publication*, vol. 230, pp. 1429–1446, 2005.
- [55] M. G. Phillips, "Prediction of long-term stress-rupture life for glass fibre-reinforced polyester composites in air and in aqueous environments," *Composites*, vol. 14, no. 3, pp. 270–275, 1983.
- [56] B. Benmokrane, P. Wang, T. M. Ton-That, H. Rahman, and J. Francois, "Durability of glass fiber-reinforced polymer reinforcing bars in concrete environment," *Journal of Composites for Construction*, vol. 6, no. 3, 2002.
- [57] JSCE, "Recommendations for design and construction of high performance fiber reinforced cement composites with multiple fine cracks (HPFRCC)," in *Concrete Engineering Series 82*, Japan Society of Civil Engineers, Japan, 2008.
- [58] CSA S6, *Canadian Highway Bridge Design Code*, Canadian Institute of Steel Construction, Canada, 2014.
- [59] NS 3473, *Concrete structures-Design and Detailing Rules*, Norsk Standard, Norway, 2003.
- [60] CSA S806, *Design and Construction of Building Structures with Fibre-Reinforced Polymers*, Canadian Standards Association, Canada, 2017.
- [61] J. Huang and R. Aboutaha, "Environmental reduction factors for GFRP bars used as concrete reinforcement: new scientific approach," *Journal of Composites for Construction*, vol. 14, no. 5, pp. 479–486, 2010.
- [62] ACI Committee 440.6, *Specification for Carbon & Glass Fiber-Reinforced Polymer Bar Materials for Conc Reinforcement (Metric)*, American Concrete Institute, Farmington Hills, MI, USA, 2008.
- [63] CSA S807, *Specification for Fibre-Reinforced Polymers*, Canadian Standards Association, Canada, 2015.
- [64] Y. A. Al-Salloum and T. H. Almusallam, "Creep effect on the behavior of concrete beams reinforced with GFRP bars subjected to different environments," *Construction and Building Materials*, vol. 21, no. 7, pp. 1510–1519, 2007.
- [65] H. Fergani, M. Di Benedetti, C. Mias Oller, C. Lynsdale, and M. Guadagnini, "Long-term performance of GFRP bars in concrete elements under sustained load and environmental actions," *Composite Structures*, vol. 190, pp. 20–31, 2018.
- [66] T. D'Antino, M. A. Pisani, and C. Poggi, "Effect of the environment on the performance of GFRP reinforcing bars," *Composites Part B: Engineering*, vol. 141, pp. 123–136, 2018.
- [67] J. L. Thomason, "The interface region in glass fibre-reinforced epoxy resin composites: 2. Water absorption, voids and the interface," *Composites*, vol. 26, no. 7, pp. 477–485, 1995.

Research Article

Development of Strength for Calcium Aluminate Cement Mortars Blended with GGBS

Hee Jun Yang , Ki Yong Ann , and Min Sun Jung 

Department of Civil and Environmental Engineering, Hanyang University, Ansan 15588, Republic of Korea

Correspondence should be addressed to Min Sun Jung; msjcivil@hanyang.ac.kr

Received 5 October 2018; Revised 13 December 2018; Accepted 1 January 2019; Published 13 January 2019

Guest Editor: Joanna Rydz

Copyright © 2019 Hee Jun Yang et al. This is an open access article distributed under the Creative Commons Attribution License, which permits unrestricted use, distribution, and reproduction in any medium, provided the original work is properly cited.

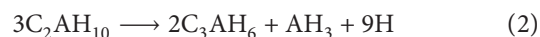
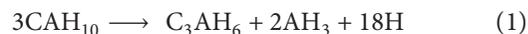
In the present study, the development of strength in different calcium aluminate cement (CAC) mixture mortars with granulated ground blast-furnace slag (GGBS) was investigated. The substitution of GGBS levels was 0, 20, 40, and 60% weight of binder, of which the CAC used in this study naturally contained C_2AS clinker as a secondary phase. To activate a hydraulic nature of the phase, in addition to the mineral additive, all specimens were cured at $35 \pm 2^\circ C$ for the first 24 hours and then stored in a 95% humidity chamber at $25 \pm 2^\circ C$. The penetration resistance of fresh mortar was measured immediately after pouring, and the mortar compressive strength was monitored for 365 days. Simultaneously, to evaluate the hydration kinetics at early ages, in terms of heat evolution, the calorimetric analysis was performed at the isothermal condition ($35^\circ C$) for 24 hours. The hydration behavior in the long term was characterized by X-ray diffraction, which was supported by microscopic observation using scanning electron microscopy with energy dispersive spectroscopy. Furthermore, an examination of the pore structure was accompanied to quantify the porosity. As a result, it was found that an increase in the GGBS content in the mixture resulted in an increased setting time, as well as total heat evolved for 24 hours in normalized calorimetry curves. In addition, the strength development of mortar showed a continuous increased value up to 365 days, accounting 43.8–57.5 MPa for the mixtures, due to a formation of stratingite, which was identified at the pastes cured for 365 days using chemical and microscopic analysis. However, GGBS replacement did not affect on the pore size distribution in the cement matrix, except for total intrusion volume.

1. Introduction

Calcium aluminate cement (CAC), mainly consisting of monocalcium aluminate (CA), has been used in the construction industry since the late 19th and early 20th centuries after patented in 1908 by J. Bied [1–3]. Although it was initially developed to enhance the resistance to aggressive ions (sulfates and chlorides), as an alternative to Portland cement, a rapid strength development at early ages (within 24 hours) led to its application to military facilities in World War I, resulting in production of the various of types of CAC [1–3]. Nowadays, the use of CAC in specific fields is involved in a wide range, including as a fire-resistant material in refractory application [4–6], a high resistance against chemical degradations in the industrial floor and wastewater application [7–9], rapid setting and hardening grout in tunnel lining [1], and resistance to abrasion in hydraulic dam spillway [7]. In addition, ability in gaining the strength

rapidly, even at lower temperatures below $0^\circ C$, makes it possible to cold weather concreting [10]. Recently, there is an increasing interest in the use of CAC with expansive agents as a repair material [11, 12].

Despite high performance, a structural use of CAC in construction has been faced with a critical problem, a loss of strength due to the conversion process; metastable hydration products (CAH_{10} and C_2AH_8) are thermodynamically transformed into stable ones (C_3AH_6 and AH_3), depending on curing regimes and ages, as follows [1,10,13–16]:



The cubic phases of C_3AH_6 and AH_3 have the higher density in CAC hydration; therefore, the space filled by low-density hexagonal phases of CAH_{10} and C_2AH_8 , which

produces a high early strength, would be decreased after the conversion process, resulting in a sudden reduction in the strength [1, 13]. Many previous studies [17–20] reported that long-term properties of CAC concrete exhibited a decreased strength, compared to the strength at early ages. It has been attempted to take some precautions for avoiding/eliminating the transformation of metastable hydrates using chemical and mineral admixtures, to overcome this anxiety about instability to the properties over time. Falzone et al. [21] recently investigated the conversion bypassing effect of calcium nitrate added in CAC paste, on the basis of the thermodynamic selectivity mechanism, but most of the studies have focused on the substitution of siliceous materials in the CAC-based binder system [22–31].

Midgley and Rao [22] raised an influence of strätlingite on mechanical properties of high alumina cement (HAC) and suggested that the possible formation of C_2ASH_8 hydrate would compensate a reduced compressive strength after conversion at the normal temperature (20°C). It was confirmed by Majumdar and coworkers [23, 24] that the formation of C_2ASH_8 hydrate improved the strength development for two types of commercial CAC (Ciment Fondu and Secar 71), replaced by GGBS in 50% weight of binder, at 20 and 40°C. Moreover, the authors investigated the properties of CAC with various pozzolanic materials, such as natural pozzolan and metakaolin, and concluded that substitution of siliceous materials in CAC enhanced the strength development and sulfate resistance depending on types of binder and their replacement ratio, which could impose the different levels of silica in the solution [25]. The ability of silicate ions in generating the strätlingite in the CAC-based binary system, consisting of fly ash or silica fume, was also reported in the previous studies [26–30]. In addition, Gosselin et al. [28] carried out the observation of microstructural development of CAC, containing C_2AS clinker as the secondary phase, and demonstrated that higher curing temperatures (above 38°C) for the first 24 hours imposed the formation of C_2ASH_8 hydrates, even at early ages, which in turn resulted in the densification of the matrix.

However, most of the studies [22–25] focused on the transformation of the metastable hydrates into C_2ASH_8 in the presence of reactive silicates using Ciment Fondu, consisting of the CA clinker as a main hydraulic phase. Otherwise, only hydration behavior was revealed using cement paste made with CAC containing the C_2AS clinker, which could produce the strätlingite directly [26–30]. In this study, therefore, to evaluate the influence of GGBS replacement on mechanical properties in the mortar of CAC-GGBS mixtures, the development of strength was investigated by setting time and compressive strength. The strength for mortars of CAC-GGBS mixtures cured at a given regime was monitored for 365 days. Simultaneously, isothermal calorimetry and X-ray diffraction analysis were performed to identify the hydration behavior, particularly for a formation of strätlingite and its influence on mitigation in the conversion reaction, at early and long-term age, of which the morphology of the phase was inspected by scanning electron microscopy. Furthermore, the pore

distribution was examined by the volume of mercury intruded into a specimen to verify a modification of the pore structure, arising from the substitution of GGBS in CAC. The CAC containing 52.0% of Al_2O_3 content in the cement was used, of which the C_2AS phase naturally occurred.

2. Experimental Works

To evaluate the influence of a formation of calcium aluminates hydrate containing silicates (i.e., strätlingite, C_2ASH_8) in the hydration process on the fundamental properties for CAC mortar, three levels of replacement in GGBS (20, 40, and 60% by weight of cement) were used in this study. The oxide composition of the binders determined by X-ray fluorescence (XRF) and mix proportions for the specimens are given in Tables 1 and 2, respectively, and also XRD curves of the materials are shown in Figure 1. All specimens for the experiments were manufactured without any admixtures to avoid the influence of the chemical effect on the CAC matrix and were kept at 0.4 of a total W/C. Based on the facts that CAC could achieve 80 percent of ultimate strength within 24 hours due to rapid hydration [1–3] and accelerate the formation of the C_2ASH_8 hydrate in the pozzolan blends system at above 30°C of the curing temperature [32], the specimens were cured in a humidity chamber (RH 95%) at $35 \pm 2^\circ C$ for 24 hours and after that was stored in the chamber at $25 \pm 2^\circ C$ to simulate the moderate situation for 364 days. As the elevated temperatures during evaporation of a free water from pores in the matrix (i.e., hydration stopping method) could encourage the transformation of hexagonal phases into cubic ones, the samples were immersed in isopropanol for 7 days in a low-temperature chamber (below 0°C), which was subsequently placed in a vacuum desiccator to remove the residual solvent and/or water from the sample before measurement.

2.1. Measurement of Heat Evolution. Isothermal calorimetry is a useful technique to study the kinetics of the hydration process, of which the heat flow is directly measured and monitored for a specified duration under controlled conditions. Approximately 10 g of the premixed dry powder at the given proportions (Table 2) was placed in an admix glass ampoule and set up within the calorimeter. Then, a distilled water equivalent to 0.4 of total water to binder ratio was injected from the syringe system and continuously stirred during test duration. The rate of heat evolution at the isothermal condition (35°C) was measured and recorded for 24 hours using a TAM air 3-channel calorimeter and thermostat (TA Instruments). Total heat evolution of the sample was calculated by integration of the rate curve for a given time. After obtaining the calorimetric results, it was normalized by mass of CAC content to determine an influence of CAC solely on the rate of heat evolution and its cumulative one at a given W/B.

2.2. Testing of Strength. A fresh mortar with a proportion of 1.00:0.40:2.45 for the cement:water:sand was mixed and then placed in a prism mold (100×100×400 mm) to

TABLE 1: Chemical composition of binders used in this study.

Oxides (%)	CAC	GGBS
CaO	38.83	47.18
Al ₂ O ₃	52.03	13.13
SiO ₂	5.02	29.70
Fe ₂ O ₃	0.86	0.64
SO ₃	0.09	2.30
MgO	0.42	4.55
K ₂ O	0.68	0.53
Na ₂ O	0.17	0.22
MnO	0.03	0.29
Ignition loss	0.53	1.29
Fineness (cm ² /g)	5,150	5,420
Density (g/cm ³)	3.03	2.93

TABLE 2: Mix proportions for experimental works.

	Abbreviation	Weight ratio				Experiments
		CAC	GGBS	Water	Sand	
Paste	CAC 100	1.00	0.00			Calorimetry XRD SEM/EDS
	CAC 80	0.80	0.20	0.4	—	
	CAC 60	0.60	0.40			
	CAC 40	0.40	0.60			
Mortar	CAC 100	1.00	0.00			Setting time Compressive strength MIP
	CAC 80	0.80	0.20	0.4	2.45	
	CAC 60	0.60	0.40			
	CAC 40	0.40	0.60			

determine the penetration resistance with time, which was subsequently measured using a series of standard needles (Ø4.52, 6.4, 9.1, 14.3, 20.2, and 28.6 mm) at various time intervals [33]. The test was performed in a room chamber at $35 \pm 2^\circ\text{C}$, RH 95%. After obtaining the relation between penetration resistance and time, which was fitted by a suitable function (usually, exponential one), the setting time was determined by assuming that the initial and final sets were defined as time taken to reach at 3.4 and 27.5 MPa against penetration resistance, respectively.

To monitor development of compressive strength, mortar specimens were fabricated in a cubic mold ($50 \times 50 \times 50$ mm) with the equal mix proportion to the penetration resistance test. After casting, the mortar specimens were precured in the 95% RH humidity chamber at $35 \pm 2^\circ\text{C}$ for 24 hours and then demolded. In turn, the specimens were stored in the chamber at $25 \pm 2^\circ\text{C}$ for 364 days. The compressive strength for mortar specimens was measured at various ages (1, 7, 28, 98, 180, and 365 days). The replication of each mix for the compressive strength of mortar was six, and their average value was taken in plotting the variation at a given age.

2.3. Identification of Hydration Products. To observe the formation of hydration products with time, the paste specimens were fabricated into a thin mold ($10 \times 50 \times 50$ mm), which would impose less potential to transform metastable hydrates (CAH₁₀ and C₂AH₈) into stable ones (C₃AH₆ and AH₃) arising from self-heating at early hydration. All pastes were kept at 0.4 of W/B. After curing for 1, 98, and 365 days

through the identical procedure to the mortar specimen for compressive strength, the specimens adapted the hydration stopping method and then crushed/ground to obtain the dust sample, which in turn was sieved with a $75 \mu\text{m}$ sieve. Then, the powder sample was stored in a vacuum desiccator to avoid the carbonation reaction before measurement. The XRD test was carried out with the D/MAX-2500 diffractometer (Rigaku Corp.) using Cu K α 1 radiation with a wavelength of 1.54 Å. The scan range was from 5 to 45° of 2θ at a scan rate of $4^\circ/\text{min}$. The presence of hydration products in the XRD curve was confirmed using Jade 9.5 software with PDF-2 database from International Center for Diffraction Data (ICDD).

2.4. Examination of Pore Structure. To check an influence of GGBS replacement on the pore structure of the matrix in the blends system at a given age, mercury intrusion porosimetry (MIP) was performed using the identical mortar specimens for compressive strength. After 365 days of curing, the mortars were crushed into a piece of about 1 cm^3 , followed by removal of the residual water using the alcohol-based solvent under low temperature. Then, the specimens were stored in a vacuum desiccator to remove/evaporate the free water totally, before testing. The equipment used in this study was Autopore IV 9500 (Micromeritics Instrument Corp.) with two devices, of which a low pressure of mercury was applied up to 0.2 MPa using nitrogen gas to measure large porosity, and then the pressure was progressively increased to 227.5 MPa for a small one. A contact angle and a surface tension of mercury were assumed 130° and $485 \times 10^{-3} \text{ N/m}$, respectively. The pore diameter, which was calculated by the Washburn equation at a given pressure (Equation (3)), was plotted in the cumulative and log differential intrusion curve, respectively:

$$d = \frac{-4 \gamma \cos \theta}{P}, \quad (3)$$

where d is the pore diameter (m), γ is the surface tension of mercury (N/m), θ is the contact angle of the mercury with the sample ($^\circ$), and P is the applied pressure (MPa).

2.5. Microscopic Observation of Morphology. Scanning electron microscopic (SEM) analysis is widely used for the inspection of the morphology of phases, and simultaneously, the elemental examination for the phases can be possible using the energy dispersive spectroscopy (EDS) method. The paste of CAC-GGBS mixtures, identical to the XRD test, was crushed into a piece of $1\text{-}2 \text{ cm}^2$, which subsequently was immersed in an isopropanol solvent for 7 days in a cooling chamber at below 0°C . This procedure was able to remove the free water within the specimen, preserving the hydration products unchanged during hydration stopping treatment. After stored in a vacuum desiccator to evaporate the residual water/solvent on the surface for 2 days, the sample was placed/fixed into the metallic plate and coated in platinum. The microscopic observations were performed by FE-SEM using S-4800 (Hitachi) with instrumental parameters, which were an accelerating voltage of 15 kV, the working distance

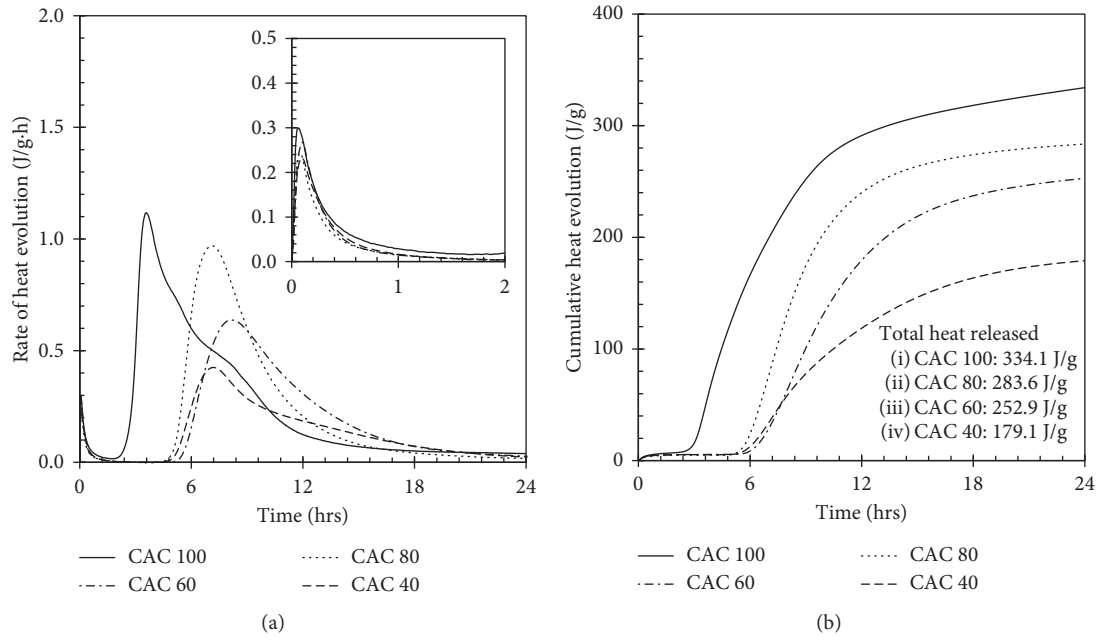


FIGURE 2: Calorimetric curves for CAC-GBS mixtures with 0.4 of W/B ratio at an isothermal of 35°C for 24 hours: (a) rate of heat evolution; (b) cumulative heat evolution.

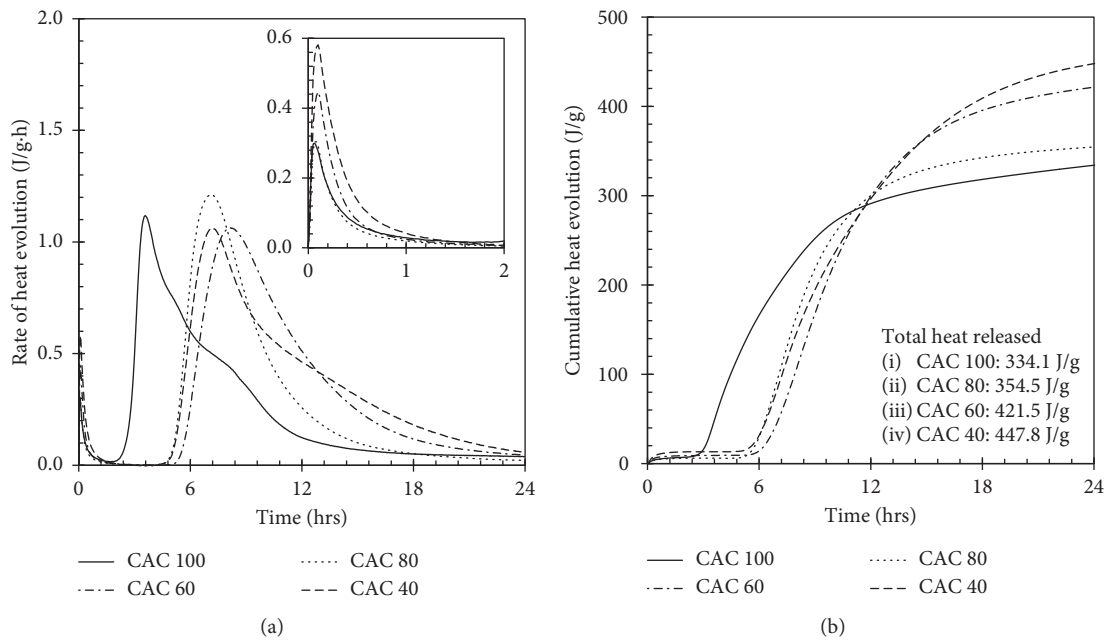


FIGURE 3: Calorimetric curves normalized to CAC content: (a) rate of heat evolution; (b) cumulative heat evolution.

disappearance of C_2AH_8 , which means the metastable hydrates fully converted. In contrast, the binary system of CAC and GGBS indicated a vanished C_2AH_8 hydrate but simultaneously a formation of C_2ASH_8 hydrate, depending on GGBS content in the CAC. In fact, CAC containing higher SiO_2 content (4-5%) naturally possesses the amount of the C_2AS phase, which has low hydraulic properties at normal temperatures (below 20°C) [29]. However, it was observed by Gosselin [32] that hydration

of C_2AS in the assemblage C_2AH_8 and C_3AH_6 (i.e., specimens cured at 38 and 70°C) resulted in the precipitation of C_2ASH_8 hydrate, even at early ages. Moreover, in the presence of pozzolanic materials (GGBS, PFA, and SF) in the CAC mixture, the formation of C_2ASH_8 hydrate can be accelerated due to a release of reactive silica into the solution, which in turn reacted with calcium aluminates hydrates in accordance to following equations [27]:

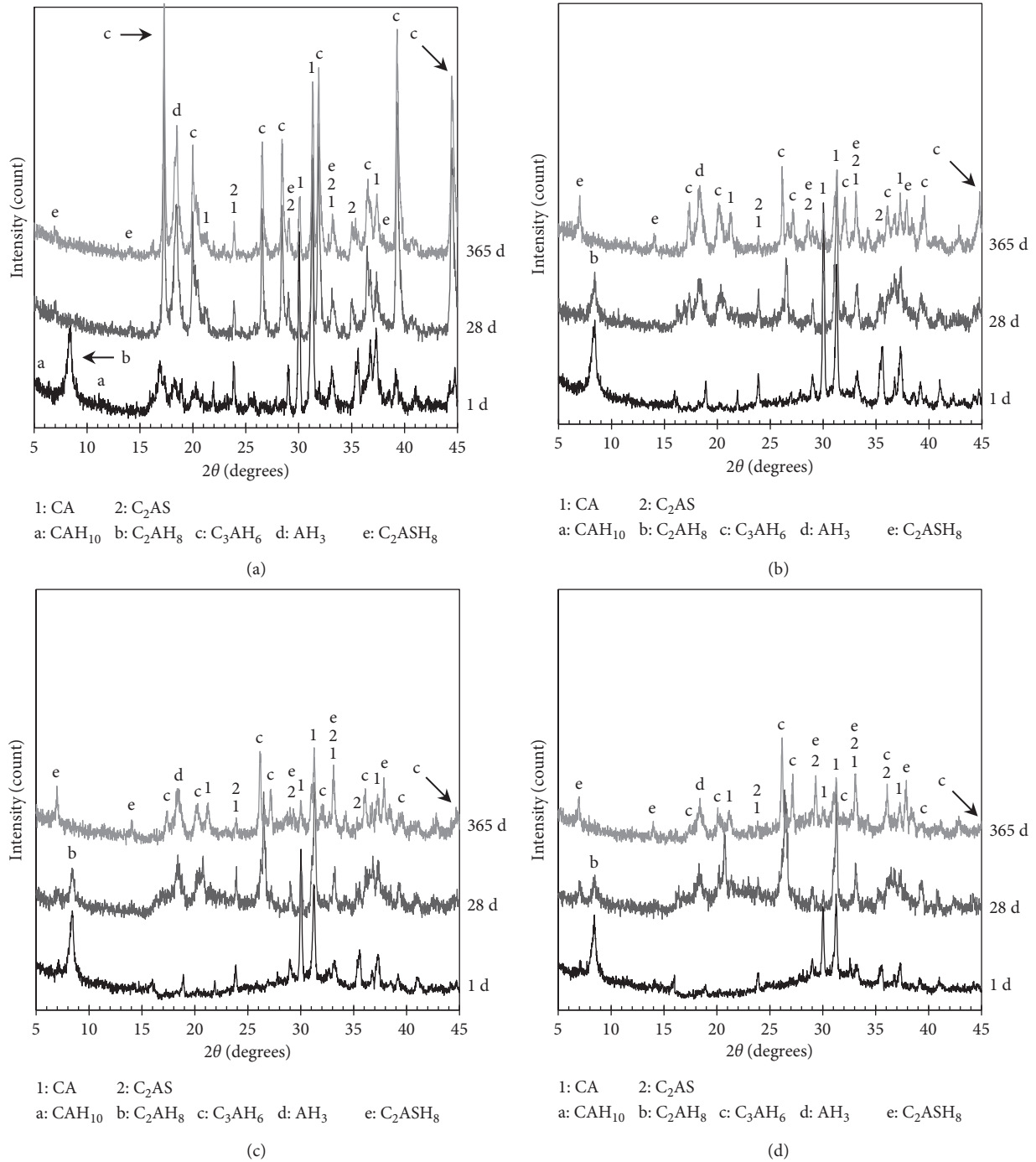
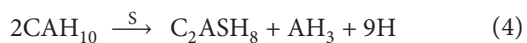


FIGURE 4: XRD curves for paste of CAC-GGBS mixtures at 0.4 of W/B with time: (a) CAC 100; (b) CAC 80; (c) CAC 60; (d) CAC 40.



This reaction could be controlled by the amounts of silicate ions in the solution (i.e., dissolution behavior of the siliceous materials). As an increased GGBS content is more probable of producing the silicate ions in the hydration process, the formation of C₂ASH₈ hydrate would be promoted at a given condition. However, the increased GGBS content would

accompany a decrease in the content of hydraulic phases in the binder system, and simultaneously, the large amounts of unreacted GGBS in the matrix may prevent further hydration in the long-term hydration, blocking the CAC particles to contact with water, thereby resulting in a low strength of CAC. This phenomenon will be discussed in the next section.

3.3. Development of Strength. The curves for the resistance against penetration of fresh CAC-GGBS blended mortars with time are given in Figure 5, of which the initial and final

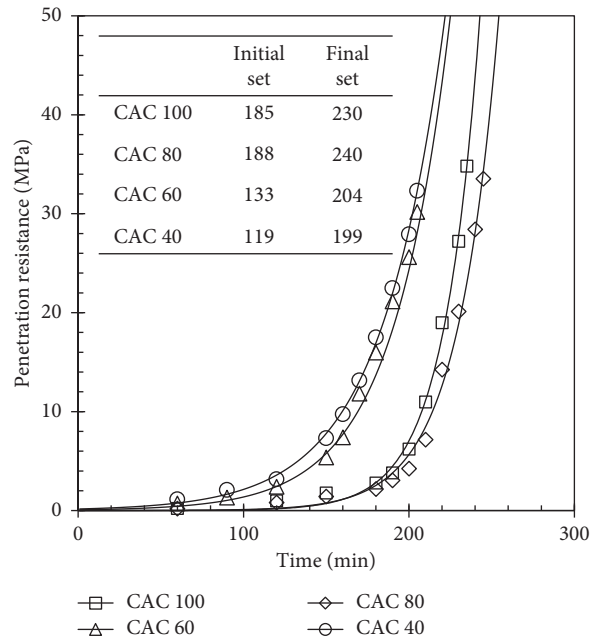


FIGURE 5: Penetration resistance with time for fresh mortar of CAC-GGBS mixtures. The curve is fitted by an exponential function ($y = ae^{bx}$).

set times were obtained from the best-fitted curve as the exponential function ($y = ae^{bx}$). It was shown that the setting time was dependent on the replacement ratio of GGBS; an increase in the GGBS content in the binder system resulted in an increase in the time for the initial and final sets, respectively, except for the case of CAC 80. For example, CAC 100 showed a rapid setting, of which the time to reach the initial and final sets was accounted for 185 and 230 min, respectively, while CAC 40 indicated 133 min and 204 min, respectively. It is notable that CAC 40 ranked the highest value for the setting time (188 and 240 min. for the initial and final sets, respectively). As the hydration process in the CAC is governed by the concentration of Ca^{2+} and $\text{Al}(\text{OH})_4^-$ ions in solution, the amount of the hydraulic phases and its solubility could be influenced on the setting and hardening of the matrix at an early age [32, 34]. Moreover, the substitution of cement by supplementary cementitious materials, such as GGBS and PFA, would encourage the hydraulic reaction in the blends system, producing more space and water for hydration [32]. It was confirmed by isothermal calorimetry analysis in this study that the curve for total heat released for 24 hours, which was normalized to CAC content, showed the remarkably highest value, compared to the case of CAC 100. In fact, as the GGBS has a lower density than CAC, the increase of GGBS content in the CAC-GGBS system results in an increase in the average volume at the given mass, thereby providing more available space for hydration. Also, relative content of water for CAC particles (i.e., W/C ratio) increases with the higher content of GGBS in the binary system. Consequently, reactive grains (i.e., CA clinker) in the cement would be more probable for reacting with water to form CAC hydration products in the early hydration. However, there was a marginal influence of GGBS replacement on setting time for the case of CAC 80.

The compressive strength for CAC mortars with the different replacement ratios of GGBS was measured at 1–365 days, as shown in Figure 6. It was seen that the strength for CAC mortars partially substituted by GGBS performed a lower strength at the early ages but continuously increased at a given curing regime for all ages, showing no reduction in the strength. For example, the compressive strength for CAC-GGBS blends at 1 day was 31.6, 23.3, and 18.6 for CAC 80, 60, and 40, respectively. In particular, CAC 60 showed a remarkable high final strength, reaching beyond 57.5 MPa at 365 days, of which the value is superior to the strength for specimen made with CAC 100%, while CAC 80 and 40 were accounted for 49.4 and 43.8 MPa, respectively. In fact, CAC specimens usually produce the sudden loss of the strength in the hydration period depending on environmental conditions, presumably due to the conversion process, of which hexagonal phases of CAH_{10} and C_2AH_8 formed at normal temperatures would be imposed the transformation into cubic ones (C_3AH_6 and AH_3) [17–20]. This phenomenon was observed in this study that the strength for CAC 100 rapidly increased up to 7 days then faced a marginal decrease from 40.8 MPa at 7 days to 38.9 MPa at 28 days, which in turn reincreased with time (45.8 MPa at 365 days), presumably due to a further reaction of the remained grains with a released water from the conversion reaction. The CAC used in this study has calcium aluminates containing silicates (gehlenite; C_2AS), as the secondary phase, which could be reacted with water to form stratlingite (C_2ASH_8) in the long term. It was reported that an increase in curing temperature for the first 24 hours resulted in an increase in the hydration degree of C_2AS and the amount of C_2AH_8 hydrate at above 38°C [28]. In the previous studies [30–32], moreover, it was stated that addition of a siliceous binder to CAC produced a steady development of the strength over time,

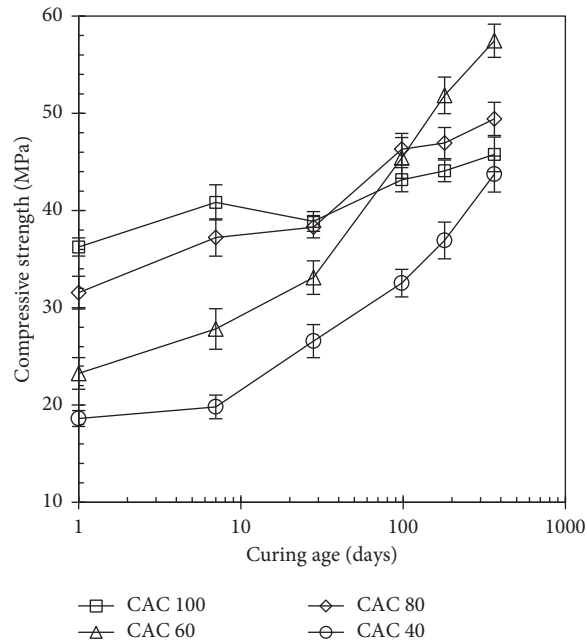


FIGURE 6: Compressive strength for mortar of CAC-GGBS mixtures with time. The error bars represent the standard deviation of measurements in six separate specimens for each mix ($n = 6$).

which is presumably due to the formation of C_2ASH_8 . In particular, the initially formed C_2AH_8 hydrate would favor the reaction with silicates released from the binder [29]. However, CAC 40 possessed a marginal CA and C_2AS for hydration, thereby exhibiting a steadily increasing strength, but the lower values at all ages. It may imply that replacement content of GGBS in the CAC-GGBS system should be determined, considering the requirement for on site.

3.4. Modification of Pore Distribution. The pore distribution of mortar in the binary binder system of CAC and GGBS at 365 days was determined by MIP to investigate the influence of GGBS replacement on the pore structure in the CAC matrix, as given in Figure 7. The MIP curves were rendered by the incremental intrusion and their cumulative volume with different sizes. The total pore volume was affected by the GGBS content in CAC; an increase in the replacement ratio of GGBS resulted in a decrease in the total intruded content of mercury into the specimen, except for CAC 40, of which the value was accounted for 0.145, 0.140, and 0.131 mL/g for CAC 100, 80, and 70, respectively. As seen in Figure 4, CAC 100 showed the overall transformation of C_2AH_8 phase into C_3AH_6 and AH_3 ones over time. It may be attributed to a higher density of cubic phases, increasing the distance between the hydrates and thus the porous matrix in the mortar. Moreover, an increased porosity of the matrix may decrease the development of the strength during hydration periods. In fact, CAC 100 showed the sudden decrease in the strength at 28 days, as seen in Figure 6, which in turn reincreased up to 365 days of curing presumably due to a further reaction with a surplus of water from the conversion reaction. In the presence of GGBS in mixture, in contrast, the conversion

reaction (equation (2)) was prevented by the transformation of the C_2AH_8 phase into C_2ASH_8 through the hydration duration, of which the stable hydrate is similar to unstable hydrate in density (1.937 and 1.950 for C_2ASH_8 and C_2AH_8 , respectively) [35, 36]. This change of composition in the matrix would produce the densified pore structure and thus a decrease in the porosity at the total. Despite modification of the matrix in the CAC-GGBS mixture, the higher ratio of GGBS replacement imposed an increased total intrusion volume (0.149 mL/g) presumably due to deficiency of hydraulic phases, as already mentioned. However, there was no particular relation in the intrusion volume at a given realm, which was in the range below 0.05 and 0.05–10 and above 10 μm for small capillaries, large capillaries, and voids, respectively.

3.5. Variation of Stoichiometric Composition. The surfaces of the fragment for cement paste of CAC-GGBS mixtures cured at 365 days were investigated using SEM analysis, as shown in Figure 8. A presence of strätlingite was obviously detected at all samples, of which the hydrates had the morphology of hexagonal plates, sometimes a thin flaky plate, and in addition, the phase seemed to be more accommodated in the matrix at pastes substituted by GGBS. To compare atomic ratios (Ca/Al and Si/Al) at the C_2ASH_8 phase in the paste of the binary mixtures, EDS analysis was simultaneously performed, measuring the 30 spots for each sample. It was clearly shown that an increase of GGBS content in the mixture resulted in an increase in the ratio of Si/Al and a decrease in Ca/Al ratio, of which an ideal ratio in the C_2ASH_8 phase is 0.5 and 1.0 for Si/Al and Ca/Al, respectively. It may be attributed to the increased GGBS content, from which the large amounts of silicate ions would

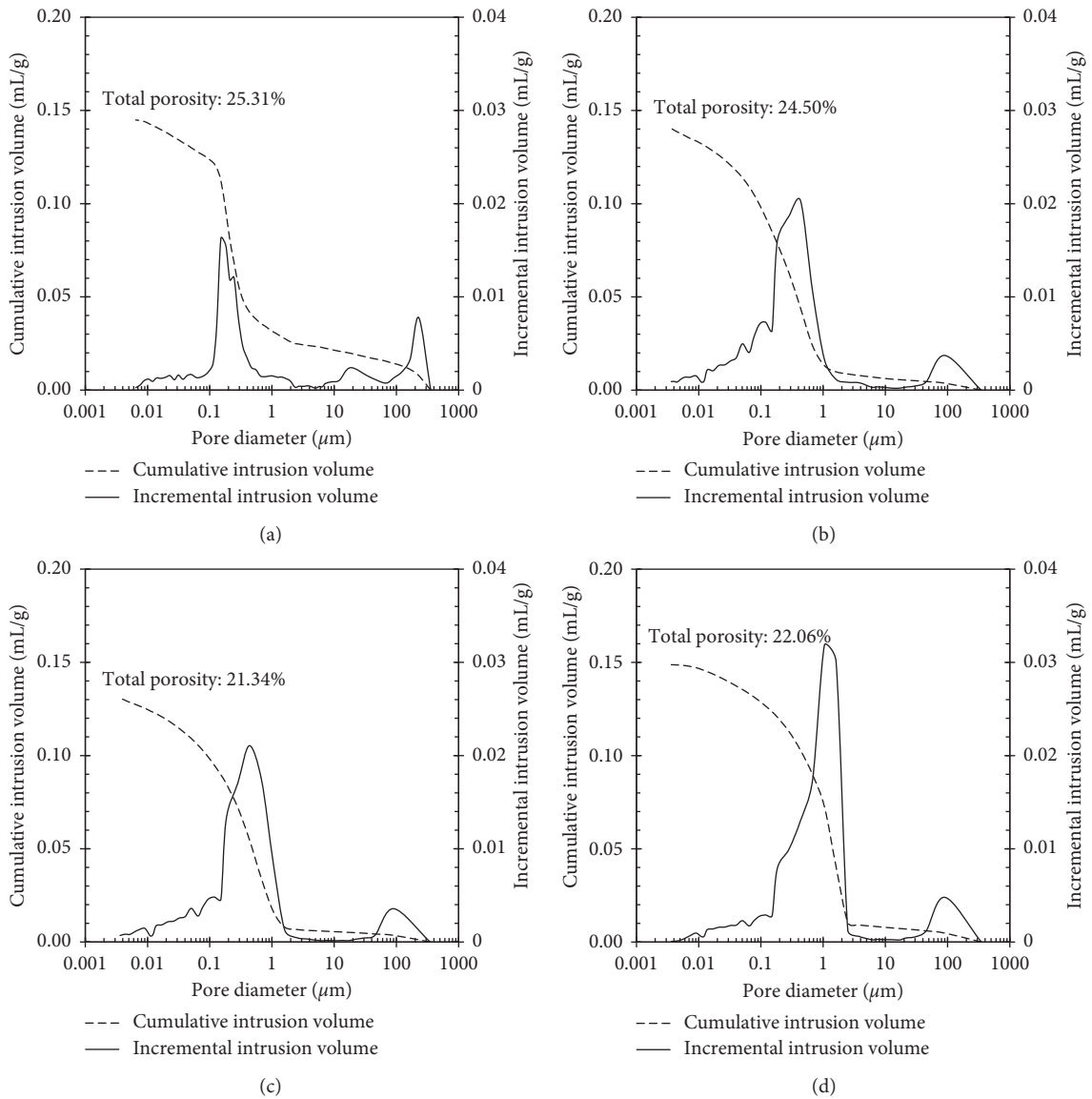


FIGURE 7: MIP results, rendered by incremental and cumulative intrusion volume with pore diameter, for mortar of CAC-GGBS mixtures: (a) CAC 100; (b) CAC 80; (c) CAC 60; (d) CAC 40.

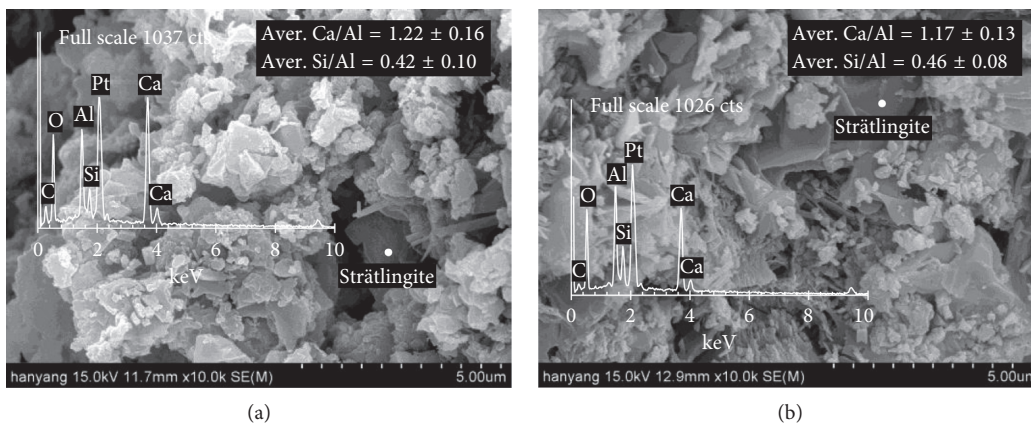


FIGURE 8: Continued.

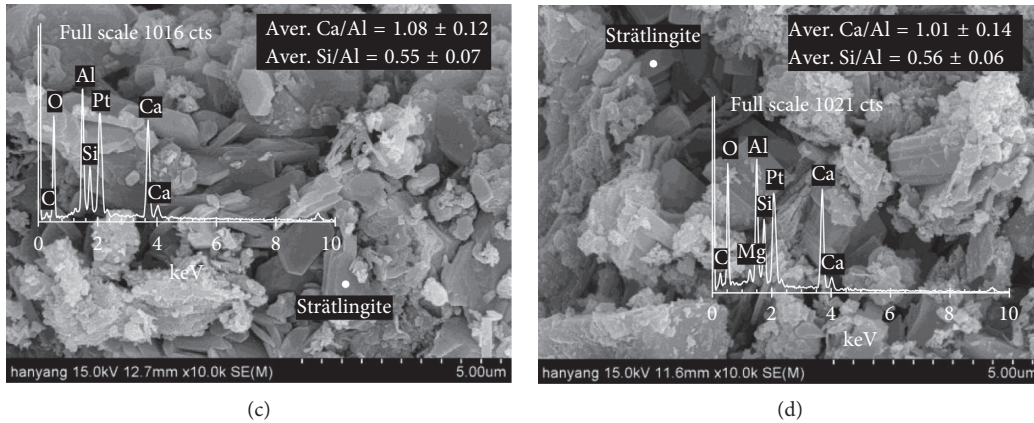


FIGURE 8: Microscopic observation for the formation of strätlingite in paste of CAC-GGBS mixtures at 365 days of curing. The standard deviation is derived from the measurements in 30 spots for each sample ($n = 30$): (a) CAC 100; (b) CAC 80; (c) CAC 60; (d) CAC 40.

be released into the pore solution during long-term hydration. As already mentioned in Section 3.3, the formation of strätlingite is affected by the amounts of dissolved silica from the siliceous materials. In addition, the stoichiometric structure is dependent on the surrounding chemical composition supplied from the grains in the solution [10, 37]. As a higher content of pozzolanic materials in a mixture produces more silicates into the solution, a probable to form silica-rich strätlingite would be increased. Thus, CAC 40 produced the highest ratio of Si/Al in the C_2ASH_8 phase, while the lower Si/Al ratio (0.42 ± 0.10) was observed at the paste made with CAC solely. However, there was no further experimentation supporting the differences of atomic ratios between CAC-GGBS mixture.

4. Conclusions

In this study, an influence of additive material containing silica on fundamental properties of CAC was investigated by development of strength, which was supported by further experimental work including hydration behavior at initial and long-term duration using isothermal calorimetry and X-ray diffraction analysis and an examination of the pores structure from mercury intrusion porosimetry. Microscopic observation for the morphology of strätlingite was performed by scanning electron microscopy, together with energy dispersive spectroscopy. The GGBS was replaced as binder with 0, 20, 40, and 60% by weight of the mass. Details derived from the present study are given as follows:

- (1) An increase in the GGBS content in the mixture, kept at 0.4 of W/B, resulted in an increase in the rate of heat evolved within 0–2 hours, in addition to the total heat released for 24 hours, in isothermal calorimetry normalized to CAC content. This may be supposed to available space in the matrix at early ages, arising from a lower density of the binary system with the increase of GGBS content.
- (2) Setting time, in terms of initial and final sets, was decreased with the increase of GGBS content, due to large amounts of water and space for hydration at the

early ages, except for the case of CAC 80. All CAC-GGBS mixed mortars exhibited a gradual development of strength with time, ranging from 43.8–57.5 MPa at 365 days, while the specimen made with CAC solely gained the strength rapidly at the early ages (40.8 MPa at 7 days), which subsequently faced to a sudden reduction due to conversion and then reincreased up to 45.8 MPa at 365 days.

- (3) The continuous increase in the strength for mixtures of CAC-GGBS was supported by XRD curves, showing a decrease in the peak intensity for the C_2AH_8 phase and simultaneously an increase in that for strätlingite with time. It may imply that the presence of GGBS prevents the conversion reaction to stable hydrates from metastable ones. However, C_2AH_8 in CAC 100 was fully transformed into C_3AH_6 and AH_3 after 28 days of curing at a given curing regime.
- (4) A modification of the pore structure, in terms of total porosity, was clearly shown that the increase of GGBS replacement ratio resulted in a decrease in the total intrusion volume of mercury at 365 days, except for the case of CAC 40, which may be attributed to a marginal CAC particle in the long-term hydration.
- (5) The formation of strätlingite in the paste cured at 365 days was confirmed by microscopic observation using SEM at all CAC-GGBS mixtures. The stoichiometric composition of the phase was in the range of 0.42–0.56 and 1.01–1.22 for atomic ratio of Si/Al and Ca/Al, irrespective of GGBS content in the mixtures.

Data Availability

The data used to support the findings of this study are included within the article.

Conflicts of Interest

The authors declare that they have no conflicts of interest.

Acknowledgments

This research was supported by a grant (18CTAP-C132998-02) from Technology Advancement Research Program funded by Ministry of Land, Infrastructure and Transport of Korean government.

References

- [1] The Concrete Society, *Calcium Aluminate Cements in Construction—A Re Assessment*, Concrete Society Technical Report 46, The Concrete Society, Camberley, UK, 1997.
- [2] K. L. Scrivener, “100 years of calcium aluminate cements,” in *Proceedings of International Conference on Calcium Aluminate Cements*, pp. 3–6, Avignon, France, June 2008.
- [3] A. Neville, “History of high-alumina cement. Part I: problems and the stone report,” *Engineering History and Heritage*, vol. 162, no. 2, pp. 81–91, 2008.
- [4] F. A. Cardoso, M. D. M. Innocentini, M. M. Akiyoshi, and V. C. Pandolfelli, “Effect of curing time on the properties of CAC bonded refractory castables,” *Journal of the European Ceramic Society*, vol. 24, no. 7, pp. 2073–2078, 2004.
- [5] C. Parr, D. Verat, C. Wöhrmeyer et al., “High purity calcium aluminate binders for demanding high temperature applications,” in *Proceedings of International Conference on Calcium Aluminate Cements*, pp. 417–428, Avignon, France, June 2008.
- [6] A. Buhr, D. Schmidtmeier, G. Wams et al., “Testing of calcium aluminate cement bonded castables and influence of curing conditions on the strength development,” in *Proceedings of International Conference Calcium Aluminate Cements*, pp. 437–449, Avignon, France, June 2008.
- [7] K. L. Scrivener, J.-L. Cabiron, and R. Letourneux, “High-performance concretes from calcium aluminate cements,” *Cement and Concrete Research*, vol. 29, no. 8, pp. 1215–1223, 1999.
- [8] M. G. Alexander and C. Fourie, “Performance of sewer pipe concrete mixtures with portland and calcium aluminate cements subject to mineral and biogenic acid attack,” *Materials and Structures*, vol. 44, no. 1, pp. 313–330, 2010.
- [9] J. Herisson, E. D. V. Hullebusch, M. Guéguen-Minerbe et al., “Biogenic Corrosion Mechanism: Study of Parameters Explaining Calcium Aluminate Cement Durability,” in *Proceedings of International Conference on Calcium Aluminate Cements*, pp. 633–644, Avignon, France, May 2014.
- [10] K. L. Scrivener and A. Capmas, “13. Calcium aluminate cements,” in *Lea’s Chemistry of Cement and Concrete*, pp. 713–782, Elsevier Science & Technology, Amsterdam, Netherlands, 2003.
- [11] R. D. Lute, “Durability of calcium-aluminate based binders for rapid repair application,” Doctoral thesis, The University of Texas at Austin, Austin, TX, USA, 2016.
- [12] Texas Department of Transportation, *Special Specification 4491: Type CAC Concrete*, Texas Department of Transportation, Austin, TX, USA, 2009.
- [13] H. G. Midgley and A. Midgley, “The conversion of high alumina cement,” *Magazine of Concrete Research*, vol. 27, no. 91, pp. 59–77, 1975.
- [14] C. Bradbury, P. M. Callaway, and D. D. Double, “The conversion of high alumina cement/concrete,” *Materials Science and Engineering*, vol. 23, no. 1, pp. 43–53, 1976.
- [15] S. Rashid and X. Turrillas, “Hydration kinetics of CaAl_2O_4 using synchrotron energy-dispersive diffraction,” *Thermochimica Acta*, vol. 302, no. 1–2, pp. 25–34, 1997.
- [16] T. R. Jensen, A. N. Christensen, and J. C. Hanson, “Hydrothermal transformation of the calcium aluminum oxide hydrates $\text{CaAl}_2\text{O}_4 \cdot 10\text{H}_2\text{O}$ and $\text{Ca}_2\text{Al}_2\text{O}_5 \cdot 8\text{H}_2\text{O}$ to $\text{Ca}_3\text{Al}_2(\text{OH})_{12}$ investigated by in situ synchrotron X-ray powder diffraction,” *Cement and Concrete Research*, vol. 35, no. 12, pp. 2300–2309, 2005.
- [17] D. C. Teychenné, “Long-term research into the characteristics of high alumina cement concrete,” *Magazine of Concrete Research*, vol. 27, no. 91, pp. 78–102, 1975.
- [18] R. J. Collins and W. Gutt, “Research on long-term properties of high alumina cement concrete,” *Magazine of Concrete Research*, vol. 40, no. 145, pp. 195–208, 1988.
- [19] K. Y. Ann, T.-S. Kim, J. H. Kim, and S.-H. Kim, “The resistance of high alumina cement against corrosion of steel in concrete,” *Construction and Building Materials*, vol. 24, no. 8, pp. 1502–1510, 2010.
- [20] M. P. Adams and J. H. Ideker, “Influence of aggregate type on conversion and strength in calcium aluminate cement concrete,” *Cement and Concrete Research*, vol. 100, pp. 284–296, 2017.
- [21] G. Falzone, M. Balonis, and G. Sant, “X-AFm stabilization as a mechanism of bypassing conversion phenomena in calcium aluminate cements,” *Cement and Concrete Research*, vol. 72, pp. 54–68, 2015.
- [22] H. G. Midgley and P. B. Rao, “Formation of stratlingite, $2\text{CaO} \cdot \text{SiO}_2 \cdot \text{Al}_2\text{O}_3 \cdot 8\text{H}_2\text{O}$, in relation to the hydration of high alumina cement,” *Cement and Concrete Research*, vol. 8, no. 2, pp. 169–172, 1978.
- [23] A. J. Majumdar, R. N. Edmonds, and B. Singh, “Hydration of secar 71 aluminous cement in presence of granulated blast furnace slag,” *Cement and Concrete Research*, vol. 20, no. 1, pp. 7–14, 1990.
- [24] A. J. Majumdar, B. Singh, and R. N. Edmonds, “Hydration of mixtures of ‘Ciment Fondu’ aluminous cement and granulated blast furnace slag,” *Cement and Concrete Research*, vol. 20, no. 2, pp. 197–208, 1990.
- [25] A. J. Majumdar and B. Singh, “Properties of some blended high-alumina cements,” *Cement and Concrete Research*, vol. 22, no. 6, pp. 1101–1114, 1992.
- [26] M. Collepardi, S. Monosi, and P. Piccioli, “The influence of pozzolanic materials on the mechanical stability of aluminous cement,” *Cement and Concrete Research*, vol. 25, no. 5, pp. 961–968, 1995.
- [27] J. Ding, Y. Fu, and J. J. Beaudoin, “Stratlingite formation in high alumina cement - silica fume systems: significance of sodium ions,” *Cement and Concrete Research*, vol. 25, no. 6, pp. 1311–1319, 1995.
- [28] C. Gosselin, E. Gallucci, and K. Scrivener, “Influence of self heating and Li_2SO_4 addition on the microstructural development of calcium aluminate cement,” *Cement and Concrete Research*, vol. 40, no. 10, pp. 1555–1570, 2010.
- [29] B. Pacewska, M. Nowacka, and M. Aleknevičius, “Investigation of early hydration of high aluminate cement-based binder at different ambient temperatures,” *Journal of Thermal Analysis and Calorimetry*, vol. 109, no. 2, pp. 717–726, 2012.
- [30] N. Y. Mostafa, Z. I. Zaki, and O. H. Abd Elkader, “Chemical activation of calcium aluminate cement composites cured at elevated temperature,” *Cement and Concrete Composites*, vol. 34, no. 10, pp. 1187–1193, 2012.
- [31] Ö. Kirca, Ö. Yaman, and M. Tokyay, “Compressive strength development of calcium aluminate cement-GGBFS blends,” *Cement and Concrete Composites*, vol. 35, no. 1, pp. 163–170, 2013.

- [32] C. Gosselin, "Microstructural development of calcium aluminate cement based systems with and without supplementary cementitious materials," Doctoral thesis, Swiss Federal Institute of Technology in Lausanne, Lausanne, Switzerland, 2009.
- [33] ASTM International, *ASTM C403/C403M-16 Standard Test Method for Time of Setting of Concrete Mixtures by Penetration Resistance*, ASTM International, West Conshohocken, PA, USA, 2016.
- [34] J. H. Ideker, "Early-age behavior of calcium aluminate cement systems," Doctoral thesis, The University of Texas at Austin, Austin, TX, USA, 2008.
- [35] H. Fryda, E. Charpentier, and J. M. Bertino, "Accelerated test for conversion of calcium aluminate cement concrete," in *Proceedings of International Conference on Calcium Aluminate Cements*, pp. 159–169, Avignon, France, June 2008.
- [36] M. Balonis and F. P. Glasser, "The density of cement phases," *Cement and Concrete Research*, vol. 39, no. 9, pp. 733–739, 2009.
- [37] D. L. Rayment and A. J. Majumdar, "Microanalysis of high-alumina cement clinker and hydrated HAC/slag mixtures," *Cement and Concrete Research*, vol. 24, no. 2, pp. 335–342, 1994.